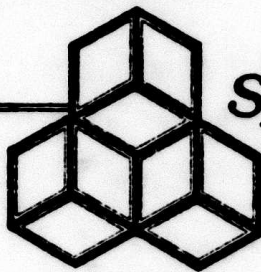


5



Systems, Science and Software

SSS-R-81-5138

(~~SECRET~~)

**THREE-DIMENSIONAL VELOCITY STRUCTURE
OF THE CRUST AND UPPER MANTLE
BENEATH THE NEVADA TEST SITE**

ADA 114241

J. B. Minster
J. M. Savino
W. L. Rodi
T. H. Jordan
J. F. Masso

FINAL REPORT

Sponsored by:

Advanced Research Projects Agency

ARPA Order No. 3291-36

Monitored by AFOSR

Under Contract No. F49620-80-C-0070

August 1981

Approved for public release;
distribution unlimited.

P. O. Box 1620
La Jolla, California
92038

(714)453-0060

DTIC FILE COPY

DTIC
SELECTED
MAY 6 1982
H

ARPA Order No. 3291-36, Program Code No. OF10

Effective Date of Contract: April 1, 1980

Contract Expiration Date: May 30, 1980

Amount of Contract: \$141,556

Contract No. F49620-80-C-0070

Principal Investigator and Program Manager:

Dr. John M. Savino, (714) 453-0060, Ext. 453

This research was supported by the Advanced Research Projects Agency of the Department of Defense and was monitored by the Air Force Office of Scientific Research under Contract No. F49620-80-C-0070.

The views and conclusions contained in this document are those of the authors and should not be interpreted as necessarily representing the official policies, either expressed or implied, of the Defense Advanced Research Projects Agency or the U. S. Government.

UNCLASSIFIED

SECURITY CLASSIFICATION OF THIS PAGE (When Data Entered)

REPORT DOCUMENTATION PAGE		READ INSTRUCTIONS BEFORE COMPLETING FORM
1. REPORT NUMBER AFOSR-TR- 82-0351	2. GOVT ACCESSION NO. AD-A114 244	3. RECIPIENT'S CATALOG NUMBER
4. TITLE (and Subtitle) THREE-DIMENSIONAL VELOCITY STRUCTURE OF THE CRUST AND UPPER MANTLE BENEATH THE NEVADA TEST SITE		5. TYPE OF REPORT & PERIOD COVERED Final Report 4/1/80 - 3/31/81
		6. PERFORMING ORG. REPORT NUMBER SSS-R-81-5138
7. AUTHOR(s) J. B. Minster T. H. Jordan J. M. Savino J. F. Masso W. L. Rodi		8. CONTRACT OR GRANT NUMBER(s) F49620-80-C-0070
9. PERFORMING ORGANIZATION NAME AND ADDRESS Systems, Science and Software P. O. Box 1620 La Jolla, California 92038		10. PROGRAM ELEMENT, PROJECT, TASK AREA & WORK UNIT NUMBERS 61102F 2309/A1
11. CONTROLLING OFFICE NAME AND ADDRESS Advanced Research Projects Agency 1400 Wilson Boulevard Arlington, Virginia 22209		12. REPORT DATE August 1981
		13. NUMBER OF PAGES 218
14. MONITORING AGENCY NAME & ADDRESS (if different from Controlling Office) Air Force Office of Scientific Research Bolling Air Force Base Washington, D. C. 20332		15. SECURITY CLASS. (of this report) Unclassified
		15a. DECLASSIFICATION/DOWNGRADING SCHEDULE
16. DISTRIBUTION STATEMENT (of this Report) Approved for public release; distribution unlimited.		
17. DISTRIBUTION STATEMENT (of the abstract entered in Block 20, if different from Report)		
18. SUPPLEMENTARY NOTES		
19. KEY WORDS (Continue on reverse side if necessary and identify by block number) Crust and upper mantle structure Nevada Test Site Generalized linear inversion Travel-time residuals Magnitude anomalies		
20. ABSTRACT (Continue on reverse side if necessary and identify by block number) We have constructed a model of the three-dimensional velocity structure in the crust and upper mantle beneath NTS. This model was obtained by inversion of teleseismic travel times from NTS explosions reported for a set of globally distributed seismograph stations. Although the geometry is conceptually the "reciprocal" of the classical geometry involving a localized network and dis- tributed teleseismic sources, several important differences emerge.		

DD FORM 1 JAN 73 1473

EDITION OF 1 NOV 58 IS OBSOLETE

UNCLASSIFIED

SECURITY CLASSIFICATION OF THIS PAGE (When Data Entered)

UNCLASSIFIED

SECURITY CLASSIFICATION OF THIS PAGE (When Data Entered)

20. ABSTRACT (continued)

In particular, the data are contaminated by different error processes, and different correction terms need be applied to the raw travel time data. We present algorithms which take advantage of the large number of raw data initially available to improve to some extent the signal-to-noise ratio, and lead to a reduction of the inverse problem to computationally manageable size. In addition, we show how projection operators can be used to formulate an equivalent inverse problem with smaller dimensions which is insensitive to unknown baseline corrections and similar "nuisance" parameters. Finally, we develop an algorithm which permits further reduction in problem size by grouping redundant data with minimal loss of information and with further noise reduction.

The main conclusion of this study is the confirmation of Spence's (1974) suggestion that a high-velocity body underlies the volcanic massif at Pahute Mesa, and that this body extends into the mantle to depths exceeding 100 km. There is a suggestion that the center of the anomaly does not extend vertically beneath the Silent Canyon Caldera, but rather migrates to the north with increasing depth, and that it is surrounded by a more diffuse anomaly which gives rise to an apparent northwest-southeast velocity gradient in the NTS region. Lateral variations beneath Yucca Flat, on the other hand, appear to be confined to the crust, and not to be associated with local anomalies in the mantle.

Although no use is made of teleseismic amplitude information in the inversion, we discuss several possible hypotheses which could account for the observed magnitude anomaly patterns at the Pahute Mesa and Yucca Flat test area, in the light of our preferred structural model.

Accession For	
NTS GRAAL	<input checked="" type="checkbox"/>
DTIC TAB	<input type="checkbox"/>
Unannounced	<input type="checkbox"/>
Justification	
By _____	
Distribution/	
Availability Codes	
and/or	
D:	Spectral
A	

DTIC
COPY
INSPECTED
2

UNCLASSIFIED

SECURITY CLASSIFICATION OF THIS PAGE (When Data Entered)

TABLE OF CONTENTS

<u>Section</u>	<u>Page</u>
I.	INTRODUCTION.
	1
1.1	PROJECT BACKGROUND AND OBJECTIVE
	1
1.2	METHOD OF APPROACH
	2
1.3	MODELING RESULTS
	3
1.4	OUTLINE OF REPORT.
	4
II.	INVERSION METHOD
2.1	RECIPROCAL TELESEISMIC TRAVEL-TIME PROBLEMS
	5
2.1.1	Standard Problem.
	5
2.1.2	Reciprocal Problem.
	11
2.2	LINEAR INVERSE FORMULATION
	15
2.3	DENUISANCING
	19
2.4	DATA GROUPING.
	23
2.5	LINEAR INVERSE ALGORITHM
	29
III.	TRAVEL-TIME DATA
3.1	ORIGINAL DATA SET.
	33
3.2	CONVERSION OF ARRIVAL TIMES TO RESIDUALS.
	39
3.3	CULLING OF TRAVEL-TIME RESIDUALS
	53
3.3.1	Dynamic Screening Procedure
	54
3.3.2	Station Data Grouping
	56
3.3.3	Culling of Station Data
	58
3.3.4	Final Data Set.
	59
3.4	COMPARISON WITH SPENCE'S DATA SET.
	67
3.5	EVENT-AVERAGED RESIDUALS
	73

TABLE OF CONTENTS (concluded)

<u>Section</u>	<u>Page</u>
IV.	INVERSION OF THE DATA SET 78
4.1	STARTING MODEL 78
4.1.1	Vertical Structure. 79
4.1.2	Horizontal Grid 82
4.2	PROBLEM DIMENSIONS AND EIGENVALUE SPECTRUM 97
4.3	DESCRIPTION OF MODEL T65-20. 103
4.4	DATA FITS. 116
V.	INTERPRETATION OF INVERSION RESULTS 125
5.1	GENERAL STRUCTURAL FEATURES OF T65-20. . 129
5.2	THE SOUTHEAST-NORTHWEST VELOCITY GRADIENT 130
5.3	THE PAHUTE ANOMALY 136
5.4	YUCCA VALLEY 140
5.5	RECAPITULATION 142
5.6	MAGNITUDE ANOMALIES. 143
VI.	CONCLUSIONS AND RECOMMENDATIONS 152
VII.	REFERENCES. 155
APPENDIX A:	STATION AND EVENT DATA BASES. 159
APPENDIX B:	NEAR SURFACE VELOCITY MODELS FOR PAHUTE MESA AND RAINIER MESA 170
APPENDIX C:	TRAVEL TIME STATISTICS FOR PAHUTE MESA AND YUCCA FLAT EVENTS 174
APPENDIX D:	VELOCITY PERTURBATIONS IN MODEL T65-20 IN CELLS. 185
APPENDIX E:	SELECTED RESOLVING VECTORS FOR MODEL T65-20. 193

LIST OF ILLUSTRATIONS

<u>Figure</u>		<u>Page</u>
2.1	Schematic illustration of the standard and reciprocal geometry for treating teleseismic travel-time residuals	6
3.1	Locations of initial set of 192 NTS explosions	35
3.2	Comparison of observed reduced travel times to predictions from Models HWA and T7 showing upper mantle triplications for western United States.	37
3.3	Locations of 369 stations in the distance range 25° to 108° from NTS.	38
3.4	Subareas defining the near-surface velocity models used in the calculation of depth corrections for Pahute Mesa events.	42
3.5	Observed travel-time residuals for 303 stations and 58 NTS events.	45
3.6	Final observed travel-time residuals after application of all culling procedures	60
3.7a	Travel-time residuals relative to DUMONT residuals, for five Pahute Mesa events from Spence (1974).	68
3.7b	Travel-time residuals, relative to DUMONT residuals, for three NTS events from Spence (1974)	69
3.8a	Residuals for the eight events used by Spence (1974) relative to DUMONT.	70
3.8b	Ibid. For takeoff angles smaller than 20°. . .	71
3.9c	Ibid. For takeoff angles greater than 20°. . .	72
3.9a	Event-averaged travel-time residuals for NTS events.	75
3.9b	Event-averaged travel-time residuals for Pahute Mesa events.	76
3.9c	Event-averaged travel-time residuals for Yucca Flat events	77

LIST OF ILLUSTRATIONS (continued)

<u>Figure</u>		<u>Page</u>
4.1	Comparison of velocity profiles inferred for the Basin and Range	80
4.2	Initial horizontally layered model of NTS crust and upper mantle velocity structure . . .	84
4.3	Outline of model grid in relation to geographical coordinates	86
4.4	Hit patterns for Layers 1 through 6	89
4.5a	Sketch of typical ray paths along the long dimension of the model grid	95
4.5b	Sketch of typical ray paths along short dimension of the grid.	96
4.6	Largest 141 eigenvalues of the scaled partial derivative matrix plotted in decreasing order .	98
4.7	Trade-off curve between RMS data misfit and norm of the three-dimensional model perturbation.	99
4.8	Velocity perturbations in Layer 1 from inversion models for six values of NDF	101
4.9	Vertical delay time predicted by inversion models for six values of NDF.	102
4.10	Orientation map for inner grid relative to geographical coordinates.	104
4.11	Velocity perturbation contours for Model T65-20.	105
4.12	Orientation map for inner grid relative to geographical coordinates.	112
4.13a	N60W-S60E vertical cross section through Model T65-20.	113
4.13b	S30W-N30E vertical section across Pahute Mesa.	114
4.13c	S30W-N30E vertical section through Yucca Flat.	115

LIST OF ILLUSTRATIONS (concluded)

<u>Figure</u>		<u>Page</u>
4.14	Calculated travel-time residuals for the same event and station sets as Figure 3.6 . . .	117
5.1	Vertical delay time calculated from Model T65-20.	131
5.2	Velocity perturbations in the six layers of Model T65-20.	132
5.3	Simplified geological features in the NTS region distinguishing between alluvial and bedrock surface geology	133
5.4	Bouguer gravity anomaly map for NTS region. . .	135
5.5a	Magnitude anomalies for NTS events.	145
5.5b	Magnitude anomalies for Pahute Mesa	146
5.5c	Magnitude anomalies for Yucca Flat events . . .	147
D.1	Velocity perturbations in each grid cell of Model T65-20.	186

LIST OF TABLES

<u>Table</u>		<u>Page</u>
3.1	Average Velocities of Media at NTS.	43
4.1	Initial Model for Inversion	83
4.2	Horizontal Grid Dimensions.	87
5.1	Model Standard Deviations for T65-20.	126
A.1	Station Data Base	160
A.2	Event Data Base	167
B.1	Near Surface Velocity Models for Pahute Mesa and Rainier Mesa	171
C.1	Station Statistics After Dynamic Screening of Residual Data from 28 Pahute Mesa Explosions.	176
C.2	Station Statistics After Dynamic Screening of Residual Data from 54 Yucca Flat Explosions.	181
E.1	Layers 1 Through 6, Cell (6,6).	195
E.2	Layers 1 Through 6, Cell (6,13)	207

I. INTRODUCTION

1.1 PROJECT BACKGROUND AND OBJECTIVE

The inversion of teleseismic travel-time residuals for determination of three-dimensional earth structure is now recognized as a powerful modeling technique in geophysics (Aki, et al., 1976 and 1977; Husebye, et al., 1976; Rodi, et al., 1980). Our objective in the study reported here is to use this technique to model the three-dimensional structure of the crust and upper mantle beneath the Nevada Test Site (NTS). The data base for this study consists of travel-times of teleseismic P-waves recorded at several hundred globally distributed seismograph stations for approximately 60 of the larger explosions detonated at NTS during the past two decades.

Motivation for this study comes from the need for more accurate estimates of explosion yields based on teleseismic information. Of particular interest are yield estimates based on the amplitudes and dominant periods (i.e., body wave magnitude, m_b) of teleseismically recorded P-waves.

Evidence for the effects of lateral variations in structure at NTS on explosion m_b 's was presented in a study by Alewine, et al., 1977. These authors noted spatial variations in m_b estimates that roughly correlate with structure at the Pahute Mesa (i.e., Silent Canyon caldera) and Yucca Flat test areas. Spence (1974), based on a detailed analysis of P-wave travel-time residuals from six explosions at Pahute Mesa, inferred the existence of a deep (i.e., 170 to 190 km) high velocity anomaly under the Silent Canyon caldera. While he did not attempt to calculate the effect of this anomalous feature on teleseismic m_b 's, he did note observed differences in attenuation of explosion generated P-waves from the BOXCAR explosion (Frasier and Filson, 1972; Trembly and Berg, 1968) that correlate with propagation outside of or through the inferred

anomalous zone. Presumably, these attenuation differences manifest themselves in the dominant periods of observed P-waves, and thus the m_b estimates.

A more recent report which summarizes the current seismological status of both near-source and receiver effects on explosion m_b estimates, with emphasis on differences in upper mantle attenuation, is that of Lundquist, et al. (1980). These authors state that one of the most important propagation effects on m_b is anelastic attenuation. If, as noted above, spatial variations in attenuation in the crust and upper mantle beneath NTS correlate with variations in the three-dimensional velocity structure, then the modeling results of this study may provide an estimate of the magnitude of this effect on explosion m_b 's.

1.2 METHOD OF APPROACH

The inversion modeling technique adopted in this study is based on a formulation of the earth structure problem originally proposed by Aki, et al., 1977. We start with a layered medium, extending over the crust and upper mantle in the region of interest, and divide each layer into blocks of varying dimensions. Within each block, we assign a parameter which describes the velocity perturbation from an average value in the respective layer. Most previous applications of this technique (Aki, et al., 1976 and 1977; Husebye, et al., 1976; Rodi, et al., 1980) have treated the case where the travel-time data set to be inverted was obtained from recording stations located above the volume of earth to be modeled and earthquake and explosion sources distributed globally at teleseismic distances. In the present study, we treat the "reciprocal" problem: modeling three-dimensional structure beneath a local array of events (i.e., NTS explosions) based on an inversion of teleseismic travel-time data obtained from

globally distributed seismograph stations. While the basic relationship between travel times and velocity structure is reciprocal with respect to source and receiver, it is necessary to consider in detail the sources of error in the travel-time data and the corrections applied to the data in order to demonstrate that the problem, as formulated in this study, is completely reversible. Spence (1974), who analyzed some of the same travel-time data that are included in our study, considered this aspect of the problem. In this study we consider it in the context of setting up a linear inverse problem.

Central to the modeling approach adopted here are linear inversion techniques based on the formulations of Backus and Gilbert (1970), Wiggins (1972) and Jordan (1973). These techniques find an optimal earth model that best fits an observed geophysical data set while maintaining a specific degree of smoothness in the model. During the course of previous applications of this technique (Savino, et al., 1977; Rodi, et al., 1980), we developed a smoothing procedure for quelling lateral variations in the inversion model that are not required to fit the observed data.

1.3 MODELING RESULTS

The more robust features of the model obtained in this study for the crust and upper mantle structure beneath NTS are the following:

1. A velocity gradient trending across the entire NTS model region from northwest (high velocity) to southeast (low velocity). This gradient is present, to some extent, in all layers of the final model which extends to a depth of approximately 150 km.
2. A high velocity anomaly localized beneath Pahute Mesa. The location of this anomaly

varies with depth: it is very nearly centered on the Silent Canyon Caldera in the shallow crustal layer and migrates northward with increasing depth.

1.4 OUTLINE OF REPORT

The remainder of this report is organized as follows. In Section II we outline the formulation of the problem as a linear inverse problem and discuss in some detail the similarities and difference between the present situation and the more classical one where teleseismic travel times are recorded at a local array of stations. In addition, we develop analytical tools designed to handle very large data sets without losing the full power of linear estimation procedures for the determination of variances, resolution and trade-offs.

The data set is then presented in Section III; editing, culling and preprocessing of the raw data represents a major task which must be a prelude to actual inversion, and which is described in detail. Inversion of the final data set is the object of Section IV, which contains a thorough description of our preferred model (Model T65-20). In addition to the presentation of the model, we shall dwell on the trade-off between model parameters, variance of estimation, and resolvability of several important features. Interpretation of the model in the geological and geophysical context of NTS is discussed in Section V, together with considerations pertaining to the effects of the three-dimensional structure beneath NTS on the teleseismic signature of NTS events. Finally, we summarize the salient conclusions of this study in Section VI, and identify several aspects of the work for which we recommend further study.

II. INVERSION METHOD

2.1 RECIPROCAL TELESEISMIC TRAVEL-TIME PROBLEMS

The inversion of teleseismic travel-time residuals for three-dimensional block models of crust and upper mantle structure is now a standard geophysical technique which has been applied in several studies (e.g., Aki, et al., 1977; Husebye, et al., 1976; Rodi, et al., 1980). In these applications, the structure beneath a local station network is determined from P wave travel times observed from teleseismic events. In the present study, we have the "reciprocal" or dual problem: determining structure beneath a local array of events (NTS explosions) from travel times observed at teleseismic stations. While the basic relationship between travel time and velocity structure is reciprocal with respect to source and receiver, it is necessary to consider the sources of error in travel-time data and the corrections applied to the data in order to demonstrate the equivalence of the dual inverse problems. Spence (1974), who analyzed some of the same data as we use here, considered this aspect of the problem. Here we consider it in more detail.

2.1.1 Standard Problem

In Figure 2.1 we compare the basic geometries of the standard and reciprocal teleseismic travel-time problems. In the standard problem (Figure 2.1a) the station network is at the earth's surface and records each of several globally distributed teleseismic earthquakes. The velocity structure beneath the station network, extending from sea level (or some other datum plane) to a depth roughly twice the horizontal aperture of the network, is modeled as a three-dimensional grid of homogeneous blocks. The velocity of each block is to be determined from arrival time data measured from each event.

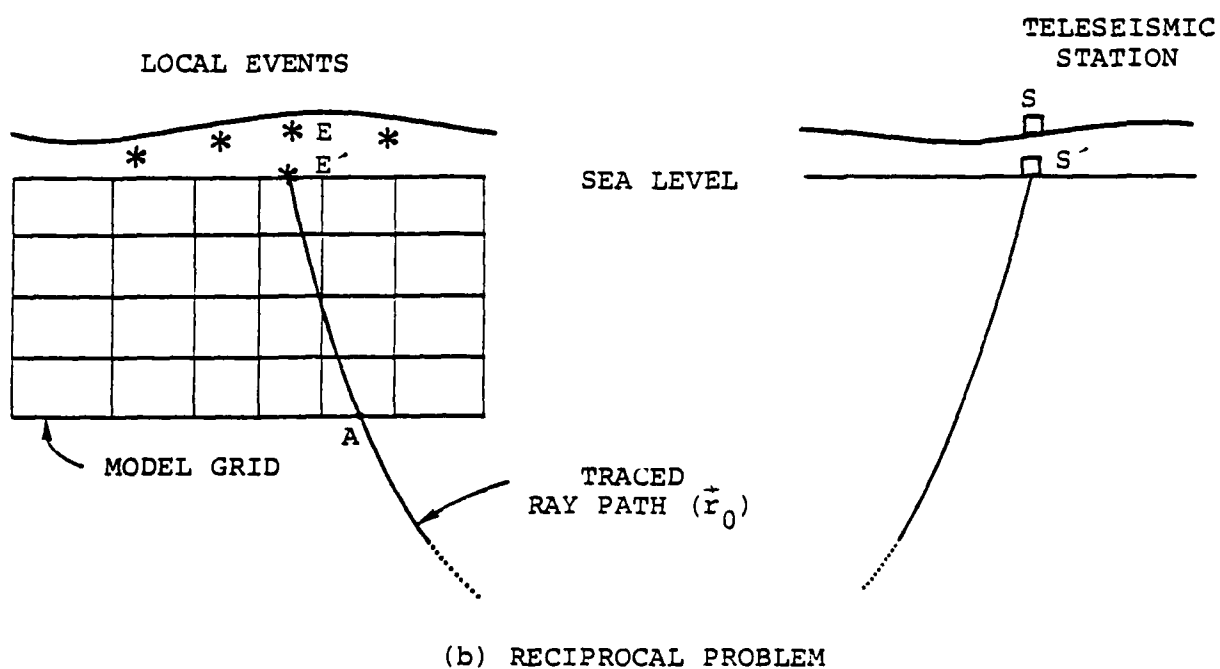
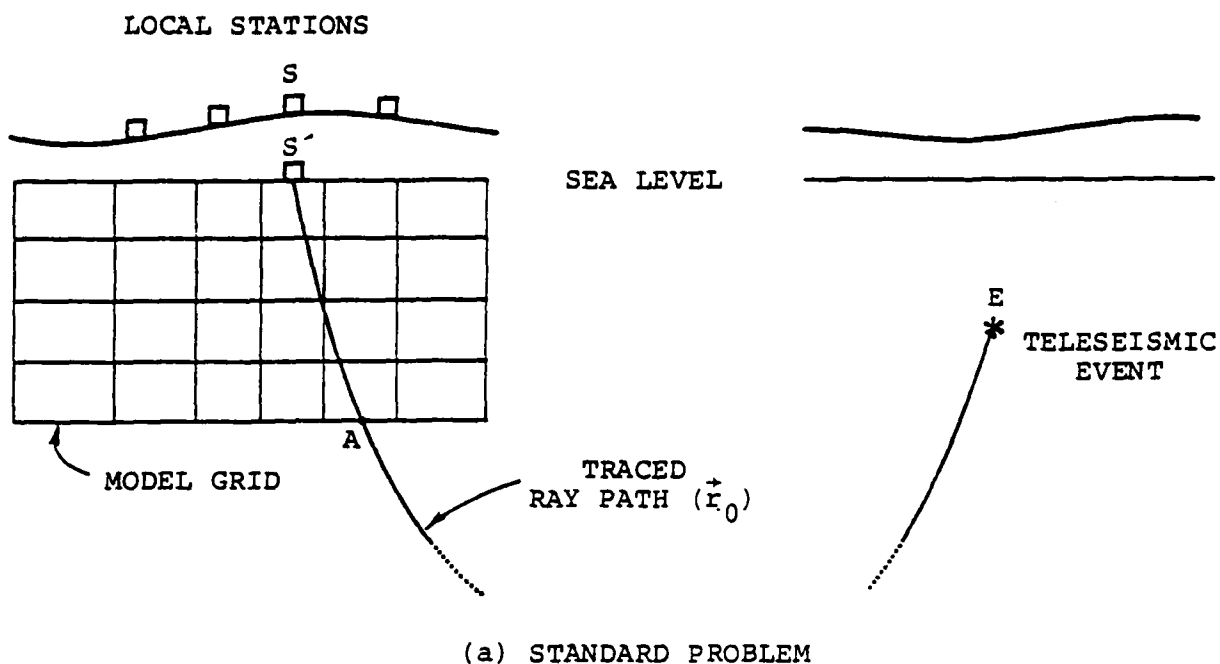


Figure 2.1. Schematic illustration of the standard and reciprocal geometry for treating teleseismic travel-time residuals.

A raw datum is the observed first-motion arrival time, T_{ES} , from an Event E to a Station S. It is assumed that reasonably accurate estimates of the event origin time T_E^{orig} , focal depth z_E , epicentral distance Δ_{ES} , and back-azimuth β_{ES} are available. The arrival time is then converted to a travel-time residual, Δt_{ES} , by the formula

$$\Delta t_{ES} = T_{ES} - T_E^{\text{orig}} - t_{ES}^{\text{table}} - t_{SS'}^{\text{elev}} \quad (1)$$

where

Δt_{ES} = observed travel-time residual
(from Event E to Station S)

T_{ES} = observed arrival time

T_E^{orig} = estimated origin time of event

t_{ES}^{table} = Herrin (or J-B) table travel time
for distance Δ_{ES} and focal depth z_E

$t_{SS'}^{\text{elev}}$ = station elevation correction.

Referring to Figure 2.1a, the Herrin table correction predicts the travel time through a spherically symmetric average earth between the estimated event location (Point E) to the point at sea level below the station (Point S'). The station elevation correction predicts the difference between the travel time from E to S' and that between E and the true station location S. The elevation correction requires that the velocity structure between S and S' be known.

The dependence of the travel-time residual Δt_{ES} on the slowness structure $u(x,y,z)$ in the model grid ($u = v^{-1}$, $v =$ P velocity) is given in terms of an initial plane-layered slowness model $u_0(z)$ and the ray path \vec{r}_0 traced through the initial model. The ray is traced from the point S' in the

direction of the back-azimuth β_{ES} downward to the bottom of the model grid (Point A), using the ray parameter predicted by the Herrin table. To first order in $(u - u_0)$ then,

$$\Delta t_{ES} = \int_A^{S'} ds \Delta u(\vec{r}_0) + b_E + c_S + e_{ES} \quad (2)$$

where

$$\begin{aligned} \Delta u(x, y, z) &= \text{unknown slowness perturbation} \\ &= u(x, y, z) - u_0(z) \\ b_E &= \text{event-dependent baseline error} \\ c_S &= \text{station-dependent baseline error} \\ e_{ES} &= \text{error varying with station and event.} \end{aligned}$$

The first term in Equation (2) is the integral of the slowness perturbation along the ray path \vec{r}_0 between sea level (Point S') and the bottom of the model grid (Point A). All other contributions to the travel-time residual are considered as one of three types of error: errors which are constant among the data at all stations for a given event (b_E), errors constant among the data from all events at a given station (c_S), and errors which vary from event to event and station to station (e_{ES}). The errors b_E and c_S are effectively event and station time terms, respectively.

The e_{ES} term represents measurement errors (reading errors) in the observed arrival times. The measurement errors can be treated as zero-mean, random and uncorrelated between data. We thus treat them stochastically as

$$\begin{aligned} E[e_{ES}] &= 0 \\ \text{Var}[e_{ES}] &= \sigma_{ES}^2 \end{aligned} \quad (3)$$

where the variance σ_{ES}^2 is given. There are other error terms which are also event and station dependent, but the variation with either station or event is very small. Therefore, we treat them as baseline errors.

We identify only one station baseline error (c_S): an error in the station elevation correction caused by the use of inexact elevation or inexact model of the surface to sea level velocity structure. At a given station this error, and the correction itself, varies only slightly from event to event (see Section 3.2). Typically, the elevation correction error is very small compared to the expected measurement error (σ_{ES}) so c_S can be ignored.

In the event baseline error b_E we include the following contributions:

1. Error in the estimated origin time.
2. Error in the Herrin table time due to a mislocation of the event (error in Δ_{ES} or z_E).
3. Error in the Herrin table time due to the earth's ellipticity.
4. Network clock (timing) error, causing all stations to be mistimed by an equal amount.
5. Waveform bias: reading the arrival time of a point other than first motion on the waveform, such as the first peak or trough. This can give more accurate readings and if the waveforms from an event copy from station to station, the resulting bias sets acts as a baseline error (Savino, et al., 1977).
6. The quantity $\int_A^{S'} ds (u_0 - u_H)$ (see Figure 2.1a), where u_0 is the initial model and u_H is the Herrin earth model.

7. The quantity $\int_E^A (u - u_H)$, which represents travel-time delays caused by velocity perturbations below the model grid all the way back to the source.

We note that Errors 3 and 6 could be corrected for but as long as the other event baseline errors are present there is no advantage in doing so.

The treatment of Errors 2, 3, and 6 as station-independent baseline errors is an approximation which requires the variation in ray parameter across the network to be small, thus making the ray paths from a given event nearly parallel beneath the network. This approximation is very good when the aperture of the network is small compared to the epicentral distance. The station dependence of Error 7 is likewise negligible, at least when the earth's slowness below the model grid has no lateral variations; i.e., when $(u - u_H)$ is one-dimensional.

The travel-time delays (or advances) caused by lateral variations in velocity outside the model grid (Error 7) can be a problem. It is appropriate to treat such delays from a particular event as a station-independent baseline error only if the horizontal scale of the velocity anomaly exceeds the width of the packet of ray paths intersecting the anomaly. The closer the anomaly is to the event, the easier it is to satisfy this requirement, a limiting case being an anomaly in the source region which uniformly delays the travel times to all stations. The worst problem then stems from velocity anomalies below but near the model grid. If these are of small-scale and large amplitude, their effect cannot be treated as a baseline error and should be modeled either with a deeper model grid or as a spatially varying error term (e.g., linear trend). We note, however, that this analysis of the deep anomaly problem is based on a first-order theory of travel-times. The actual nonlinear dependence of travel time on slowness may actually reduce the effect of deep small-scale anomalies. A

wavefront perturbed by a velocity anomaly heals as it propagates (Claerbout, 1976).

Given that c_s is negligible, Equation (2) thus takes the form of a linear inverse problem, with the observed residuals Δt_{ES} linear functions of the unknown model Δu and containing a combination of baseline errors (b_E) and random measurement errors (e_{ES}). We will later formulate the problem with the baseline errors as "nuisance parameters" and convert the problem to a more standard form.

We note that the presence of c_s , if it were not negligible, would not make the inverse problem intractable. Any number of nuisance parameters can be accommodated. However, having to deal with both station and event baseline errors would make the inverse calculations less efficient and, more importantly, the presence of both would seriously degrade the resolving power of the data for the velocity structure.

2.1.2 Reciprocal Problem

The geometry of the reciprocal travel-time residual problem is illustrated in Figure 2.1b. In this problem, the three-dimensional structure beneath a "network" of buried explosions is to be determined from arrival times observed at globally distributed seismic stations. We assume that the shots are above sea level so we can use sea level as a datum plane. The travel-time residual Δt_{ES} for a given station and event is then obtained as

$$\Delta t_{ES} = T_{ES} - T_E^{\text{orig}} - t_{ES}^{\text{table}} - t_{EE'}^{\text{elev}} \quad (4)$$

where T_{ES} and T_E^{orig} are as before and

t_{ES}^{table} = Herrin table travel-time for distance Δ_{ES} and surface focus.

$t_{EE'}^{elev}$ = event elevation correction.

The event elevation correction plays the role of the station elevation correction in Equation (1), although the correction now involves the structure only below the shot depth to sea level. The use of the surface-focus Herrin correction would seem to warrant a second elevation correction in Equation (4), for the teleseismic station. However, this correction acts like a focal depth error in the standard problem and can be overlooked.

The travel-time residual Δt_{ES} can be modeled as in the standard problem; an initial plane layered model of the structure below the events is used for tracing a ray path from the Point E' downward through the model grid to the Point A (see Figure 2.1b). (The direction of the ray is now the event-station azimuth instead of the back-azimuth.) We thus write

$$\Delta t_{ES} = \int_A^{E'} ds \Delta u(\vec{r}_0) + b_S + c_E + e_{ES} . \quad (5)$$

This is Equation (2) with E and S interchanged. While most of the sources of error are the same in the two problems, their distributions into the three error terms differ. For the reciprocal problem to be identical in form to the standard problem, we must demonstrate that c_E in Equation (5) is negligible and that e_{ES} can be treated as a random error term.

The station-dependent, event-dependent errors, e_{ES} , now include:

1. measurement error,
2. station clock errors,

3. error in the Herrin table time due to event mislocation.

Since globally distributed stations are timed independently, and the events are widely separated in time, station timing errors cannot be treated as baseline errors. While the timing errors at a station may have a systematic (nonrandom) variation with time, depending on the intervals between clock calibration, there is inadequate information available to account for this correlation. Therefore, we must treat timing errors like measurement errors: zero-mean and independent. In the reciprocal problem, errors due to event mislocation (Error 3) are event and station dependent. However, they vary systematically with station location and cannot be treated as independent between data. For NTS explosions, precise locations are available so this error can be neglected. Without precise locations, the event mislocations would have to be treated as nuisance parameters in a joint hypocenter/velocity determination.

Contributions to the station baseline errors (b_s) include:

1. The quantity $\int_A^{E'} ds (u_0 - u_H)$.
2. The quantity $\int_s^A ds (u - u_H)$: delays from velocity anomalies outside the model region.
3. Station elevation correction, which was not applied to the travel-time residual.

Errors 1 and 2 were discussed above with regard to the standard problem, where they acted as event baseline errors. Error 3 is analogous to a Herrin time error in the standard problem caused by errors in focal depth.

The remaining sources of error act as event baseline errors (c_E):

1. Error in the event origin time.
2. Error in the event elevation correction.

For an NTS explosion, the origin time error is insignificant. The errors in the event elevation corrections are assumed to be smaller than the expected measurement error, as we assumed for the station elevation correction errors in the standard problem.

We have ignored waveform bias as an error because the peak-and-trough reading method is not appropriate for the reciprocal problem.

We see that the standard and reciprocal teleseismic travel-time problems have identical forms, given certain assumptions about the sources of data errors. For the reciprocal problem, this form reduces to

$$\Delta t_{ES} = \int ds \Delta u + b_S + e_{ES} \quad (6)$$

To summarize, we drop the c_E term in Equation (5) and treat e_{ES} as an independent zero-mean error under the following assumptions:

- Station clock errors and measurement errors are independent and zero-mean.
- Event elevation corrections are accurate.
- The locations and origin times of the events are known exactly.

Departing from these assumptions would require adding additional terms to Equation (6) and treating them as additional nuisance parameters in the inverse problem.

2.2 LINEAR INVERSE FORMULATION

Given travel-time residuals from several stations ($S = 1, 2, \dots$) and events ($E = 1, 2, \dots$), and a block model representation of the slowness perturbation $\Delta u(x,y,z)$, we can express Equations (3) and (6) as a discrete linear inverse problem of the form

$$E[d] = Am + Bn$$

$$\text{Var}[d] = \Sigma \tag{7}$$

where d is the data vector, m a model parameter vector, n a nuisance parameter vector, and Σ a data covariance matrix. These are defined by

$$d = (\Delta t_{11}, \Delta t_{21}, \Delta t_{31}, \dots, \Delta t_{12}, \Delta t_{22}, \dots)^T$$

$$\Sigma = \text{diag} (\sigma_{11}^2, \sigma_{21}^2, \sigma_{31}^2, \dots, \sigma_{12}^2, \sigma_{22}^2, \dots)$$

$$m = (\Delta u_{111}, \Delta u_{211}, \Delta u_{311}, \dots, \Delta u_{121}, \Delta u_{221}, \dots)^T$$

$$n = (b_1, b_2, \dots)^T$$

We have denoted the slowness perturbation in the (i,j,k) 'th block of the three-dimensional model grid as Δu_{ijk} .

The matrices A and B , respectively, contain the partial derivatives of travel-time with respect to the block slownesses and station baseline errors. From Equation (6) we see that the derivative of a residual with respect to the slowness of a block is the length of the ray path segment intersecting the block. A given ray path intersects very few of the blocks so most elements in A are zero. Also from Equation (6), we see that a given residual depends on only one baseline; given the ordering of the data defined above (event counter varying the fastest), B has the blocked structure

$$B = \begin{bmatrix} 1 & 0 & 0 & 0 \\ 1 & 0 & 0 & 0 & \dots \\ 1 & 0 & 0 & 0 \\ \vdots \\ 0 & 1 & 0 & 0 \\ 0 & 1 & 0 & 0 & \dots \\ 0 & 1 & 0 & 0 \\ \vdots \\ \vdots \end{bmatrix} \quad (8)$$

We should mention that in setting up the problem in this form, there is no requirement that the data set be complete; i.e., that a residual Δt_{ES} exist for every event-station pair. Our NTS data set, in fact, is very incomplete: data were available for only 20 percent of the possible event-station pairs defined by our final event and station sets (see Section III).

Even though the NTS data set is incomplete, the system represented by Equation (7) is quite large. After several steps of data culling (see Section III), the data set consists of 2597 residuals observed at 221 stations. The model grid we designed (Section IV) contains 1188 blocks. Therefore, the system contains 2597 equations and 1409 unknowns (1188 in m and 221 in n). The 221 nuisance parameters (station baselines), however, are of no interest.

Instead of applying generalized linear inverse techniques directly to a system this large, we first employed two special techniques that reduce the system to a simpler and smaller one: a "data grouping" technique, which effectively averages together redundant data and thus reduces their number, and a "denuisancing" technique, which eliminates the nuisance vector n from the system by constructing an equivalent inverse problem involving only m . Together these procedures reduced

the problem to a 1173 by 1188 system, which costs about a third as much to solve as the original system. Before describing these special techniques and the inversion algorithm itself, let us define the optimality criterion we use to obtain a solution to Equation (7).

We define a solution to Equation (7) as estimates \tilde{m} and \tilde{n} which satisfy the damped least squares criterion

$$(\mathbf{d} - \mathbf{A}\tilde{m} - \mathbf{B}\tilde{n})^T \Sigma^{-1} (\mathbf{d} - \mathbf{A}\tilde{m} - \mathbf{B}\tilde{n}) + \theta \tilde{m}^T \mathbf{W}^{-1} \tilde{m} + \phi \tilde{n}^T \mathbf{Z}^{-1} \tilde{n}$$

is minimum (9)

where θ and ϕ are scalar trade-off parameters and \mathbf{W} and \mathbf{Z} are specified parameter weighting matrices, both assumed positive definite. This criterion is equivalent to the optimality criteria defined by Backus and Gilbert (1970) and Jordan (1972), but we have expressed it in terms of two parameter vectors instead of the usual one.

The first term in Equation (9) is a measure of the "misfit" between the observed data, \mathbf{d} , and the data predicted by the solution (\tilde{m}, \tilde{n}) . The second and third terms are norms of \tilde{m} and \tilde{n} , respectively. These terms stabilize the solution by damping components of \tilde{m} and \tilde{n} that do not contribute much to fitting the data, but which may cause the solution to become physically implausible.

In the teleseismic residual problem, where the nuisance parameters are baseline errors, it is useful to interpret the product $\phi^{-1}\mathbf{Z}$ as a prior variance assigned to \mathbf{n} :

$$\text{Var}[\mathbf{n}] = \phi^{-1}\mathbf{Z} \quad . \quad (10)$$

Considering the sources of error contributing to \mathbf{n} , it is appropriate to make this variance very large compared to the variance assigned to the measurement errors, Σ . In our

computations, we used $\Sigma = I$, $Z = I$, $\phi = 10^{-6}$ (I = unit matrix); i.e., the baseline errors are expected to be of order 1000 times larger than the measurement errors. The effect of this is that \tilde{n} is barely damped, closely approximating $\phi = 0$ in Equation (9). This allows \tilde{n} to adjust freely to fit the data.

In selecting θ and W for the damping of \tilde{m} , the prior variance interpretation is not very useful. Instead, we set up the model norm to be a measure of the roughness of the velocity structure. That is, we construct W^{-1} as a nondiagonal matrix such that the model norm is a discrete approximation to the following integral:

$$\tilde{m}^T W^{-1} \tilde{m} \doteq \int dx \int dy \int dz [(\partial_x \Delta \tilde{u})^2 + (\partial_y \Delta \tilde{u})^2 + \lambda^{-2} (\Delta \tilde{u})^2]. \quad (11)$$

With this definition, $\tilde{m}^T W^{-1} \tilde{m}$ is sensitive to lateral gradients in $\Delta \tilde{u}$ of a scale smaller than λ , which we set to a large value (300 km). In this way, θ allows us to control a trade-off between the smoothness of the velocity model \tilde{m} and the fit it provides to the data. The best value of θ cannot be determined in advance. Rather, it must be selected on the basis of examining models and their predicted data computed with several values of θ .

In the following developments we will use some abbreviations to simplify expressions. We will use a circumflex above symbols to denote that quantities have been normalized by the factor $\Sigma^{-\frac{1}{2}}$. Thus,

$$\begin{aligned} \hat{d} &= \Sigma^{-\frac{1}{2}} d \\ \hat{A} &= \Sigma^{-\frac{1}{2}} A \\ \hat{B} &= \Sigma^{-\frac{1}{2}} B \end{aligned} \quad (12)$$

We will also apply this notation to quantities defined later, without further explanation.

2.3 DENUISANCING

In the reciprocal teleseismic residual problem, in which the nuisance parameters are station baseline errors, denuisancing reduces to a zero-meaning operation performed on the data and partial derivatives. The mean residual at each station is subtracted from all the individual residuals determined for the station. Denoting the mean residual at Station S as $\overline{\Delta t}_S$ and the zero-meaned residuals as Δt_{ES}^{zm} , we have

$$\overline{\Delta t}_S = \frac{\sum_E \sigma_{ES}^{-2} \Delta t_{ES}}{\sum_E \sigma_{ES}^{-2}},$$

$$\Delta t_{ES}^{zm} = \Delta t_{ES} - \overline{\Delta t}_S, \quad (13)$$

where the sums in Equation (13) are over only those events recorded by the station. We see from Equation (13) that $\overline{\Delta t}_S$ is a weighted mean, each residual weighted by its inverse variance. Equations (6) and (13) imply that the dependence of Δt_{ES}^{zm} on the slowness structure is given by

$$\Delta t_{ES}^{zm} = \int ds \Delta u(\vec{r}_{ES}) - \frac{\sum_E \sigma_{ES}^{-2}}{\sum_E \sigma_{ES}^{-2}} \int ds \Delta u(\vec{r}_{ES}) + e_{ES} - \bar{e}_S \quad (14)$$

where $\rho_{ES} = \sigma_{ES}^{-2} / \sum_E \sigma_{ES}^{-2}$ and \vec{r}_{ES} is the initial ray path traced from Event E toward Station S. Thus Δt_{ES}^{zm} depends on the structure beneath all the events recorded by S. However, the zero-meaning cancels the dependence on b_S . In terms of the discrete block model of Δu , the combination of integrals in Equation (14) corresponds to zero-meaning the partial derivatives of Δt_{ES} in the same way that the data are zero-meaned.

Another common procedure for removing the dependence of the residuals on b_s is to reference the residuals to those of a fixed event E_0 :

$$\Delta t_{ES}^{\text{ref}} = \Delta t_{ES} - \Delta t_{E_0S} \quad (15)$$

Relative residuals are useful for data display and were used by Spence (1974) in his analysis of the NTS data. However, zero-meaning is the proper denuisancing procedure to use in a formal inversion of the data.

The zero-meaning of travel-time residuals and their partial derivatives, as a way to eliminate baseline errors from the inverse problem, was derived by Aki, et al. (1977). This basic denuisancing technique has been extended and generalized by Savino, et al. (1977), Pavlis and Booker (1980), Spencer and Gubbins (1980) and Rodi, et al. (1981). Here we summarize the algorithm of Rodi, et al. (1981) in the context of solving Equations (7) and (9). The general denuisancing algorithm is a required part of the data grouping algorithm described in Section 2.4.

To begin, we note that Equation (9) is equivalent to the coupled normal equations:

$$(\hat{A}^T \hat{A} + \theta W^{-1}) \tilde{m} + \hat{A}^T \hat{B} \tilde{n} = \hat{A}^T \hat{d} \quad (16a)$$

$$\hat{B}^T \hat{A} \tilde{m} + (\hat{B}^T \hat{B} + \phi Z^{-1}) \tilde{n} = \hat{B}^T \hat{d} \quad (16b)$$

Solving Equation (16a) for \tilde{n} we obtain

$$\tilde{n} = \hat{B}^- (\hat{d} - \hat{A} \tilde{m}) \quad (17)$$

where

$$\hat{B}^- = (\hat{B}^T \hat{B} + \phi Z^{-1})^{-1} \hat{B}^T \quad (18)$$

The matrix \hat{B}^- is a damped generalized inverse of \hat{B} . Now we define the symmetric matrix Q_B by

$$Q_B = I - \hat{B}\hat{B}^- . \quad (19)$$

Then substituting \tilde{n} in Equation (17) into Equation (16a) gives

$$(\hat{A}^T Q_B \hat{A} + \theta W^{-1}) \tilde{m} = \hat{A}^T Q_B \hat{d} . \quad (20)$$

We can simplify this with the following substitutions:

$$\hat{A}_V = Q_B^{\frac{1}{2}} \hat{A} \equiv \Sigma^{-\frac{1}{2}} A_V \quad (21a)$$

$$\hat{d}_V = Q_B^{\frac{1}{2}} \hat{d} \equiv \Sigma^{-\frac{1}{2}} d_V . \quad (21b)$$

Then Equation (20) becomes

$$(A_V^T \Sigma^{-1} A_V + \theta W^{-1}) \tilde{m} = A_V^T \Sigma^{-1} d_V . \quad (22)$$

Equation (22) is the normal equation that results from the minimization condition

$$(d_V - A_V \tilde{m})^T \Sigma^{-1} (d_V - A_V \tilde{m}) + \theta \tilde{m}^T W^{-1} \tilde{m} \text{ is minimum} . \quad (23)$$

Comparing to Equations (7) and (9), we see that \tilde{m} is a solution to an equivalent inverse problem that does not involve the nuisance vector \tilde{n} ; namely,

$$E[d_V] = A_V m$$

$$\text{Var}[d_V] = \Sigma . \quad (24)$$

Equations (23) and (24) are a standard linear inverse problem and we discuss its solution in Section 2.5.

We call the operator $Q_B^{\frac{1}{2}}$ in Equation (21) a denuisancing operator, and d_v and A_v denuisanced data and partial derivatives, respectively. It is convenient for computation to evaluate $Q_B^{\frac{1}{2}}$, and the damped generalized inverse \hat{B}^- , in terms of the singular value decomposition (SVD) of \hat{B} (Lanczos, 1961; Wiggins, 1972). Let

$$\hat{B} Z^{\frac{1}{2}} = S \Gamma T^T \quad (25)$$

where the columns of S and T are orthonormal eigenvectors and Γ is a diagonal matrix of positive eigenvalues:

$$S^T S = T^T T = I$$

$$\Gamma = \text{diag} (\gamma_1, \gamma_2, \dots) > 0. \quad (26)$$

Then we have

$$\begin{aligned} \hat{B}^- &= Z^{\frac{1}{2}} T \Gamma (\Gamma^2 + \phi I)^{-1} S^T \\ Q_B &= I - S \Gamma^2 (\Gamma^2 + \phi I)^{-1} S^T \\ Q_B^{\frac{1}{2}} &= I - S [I - \phi^{\frac{1}{2}} (\Gamma^2 + \phi I)^{-\frac{1}{2}}] S^T \end{aligned} \quad (27)$$

When $\phi \ll \gamma_k^2$, which is the case for the value of ϕ we selected for the NTS inversion (see Section 2.2), $Q_B^{\frac{1}{2}}$ approximates an orthogonal projection operator:

$$Q_B^{\frac{1}{2}} \underset{\phi \approx 0}{\approx} I - S S^T. \quad (28)$$

Denuisancing then removes the projections of d and A onto the null space of B .

In the reciprocal teleseismic residual problem, B has the simple structure shown in Equation (8). The denuisancing

operator $Q_B^{\frac{1}{2}}$ then reduces to a block diagonal matrix. With $\phi=0$, each block acts as a zero-meaning operator on the data and partial derivatives from a particular station, as in Equation (13).

2.4 DATA GROUPING

It is well known that a group of data having an identical dependence on unknown parameters can, with no loss of information about the parameters, be replaced by an average datum. Thus,

$$E[d_i] = a^T_m$$

$$\text{Var}[d_i] = \sigma_i^2, \quad i = 1, \dots, N,$$

where the d_i are N scalar data and a is a vector of partial derivatives, is equivalent to

$$E[\bar{d}] = a^T_m$$

$$\text{Var}[\bar{d}] = \bar{\sigma}^2$$

where

$$\bar{\sigma}^{-2} = \sum_i \sigma_i^{-2}$$

$$\bar{d} = \bar{\sigma}^2 \sum_i \sigma_i^{-2} d_i$$

Of course, there would be a cost advantage in replacing the N data d_i by the single datum \bar{d} in an inversion.

In the NTS inverse problem, we have a situation similar to this. Travel-time residuals at a group of close-together stations have ray paths which predominantly hit the same model blocks. Therefore, their partial derivatives with respect to Δu are approximately equal and can be replaced by a common set

of partial derivatives obtained from an average ray path. The same group of data are not, however, redundant with respect to the station baselines; each datum depends on a different baseline error. Therefore, a simple averaging of the data does not produce a datum with the same information about the parameters.

If we approximate the dependence of N travel-time residuals on Δu by N_0 distinct ray paths ($N_0 < N$), then the partial derivative matrix A has only N_0 distinct rows and $(N - N_0)$ repeated rows. We can express this as

$$A = FA_0 \quad (29)$$

where A_0 contains the distinct rows. The matrix F is $N \times N_0$ and expands A_0 into A . Each row of F contains a one and $(N_0 - 1)$ zeros.

The inverse problem can now be written as

$$E[d] = FA_0 m + Bn$$

$$\text{Var}[d] = \Sigma \quad (30)$$

where we assume that B cannot be factored with the matrix F .

If B were zero, simple variance-weighted averaging of d would be the appropriate way to reduce the problem size without losing information about m . Formally, this can be written as

$$\begin{aligned} \Sigma_0^{-1} &= F^T \Sigma^{-1} F, \\ d_0 &= \sum_0 F^T \Sigma^{-1} d, \end{aligned} \quad (31)$$

implying, with $B = 0$, that

$$E[d_0] = A_0 m$$

$$\text{Var}[d_0] = \Sigma_0 .$$

We note that

$$(\Sigma_0 F^T \Sigma^{-1}) F = I . \quad (32)$$

With B not zero we must take a different approach. Let us seek a new nuisance matrix B_1 and new data vector d_1 , where d_1 has length N_0 and covariance Σ_0 , such that an optimal solution \tilde{m} to

$$E[d_1] = A_0 m + B_1 n_1$$

$$\text{Var}[d_1] = \Sigma_0 \quad (33)$$

is identical to the \tilde{m} solving the original problem in Equation (7). Since the original nuisance vector n is of no interest, we allow d_1 to depend on a different nuisance vector which we have denoted n_1 . In analogy with Equation (9), an optimal solution to Equation (34) is defined by the criterion

$$\begin{aligned} (d_1 - A_0 \tilde{m} - B_1 \tilde{n}_1)^T \Sigma_0^{-1} (d_1 - A_0 \tilde{m} - B_1 \tilde{n}_1) + \theta \tilde{m}^T W^{-1} \tilde{m} + \phi_1 \tilde{n}_1^T Z_1^{-1} \tilde{n}_1 \\ = \text{minimum} . \end{aligned} \quad (34)$$

We also allow ϕ and Z to differ from the original problem. The objective then is to find the d_1 , B_1 , ϕ_1 and Z_1 that make the \tilde{m} satisfying Equation (34) identical to the \tilde{m} satisfying the original criterion in Equation (9).

For convenience, we define the following normalized quantities:

$$\begin{aligned}
\hat{F} &= \Sigma_0^{-\frac{1}{2}} F \Sigma^{\frac{1}{2}} \\
\hat{A}_0 &= \Sigma_0^{-\frac{1}{2}} A_0 \\
\hat{B}_1 &= \Sigma_0^{-\frac{1}{2}} B \\
\hat{d}_0 &= \Sigma_0^{-\frac{1}{2}} d_0 \\
\hat{d}_1 &= \Sigma_0^{-\frac{1}{2}} d_1 \quad .
\end{aligned} \tag{35}$$

We note that $\hat{F}^T \hat{F} = I$, and $\hat{A} = \hat{F} \hat{A}_0$.

Using the development of Section 2.3, we can immediately write the denuisanced normal equation for \tilde{m} resulting from Equation (34):

$$(\hat{A}_0^T Q_{B_1} \hat{A}_0 + \theta W^{-1}) \tilde{m} = \hat{A}_0^T Q_{B_1} \hat{d}_1 \tag{36}$$

where

$$\begin{aligned}
Q_{B_1} &= I - \hat{B}_1 \hat{B}_1^{-1} \\
\hat{B}_1^{-1} &= (\hat{B}_1^T \hat{B}_1 + \phi_1 Z_1^{-1})^{-1} \hat{B}_1^T \quad .
\end{aligned} \tag{37}$$

In terms of \hat{A}_0 and \hat{F} , the denuisanced normal equation in the original problem, Equation (20), becomes

$$(\hat{A}_0^T \hat{F}^T Q_B \hat{F} \hat{A}_0 + \theta W^{-1}) \tilde{m} = \hat{A}_0^T \hat{F}^T Q_B \hat{d} \quad . \tag{38}$$

For Equations (36) and (38) to be equivalent, we must require that

$$\hat{B}_1 (\hat{B}_1^T \hat{B}_1 + \phi_1 z_1^{-1})^{-1} \hat{B}_1^T = \hat{F}^T \hat{B} \hat{B}^{-1} \hat{F} , \quad (39a)$$

$$Q_{B_1} \hat{d}_1 = \hat{d}_0 - \hat{F}^T \hat{B} \hat{B}^{-1} \hat{d} , \quad (39b)$$

where we have used Equations (31) and (35).

Several choices of \hat{B}_1 , ϕ_1 and z_1 solve Equation (39a). We define one choice as follows. Let

$$M_B = z^{\frac{1}{2}} \hat{B}^T \hat{B} z^{\frac{1}{2}} + \phi I . \quad (40)$$

The right hand side of Equation (39a) is then

$$\text{R.H.S (39a)} = \hat{F}^T \hat{B} z^{\frac{1}{2}} M_B^{-1} z^{\frac{1}{2}} \hat{B}^T \hat{F} . \quad (41)$$

We now define S_1 , Γ_1 , and T_1 through the singular value decomposition

$$\hat{F}^T \hat{B} z^{\frac{1}{2}} M_B^{-1} z^{\frac{1}{2}} \hat{B}^T \hat{F} = S_1 \Gamma_1 T_1^T \quad (42)$$

where $S_1^T S_1 = T_1^T T_1 = I$ and Γ_1 is diagonal. Then

$$\text{R.H.S. (39a)} = S_1 \Gamma_1^2 S_1^T \quad (43)$$

The following then obey Equation (39a)

$$\begin{aligned} \hat{B}_1 &= S_1 \Gamma_1 \\ \phi_1 z_1^{-1} &= I - \Gamma_1^2 . \end{aligned} \quad (44)$$

This implies

$$Q_{B_1} = I - S_1 \Gamma_1^2 S_1^T . \quad (45)$$

We note that if $\phi > 0$, then $0 < \Gamma_1 < I$.

Using Equations (42), (44) and (45) we can now rewrite Equation (39b) as

$$(I - S_1 \Gamma_1^2 S_1^T) \hat{d}_1 = \hat{d}_0 - S_1 \Gamma_1 T_1^T M_B^{-\frac{1}{2}} Z^{\frac{1}{2}} \hat{B}^T \hat{d} . \quad (46)$$

This is solved by

$$\hat{d}_1 = \hat{d}_0 + S_1 \Gamma_1 (I - \Gamma_1^2)^{-1} [\Gamma_1 S_1^T \hat{d}_0 - T_1^T M_B^{-\frac{1}{2}} Z^{\frac{1}{2}} \hat{B}^T \hat{d}] . \quad (47)$$

Thus d_1 equals d_0 , the simple variance-weighted average of d , plus an extra "correction" term. We note two situations in which the correction term is zero. First, if

$$F^T \Sigma^{-1} B = 0$$

then B_1 and hence Γ_1 and zero. Second, if B can be factored as

$$B = FB_0 \quad (48)$$

then the two terms inside the brackets in Equation (47) cancel.

This grouping algorithm applies to any problem in which A can be factored as FA_0 , regardless of what F is. In this problem, where F simply repeats rows and where B is block diagonal, the computations become particularly simple. The matrix $F^T \Sigma^{-1} B$ is block diagonal and M_B is diagonal.

In obtaining B_1 , one automatically obtains the denuisancing operator $Q_{B_1}^{\frac{1}{2}}$:

$$Q_{B_1}^{\frac{1}{2}} = I - S_1 [I - (I - \Gamma_1^2)^{\frac{1}{2}}] S_1^T . \quad (49)$$

This operator is used to define the denuisanced matrix and data vector:

$$\begin{aligned}\hat{A}_{0v} &= Q_{B_1}^{\frac{1}{2}} \hat{A}_0 \\ \hat{d}_{1v} &= Q_{B_1}^{\frac{1}{2}} \hat{d}_1\end{aligned}\quad (50)$$

In terms of these, Equation (36) becomes

$$(\hat{A}_{0v}^T \hat{A}_{0v} + \theta W^{-1}) \tilde{m} = \hat{A}_{0v}^T \hat{d}_{1v}, \quad (51)$$

which is analogous to Equation (22).

2.5 LINEAR INVERSE ALGORITHM

We have reduced the teleseismic residual problem to a standard linear inverse problem of the form:

$$\begin{aligned}E[\hat{d}_{1v}] &= \hat{A}_{0v} m \\ \text{Var}[\hat{d}_{1v}] &= I\end{aligned}\quad (52)$$

where m represents the slowness perturbation Δu and \hat{d}_{1v} represents the grouped, denuisanced travel-time residuals. A solution \tilde{m} to Equation (52) has been defined by

$$(\hat{d}_{1v} - \hat{A}_{0v} \tilde{m})^T (\hat{d}_{1v} - \hat{A}_{0v} \tilde{m}) + \theta \tilde{m}^T W^{-1} \tilde{m} = \text{minimum} \quad (53)$$

This defines \tilde{m} as a linear estimator of the form

$$\tilde{m} = \hat{A}_{0v}^{-1} \hat{d}_{1v} \quad (54)$$

where \hat{A}_{0v}^{-1} is the damped generalized inverse of \hat{A}_{0v} .

The algorithm we use to obtain \hat{A}_{0v}^{-1} is very similar to the algorithm described in Section 2.3 for obtaining \hat{B}^{-1} . In this case, we factor the weighting matrix as

$$W^{-1} = H^T H \quad (55)$$

where H is a square nonsingular matrix. (We actually specify H instead of W^{-1} .) Then we obtain the SVD

$$\hat{A}_{0v} H^{-1} = U \Lambda V^T, \quad (56)$$

where

$$U^T U = V^T V = I$$

$$\Lambda = \text{diag} (\lambda_1, \lambda_2, \dots, \lambda_K) > 0. \quad (57)$$

Even after grouping, \hat{A}_{0v} is a very large matrix (1173 by 1188) so the SVD requires a core-to-disc computer algorithm. The inverse \hat{A}_{0v}^{-1} is then obtained as

$$\hat{A}_{0v}^{-1} = H^{-1} V \Lambda (\Lambda^2 + \theta I)^{-1} U^T. \quad (58)$$

Since Λ is diagonal this expression is readily evaluated for varying θ .

Equations (52) and (54) imply

$$E[\tilde{m}] = Rm$$

$$\text{Var}[\tilde{m}] = V \quad (59)$$

where

$$\begin{aligned}\mathcal{R} &= \hat{A}_{0v}^{-1} \hat{A}_{0v} = H^{-1} V \Lambda^2 (\Lambda^2 + \theta I)^{-1} V^T H \\ \mathcal{V} &= \hat{A}_{0v}^{-1} \hat{A}_{0v}^{-T} = H^{-1} V \Lambda^2 (\Lambda^2 + \theta I)^{-2} V^T (H^{-1})^T\end{aligned}\quad (60)$$

\mathcal{R} is the resolution matrix and \mathcal{V} the covariance matrix of the model \tilde{m} . These matrices provide a means for assessing the uniqueness of \tilde{m} . Equation (60) states that \tilde{m} is an estimate of m "filtered" by \mathcal{R} , and not of m itself. With \tilde{m} as a three-dimensional block model of the earth, each component \tilde{m}_i estimates a spatial average of the true structure; the i 'th row of \mathcal{R} is a discrete three-dimensional function which shows the spatial extent of the averaging or filtering. In addition to the filtering, \tilde{m} is also contaminated by a random error whose variance is \mathcal{V} .

The quantities \mathcal{R} and \mathcal{V} aid in selecting a "best" single model among the family of models $\tilde{m}(\theta)$ defined over $0 < \theta < \infty$. Backus and Gilbert (1970) showed that as θ increases ($I - \mathcal{R}$) increases (resolution degrades) and \mathcal{V} decreases, thus giving a trade-off between resolution and variance. One should attempt to choose θ such that $(I - \mathcal{R})$ and \mathcal{V} are both acceptably small.

The parameter θ also controls a trade-off between model smoothness and data misfit, as one can see from the minimization criterion Equation (53). The quantity ε_0 , given by

$$\varepsilon_0^2 = \frac{1}{N_0} (d_{1v} - A_{0v} \tilde{m})^T \Sigma_0^{-1} (d_{1v} - A_{0v} \tilde{m}), \quad (61)$$

where N_0 is the number of grouped data, is the r.m.s. misfit between the observed (grouped, denuisanced) data and the data predicted by \tilde{m} , $A_{0v} \tilde{m}$. The model norm, $\tilde{m}^T W^{-1} \tilde{m}$, measures the

average "roughness" of the model. As a function of increasing θ , ϵ_0 increases and the model norm decreases. While these scalar quantities are useful, it is desirable to visually examine the smoothness of the entire model and to compare the full observed and predicted data sets, in selecting and assessing a final model.

We must comment here on the equivalence between inversions of grouped and ungrouped data. We know from Section 2.4 that the same \tilde{m} is obtained from the inversion of either data set. This is true also for \mathcal{R} and \mathcal{V} and, of course, the model norm. (Thus, we could have equally well used d_v and A_v in Equations (52) through (60).) However, grouped and ungrouped r.m.s. misfits are different. Letting

$$\epsilon^2 = \frac{1}{N} (d_v - A_v \tilde{m})^T \Sigma^{-1} (d_v - A_v \tilde{m}) \quad (62)$$

this means $\epsilon \neq \epsilon_0$. Furthermore, the relationship between grouped and ungrouped predicted data is not simple: one is not a simple variance weighted average of the other.

In the next section, on inversion results, we show ungrouped predicted data for our final model and compare them to the ungrouped observed data. Both are denuisanced (zero-meanned), however. We also use the ungrouped r.m.s. misfit ϵ in a trade-off curve. In using ungrouped rather than grouped quantities, we essentially are treating grouping as a computational step in the inversion rather than as a data processing procedure.

For our results, we also convert the trade-off parameter to a dimensionless quantity which is the effective number of degrees of freedom (NDF) in the model $\tilde{m}(\theta)$. NDF is defined as

$$\text{NDF} = \sum_{k=1}^K \lambda_k^2 / (\lambda_k^2 + \theta) \quad (63)$$

and equals the rank of \mathcal{R} .

III. TRAVEL-TIME DATA

3.1 ORIGINAL DATA SET

The basic data for this study consist of arrival times of globally recorded P-waves from NTS explosions as reported in the bulletins of the International Seismological Centre (ISC). This particular data source was chosen since it is the most comprehensive compilation of seismic event-station arrival time readings generally available.

The first step involved in acquiring the data for this study was to determine the time period of availability of ISC bulletins. This turned out to be the latter part of 1964 through mid 1978, with occasional gaps. Taking the bulletins in conjunction with published announcements of NTS explosions (Springer and Kinnaman, 1971; Springer and Kinnaman, 1975; USGS Preliminary Determination of Epicenters, Monthly Listings), the appropriate sections of the ISC bulletins were xeroxed and edited for subsequent processing. The principal editing, or selection criterion imposed on the acceptable arrival time data at this point in the experiment was that the P-wave arrivals be reported as impulsive. While this criterion reduced the available data base for explosions by as much as 50 percent, especially in the case of low magnitude events, we note that the preponderance of emergent P-wave arrival times are only specified to the nearest second in the ISC bulletins. In contrast, arrival times of impulsive P-waves are reported to the nearest tenth of a second. After we discuss the subsequent culling and processing operations that had to be applied to these data, it should be evident that, rather than sacrificing valid information, this selection criterion most likely contributed to reducing the amount of noisy data.

The reported arrival times for all NTS explosions for which ISC bulletins were available, a total of 192 events,

were keypunched and verified (i.e., double punched by two different keypunch operators). Included with each arrival time was the corresponding seismograph station code, and event-station epicentral distance and azimuth. Station location information was taken from the "Regional Catalogue of Earthquakes" bulletin published biannually by the ISC. The station and explosion locations were further verified by comparing distances and azimuths, computed using a standard program, with the bulletin values. The data base at this stage of the experiment consisted of approximately 9706 impulsive P-wave arrival times reported from 663 seismograph stations for 192 NTS explosions.

In Figure 3.1, we plot the locations of the 192 NTS explosions for which arrival time data were acquired. The different symbols follow the yield range scheme given in Springer and Kinnaman (1971 and 1975), with the exception that explosions occurring after 1973 (i.e., post Springer and Kinnaman) are designated by a + symbol. The hypocentral information for these later explosions was taken from the PDE Monthly listings. As is evident from Figure 3.1, the majority of NTS explosions occur in two primary test areas at NTS: Pahute Mesa and Yucca Flat. Secondary test areas include Rainier Mesa, Frenchman Flat, Shoshone Mountain and the Climax Stock at the northern end of Yucca Valley (the PILEDRIVER explosion). As is well known, the largest yield explosions are detonated at Pahute Mesa (i.e., the ■'s and ●'s in Figure 3.1). These events provide the greatest number of far-field impulsive P-wave arrivals and, as we shall see, comprise the majority of our final processed data set. The bimodal distribution of sources at NTS also plays an important role in the selection of the model grid (Section IV) and the interpretation of the modeling results. This will be discussed in greater detail in subsequent sections of this report.

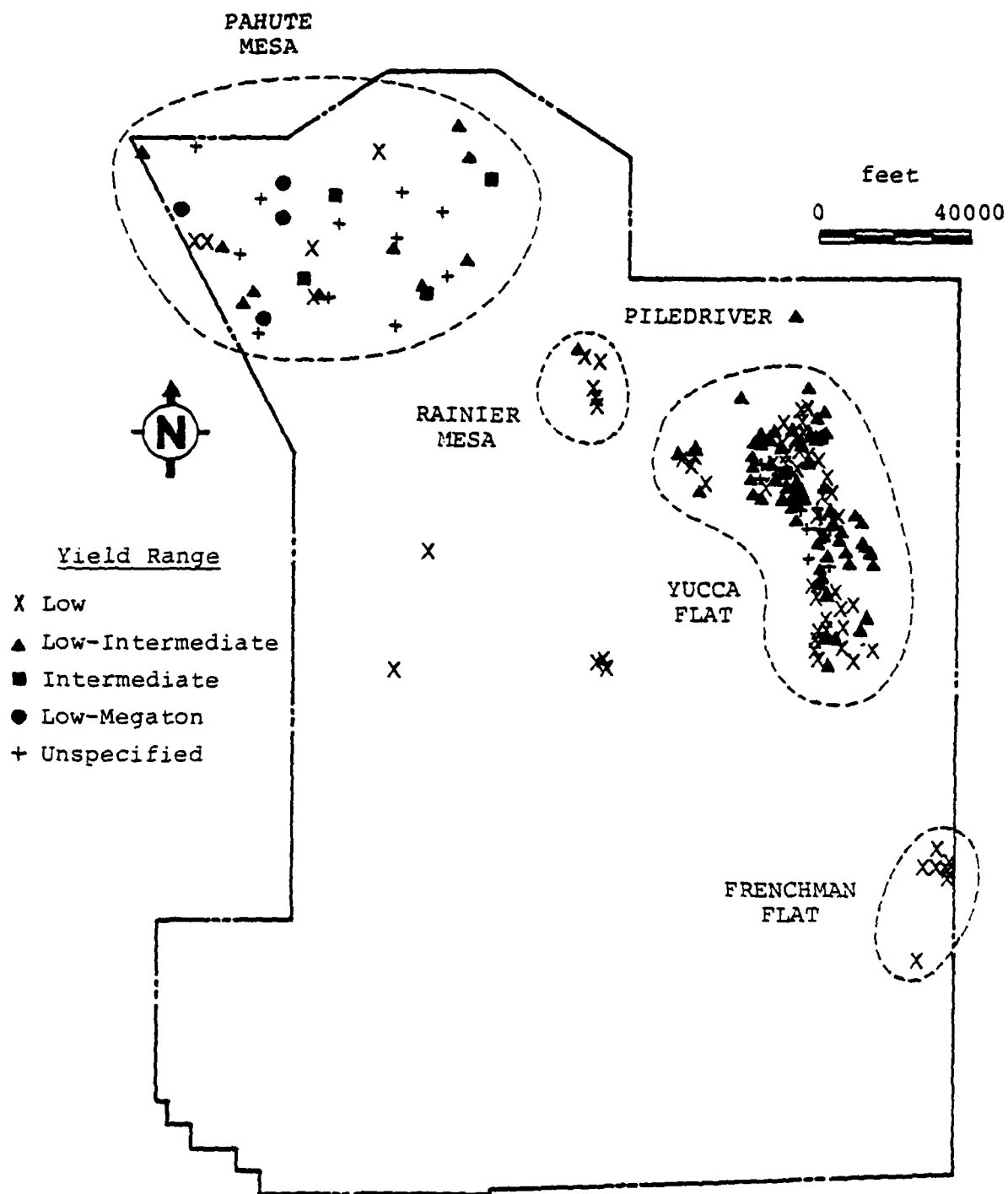


Figure 3.1. Locations of initial set of 192 NTS explosions.

An additional culling criterion applied to the data set was the restriction of the epicentral distance range for inclusion of P-wave arrival times. Perusal of the ISC bulletins clearly indicated a long distance cutoff of approximately 100° , into the core diffraction range. Actually, for all but the largest Pahute Mesa explosions, the epicentral distance range for reported P-wave arrivals is generally characterized by a gap between approximately 95° and 125° . Since we chose not to get involved with the complexities of the various PKP arrivals, we decided on a bulletin cutoff of approximately 100° . For the short distance cutoff we refer to the study by Burdick and Helmberger (1978) on the P-wave velocity structure of the upper mantle beneath the western United States, including the NTS region. Figure 3.2 is a reproduction of one of the figures from their study. This figure indicates that for sources in the western United States, at distances greater than about 25° the P-wave arrivals are beyond the major triplication range. Based on these observations, we chose a close-in distance cutoff of 25° (e.g., the closest station in the remaining data set is at a distance of 25.3° from the center of NTS).

The restricted distance range results in a significant reduction in the number of NTS explosions, from 192 to 82, and the number of seismograph stations, from 663 to 369, remaining in the data set. Approximately 40 of the 110 explosions dropped at this stage of the experiment were omitted because of too few reports of P-wave arrivals (i.e., ≤ 5) remaining after applying the distance range criterion. Figure 3.3 shows the locations of the 369 seismograph stations in the distance range 25° to 108° relative to NTS. As seen in this figure, station coverage varies significantly with distance and azimuth. In general, the northeastern quadrant is well recorded over most of the teleseismic distance range by stations in eastern Canada and the United States, Greenland, Iceland and Europe. This

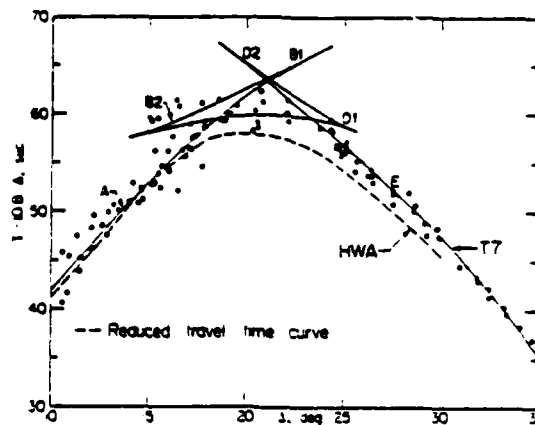


Figure 3.2. Comparison of observed reduced travel times to predictions from Models HWA and T7 showing upper mantle triplications for western United States. From Burdick and Helmberger (1978).

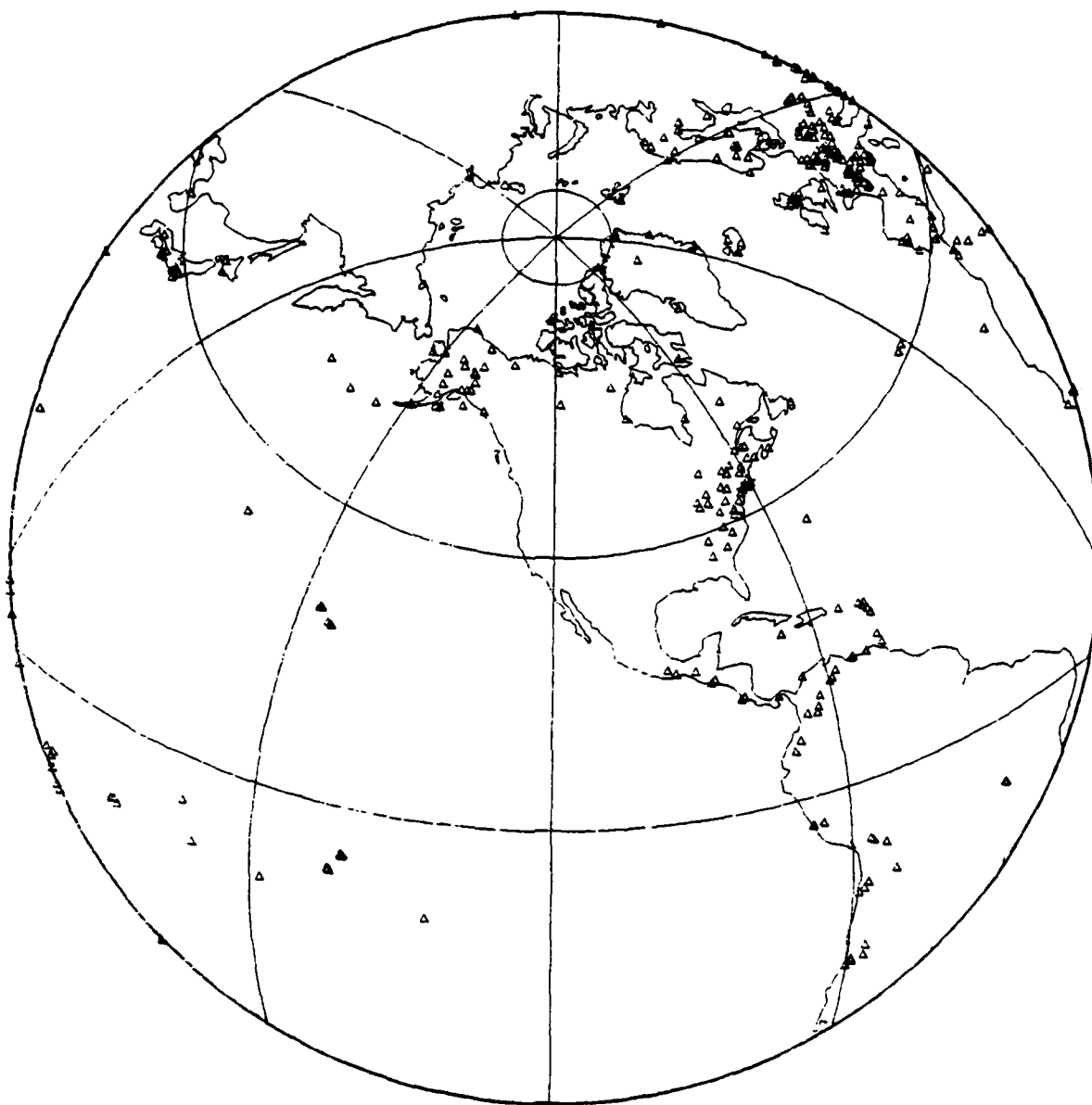


Figure 3.3. Locations of 369 stations in the distance range 25° to 108° from NTS. (Stations with $\Delta > 90^{\circ}$ are plotted along the edge of the map.)

situation is in sharp contrast to several other azimuths, in particular the swath extending due south of NTS where there is a complete lack of coverage. The significance of this highly variable station distribution will be pointed up in subsequent sections dealing with the ray path sampling of the model region and the final modeling results.

In summary, after applying several selection criteria to the ISC bulletin data the resulting data set consists of 4484 P-wave arrival times reported by 369 seismograph stations from 82 NTS explosions. Tables of station and explosion information are given in Appendix A. For each of the 369 seismograph stations, the following information is listed: station code and full name, geographical coordinates, distance and azimuth with respect to the approximate center of NTS, elevation and number of P-wave arrivals reported. The explosion information consists of the following: an event number, date, origin time, location, depth-of-burial, elevation and number of stations reporting.

3.2 CONVERSION OF ARRIVAL TIMES TO RESIDUALS

As described in Section II (Equation 4), there are three major corrections that have to be applied to the P-wave arrival times in order to convert them to travel-time residuals. The first of these is T_E^{orig} , the event origin time. In the case of the NTS explosions, we are in a rather unique situation. The origin times of these events are very accurately known, being specified to 0.01 seconds (Springer and Kinnaman, 1971; 1975). Obviously, the origin times can be considered free of error for this problem.

The next correction applied is t_{ES}^{table} , the Herrin (1968) calculated travel time for a surface focus event at distance Δ_{ES} . The locations of NTS explosions are accurately known

and specified to 0.1 seconds of arc, an approximate 3 m location uncertainty. Thus, as in the case of the origin times, the errors associated with location uncertainty are considerably smaller than measurement errors which we estimate as approximately 0.2 to 0.3 seconds.

The last routine correction to be applied is $t_{EE'}^{elev}$, the event elevation correction. As outlined in Section II, the purpose of this correction is to reduce the observed P-wave travel times from the NTS explosions to a common datum plane. While the depths-of-burial of the explosions vary by as much as 1 km, all the explosions are above sea level. Thus, we devised a correction that places all the explosions at sea level.

Given a plane-layered model of the velocity structure below an event E, consisting of layer thicknesses $h_{E\ell}$ and velocities $V_{E\ell}$, $\ell = 1, \dots, L$ (L = number of layers), the elevation correction for the event E and a station S is given by

$$t_{EE'}^{elev} = \sum_{\ell=1}^L \frac{h_{E\ell}}{V_{E\ell}} (1 - p_{ES}^2 V_{E\ell}^2)^{1/2} \quad (64)$$

where p_{ES} is the ray parameter determined from the Herrin table. (Though not shown explicitly by Equation (64), the summation is understood to not include layers or portions of layers above the depth-of-burial or below sea level.) The square-root factor in Equation (64) is $\cos \theta_{ES\ell}$, where $\theta_{ES\ell}$ is the angle of the ray path from vertical in the ℓ 'th layer. Teleseismic ray paths are near vertical so this factor is close to one, implying that the elevation correction is approximately a vertical delay and thus only weakly station dependent.

For the events at Pahute Mesa and Rainier Mesa, the elevation correction was computed using near-surface velocity

models taken from a study by Bache, et al. (1979). A total of eight different models was used for the Pahute Mesa test area. Figure 3.4 shows how we subdivided this test area. The ground zero locations of each of the explosions within any given sub-region have approximately the same elevation. The eight Pahute Mesa and Rainier Mesa velocity models used for this correction are tabulated in Appendix B.

For all other explosion test areas at NTS (e.g., Yucca Flat, Shoshone Mountain and Climax Stock), the near-surface velocity models for the elevation correction were specified in a somewhat different manner. These test areas are collectively referred to as Yucca Flat in the remainder of this report. Ramspott and Howard (1975) identify three media controlling the predominant velocity variations below Yucca Flat shots: alluvium or tuff above the water table, alluvium or tuff below the water table and "hard rock." Included in the hard rock category are the widespread Paleozoic rocks and the mesozoic granites comprising the Climax Stock. These three basic media are assigned average working point (e.g., shot depth) compressional wave velocities, with a further subdivision of Yucca Flat into a northern and southern portion (the dividing line being at approximately 37.1°N latitude). These average velocities are listed in Table 3.1. A velocity model for each shot, then, is obtained by using the appropriate velocities from Table 3.1 in conjunction with estimates of the depths to the water table and Paleozoic rocks, as well as elevation, depth-of-burial and rock type at the shot point. This latter information was taken from Springer and Kinnaman (1971; 1975). Exceptional explosions include PILEDRIIVER (Event Number 40, Appendix A) detonated in granite and two explosions (NASH #54, BOURBON #55) detonated in dolomite. For these three events we used a single layer model from shot point to sea level and velocities for granite and Paleozoics (Table 3.1).

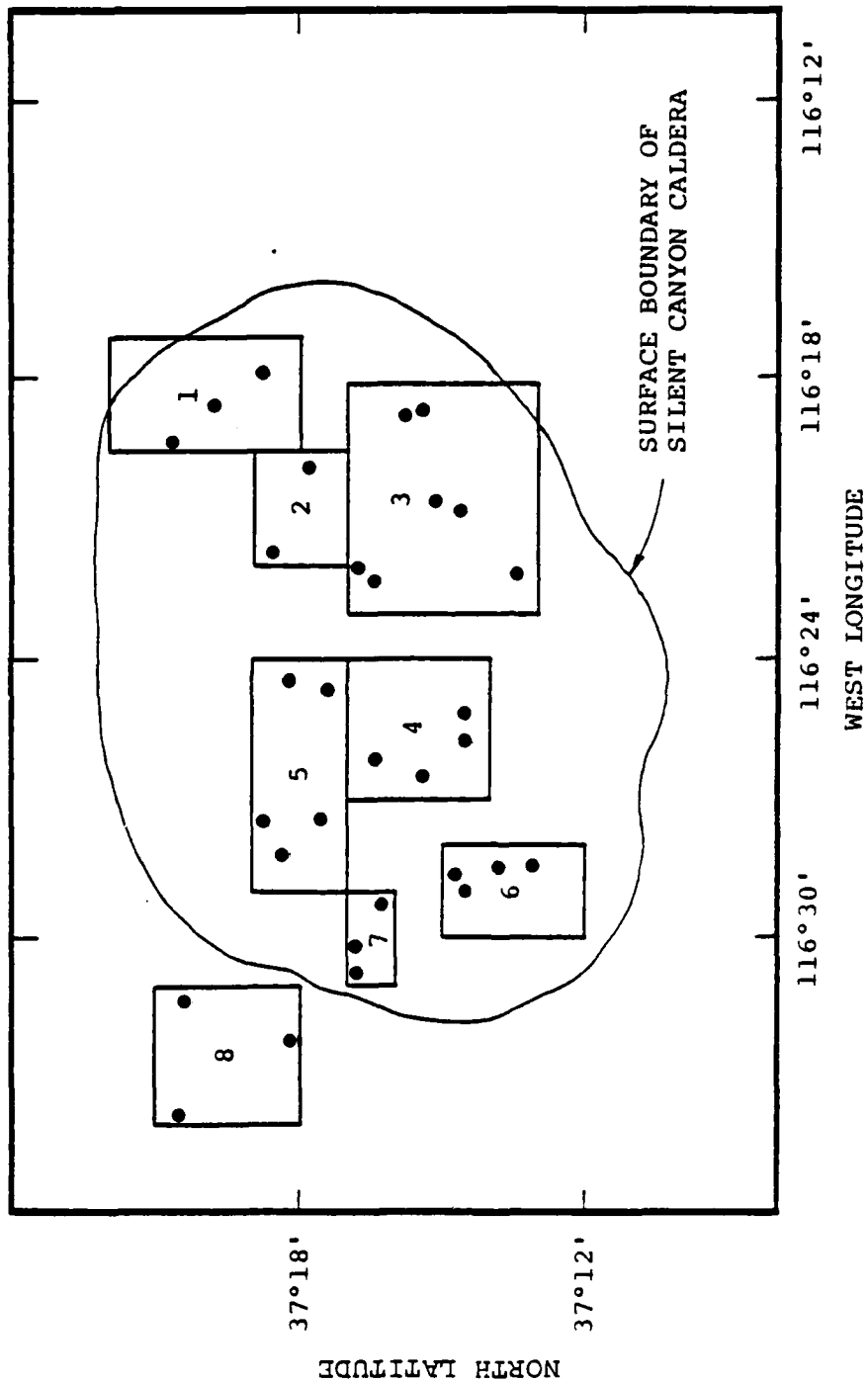


Figure 3.4. Subareas defining the near-surface velocity models used in the calculation of depth corrections for Pahute Mesa events. The integers shown refer to the model numbers given in Appendix B (after Bache, et al., 197).

TABLE 3.1
AVERAGE VELOCITIES OF MEDIA AT NTS

Region/Rock Type	Mean Velocity (km/sec)
<u>Northern Yucca Flat</u>	
Alluvium Above Water Table	1.97
Tuff Water Table	1.79
Tuff Below Water Table	2.45
Paleozoic	5.40
<u>Southern Yucca Flat</u>	
Alluvium Above Water Table	1.58
Tuff Above Water Table	1.90
Tuff Below Water Table	2.33
Paleozoic	5.40
<u>Climax Stock</u>	
Granite	5.70

Since each Yucca Flat event was effectively assigned a different velocity model, it was convenient to evaluate the elevation correction with a first-order approximation to Equation (65):

$$t_{EE'}^{elev} \approx \sum_l \frac{h_{El}}{V_{El}} - \frac{1}{2} P_{ES}^2 \sum_l h_{El} V_{El} \quad . \quad (65)$$

It was easier to tabulate the summations of h_{El}/V_{El} and $h_{El} V_{El}$ directly from the data sources than to tabulate the models themselves. This first-order expansion is accurate to 0.01 sec or better. We note that the majority of the elevation corrections calculated for Yucca Flat events are in the 0.1 to 0.2 sec range, with occasional corrections as large as 0.4 sec.

This completes our discussion of the major corrections that we applied to the observed P-wave arrival times in order to convert them to travel-time residuals. In Figure 3.5 we show the observed travel-time residuals based on data from the 369 seismograph stations listed in Appendix A for 58 of the larger magnitude, better recorded NTS explosions. We have restricted the number of explosions plotted in this figure in order to avoid overlapping of event and travel-time residual symbols.

The format we have adopted for showing these data is the following. A circle is drawn around the location of each explosion. The circumference of each circle corresponds to a zero travel-time residual. Positive residuals are represented by lines extending out from the circumference at azimuths corresponding to the contributing stations. Negative residuals are drawn in toward the center of the circle. The length of any particular line is scaled according to the size, or absolute value, of the residual. In this and all subsequent data figures a circle radius equals a residual of one second. While this form of data representation has the advantage of

Figures 3.5a through 3.5f are on the following pages.

Figure 3.5. Observed travel time residuals (zero-meaned, before culling) for 303 stations and 58 NTS events (see text). Station and event information is given in Appendix A. Residuals are represented according to a format described in the text. Figures 3.5a and 3.5b represent events in Pahute Mesa test area, Figures 3.5c to 3.5f show events from the other test areas. Outlines of the corresponding rectangular frames are shown on Figure 4.3 in relation to the NTS geography. Frames are labeled along north-south and east-west axes with UTM (Universal Transverse Mercator) northing and easting coordinates (in kilometers), with respect to a central meridian of 117°W (500 km easting).

NTS-INDIU-25 >>DEMEANED NON-GROUPED DATA (2.5 S SCREEN)<< 82 EVENTS 07-09-81

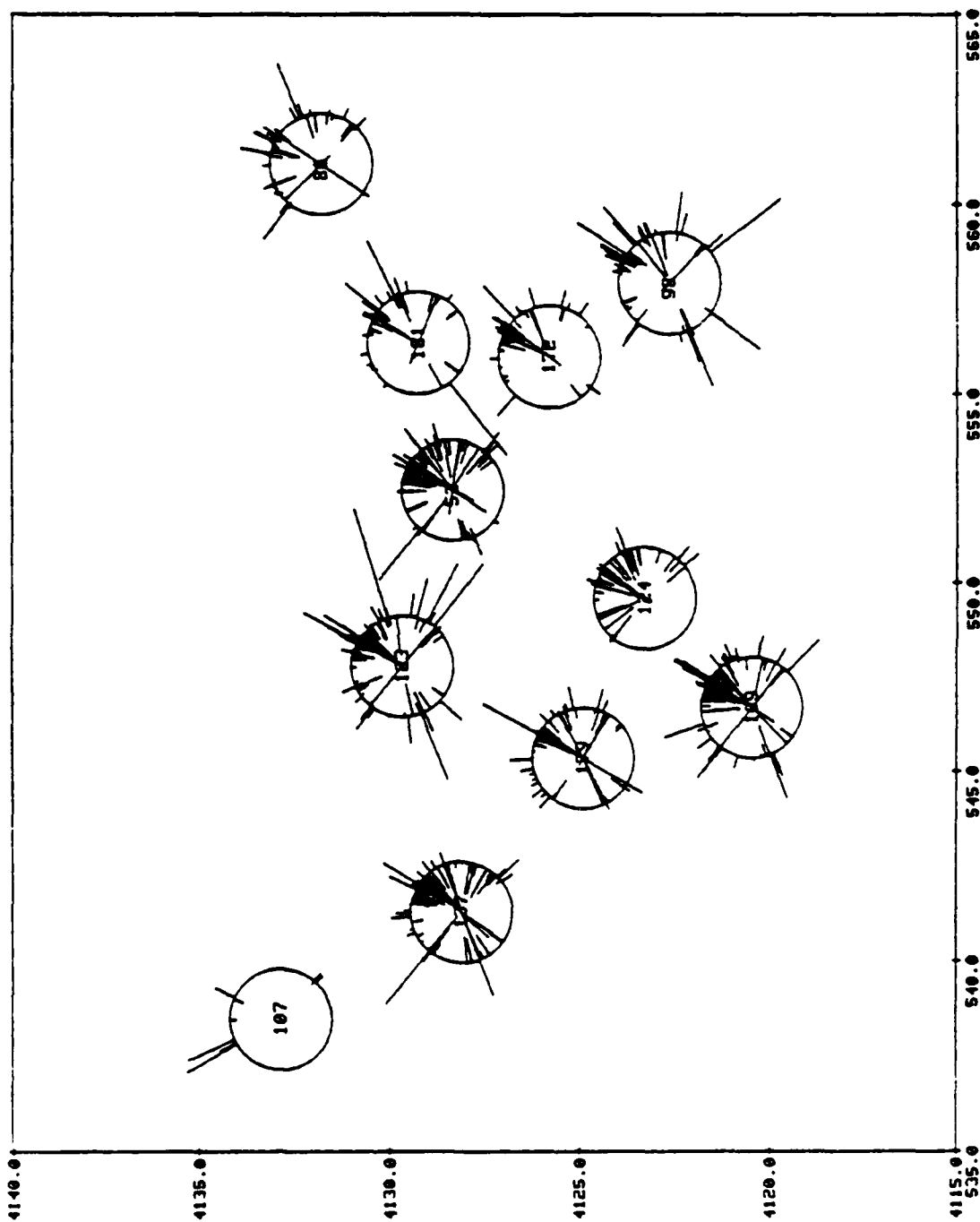


Figure 3.5a. Pahute Mesa.

NTS-INDIV-25 >>DEMEANED NON-GROUPED DATA (2.5 S SCREEN)<< 82 EVENTS 07-09-81

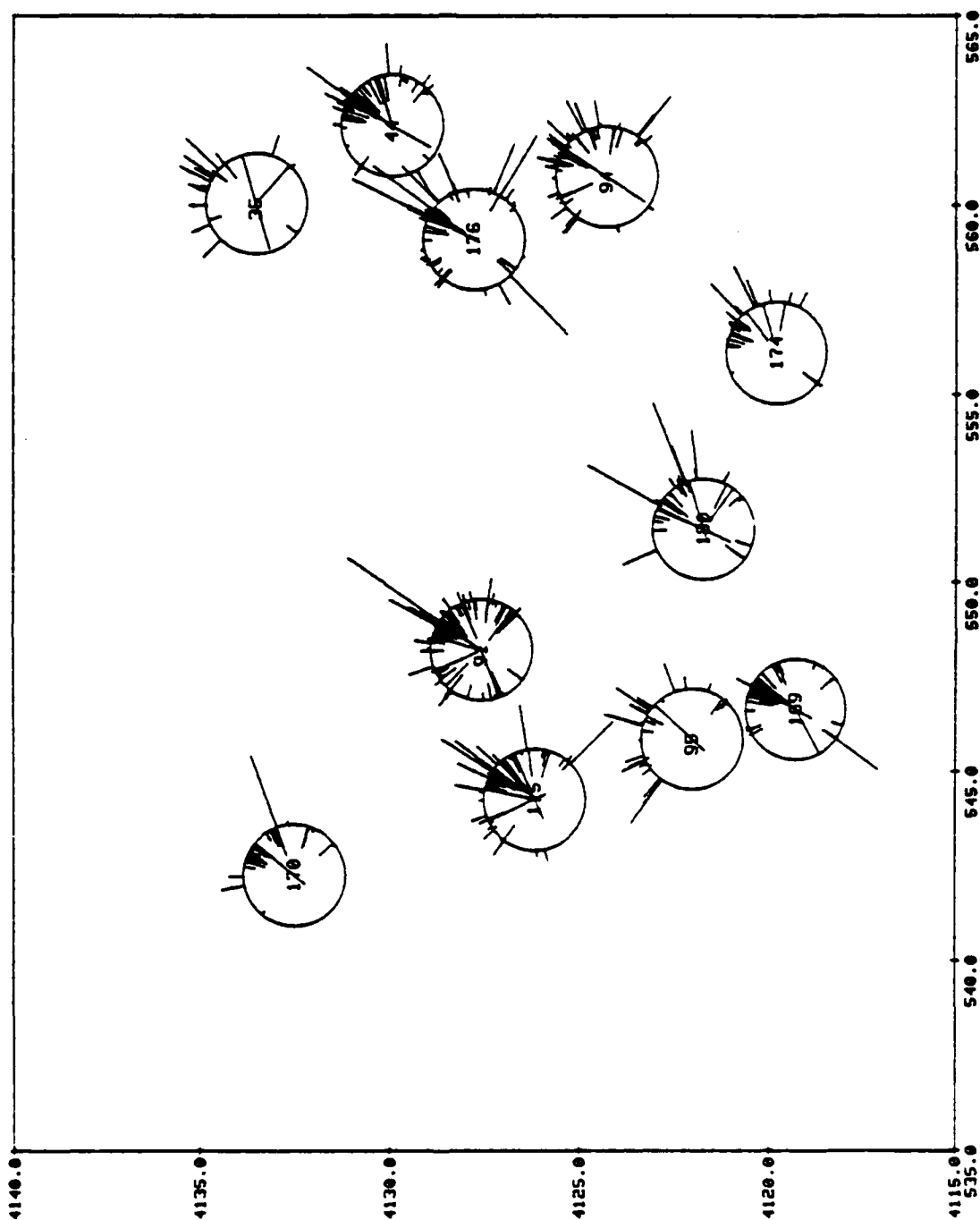


Figure 3.5b. Pahute Mesa.

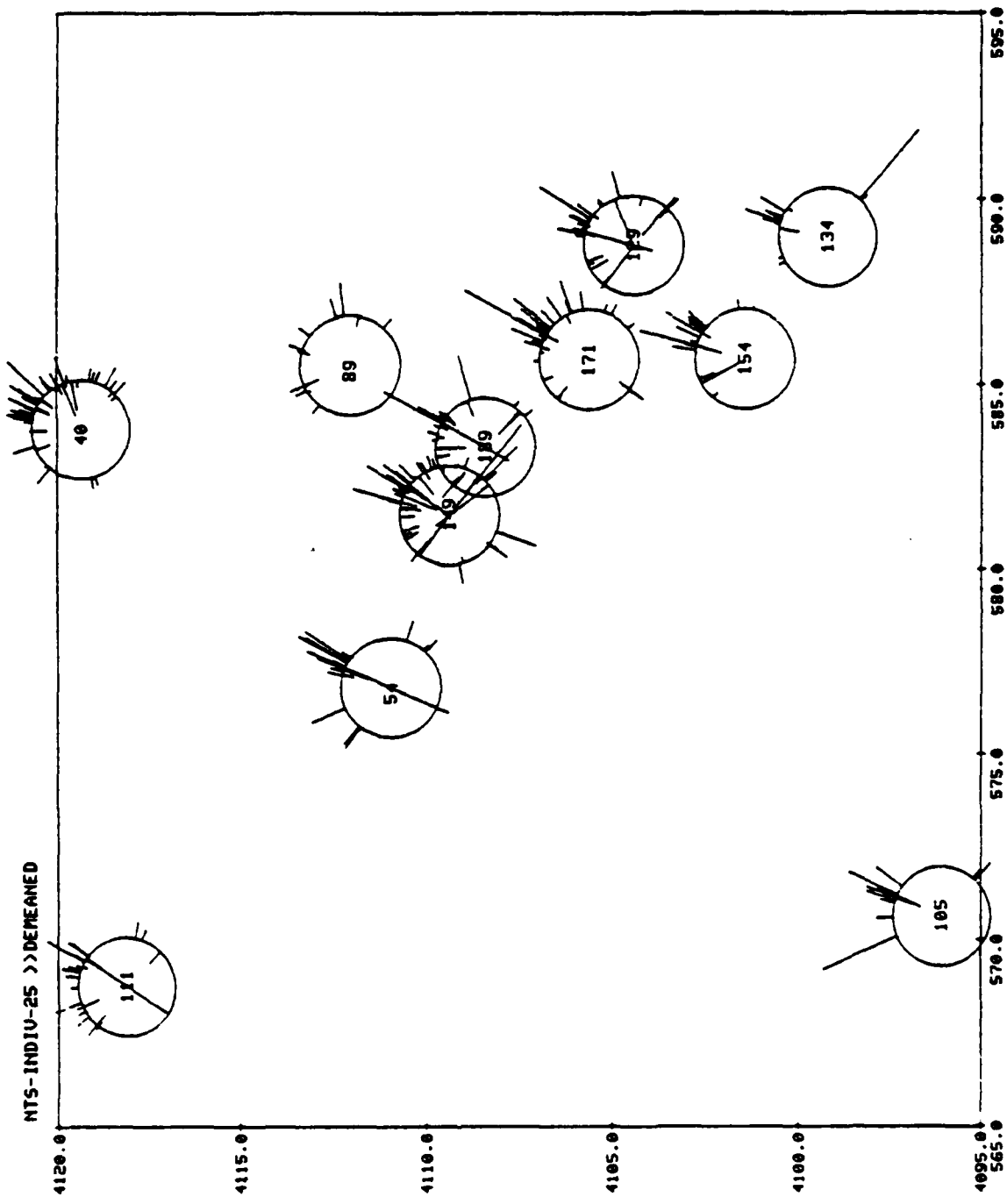


Figure 3.5c. Yucca Flat.

NTS-INDIU-25 >>DENEARED NON-GROUPED DATA (2.5 S SCREEN)<< 82 EVENTS 07-09-81

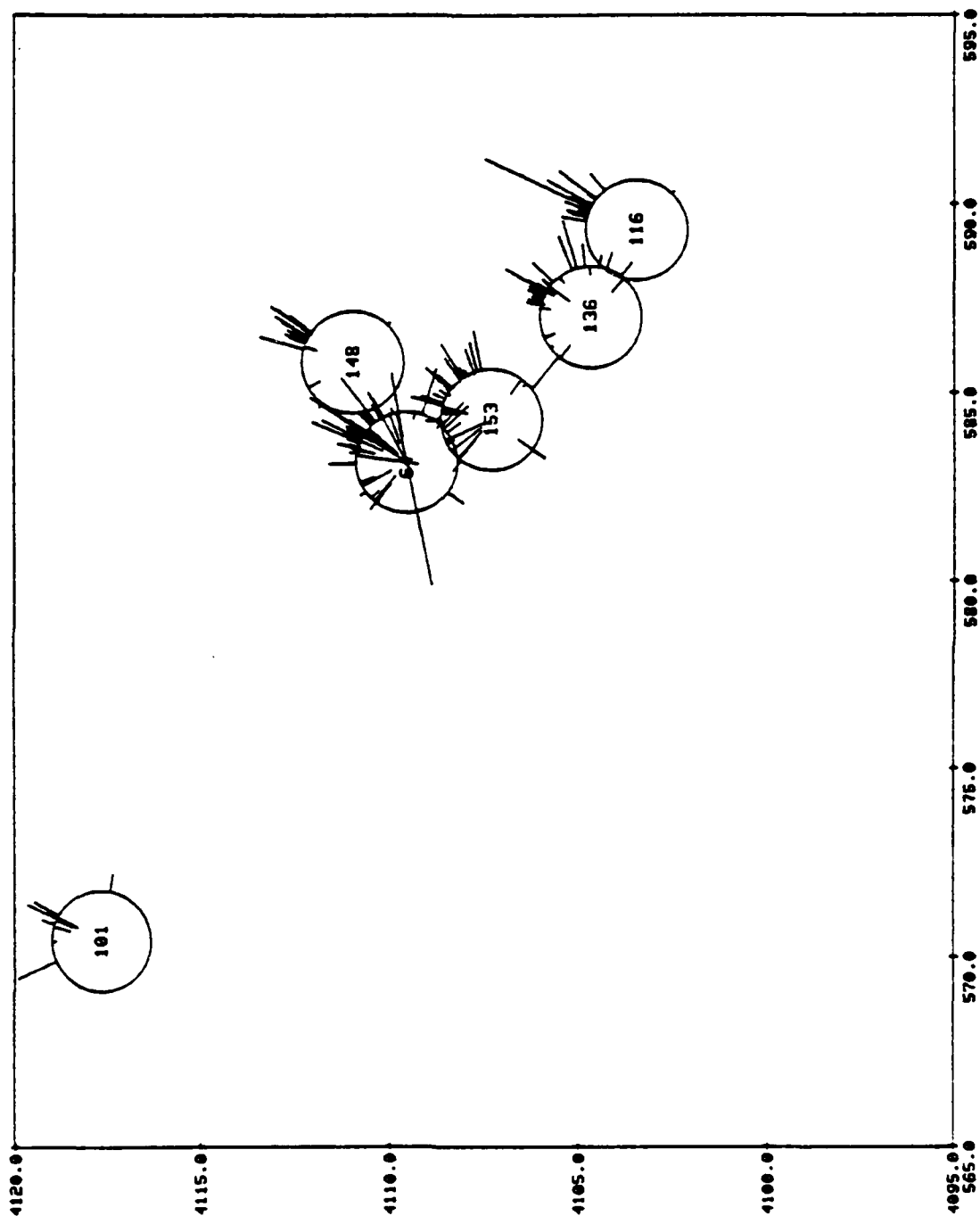


Figure 3.5d. Yucca Flat.

NTS-INDIU-25 >>DEMERGED NON-GROUPED DATA (2.5 S SCREEN)<< 82 EVENTS 07-09-91

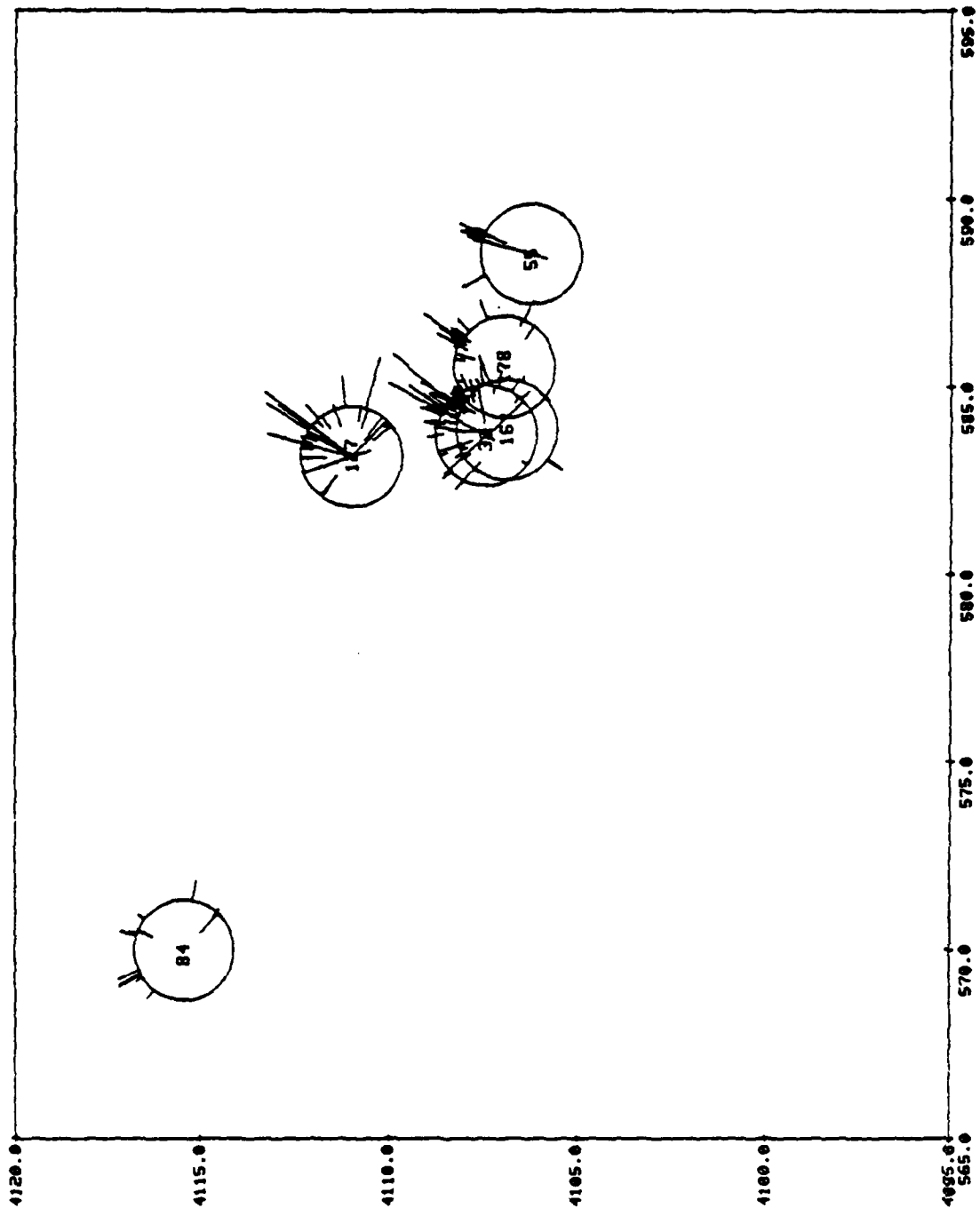


Figure 3.5e. Yucca Flat.

NTS-INDIU-25 >>DEMANED NON-GRUPEP DATA (2.5 S SCREEN)<< 82 EVENTS 07-09-81

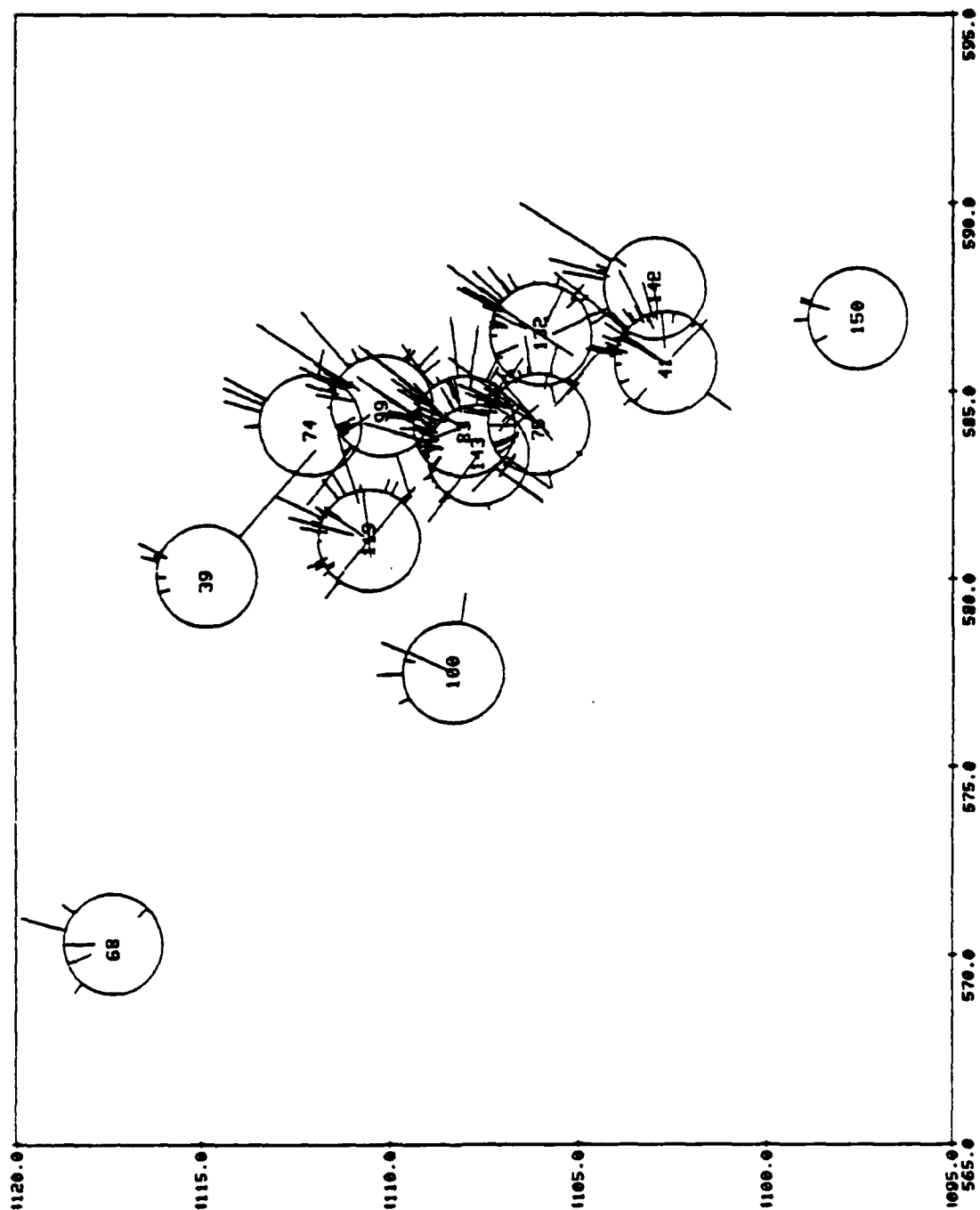


Figure 3.5f. Yucca Flat.

showing the behavior - that is the sign, size and azimuthal distribution - of event residuals over the model region, there are two main disadvantages to be noted. First, residuals with values near zero seconds (i.e., ± 0.05 secs) are hard to distinguish. Second, possible correlations between residuals and takeoff angles for rays exiting the model region are obscured by combining results from stations over the entire 25° to 108° epicentral distance range. This latter point will be addressed in more detail in later sections where we consider model block-hit patterns which describe the ray path sampling of the model volume.

The residuals in Figure 3.5 have been zero-meaned (see Section 2.3). For each station, we subtract the average value of the residuals based on all the NTS explosions recorded at that particular station from each individual explosion residual. In addition, we have applied a screen which automatically rejects residuals from any given station that differ by more than 2.5 seconds from the mean at that station. Application of this screen resulted in a reduction of the number of stations from 369 to 303, and residuals from 4484 to 4332. The purpose of this screen is to remove excessively noisy data and produce reasonably legible plots.

The travel-time residual plots in Figure 3.5 are subdivided as follows. Figures 3.5a and 3.5b cover explosions at Pahute Mesa, Figures 3.5c through 3.5f include explosions at all other test areas. They are labeled "Yucca Flat" for convenience. Some of the more obvious features of these data are the following:

1. a preponderance of observations from northerly azimuths,
2. generally positive residuals for Yucca Flat events, negative residuals for Pahute Mesa events, and
3. a rather significant number of inconsistent or noisy residuals, both in

terms of size and sign. The r.m.s. of the zero-measured residuals from the 303 acceptable stations is 0.45 sec, and a large component of this is contributed by noise rather than signal.

The reduction of the noise component in this data set is the topic of the following subsection of this report.

3.3 CULLING OF TRAVEL-TIME RESIDUALS

The rather large noise component evident in the travel-time residual plots shown in Figures 3.5a through 3.5f prompted us to consider procedures for increasing the signal-to-noise ratio (S/N) of these data. Examination of detailed listings of individual station-event residuals clearly indicated that the data set was contaminated by a combination of particularly noisy stations and anomalous residuals (outliers) reported by otherwise highly consistent stations. We arrived at this conclusion by examining individual residuals and the r.m.s. residual at each station. For each station, a separate r.m.s. residual was computed for Pahute Mesa events and for Yucca Flat events. A given r.m.s. for one of the areas represents an average signal (due to structural variations within the area) plus noise. With certain well-recording stations, we could establish that the signal contribution (within each area separately) was of order 0.3 sec. An individual residual much larger than this is probably contaminated by a large noise component and a station whose r.m.s. residual is much larger than this probably has several very noisy data. Of course, in estimating noise levels in this way one must allow for the fact that stations at different distances and azimuth see a different signal contribution.

Given this basic approach to identifying noisy data, we implemented two data culling procedures, each applied separately to the Pahute Mesa data and to the Yucca Flat data:

1. A dynamic screening procedure designed to cull individual residuals that had symptoms of large noise (outliers).
2. Rejection of all the data from a station whose r.m.s. residual was symptomatic of several noisy residuals. Data from stations recording very few events were also rejected.

The second procedure involved comparing the r.m.s. residuals at stations with similar locations, such that the signal seen by the stations could be assumed to be similar. For this purpose, we defined "station groups" based on distance and azimuth ranges from NTS. This same station grouping was eventually used to combine the remaining unculted data into group averages, using the data grouping technique described in Section 2.4.

3.3.1 Dynamic Screening Procedure

The first culling technique adopted is referred to as a dynamic screening procedure. It consists of a modified Student-t test for eliminating outliers from the data set.

To apply this test we compare a given travel-time residual at a station to the mean of the remaining residuals from the same station.

N_S = the number of residuals (i.e., the number of events) recorded at a particular station,

Δt_{ES} = the residual to be tested,

$\overline{\Delta t}_S$ = the mean of the N_S residuals,

σ_S = the sample standard deviation of these residuals.

Where

$$\overline{\Delta t}_S = \frac{1}{N_S} \sum_E \Delta t_{ES}$$

$$\sigma_S^2 = \frac{1}{N_S} \sum_E (\Delta t_{ES} - \overline{\Delta t}_S)^2.$$

The sums are restricted to events in one or the other test area. (We note that the standard deviation σ_S is the same as the r.m.s. zero-measured residual from a station.)

The tests we apply are the following:

1. If $|\Delta t_{ES} - \overline{\Delta t}_S| \leq 0.4$ sec, accept residual Δt_{ES} .
2. If $|\Delta t_{ES} - \overline{\Delta t}_S| \geq 0.8$ sec, reject Δt_{ES} .
3. If $0.4 \text{ sec} < |\Delta t_{ES} - \overline{\Delta t}_S| < 0.8 \text{ sec}$, then apply additional test.

If $|\Delta t_{ES} - \overline{\Delta t}_S| \geq k(N_S) t_{N_S-2}(0.99) \sigma_S$, reject Δt_{ES} ,

where

$$k(N_S)^2 = (N_S - 1) / [1 + (N_S - 2) / t_{N_S-2}^2]$$

Here $t_{N_S-2}(0.99)$ is the 0.99 point on the cumulative t-distribution curve with $(N_S - 2)$ degrees of freedom. For large N_S , $t(0.99) = 2.33$ and increases as N_S decreases. The factor $k(N_S)$ is included so that Δt_{ES} is effectively tests against the mean and standard deviation of the remaining $N_S - 1$ residuals.

The motivation and results of these three tests are as follows:

- Test 1 allows for the fact that the Δt_{ES} are not identically distributed and random; i.e., they consist of signal and random noise. Thus, even if a Δt_{ES} is small, it may appear as an outlier when compared to the remaining station residuals simply because its signal component is different.

- Test 2 is a formulation of the conclusion arrived at after extensive examination of the entire data set, that the relative signal level within the Pahute Mesa and Yucca Flat regions, considered separately, is much less than 0.8 seconds. Thus, residuals differing from the station mean by 0.8 sec or more are identified as noise even if they do not appear as statistical outliers when compared to the other station data.
- Test 3 is designed to reject outliers at the 98 percent confidence level, given that the residuals are normally distributed.

This screening procedure is said to be a dynamic one since once a particular residual (Δt_{ES}) is rejected it remains excluded from all subsequent calculations of means and standard deviations used to test remaining station data. The results of applying this procedure to separate data sets for Pahute Mesa and Yucca Flat events are the following:

1. 2052 accepted travel-time residuals for 28 Pahute Mesa explosions recorded at 278 teleseismic stations. The r.m.s. zero-measured residual (standard deviation) among all Pahute Mesa data, $\bar{\sigma}_{PM}$, is 0.247 sec.
2. 1893 accepted travel-time residuals for 54 Yucca Flat explosions recorded at 196 stations. $\bar{\sigma}_{YF} = 0.263$ seconds.

3.3.2 Station Data Grouping

While the dynamic screening procedure discussed above removed a high percentage of the noisy station-event travel-time residuals in the data base, we are still left with a

number of stations exhibiting data with large a r.m.s. residual (σ_s). The objectives of the remaining culling procedure that was applied to the data are (1) to further reduce the noise component, and (2) reduce the size, but not the information content, of the data vector that we invert for structure. The latter objective is a result of dimensional constraints on the number of model parameters and data imposed by the particular computer system (i.e., UNIVAC 1100/81) at our disposal.

As noted earlier in this section, the distribution of teleseismic stations (Figure 3.3) is quite uneven, ranging from an extremely large number in restricted azimuth-distance ranges (e.g., Europe) to few, or none, in other regions (e.g., the south Pacific). The dense station coverage, exemplified by the European stations, presents us with a data redundancy situation which can be exploited to further cull the data base. In the case of approximately colocated stations we have two options. The first is to simply delete stations that either appear excessively noisy (i.e., have large r.m.s. residuals) or are poorly recording. The other option is to devise a scheme whereby we average, or combine, data from nearly stations. The advantage of this latter option is that we reduce the size of the data base but retain the information content.

In Section II we described a procedure for averaging data that are redundant with respect to model parameters (velocity structure) but not redundant with respect to nuisance parameters (station baselines). In this problem, redundancy with respect to velocity structure occurs when ray paths are close to one another and, thus, predominantly sample the same model blocks. This occurs when either the originating events or recording stations are close. In this study we chose not to make any assumptions about similarity of structure for closely spaced explosions but combined, or grouped, data from stations instead.

Given a set of stations assigned to a particular group, their travel-time data from each event were averaged according

to the procedure described in Section 2.4. The average datum is then assigned to a fictitious station located at the centroid of the group. There are two criteria to be satisfied in defining station groups. One is to minimize the greatest separation between ray paths within the model volume to individual stations within a group. The second is to minimize the number of groups (e.g., avoid single-station groups). The algorithm adopted was to grid that portion of the world occupied by stations into azimuth and distance elements. Azimuth was divided into 36 10° sectors. Epicentral distance was divided into six ranges with cutoffs of 0° , 25° , 45° , 56° , 68° , 78° and 110° . This defines a total of 216 possible elements, or groups, including those for $\Delta < 25^\circ$. Of these, 154 are empty (no stations) leaving 62 station groups.

The distance ranges defined above correspond to roughly uniform angle-of-incidence (aoi) ranges of about 3° , with slight modification to avoid splitting obvious clusters of stations. A 10° azimuthal gridding implies a lateral angular separation of 3° to 4° for ray paths exiting the model volume to teleseismic distances. Thus, rays to stations within a group have no more than about a 5° total angular separation. (The actual maximum separation of rays in a group is typically much less than this.) Given the dimensions of the model blocks used in this study (see Section 4.1), the approximation of the different rays to stations in a group, as defined here, by a single ray to the centroid is quite sufficient.

3.3.3 Culling of Station Data

Mean values and standard deviations (r.m.s.'s) of travel-time residuals from the entire set of stations in the data base as it stands at this stage of the experiment are listed in Appendix C for Pahute Mesa and Yucca Flat explosions, separately. The stations are ordered by group number given by the five digit number in the last column of these tables. The first two digits

define the distance range (i.e., 02 implies 25° to 45°), while the final three digits identify the azimuth sector (i.e., 001 equals the 0° to 10° sector).

The station culling procedure that we adopted is best described as analyst intensive. That is, we considered several different aspects of the data before deciding whether to accept or reject a particular station. Criteria for rejecting a station were

1. that it had a large r.m.s. residual,
2. that it contributed only a small number of data.

These criteria were applied by considering the Pahute and Yucca event groups separately, so as to avoid culling stations based on large signal differences (as opposed to large noise).

In practice, a hard and fast rule was to reject any station with r.m.s. residual (based on any number of readings) in excess of 0.6 sec. Deleted stations are tagged with an "x" in Appendix C. Furthermore, stations with a fairly high r.m.s. residual were also rejected if high quality stations could be found in the same azimuth-distance group. (A high quality station was defined as one with a small r.m.s. residual, < 0.3 sec, based on ten or more events).

3.3.4 Final Data Set

The procedures described above led to a final set of 2497 data suitable for inversion. These data (ungrouped) are displayed in Figures 3.6a through 3.6f according to the same format as Figures 3.5a through 3.5f. The gross differences between residual patterns at Pahute and Yucca are rather more visible on this final data set because of the noise reduction achieved. Nevertheless, the data still appear to contain significant noise, as evidenced by the rather erratic distribution of residuals within single events. This is in contrast

Figures 3.6a through 3.6f are on the following pages.

Figure 3.6. Final observed travel-time residuals (zero-meaned) after application of all culling procedures. Residuals are represented in the same format as for Figure 3.5. Figures 3.6a and 3.6b represent events in the Pahute Mesa test area, Figures 3.6c to 3.6f show events from the other test areas. Outlines of the corresponding rectangular frames are shown on Figure 4.3 in relation to the NTS geography. Frames are labeled along north-south and east-west axes with UTM (Universal Transverse Mercator) northing and easting coordinates (in kilometers), with respect to a central meridian of 117°W (500 km easting).

PM-YF-T65 >>OBSERVABLE DATA VECTOR<< 58 NTS EVENTS AT 52 STA GROUPS 07-20-81

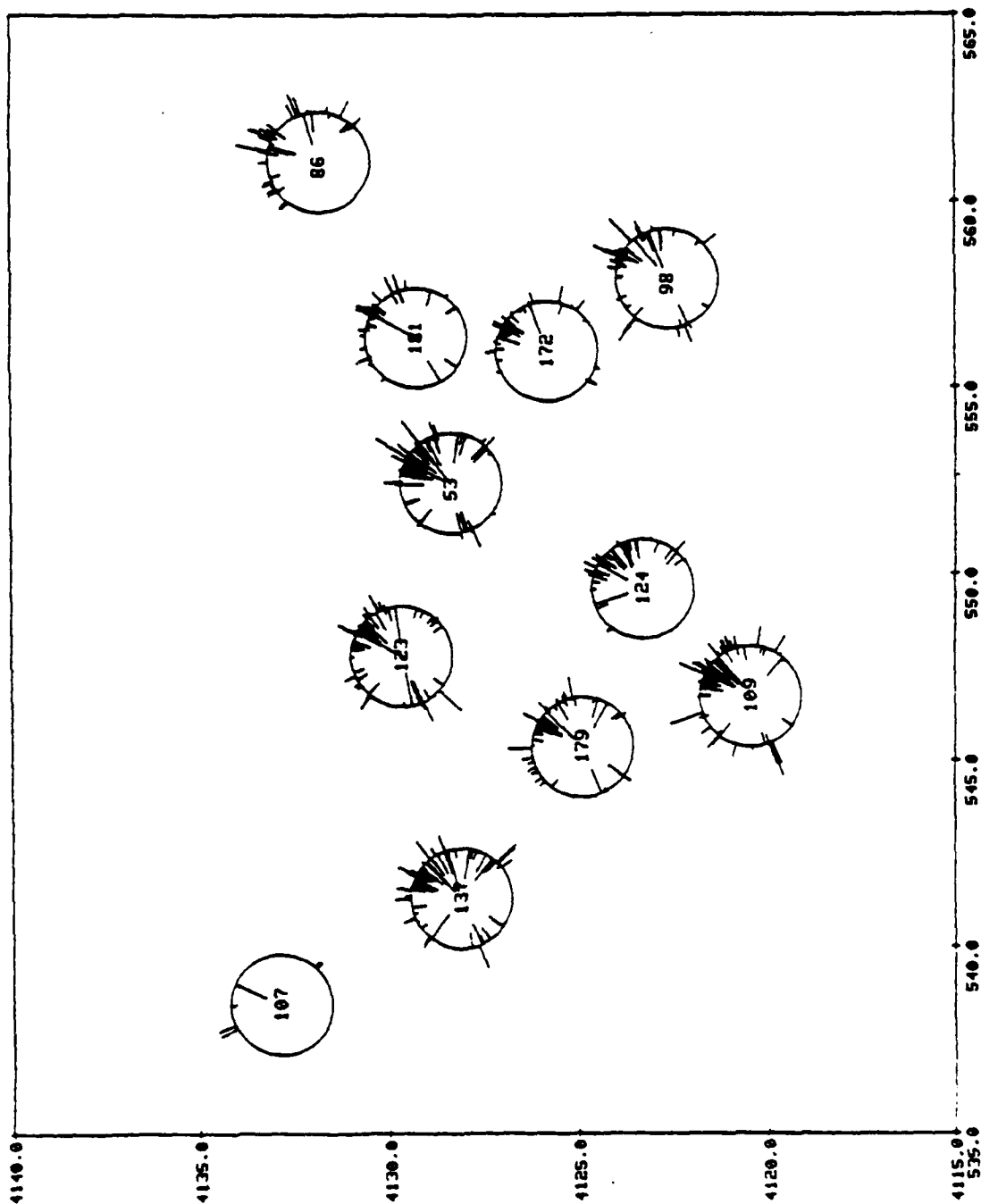


Figure 3.6a. Pahute Mesa.

PM-YF-T65 >>OBSERVABLE DATA VECTOR<< 58 NTS EVENTS AT 52 STA GROUPS 07-20-81

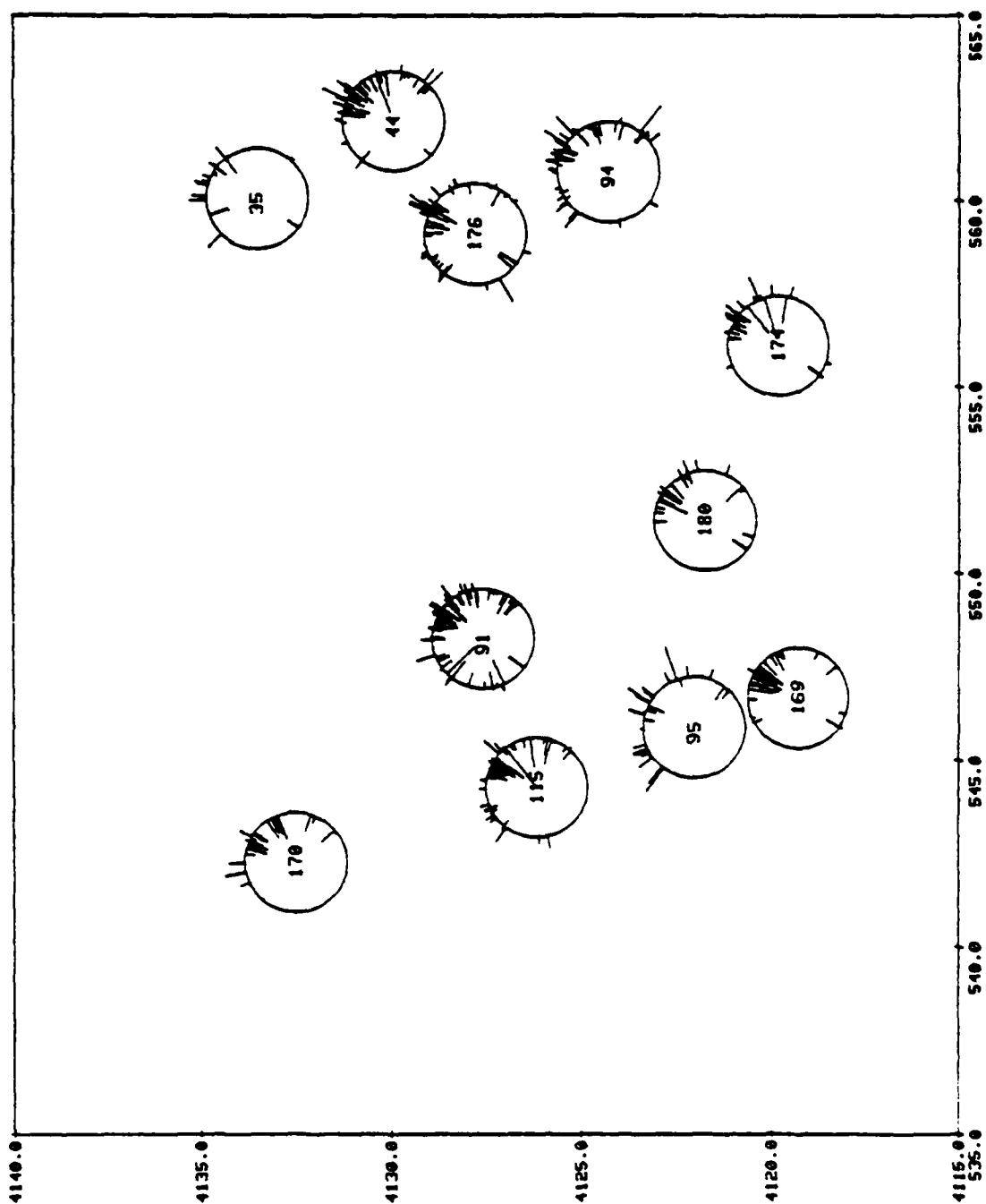


Figure 3.6b. Pahute Mesa.

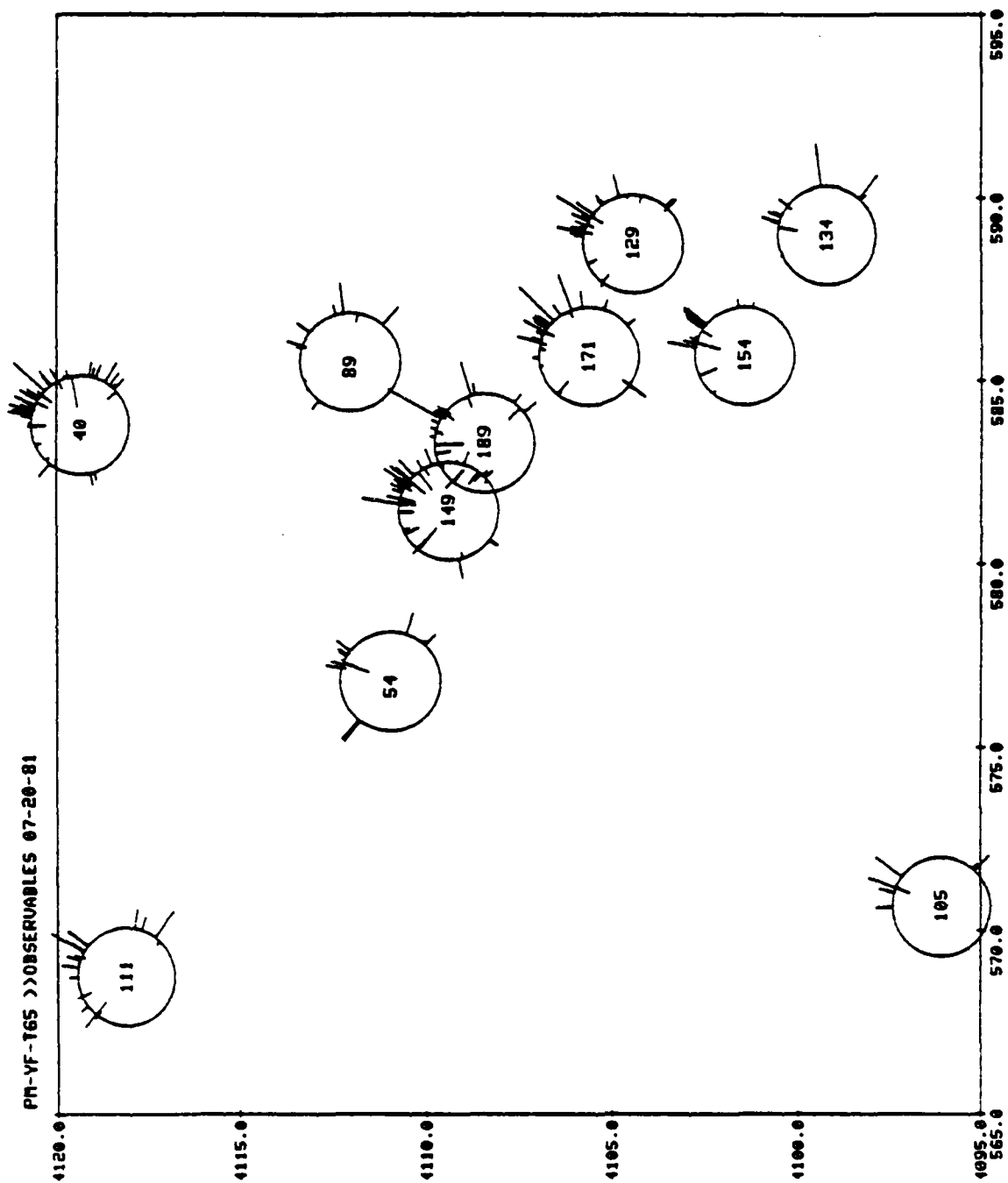


Figure 3.6c. Yucca Flat.

PH-YF-T65 >>OBSERVABLE DATA VECTOR<< 58 NTS EVENTS AT 52 STA GROUPS 07-20-81

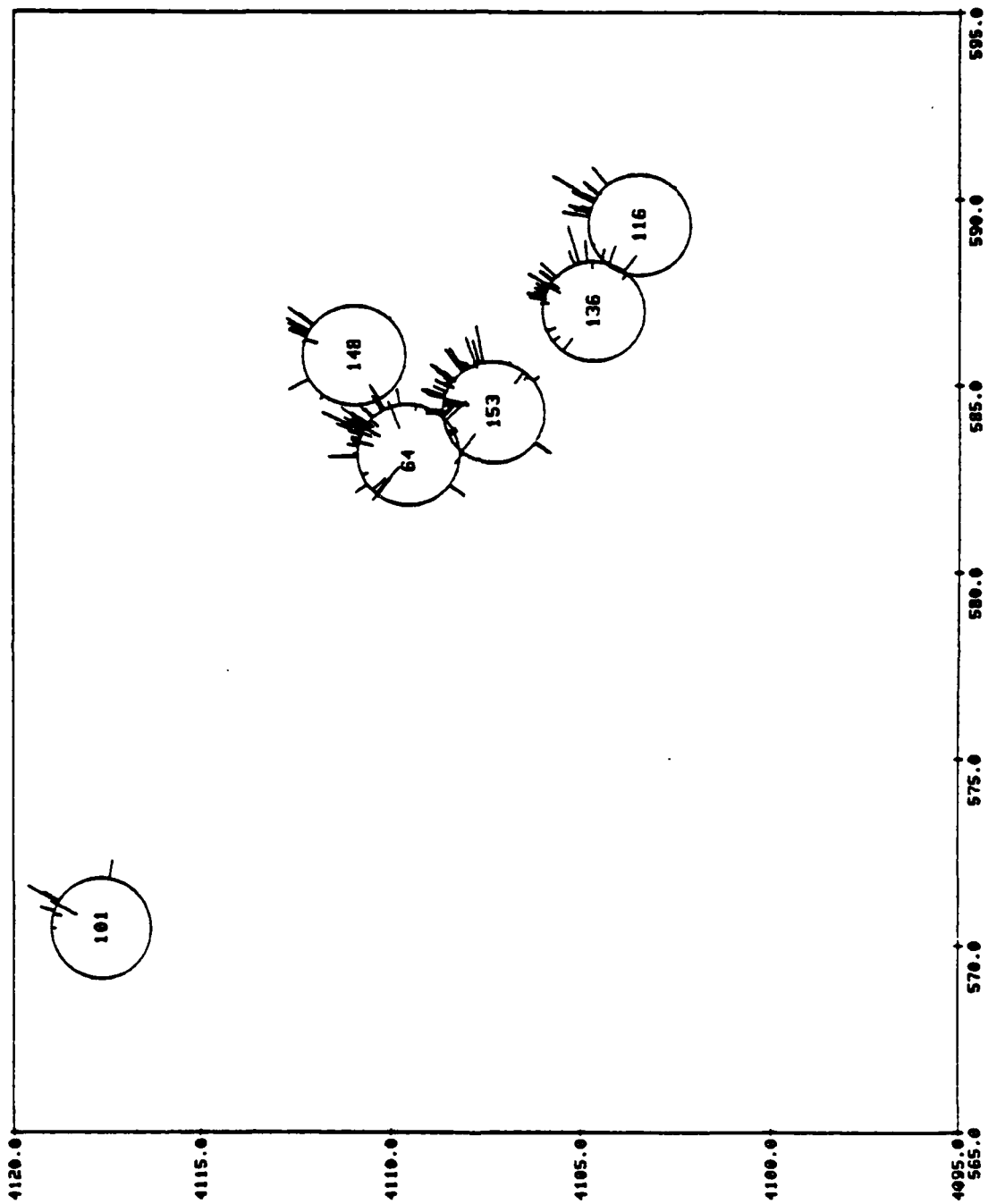


Figure 3.6d. Yucca Flat.

PM-YF-T65 >>OBSERVABLE DATA VECTOR<< 58 NTS EVENTS AT 52 STA GROUPS 07-20-81

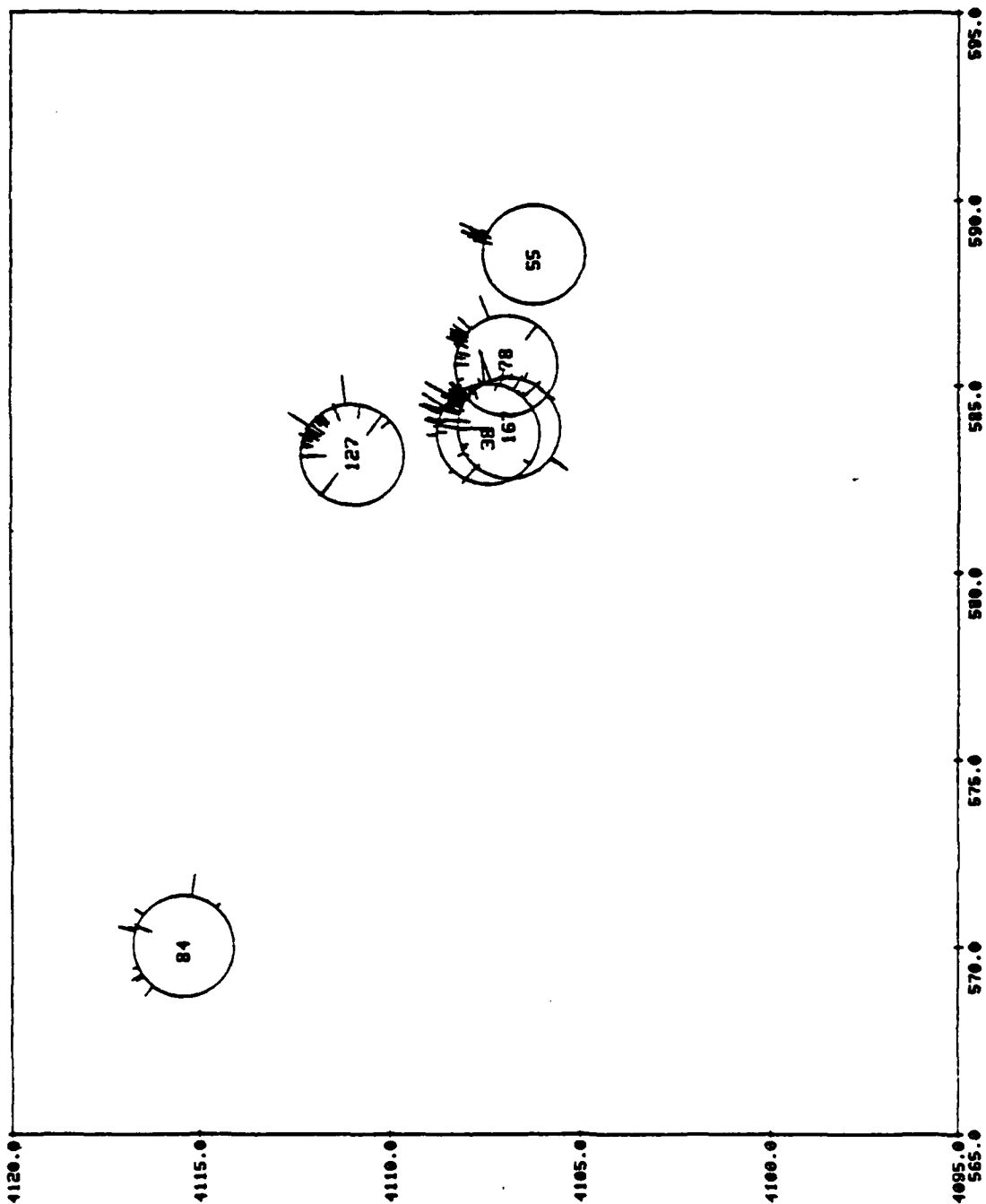


Figure 3.6e. Yucca Flat.

PH-YF-T65 >>OBSERVABLE DATA VECTOR<< 58 NTS EVENTS AT 52 STA GROUPS 07-20-81

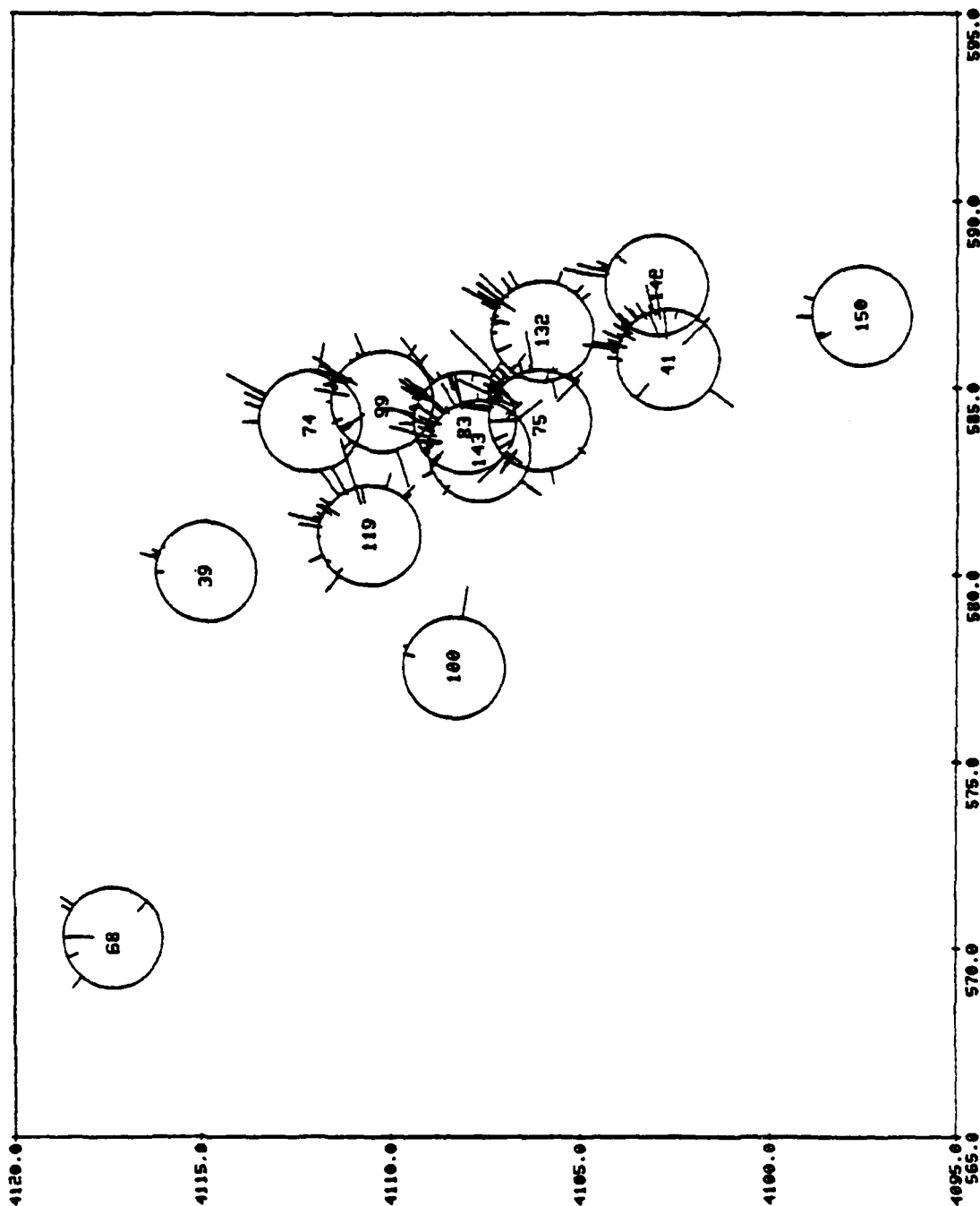


Figure 3.6f. Yucca Flat.

with the much more organized patterns of residuals we had encountered in previous studies using the reciprocal problem (Rodi, et al., 1980). Discussion of the more subtle features of these observations will be deferred to Section V where such features will be compared to corresponding properties of the inversion model.

3.4 COMPARISON WITH SPENCE'S DATA SET

In his study of crust and upper mantle inhomogeneities beneath the Silent Canyon Caldera, Spence (1974) used tele-seismic residuals of eight large shots, and used DUMONT as a reference event in his display of the data. Figures 3.7a and 3.7b show Spence's data for these eight explosions. Because we use the denuisancing techniques described above, our final data set (Figure 3.6) is not directly comparable with Spence's representation of the travel time anomalies. In order to verify that the two data sets are compatible, at least for this limited number of events, we show on Figure 3.8 the residuals of the same eight explosions, referenced to DUMONT. Figure 3.8a shows all travel time residuals to stations which recorded both DUMONT and any one of these eight events. Figures 3.8b and 3.8c show subsets of these observations partitioned according to whether the takeoff angles is smaller or greater than 20° respectively.

Although these figures do not lend themselves to a one-to-one comparison of individual data, the general properties of Figures 3.7 and 3.8 are well matched. In particular, the drastic shift from negative to positive residuals for steep rays (Figure 3.8b) as one leaves the caldera region to the southwest, as well as the mixed character of residuals for shallow rays (Figure 3.8c) are in agreement with Spence's description. A key event in Spence's reasoning is GREELEY, which exhibits strongly negative residuals for steep rays, a feature also present in our data set.

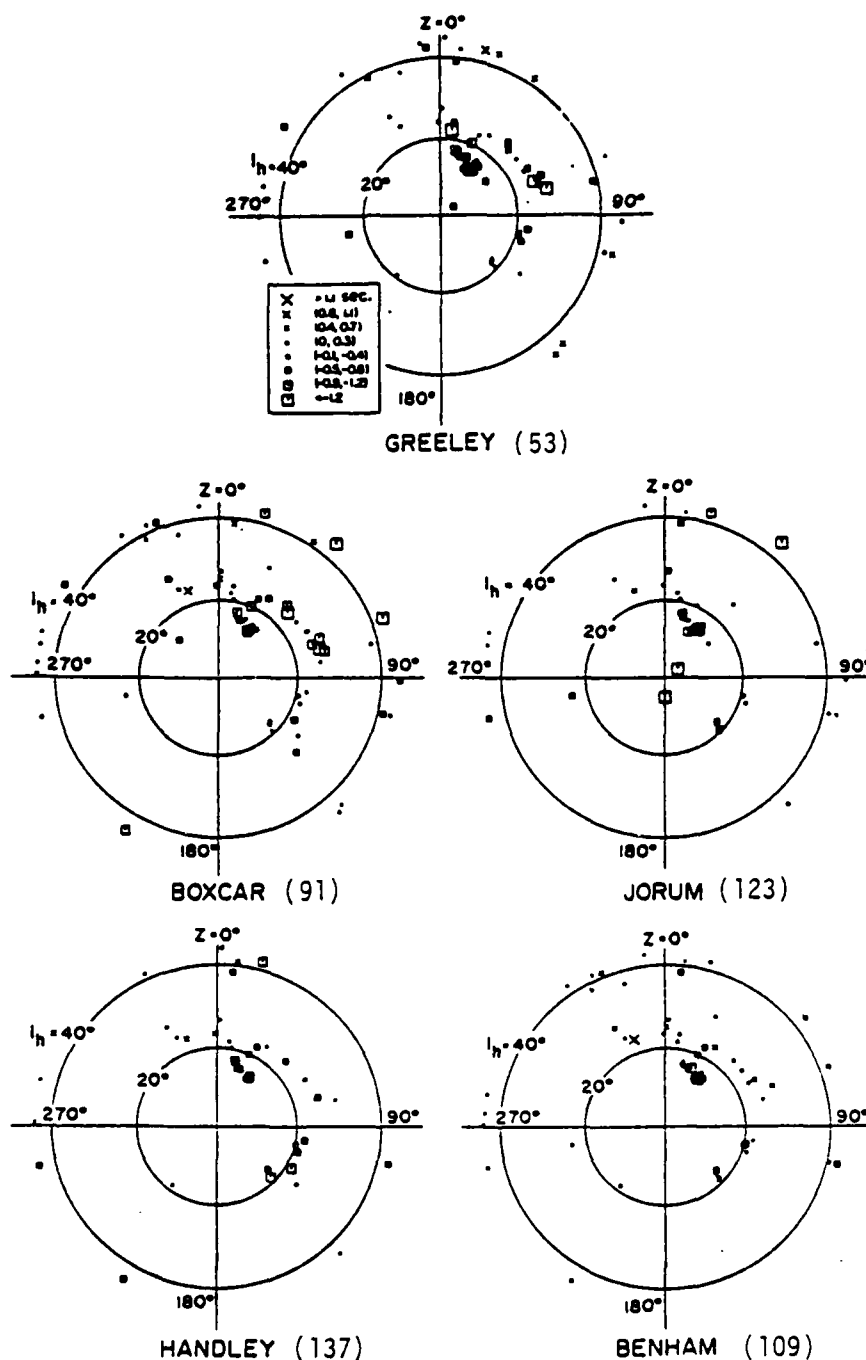


Figure 3.7a. Travel-time residuals relative to DUMONT residuals, for five Pahute Mesa events (from Spence, 1974). Our event numbers (used in Figures 3.5, 3.6 and 3.8) are shown after the event names.

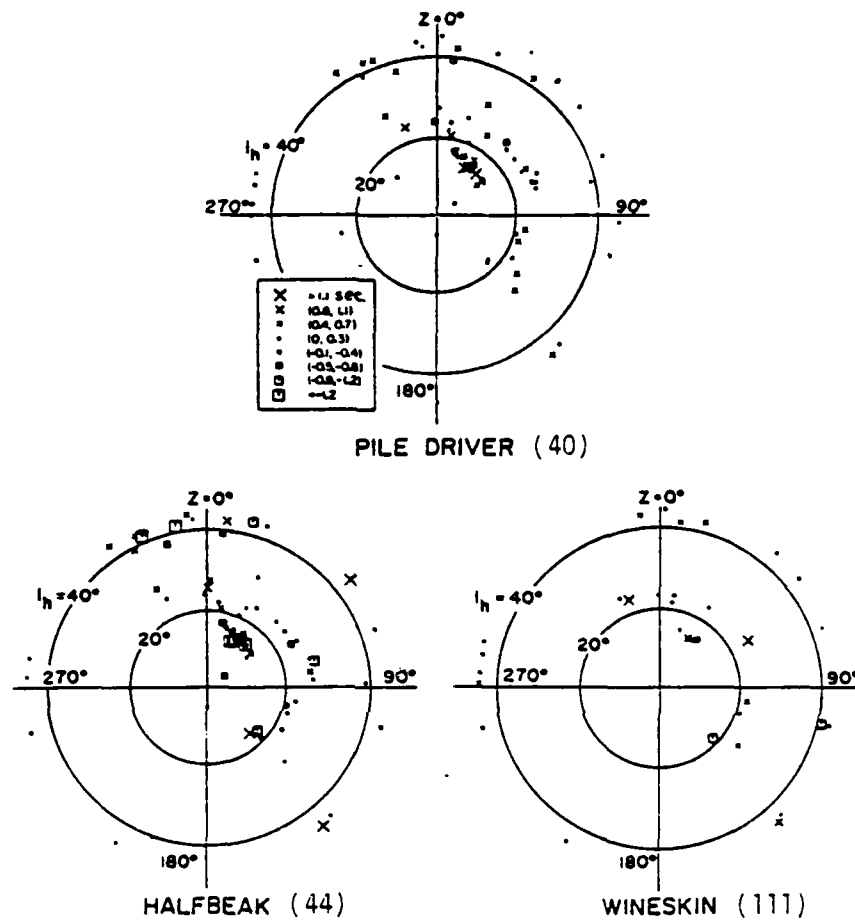


Figure 3.7b. Travel-time residuals, relative to DUMONT residuals, for three NTS events.

PH-YF-T65 RESIDUALS RELATIVE TO DUMONT (038) • < AOI < 90 07-20-81

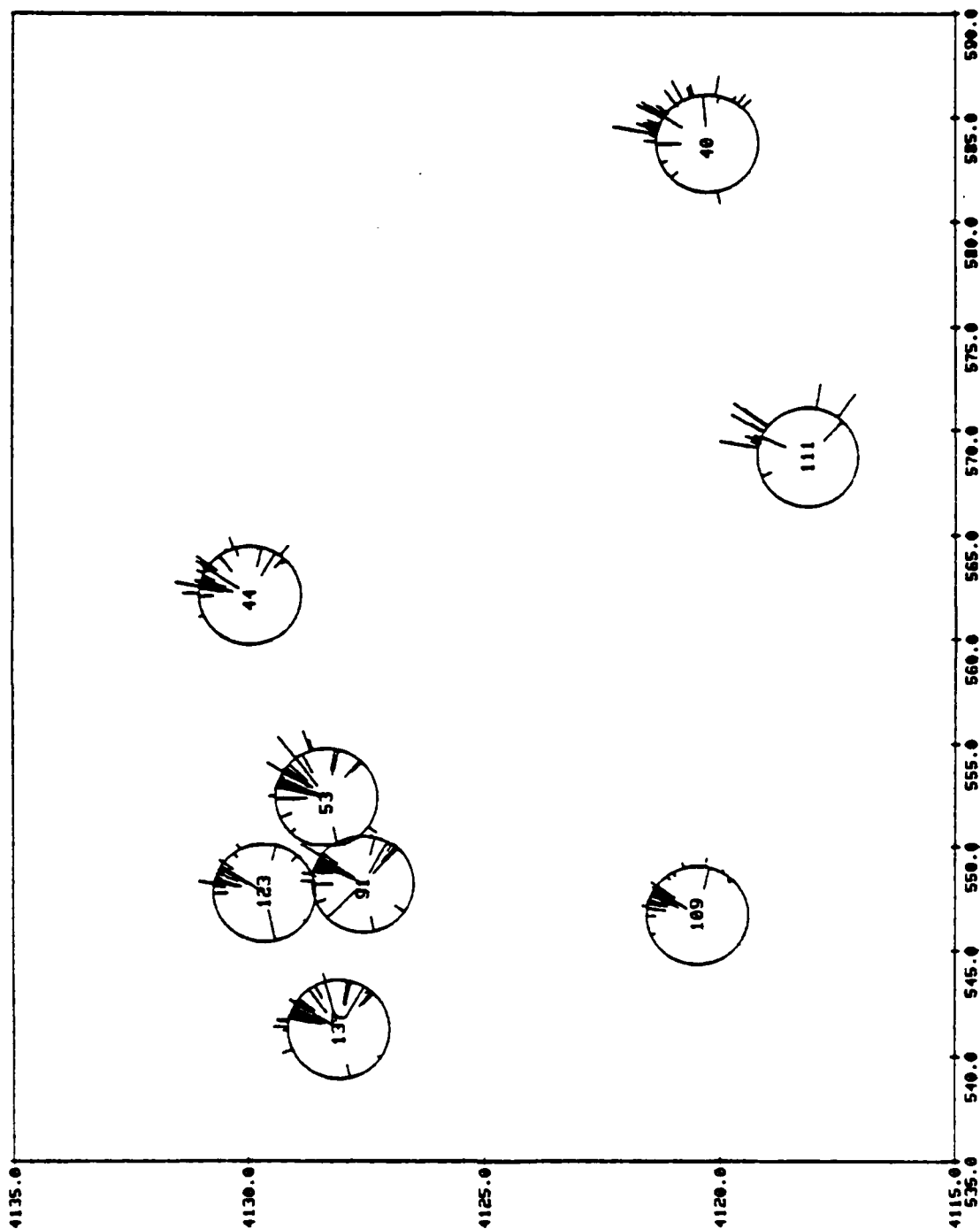


Figure 3.8a. Residuals for the eight events used by Spence (1974) relative to DUMONT; see Figures 3.7a and 3.7b for corresponding event names.

PR-YF-T65 RESIDUALS RELATIVE TO DUMONT (038) • < A01 < 20 07-20-81

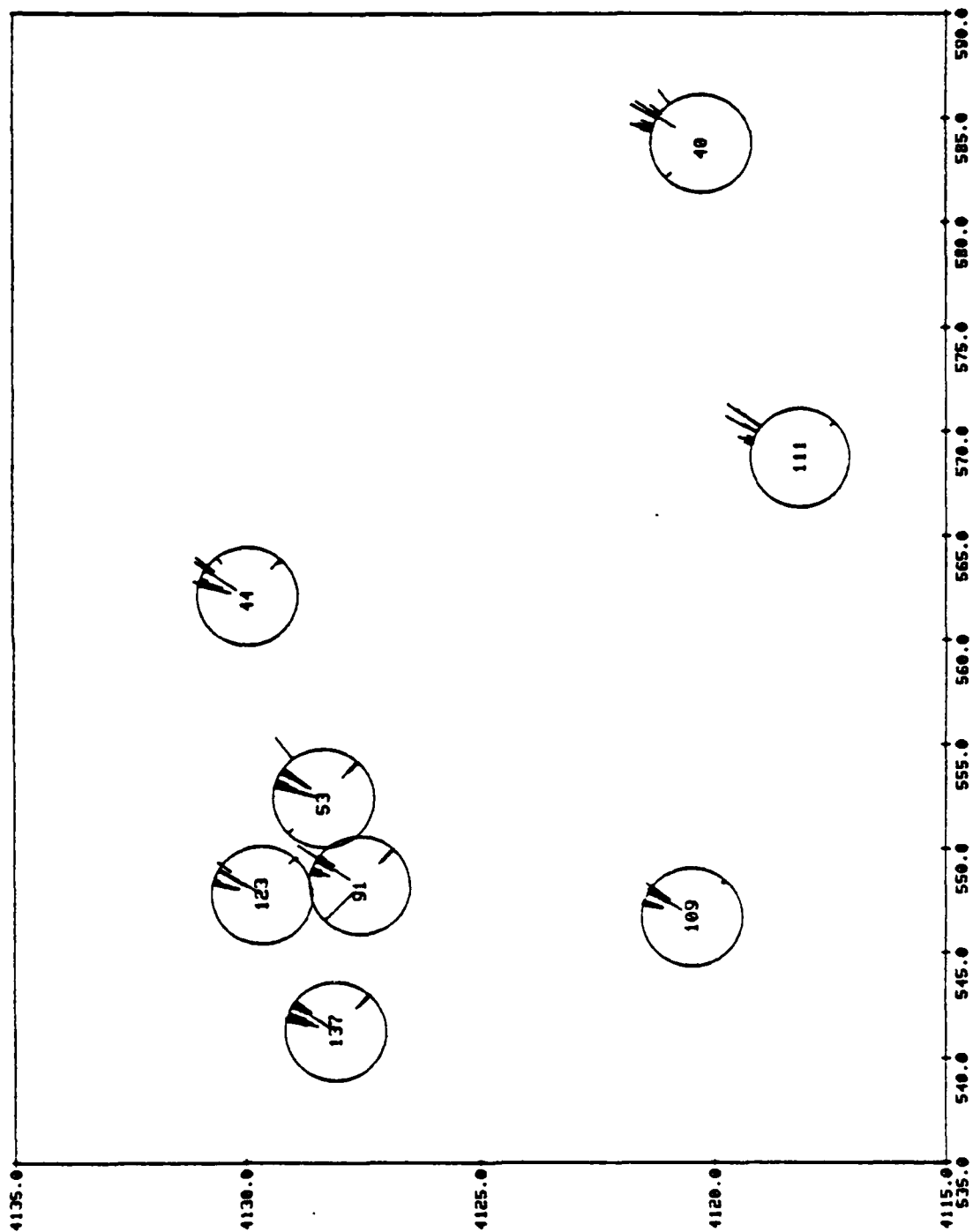


Figure 3.8b. Same as Figure 3.8a, for steep rays with takeoff angle between 0 and 20°.

PM-VF-T65 RESIDUALS RELATIVE TO DUPONT (038) 20 < A01 < 90 07-20-81

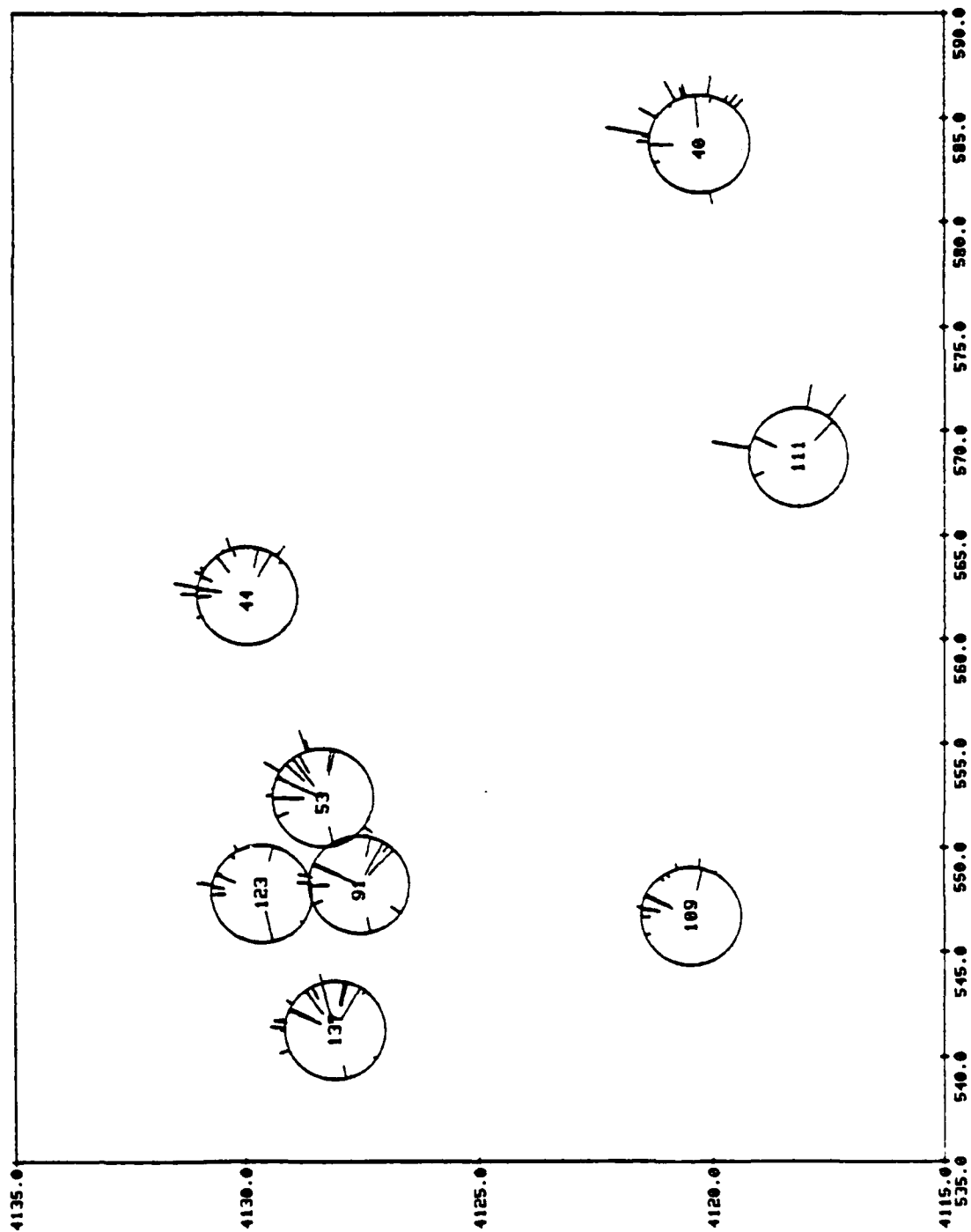


Figure 3.8c. Same as Figure 3.8a, for rays with takeoff angles greater than 20°.

Thus, the small subset of our data which corresponds to Spence's data set does not reveal any obvious discrepancies. However, in his analysis of Pahute Mesa residuals, Spence applied a large correction to the travel times ($\sim +0.4$ sec) in an attempt to account for the thick (~ 5 km) low velocity caldera fill; this resulted in an enhanced contrast between Pahute Mesa residuals and residuals from other test areas. We shall discuss this point in detail in Section V.

3.5 EVENT-AVERAGED RESIDUALS

One final method of summarizing the data is depicted on Figures 3.9a through 3.9c, which shows the mean residual associated with each event, after averaging over all stations recording this event. This representation provides a measure of the average vertical delay due to crust and mantle beneath each epicenter. This information is not completely free of bias insofar as the sampling of crust and upper mantle structure by rays leaving an event is not azimuthally uniform. On the other hand, prior zero-meaning of the entire set of residuals tends to remove baseline effects in the sense described earlier so that we can regard Figure 3.9a as an image of the relative variations of travel times across NTS.

Similarly, Figures 3.9b and 3.9c show the patterns for the Pahute and Yucca groups, respectively. The principal feature which emerges is that arrivals from Pahute events are generally early, compared to arrivals from shots in other test areas. The range of variation in mean residuals exceeds 0.5 sec. In addition, internal variations within the Pahute group, and within the Yucca group are illustrated on Figures 3.9b and 3.9c, respectively.

The east-southeast sector of the Pahute event group is characterized by a clear gradient in the mean residuals, and

points to the existence of a transition region between the Pahute test area and the Rainier Mesa-Yucca Flat test areas. However, isolated positive residuals are also found on the periphery of the group, to the south and west, which is a mild suggestion that the region of negative anomalies is not open-ended in those directions but is a localized anomaly centered on the Silent Canyon caldera. We note that Ryall (1978) also observed early P-wave arrivals from teleseismic events recorded at stations located on and around Pahute Mesa.

The main feature which characterizes the Yucca event group is the dichotomy between events along the eastern portion of Yucca Valley, which exhibits strongly negative residuals, and events west of the Yucca fault which tend to yield somewhat earlier arrivals.

As we shall see, the mean residuals shown on Figures 39a through 39c permit a convenient comparison between gross features of the data set and of the inversion models. Because this information relies on extensive averaging of individual data, it tends to be relatively insensitive to most sources of noise, and hence to enhance the more robust aspects of the data set. We use it extensively in Sections IV and V.

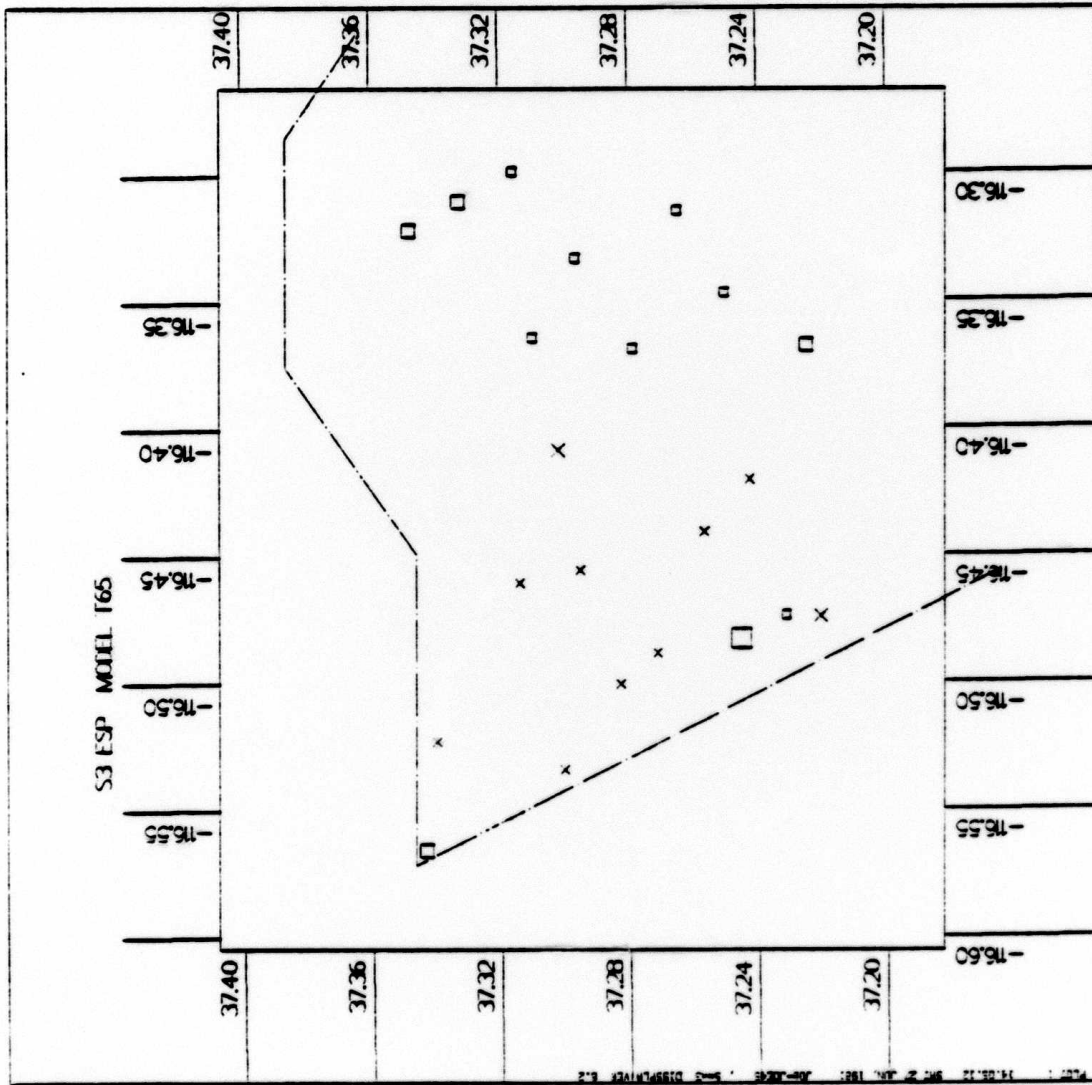


Figure 3.9b. Event-averaged travel-time residuals for Pahute Mesa events, obtained by averaging residuals which were first zero-measured among only Pahute Mesa events.

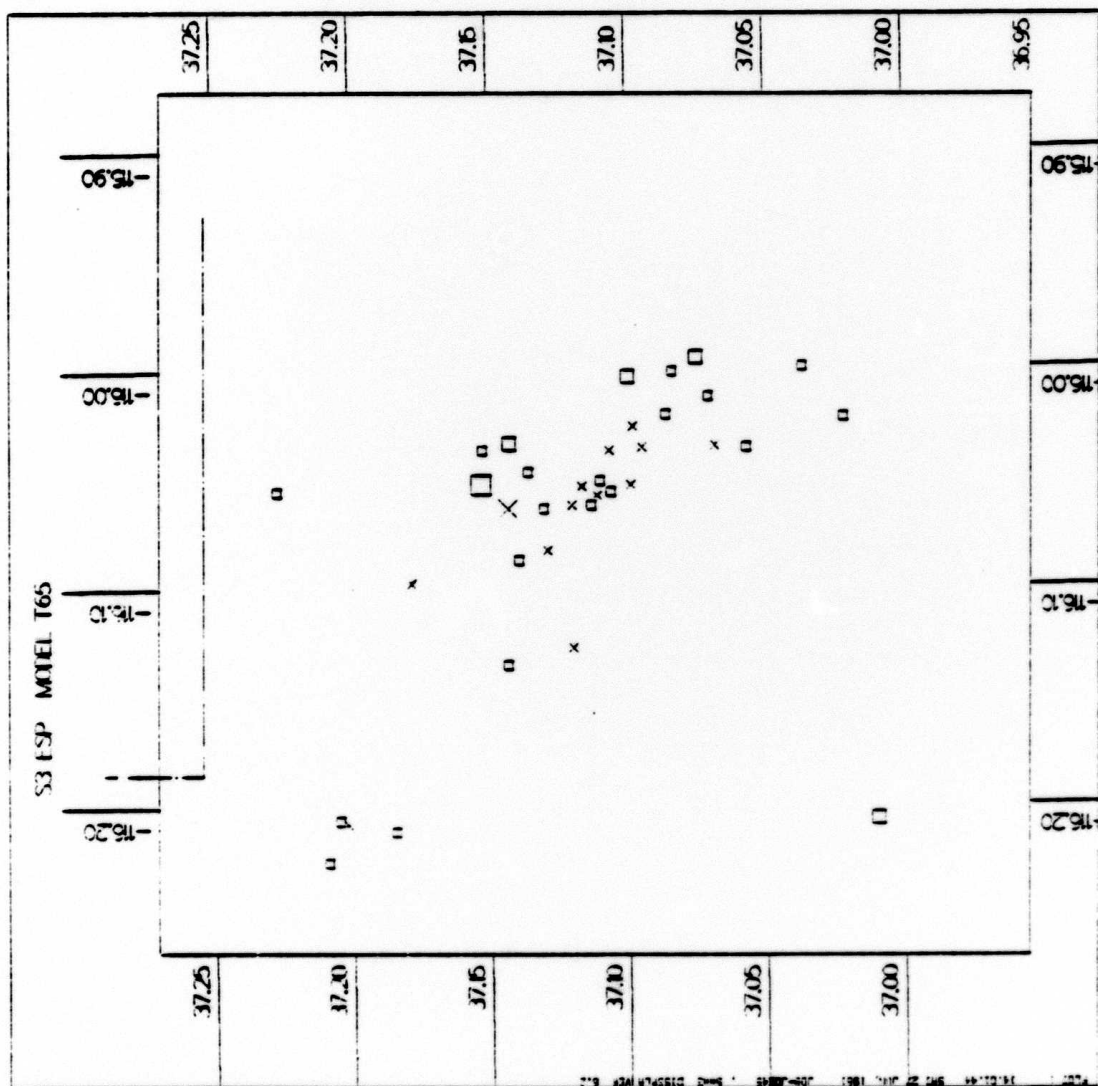


Figure 3.9c. Event-averaged travel-time residuals for Yucca Flat events (plus Rainier Mesa events and PILEDRIVER), obtained by averaging residuals which were first zero-measured only over these events.

IV. INVERSION OF THE DATA SET

The final data set obtained through the procedure outlined in the previous section constitutes the input to the inversion algorithm developed in Section II. In this section, we describe the actual application of the inversion technique to the derivation of a sequence of three-dimensional models for the crust and upper mantle beneath NTS.

4.1 STARTING MODEL

Because the problem has been linearized in order to permit full application of linear estimation theory (Section II), the first order of business is to construct a starting model. As mentioned earlier, this starting model consists of a one-dimensional seismic structure superimposed on a three-dimensional grid of rectangular blocks. The output of the inversion algorithm consists of three-dimensional departures from the horizontally layered starting model.

Since we make no attempt to account for the nonlinearity of the problem by iterating on the model and tracing three-dimensional rays, the rays along which slowness anomalies are integrated in solving the forward problem are those which can be traced through the starting model. The ray parameter pertinent to a specific event and a specific station (or station group) is taken from the 1968 travel time tables of Herrin, et al. (1968), and corresponds therefore to ray tracing through a spherically symmetric earth model, approximated locally beneath NTS by horizontal plane layers.

Since these rays are not perturbed in this simple iteration scheme, the main consideration should be that theoretical rays be a good approximation to the actual ray paths. In view of the fact that we only use only teleseismic rays

and thus do not consider the case of turning points within the model grid, the inversion results are only mildly dependent on errors in the initial velocity structure; this is a consequence of Fermat's principle (e.g., Aki, et al., 1977; Rodi, et al., 1980).

Insofar as the grid is concerned, we must achieve an acceptable trade-off between two dominant constraints: (1) we must avoid under-parameterization of the model, which would result in implicit constraints difficult to analyze, and (2) we must limit the length of the vector of unknown parameters so as to keep the numerical problem within manageable size. Although it is possible to construct solutions to very large systems of simultaneous linear equations, (e.g., Wiggins, et al., 1976) application of the full power of linear estimation theory, as presented in Section II, requires manipulation and decomposition of matrices with $M \times N$ elements, where M is the number of unknown parameters and N the number of data.

4.1.1 Vertical Structure

The variation of seismic velocities with depth in the crust and upper mantle beneath NTS can be estimated by using a Basin and Range model; seismic structure in the Basin and Range has been the object of several studies (e.g., Archambeau, et al., 1969; Helmberger and Engen, 1974; Burdick and Helmberger, 1978). Figure 4.1 shows several such models. The principal feature of importance for our purposes is the presence of a well-developed Low Velocity Zone (LVZ), which may be capped by a "normal" velocity "lid." As a result, the rays show relatively small average curvature in the upper mantle, in that the angle of incidence does not vary very much below the crust.

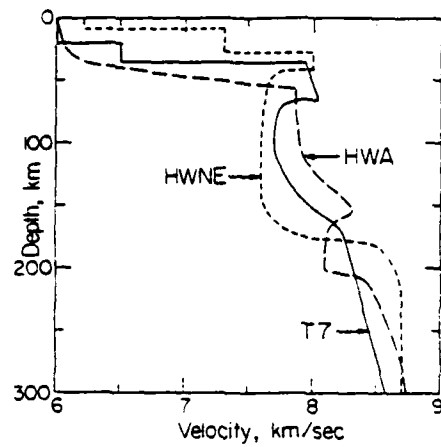


Figure 4.1. Comparison of velocity profiles inferred for the Basin and Range (after Burdick and Helmberger, 1978).

We have approximated this vertical structure, subject to the following considerations.

1. The number of horizontal homogeneous layers included in the starting model is limited to six. Introduction of finer layering leads to a rapid increase in the number of unknown parameters and results in an unmanageably large problem. In addition, the narrow range of teleseismic incidence angles sampled by our data set limits the vertical resolving power, so that vertical oversampling results in an unnecessary waste of computer resources.
2. The crust-mantle boundary, which is the most important seismic discontinuity in the model, should be well approximated by the grid, in an average sense. Therefore, we impose that one of the grid interfaces be at a depth of 28 km, the average Moho depth beneath NTS (Pakiser and Hill, 1963).
3. The maximum depth extent of the model grid is chosen to be about 150 km, for three reasons. The first is that this represents grossly twice the horizontal extent of the grid (the greatest horizontal separation between events is about 60 km, and the greatest horizontal dimension of the grid is about 80 km - see below). We have found in previous work that this scaling constitutes a useful rule of thumb in this type of modeling. The second is that Spence (1974) argued that significant lateral variations exist beneath NTS down to 150 km or deeper. The third is that thin lens models of lateral variations (e.g., Haddon and Husebye, 1978; Walck and Minster, 1981) tend to favor 100 km to 150 km as the optimal thin lens depth in regions as different as NORSAR and the Transverse Ranges in Southern California. Of course, the best justification must be made a posteriori, on the basis of whether strong lateral variations can be inferred at this depth upon inversion.
4. Because of decreasing vertical resolution with increasing depth, layer thicknesses can be allowed to increase with depth, but successive layers should not differ in thickness too abruptly, for fear of implicitly over-constraining (or under-parameterizing) the model.

Based on these considerations, we constructed the six-layer model listed in Table 4.1 and shown on Figure 4.2. It consists of a two-layer crust over a uniform velocity mantle. Because the lid is quite thin, we did not attempt to include it explicitly in the top mantle layer (Layer 3), since it is the source of only minor perturbations in the teleseismic ray paths. The surface layer was chosen to be 12 km thick since most crustal models in different portions of NTS merge at approximately this depth. The seismic velocity in that layer was chosen to be 6 km/sec, which is in the upper range of shallow crustal velocities in the western United States, and is typical of midcrustal velocities in many regions (Pakiser, 1963). The mean crustal velocity is about 6.3 km/sec. It must be noted that perturbations to the mean velocity in any layer results in a baseline correction to all travel times, and thus trades off perfectly with the baseline errors contained in the data. Therefore, such linear functions of the unknown parameters are treated as nuisance parameters and handled using the denuisancing techniques described in Section II. As a result, estimates of lateral variations are quite insensitive to mean layer velocities, since their only effects are on the theoretical ray paths.

4.1.2 Horizontal Grid

The next task is to design a horizontal rectangular grid capable of representing lateral velocity variations across NTS. Our design obeys the following constraints:

1. The grid samples the entire area covered by the set of events retained for analysis, with minimal waste of unsampled blocks. This is achieved by taking the long axis of the grid along N60W, the approximate azimuth of Pahute Mesa relative to Yucca Valley.

TABLE 4.1
INITIAL MODEL FOR INVERSION

Layer	Depth to Bottom (km)	Thickness (km)	Initial Velocity (km/s)	Density- Velocity Coefficient
1	12	12	6.0	0.3
2	28	16	6.5	0.3
3	48	20	7.8	0.3
4	74	26	7.8	0.3
5	108	34	7.8	0.3
6	152	44	7.8	0.3

0	LAYER = 1 THICKNESS = 12 KM VELOCITY = 6.0 KM/S		
12	2	16	6.5
28	3	20	7.8
48	4	26	7.8
74	5	34	7.8
108	6	44	7.8
152			

Figure 4.2. Initial horizontally layered model of NTS crust and upper mantle velocity structure.

2. Grid elements are smaller in areas well populated by explosions, particularly Pahute Mesa and Yucca Flat, where grid elements are as small as 4 km.
3. The grid consists of an inner grid of finite blocks, containing all events, and is surrounded by a buffer zone of semi-infinite elements, (the outer grid) for which structural modeling is necessarily imprecise and unreliable due to poor parameterization.

The 9 x 16 element inner grid and associated outer grid are depicted on Figure 4.3 on a background of geographical coordinates. Also shown are the events retained in the final data set, an outline of NTS and two rectangular boxes corresponding to the partitioning of the data set as described in Section III. The actual dimensions of grid elements are listed in Table 4.2.

Figure 4.3 illustrates both the qualities and shortcomings of data set and model parameterization. Because the event distribution is elongated along N60W, it is immediately clear that shallow structure can only be determined reliably within a narrow (~ 70 km x 20 km) strip linking Yucca Valley to Pahute Mesa. Any shallow structure outside this strip will be almost exclusively controlled by the smoothness constraint imposed on the model in the inversion. A more quantitative measure of this observation is provided by the "hit patterns" described on Figures 4.4a through 4.4f.

A hit pattern is a map showing for each three-dimensional grid element the total length of all rays crossing this element, normalized to the thickness of the corresponding layer. In that sense, it is an approximate measure of the norm of the corresponding column of the data matrix A (Section II).

An element with a hit pattern of 0 is such that the corresponding velocity perturbation is not really determined

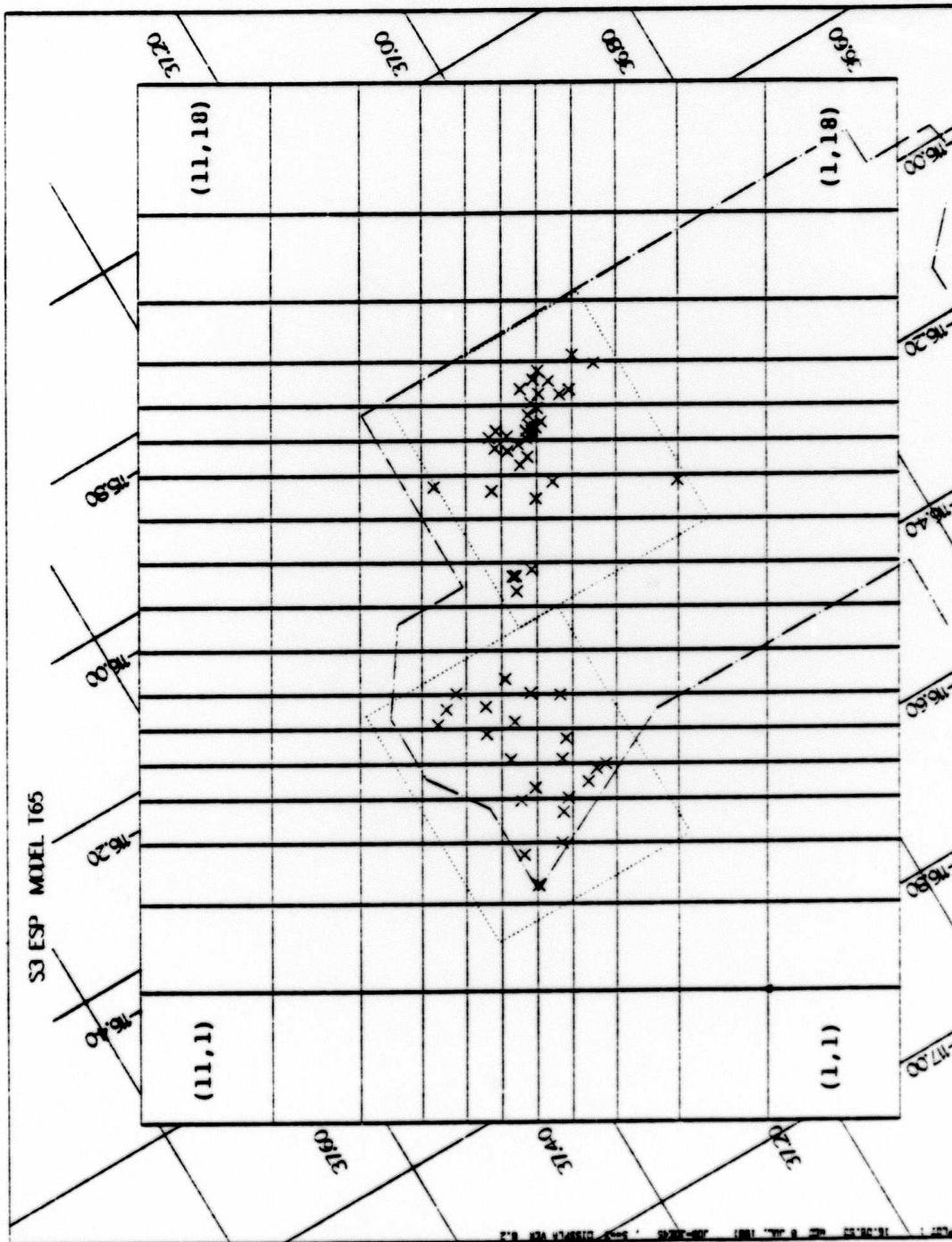


Figure 4.3. Outline of model grid (both inner and outer grid) in relation to geographical coordinates. Also shown are the locations of events retained in the data set, the outlines of boxes used in Figures 3.5, 3.6, 3.7, 3.9 and 4.14, as well as the outer boundary of the NTS. For purposes of identification, cells are numbered according to a cartesian indexing scheme, as indicated on the corner cells.

TABLE 4.2
HORIZONTAL GRID DIMENSIONS

Along N30°E Axis* (Listed from SW to NE)		Along S60°E Axis (Listed from NW to SE)	
Block Width (km)	Model Grid Coordinate† (km)	Block Width (km)	Model Grid Coordinate (km)
∞	$-\infty$	∞	$-\infty$
10	0	10	0
7	10	7	10
5	17	5	17
4	22	4	22
4	26	4	26
4	30	4	30
5	34	5	34
7	39	5	39
10	46	5	44
∞	56	5	49
	$+\infty$	5	54
		4	59
		4	63
		5	67
		7	72
		10	79
		∞	89
			$+\infty$

* The model grid is rotated 30° from north.

† The model grid origin (0,0) is located at 4116.5 km northing, 515.0 km easting in Universal Transverse Mercator (UTM) coordinates with respect to a central meridian of 117°W. The origin coordinates are thus 37.197°N, 116.831°W.

directly by the data, but is rather determined by the perturbations in the neighboring elements through the smoothing constraint. Conversely, an element with a large number on the hit pattern will have a much better determined perturbation.

The patterns for both crustal layers (Figure 4.4a and 4.4b) show that well determined structural features can only be obtained in the immediate vicinity of the epicenters. Layer 3 (Figure 4.4c) exhibits a much more even distribution of rays. In Layer 4 (Figure 4.4d), we already detect the outward fanning of the ray bundles, and some cells beneath Pahute Mesa are not sampled at all. In Layers 5 and 6 (Figures 4.4e and 4.4f), the ray distribution is heavily biased toward the outer grid, with a particularly dense concentration to the northeast, corresponding to the numerous European stations (Figure 3.3). Based on Figure 4.4f, it is clear that any attempt to model structure below 150 km would be futile since practically all blocks sampled would belong to the outer grid.

This picture is confirmed by the ray sketches shown on Figures 4.5a and 4.5b. In spite of their relatively small mean curvature many rays exit the grid without sampling the bottom layer adequately. This problem is, of course, much more severe for northeastern and southwestern azimuths, since the grid is narrower in these directions.

Thus, even before performing any inversion, we can make some general judgments concerning the validity of the method. The best constrained layers (based on optimal intersection of ray paths) will be Layers 2, 3 and 4. The top layer is only well sampled near the epicenters, and the bottom layers are poorly sampled near the center of the grid. These features will be called upon when interpreting the inversion results.

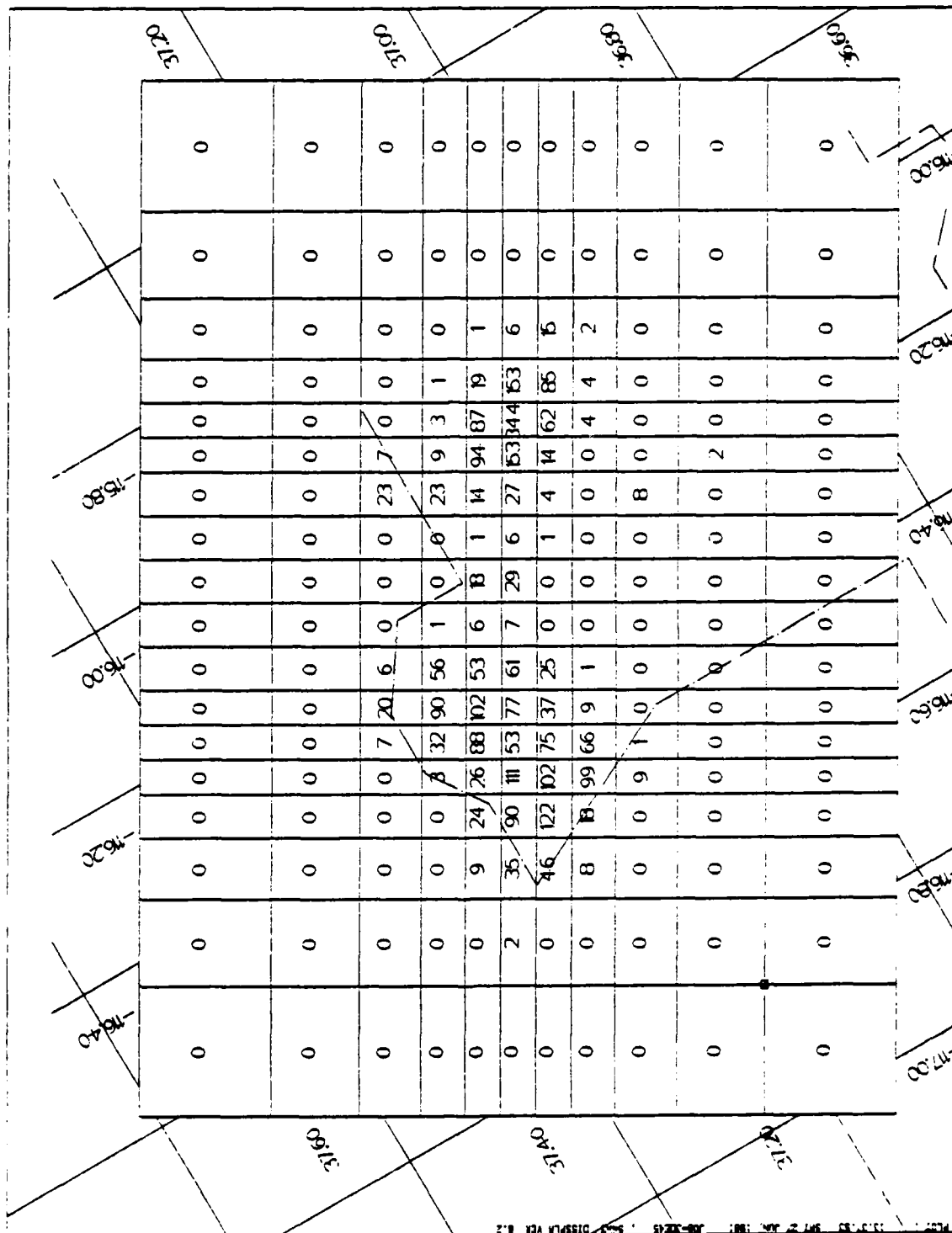


Figure 4.4a. Hit pattern for Layer 1 (0 - 12 km).

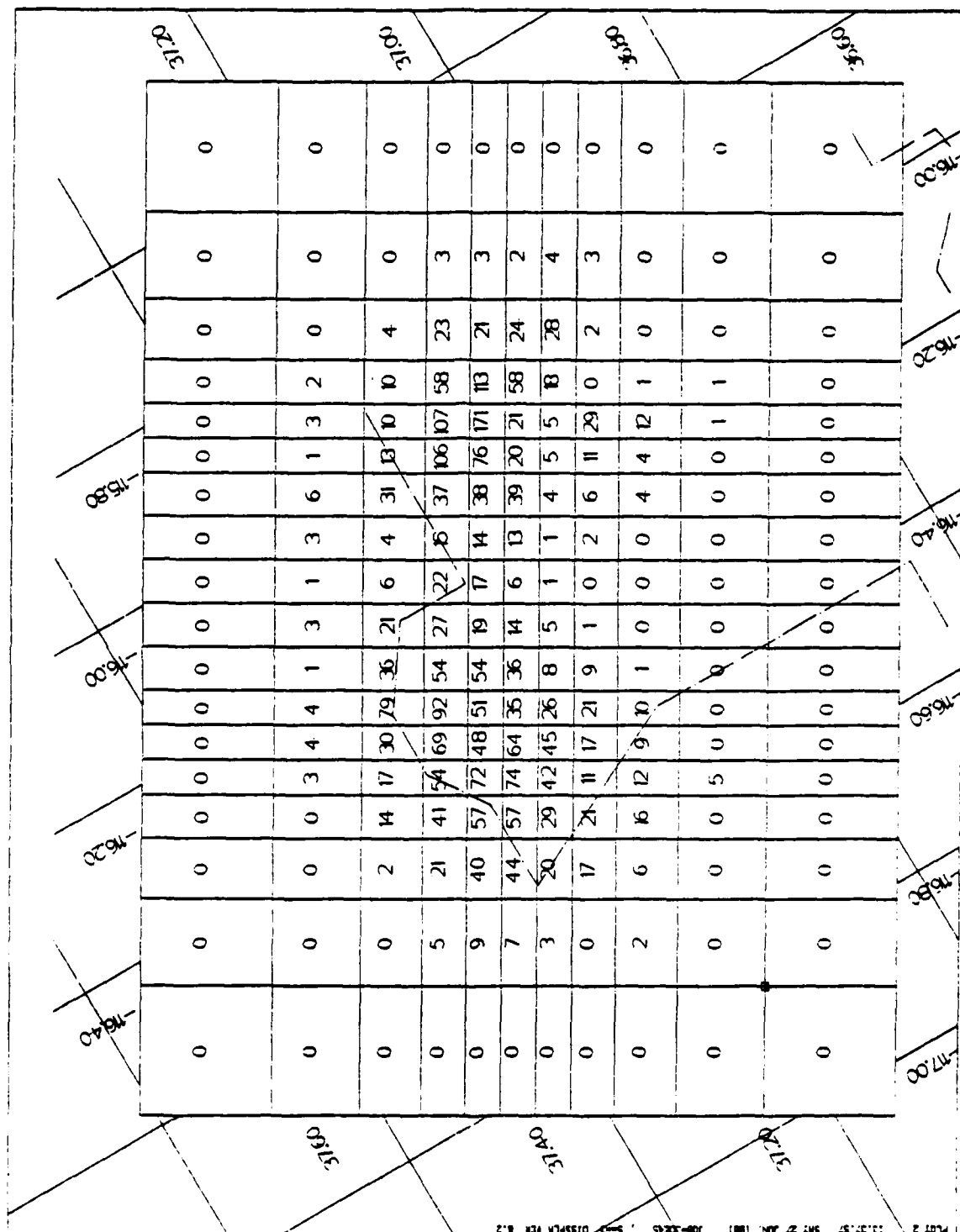


Figure 4.4b. Hit pattern for Layer 2 (12 - 28 km).

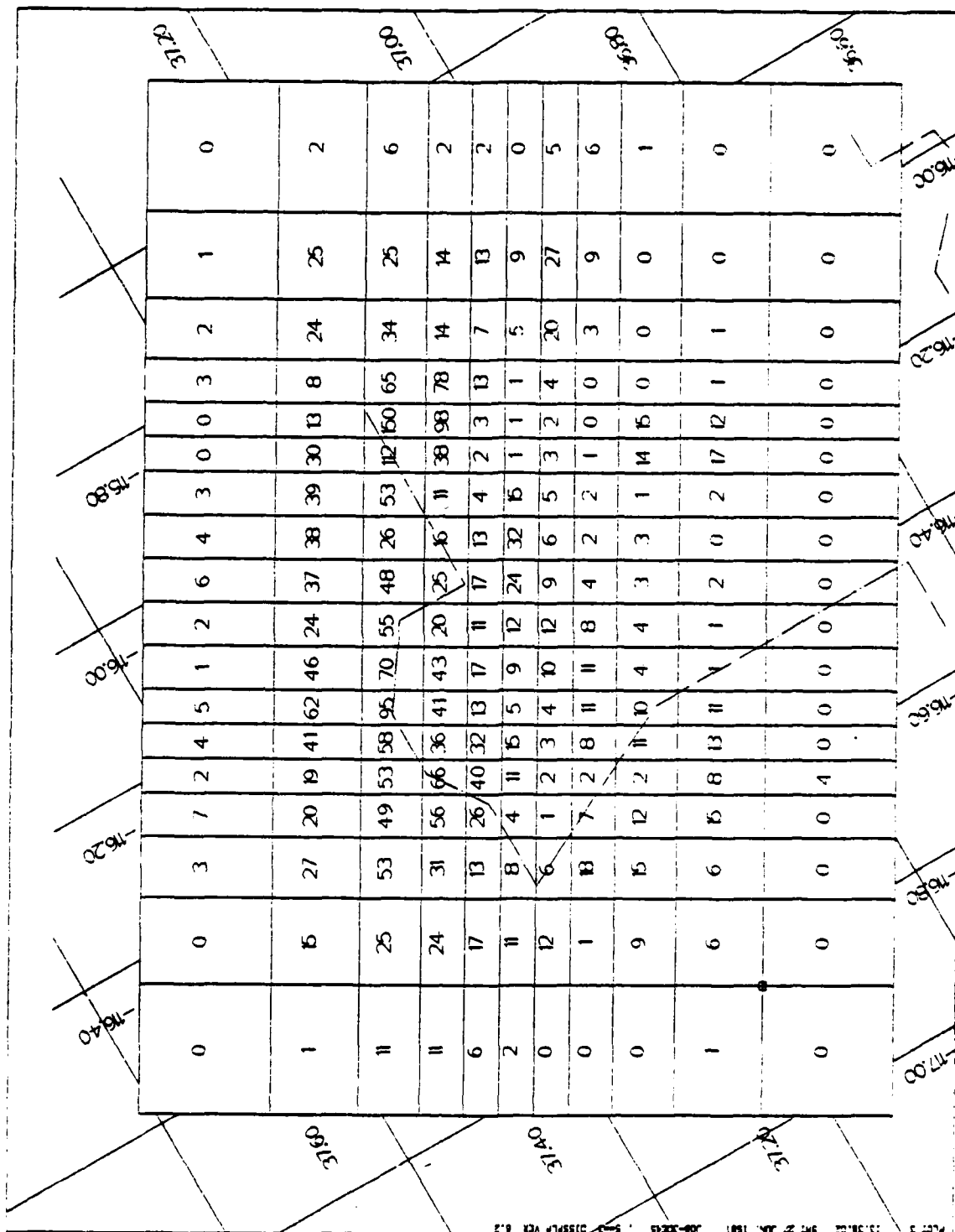


Figure 4.4c. Hit pattern for Layer 3 (28 - 48 km).

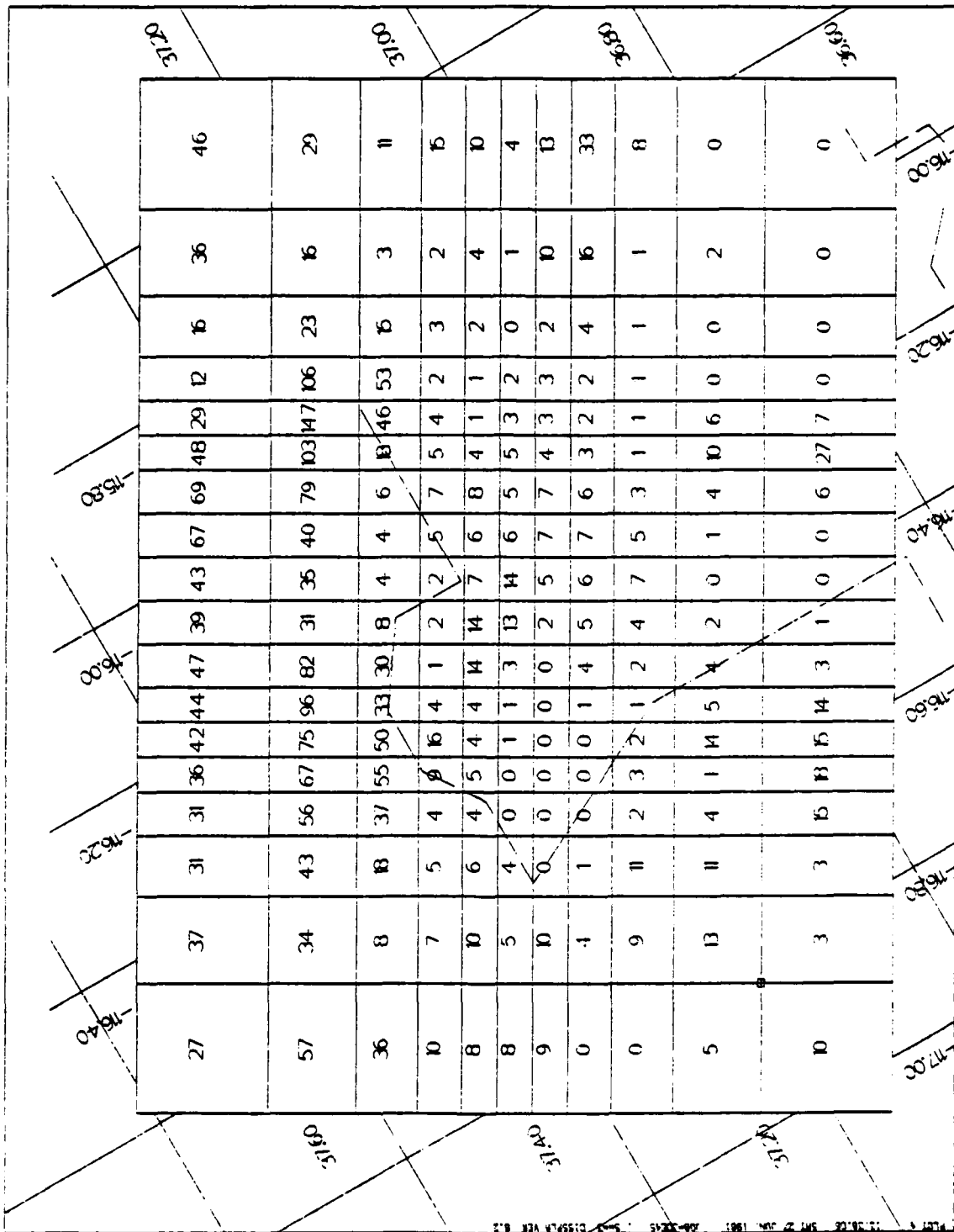


Figure 4.4d. Hit pattern for Layer 4 (48 - 74 km).

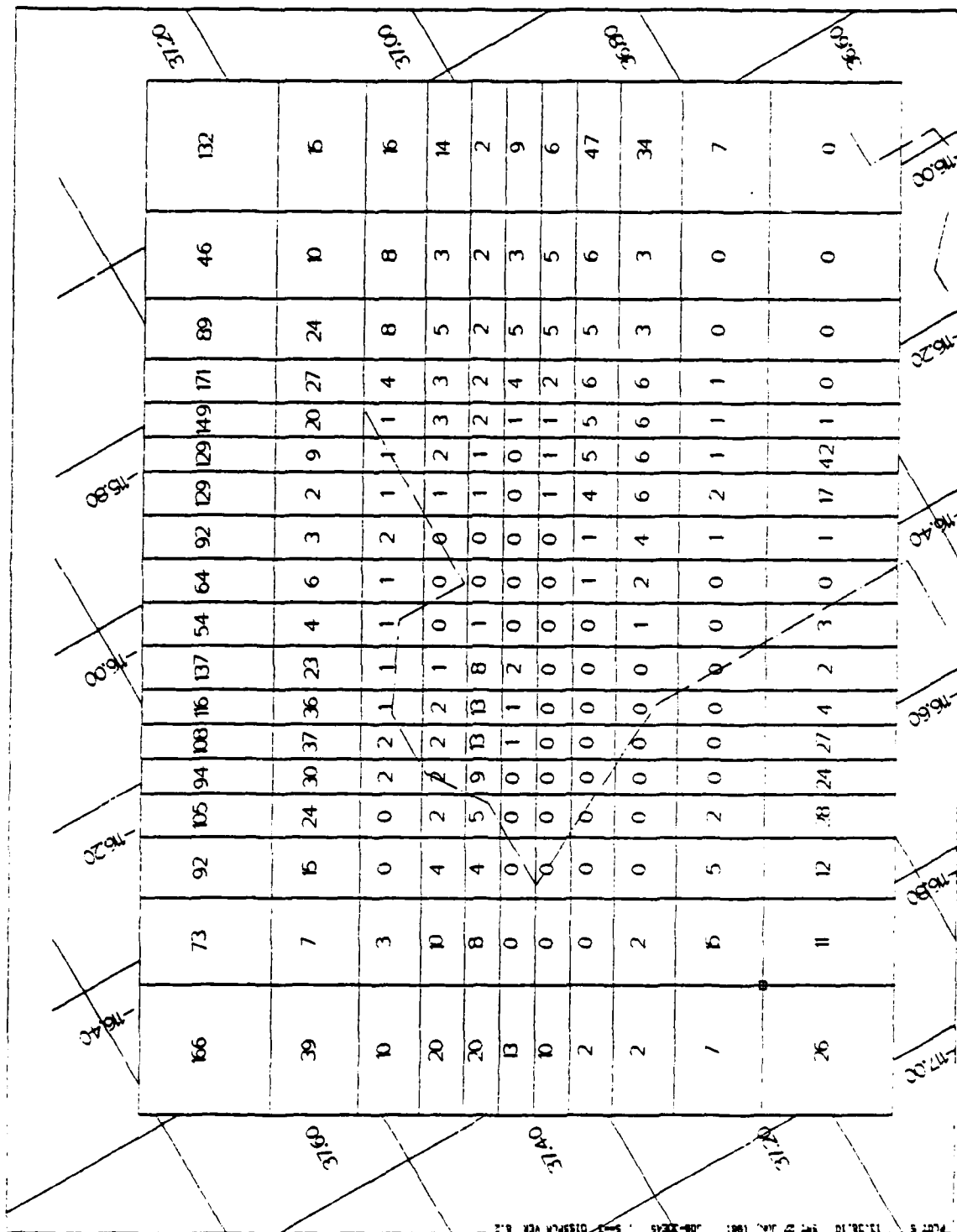


Figure 4.4e. Hit pattern for Layer 5 (74 - 108 km).

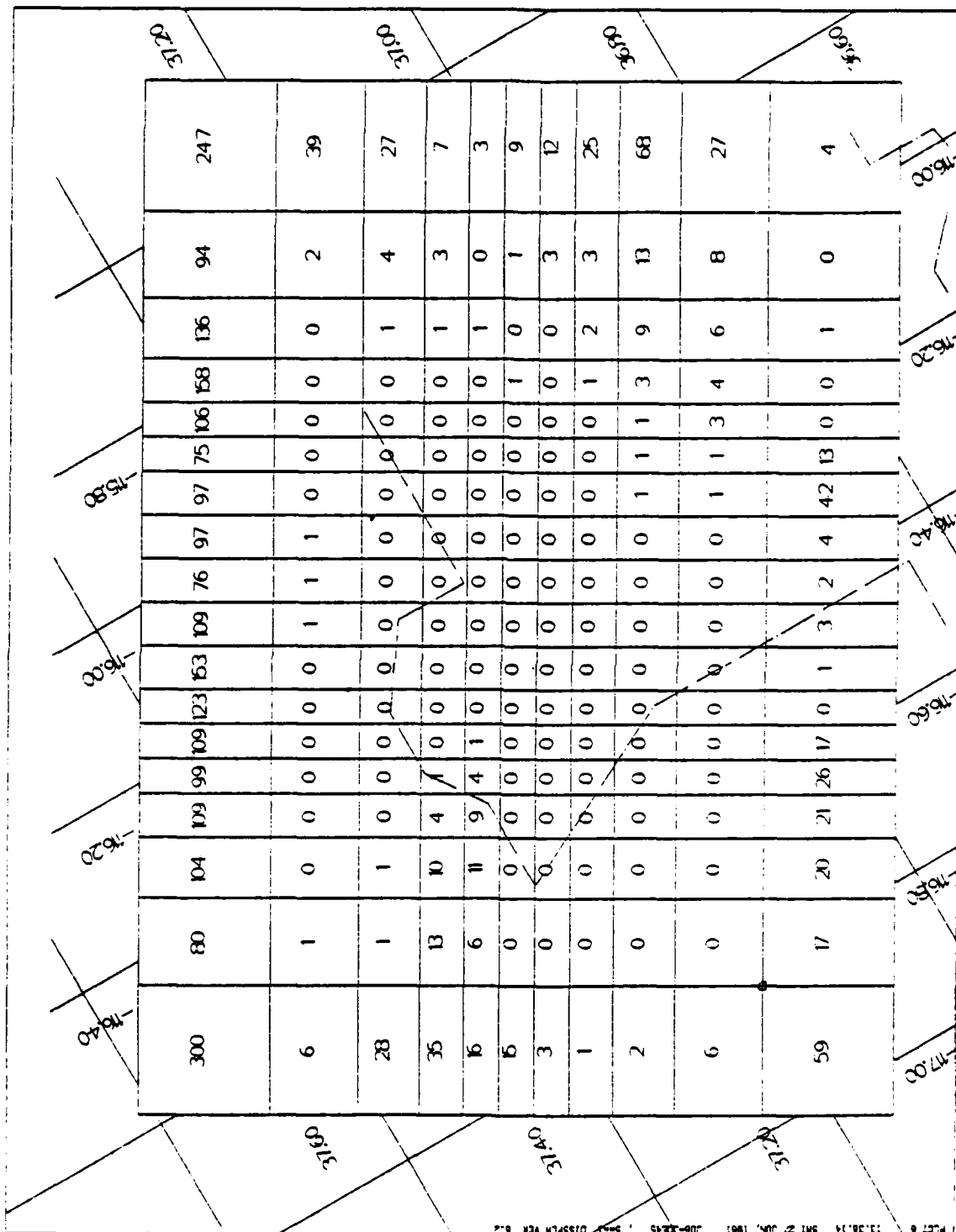


Figure 4.4f. Hit pattern for Layer 6 (108 - 152 km).

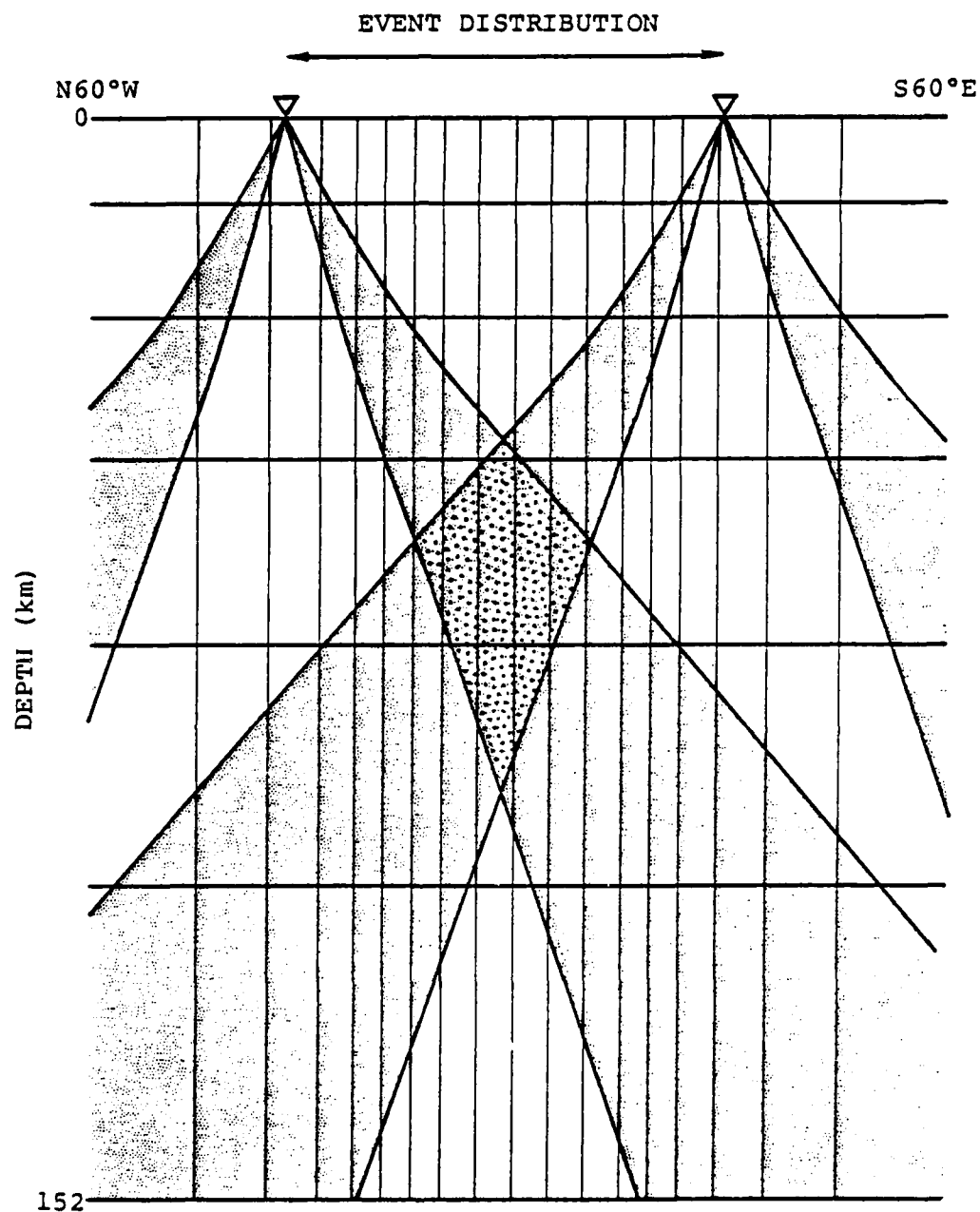


Figure 4.5a. Sketch of typical ray paths along the long dimension of the model grid. Shaded areas indicate the range of rays to teleseismic stations (25° - 100°).

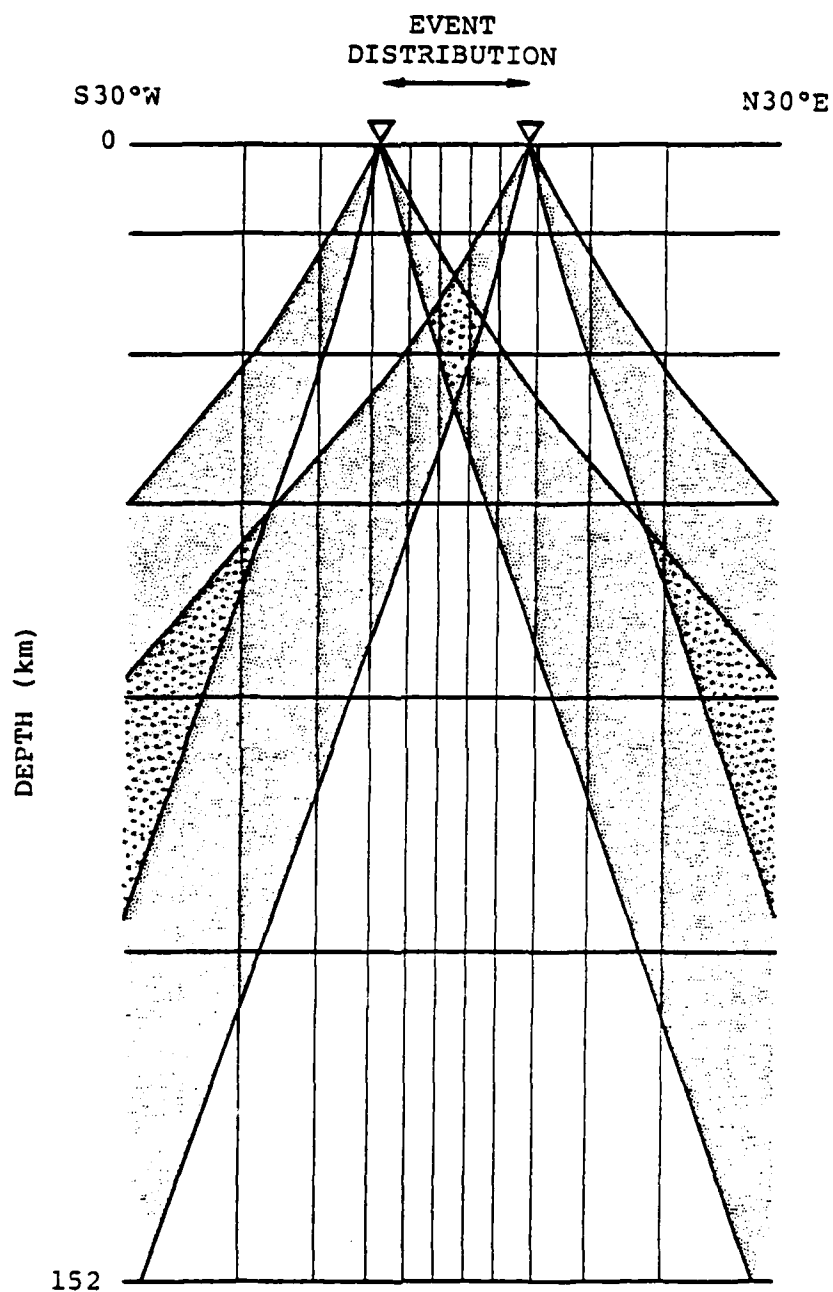


Figure 4.5b. Same as Figure 4.5a. Cross section along short dimension of the grid.

4.2 PROBLEM DIMENSIONS AND EIGENVALUE SPECTRUM

The grid described above consists of a total of 1188 blocks. This is comparable to the length of the data vector (1173) isolated in Section II. This means that the data matrix contains about $1.4 \cdot 10^6$ elements. Thus, in spite of our efforts toward reducing the problem size, we are still left with the task of manipulating extremely large arrays if we are to use all aspects of the theory. For this problem size, a complete inversion requires several hours of CPU time on our UNIVAC 1100/81 computer.

It is clear that any approach involving explicit construction of the normal equations and matrix inversion would be prohibitively expensive, and that construction of trade-off curves by a sequence of such inversions with different trade-off parameters would be unfeasible.

The SVD algorithm described in Section II by and large circumvents this difficulty, since construction of different models (for different NDF(θ)) represents only a marginal cost increase when the singular values and associated eigenvectors have been computed and stored. In addition, it can be shown that this approach is much less sensitive to round-off errors than the direct method.

Figure 4.6 shows the distribution of the 141 largest singular values in decreasing order, as well as the position of the critically damped eigenvalue for several NDF. The spectrum decays exponentially with increasing index, which indicates that practically all relevant features of the model can be adequately represented by the few largest eigenvalues and eigenvectors. This is confirmed by the aspect of the trade-off curve between RMS data fit and model norm shown on Figure 4.7. It is seen that models with NDF > 20 achieve only marginal improvement in the RMS data fit, at the cost of rapid increase in model norm. This is perhaps not surprising

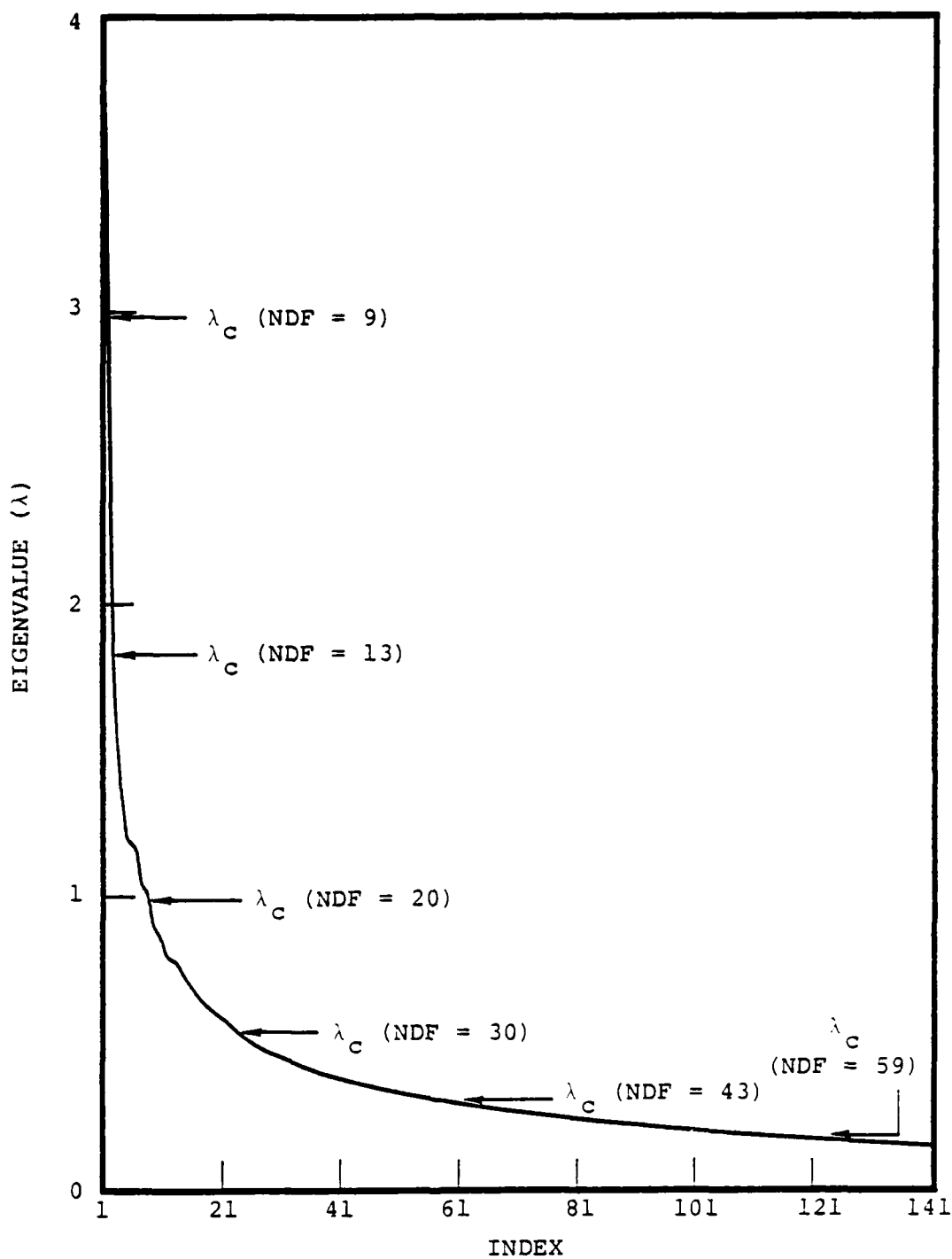


Figure 4.6. Largest 141 eigenvalues of the scaled partial derivative matrix plotted in decreasing order. The critically damped eigenvalues ($\lambda_c^2 = \theta$ (NDF), where θ is the damping parameter) are shown for the six values of NDF for which models were computed in this study.

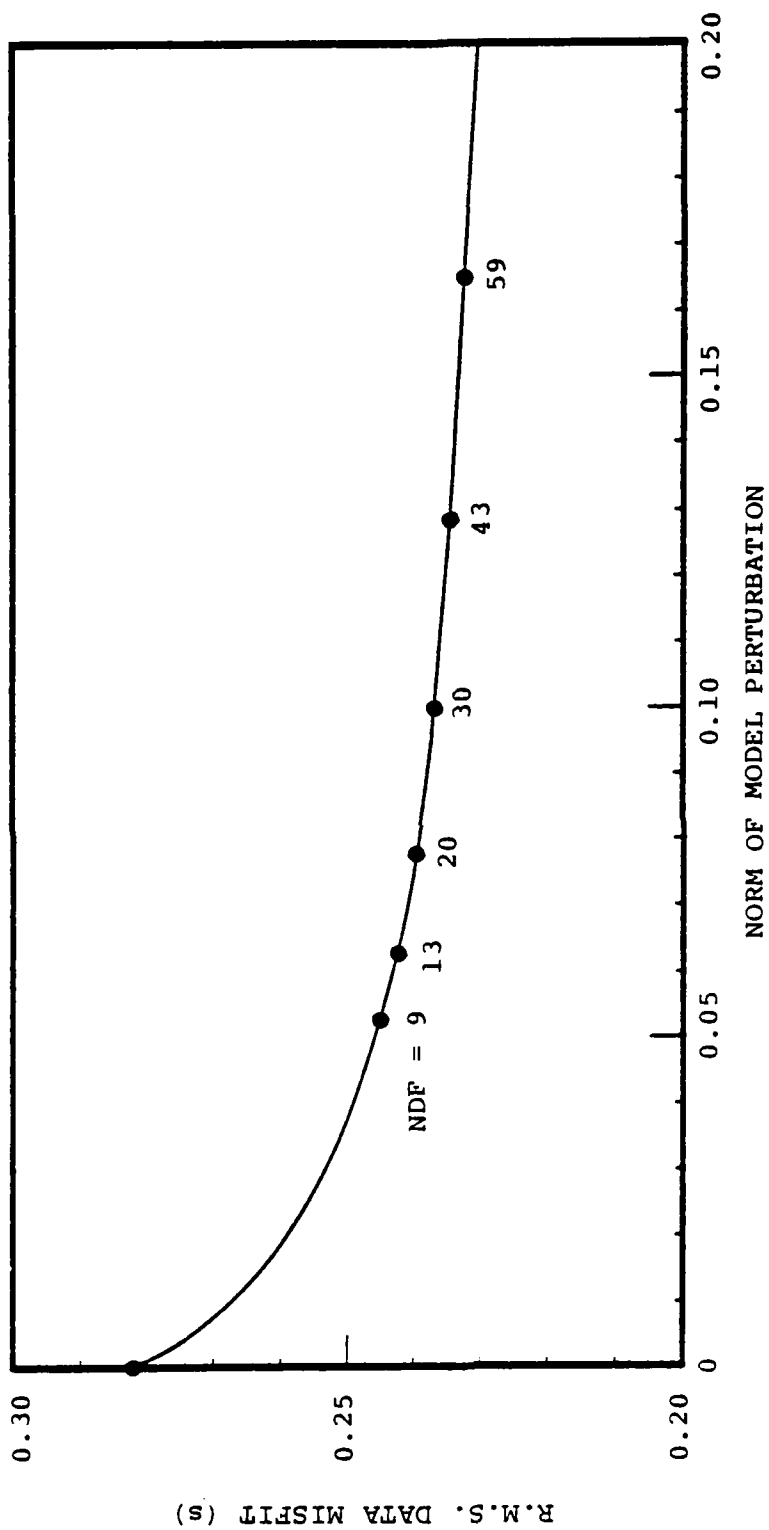


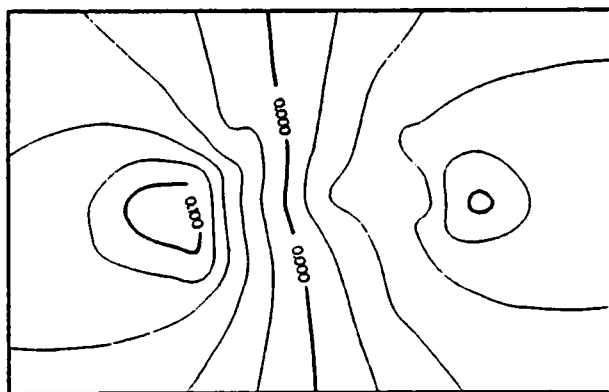
Figure 4.7. Trade-off curve between RMS data misfit and norm of the three-dimensional model perturbation. The points represent the models actually calculated, and are labeled with the corresponding NDF. The intercept corresponds to the RMS data misfit for the starting model (NDF = 0). This curve shows that the RMS data fit improves only very slowly with increasing NDF for NDF > 20.

in view of the relatively poor signal to noise ratio which can be detected in the data (Section III): with increasing NDF, the inversion procedure attempts to fit more and more subtle features in the observations, which are undoubtedly heavily contaminated by noise. An illustration of the phenomenon is provided by Figure 4.8 which shows contour maps of the model perturbations in the top layer calculated for several NDF (NDF = 9, 13, 20, 30, 43, 59). The amount of detail present in these contour maps increases dramatically for NDF > 20 but the benefit in improved RMS is in fact marginal as seen on Figure 4.7. In addition, there is a clear tendency for the contours to "hug" the geographical distribution of epicenters for the larger NDF's, which is an undesirable quality since a different choice of data would likely lead to a different model at this level of detail.

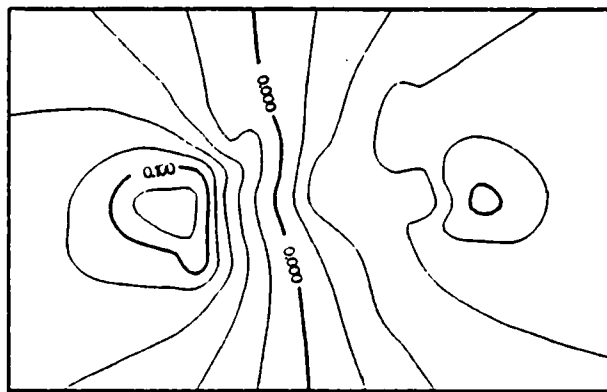
That these properties persist in other layers as well is illustrated in Figure 4.9 in which the integrated vertical travel time anomalies have been contoured for the same models. Again, the general features found for the lower NDF's can be identified on all frames, but the increase in model complexity for NDF > 20 is not justified by a corresponding improvement in RMS data fit. Note that the pattern of predicted vertical delays contoured on Figure 4.9 is generally in very good agreement with the pattern of average event residuals shown earlier in Section III (Figure 3.9).

Based on this evaluation, we judge that a model with NDF = 20 represents an optimal point on the trade-off curve between resolution and variance and that finer features found for greater NDF's are not interpretable with acceptable reliability.

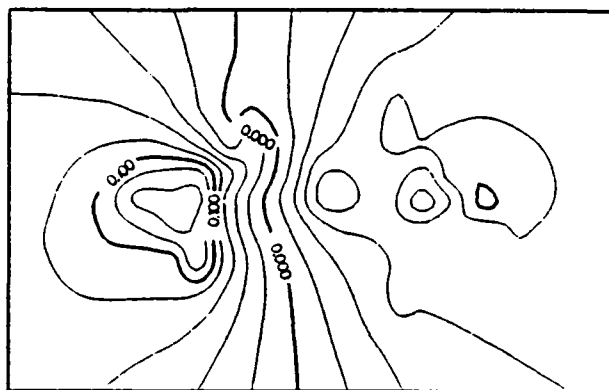
The model thus retained is described in some detail in the next subsection, and its geological and geophysical interpretation is the subject of Section V.



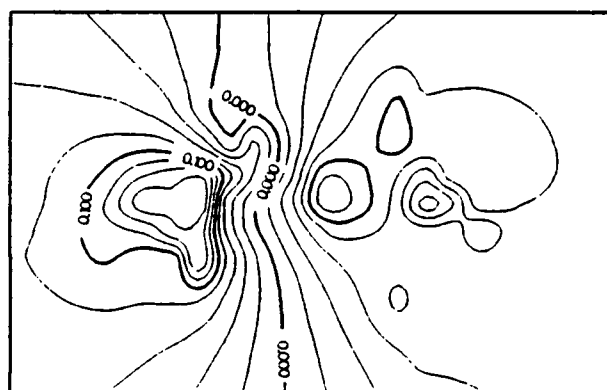
(a) NDF = 9



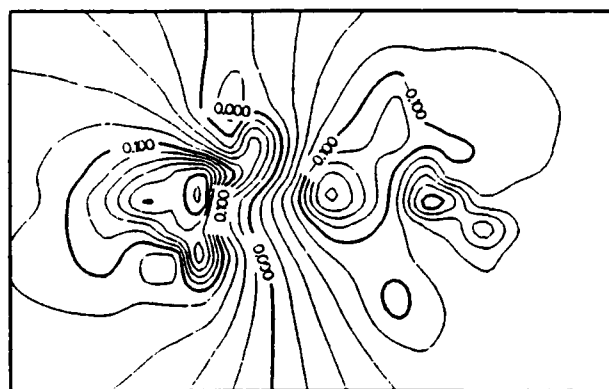
(b) NDF = 13



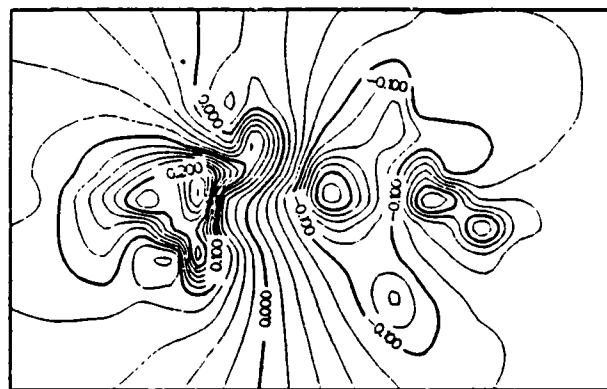
(c) NDF = 20



(d) NDF = 30

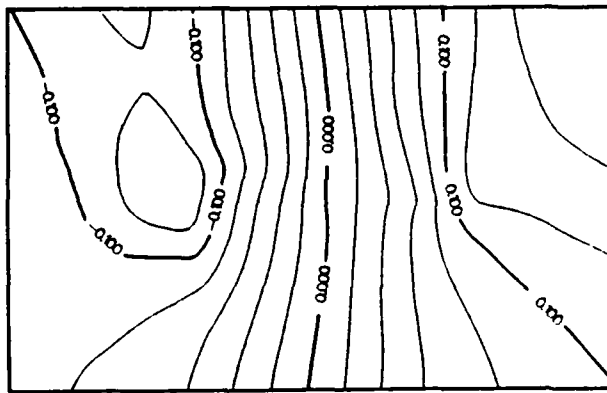


(e) NDF = 43

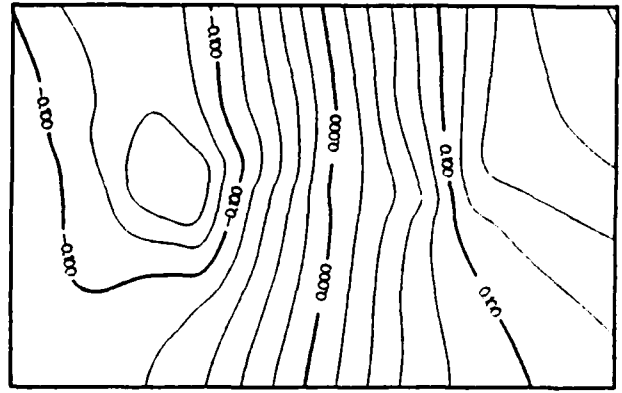


(f) NDF = 59

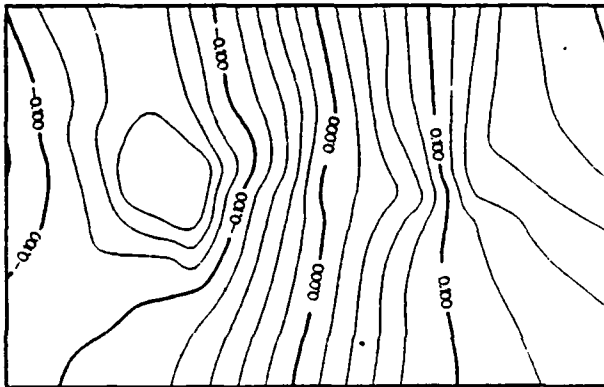
Figure 4.8. Velocity perturbations in Layer 1 (0 to 12 km) from inversion models for six values of NDF. The preferred model is NDF = 20. Contour interval is 0.02 km/sec.



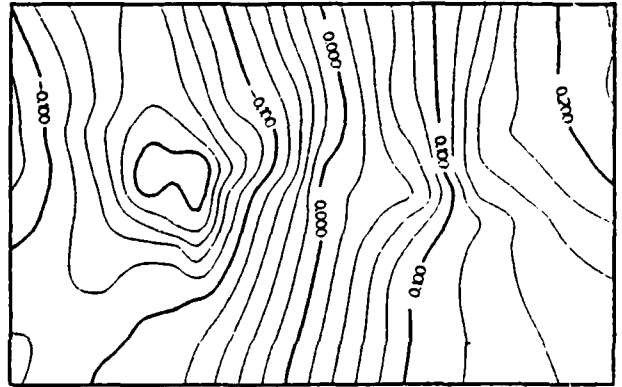
(a) NDF = 9



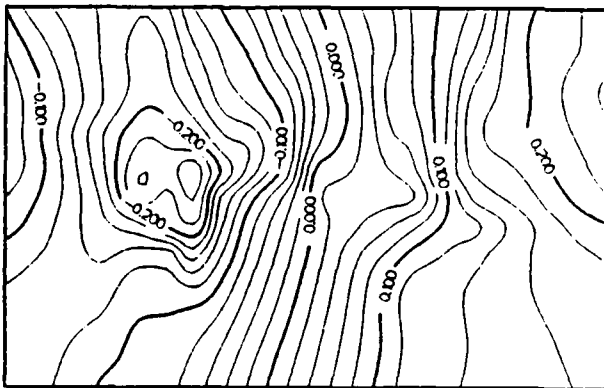
(b) NDF = 13



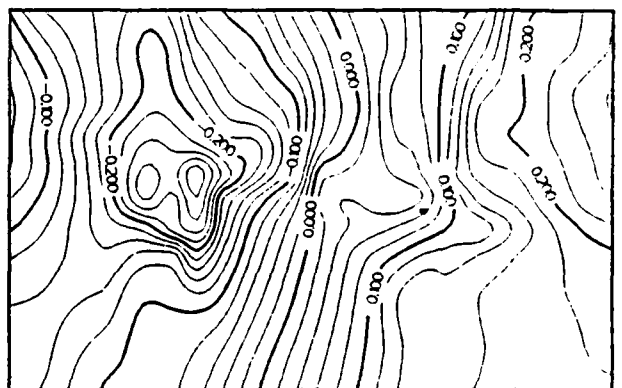
(c) NDF = 20



(d) NDF = 30



(e) NDF = 43



(f) NDF = 59

Figure 4.9. Vertical delay time predicted by inversion models for six values of NDF. Contour interval is 0.02 km/sec.

4.3 DESCRIPTION OF MODEL T65-20

Our preferred model, Model T65-20 (NDF = 20) is most conveniently displayed as a series of contour maps of velocity perturbations away from the starting model. Let us recall from the outset that these quantities have been zero-meant in the inversion procedure since baseline shifts across all of NTS have been treated as nuisance parameters, and are thus not explained by the model. As a result, the final product is a set of maps of relative variations of seismic velocities as a function of position in the crust and upper mantle, and these velocities are only known to within an arbitrary perturbation to the one-dimensional starting model.

Contour maps have been produced with a contour interval of 0.02 km/sec and are furnished here at a common scale, thereby permitting exact geographical overlays for interlayer comparisons. For more detailed analysis and for completeness, the actual values of velocity perturbations in each cell are provided in Appendix D. The complete model description includes the following set of figures.

1. An orientation map (Figure 4.10) showing the inner grid superimposed on a geographical coordinate system, as well as the set of NTS sources retained for inversion.
2. Contour maps for each of the six model layers (Figures 4.11a through 4.11f). Only the portion of the model interior to the inner grid is shown, at the correct scale to permit overlay with Figure 4.10. A summary figure showing the model will be discussed in the next section (Figure 5.2).
3. Contour maps of three vertical sections, identified as AA', BB', and CC' on Figure 4.12. Figure 4.13a shows a longitudinal (N60W) section through the model, crossing both Yucca Flat and Pahute Mesa, viewed from the southwest. Figure 4.13b shows a vertical section through Pahute Mesa along a plane trending N30E, viewed from the southeast. Figure 4.13c is a parallel section, crossing Yucca Valley.

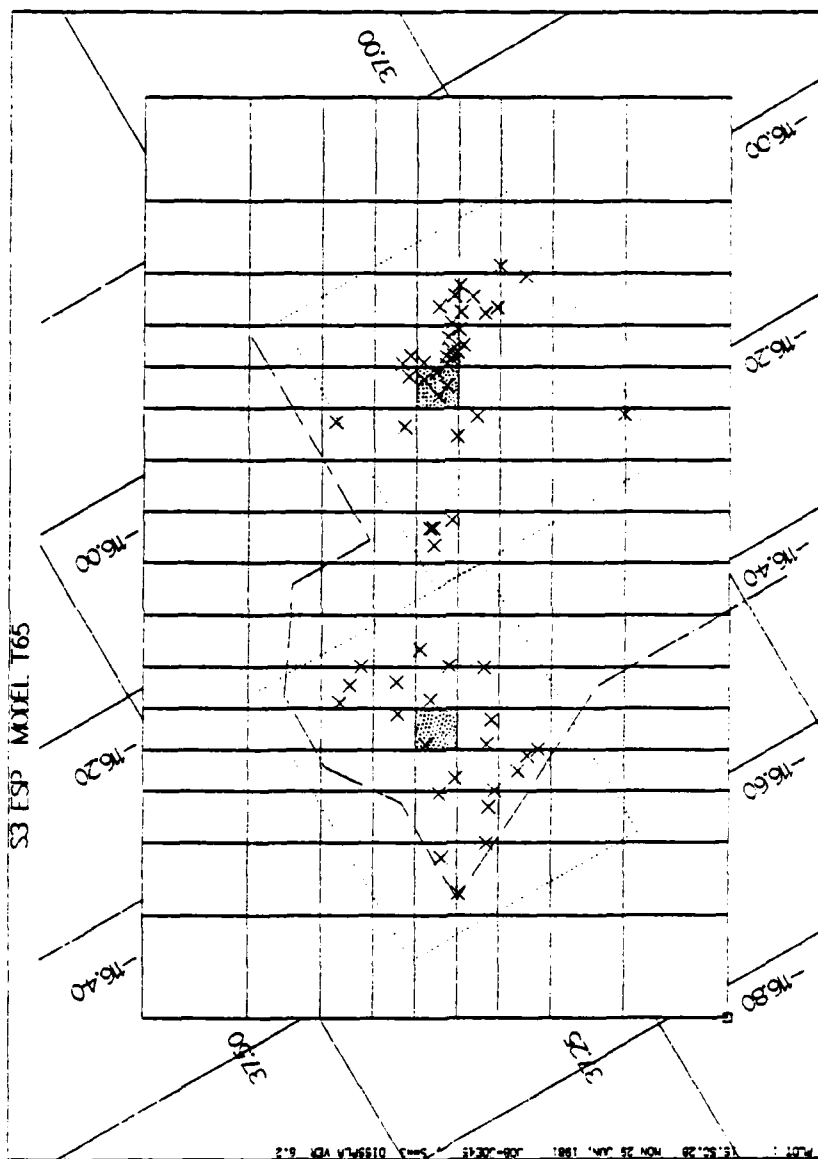


Figure 4.10. Orientation map for inner grid relative to geographical coordinates. Cells (6,6) and (6,13) are shaded; these cells are referred in Table 5.1 (variance) and Appendix E (resolution).

Figures 4.11a through 4.11f are on the following pages.

Figure 4.11. Velocity perturbation contours (contour spacing 0.02 km/sec) for Model T65-20. Figures 4.11a through 4.11f correspond to Layers 1 through 6 of the model, respectively. Contours are displayed inside inner grid only, and can be overlaid with orientation map on Figure 4.10. Actual perturbations for individual cells are given in Appendix D in a format which can be overlaid to the contour map.

T65 ND = 20 VEL LAYER= 1 MODEL

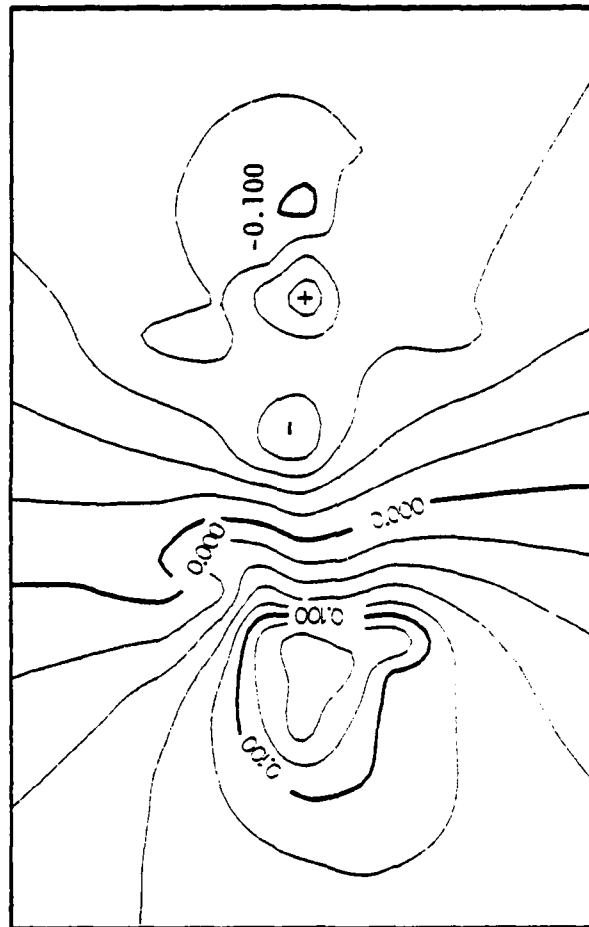


Figure 4.11a. Model T65-20, Layer 1 (0 - 12 km) .

165 NDF= 20 VEL. LAYER= 2 MODEL

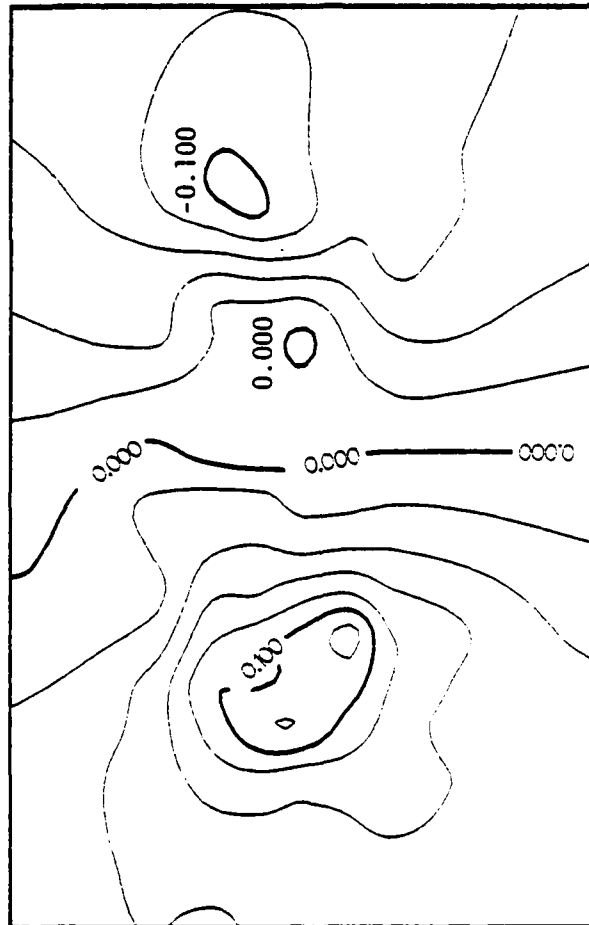


Figure 4.11b. Model T65-20, Layer 2 (12 - 28 km).

165 NUF= 20 VEL LAYER= 3 MODEL

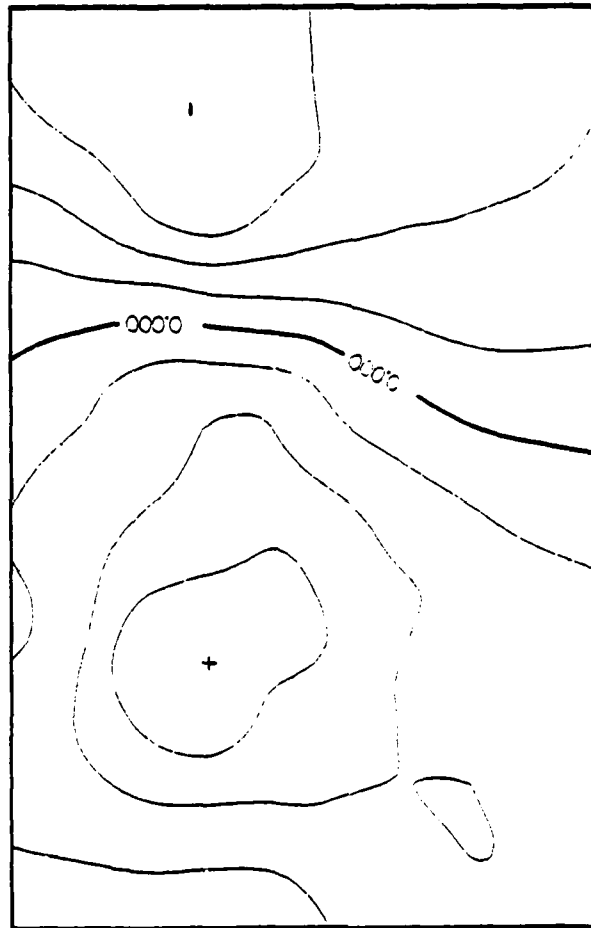


Figure 4.11c. Model T65-20, Layer 3 (28 - 48 km) .

T65 NDF= 20 VEL LAYER= 4 MOEL

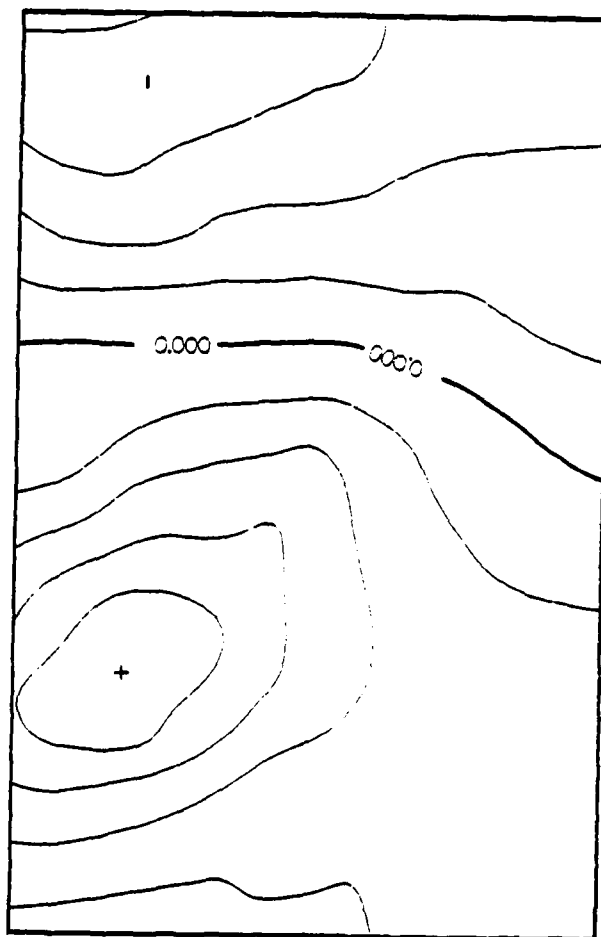


Figure 4.11d. Model T65-20, Layer 4 (48 - 74 km).

T65 NDF= 20 VEL LAYER= 5 MODEL

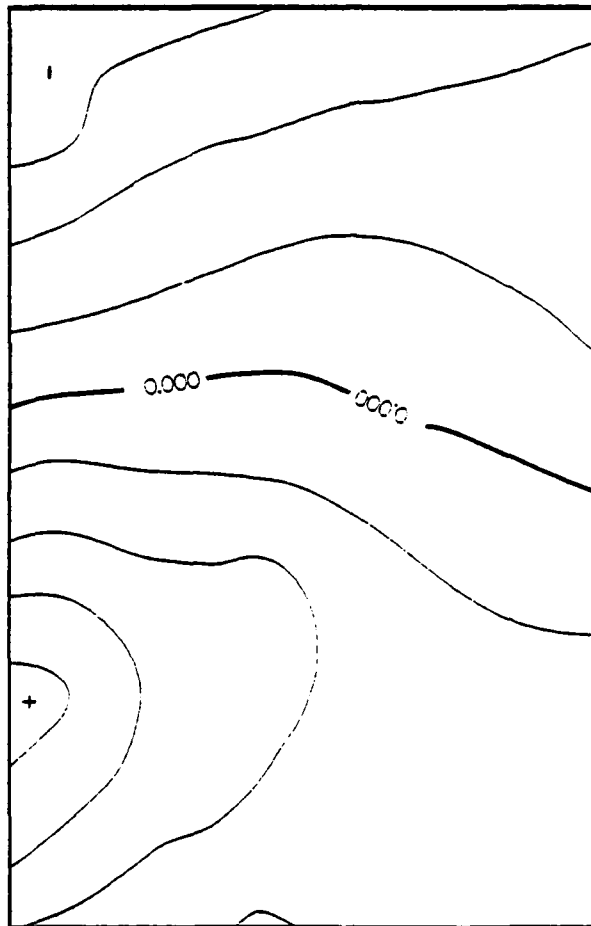


Figure 4.11e. Model T65-20, Layer 5 (74 - 108 km) .

T65 NDF= 20 VEL LAYER= 6 MODEL

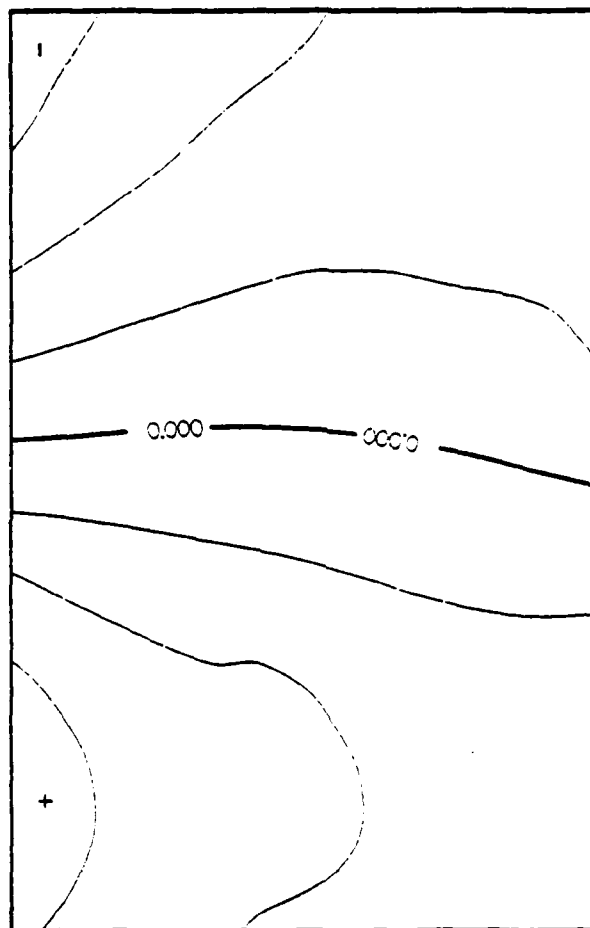


Figure 4.11f. Model T65-20, Layer 6 (108 - 152 km).

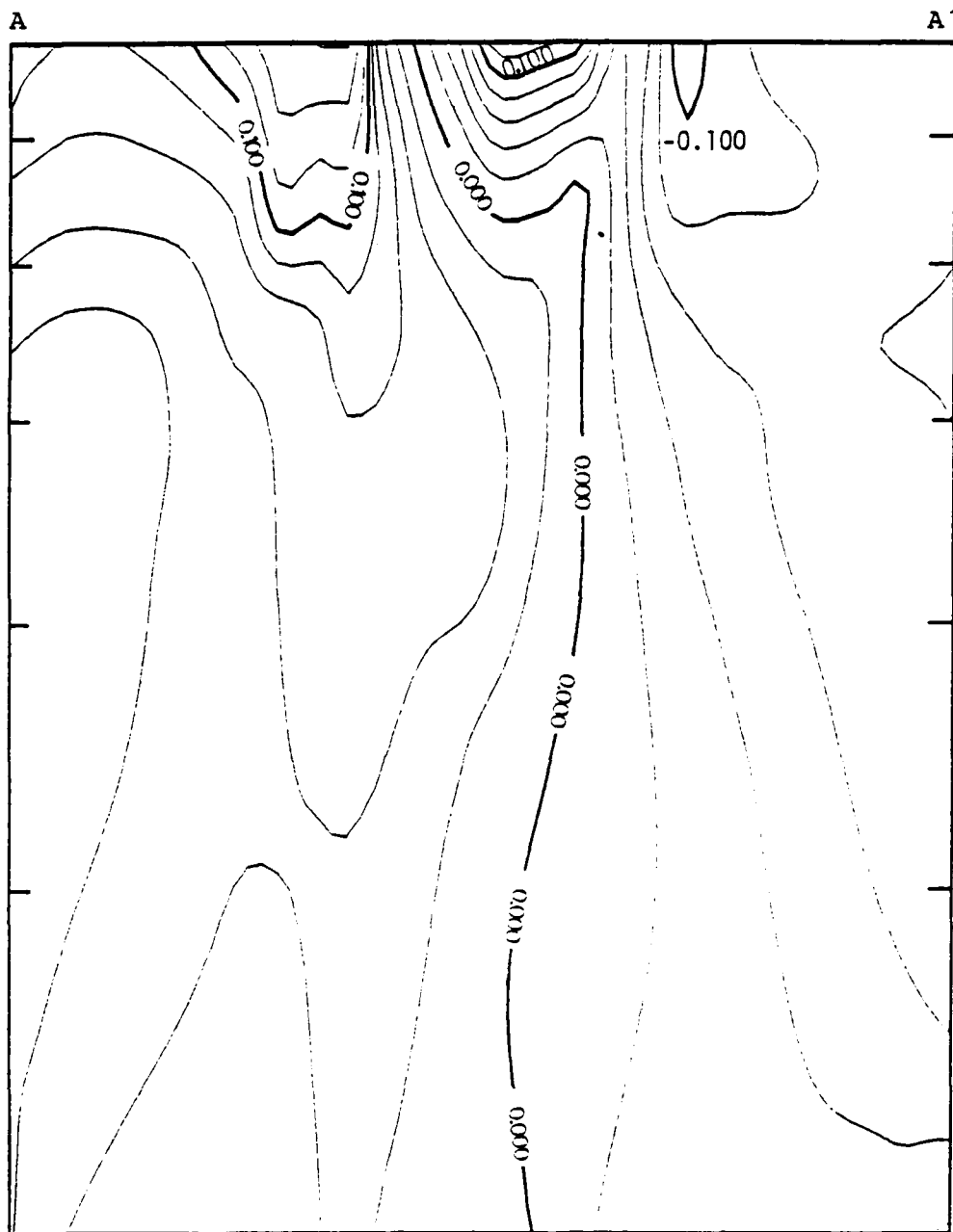


Figure 4.13a. N60W-S60E vertical cross section through Model T65-20. Contour interval 0.02 km/sec.

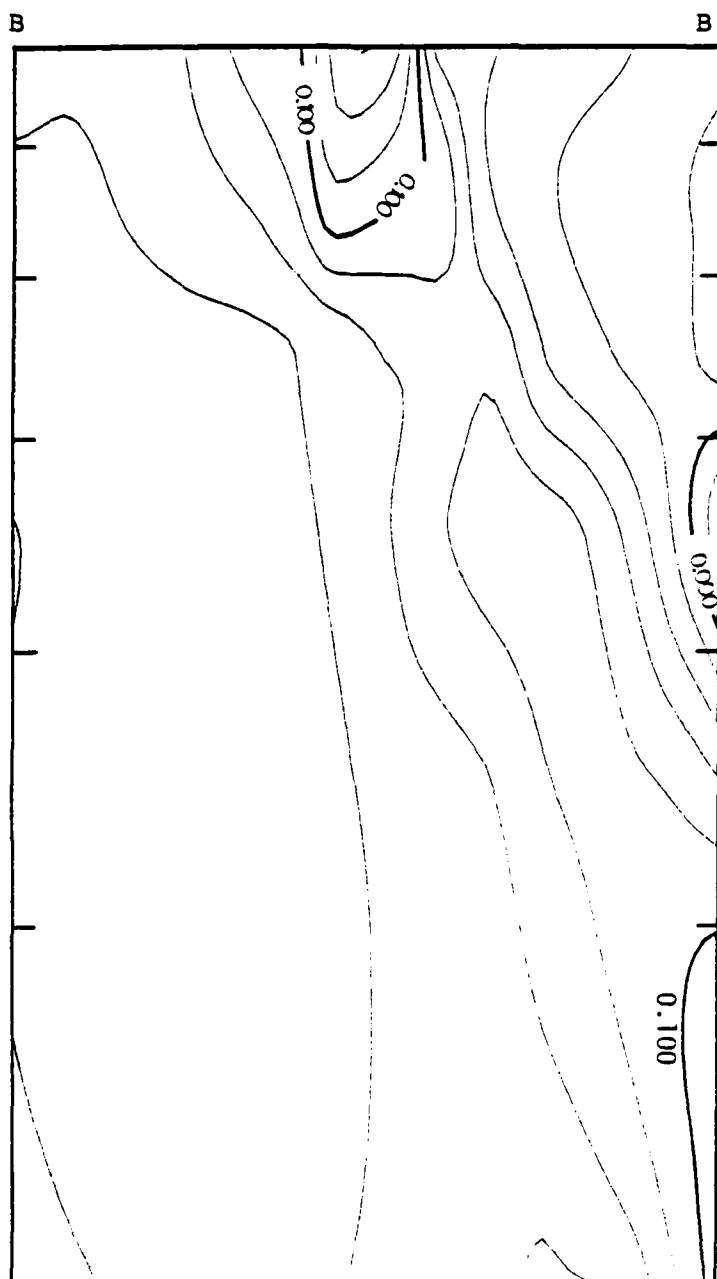


Figure 4.13b. S30W-N30E vertical section across Pahute Mesa.
Contour interval 0.02 km/sec.

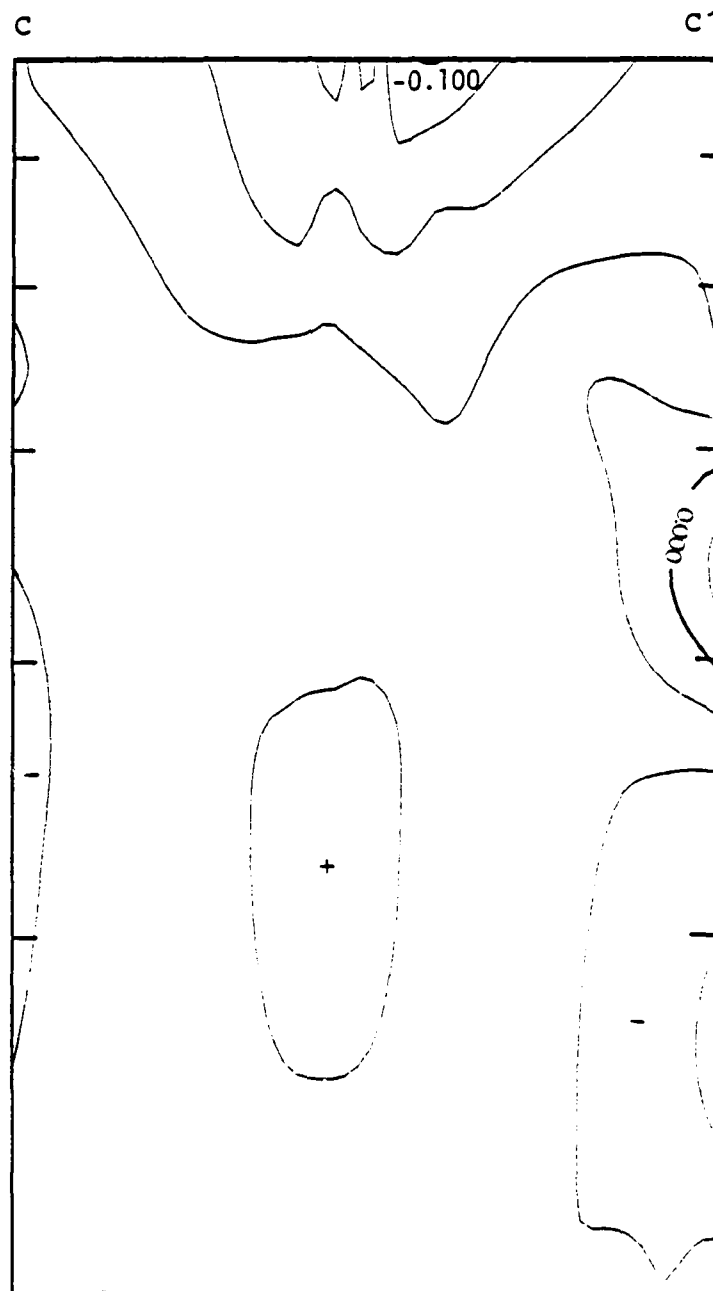


Figure 4.13c. S30W-N30E vertical section through Yucca Flat.
Contour interval 0.02 km/sec.

4. We can attach a variance-covariance matrix V as well as a resolution operator R to the model as described in Section II. The variance operator is a symmetric 1188×1188 matrix; the resolution operator possesses the same dimensions but is not symmetric. Because of the sheer size of these matrices, it is not practical to represent them fully. Instead, we shall make use of some selected resolving kernels (rows of the operator R) and of some selected estimates of variances; examples are given in Appendix E. These parameters will be important when we turn to model interpretation in the next section.

4.4 DATA FITS

A useful and informative test of our model lies in the comparison of predicted data functionals (namely, travel time anomalies) with the observed values. Figure 4.14 show the predicted travel time delays for individual (i.e., nongrouped) event-station pairs. The corresponding observables were described in Section III, and displayed in Figure 3.6.

Note that nuisance parameters such as mean station delays were removed through the denuisancing algorithm described in Section II. As a result, both in Figure 4.14 and in Figure 3.6, a given datum represents the travel time anomaly for this particular event-station pair, corrected by the mean residual at that station calculated from all events actually recorded by it. As a result, the two figures can be compared meaningfully.

This leads us to make the following observations:

1. The general features of the data set are indeed reflected in the model-predicted values. In particular, the general trend from predominantly negative residuals from Pahute Mesa events (Figures 4.14a through 4.14b) to predominantly positive residuals from Yucca Flat events (Figures 4.14c through

Figures 4.14a through 14.4f are on the following pages.

Figure 4.14. Calculated travel-time residuals (zero-meaned) for the same event and station sets as Figure 3.6. See Figure 3.6 for a description of these plots.

HAT-20-PH-VF/T65 >>DMAT PREDICTED DATA VECTOR 07-20-81

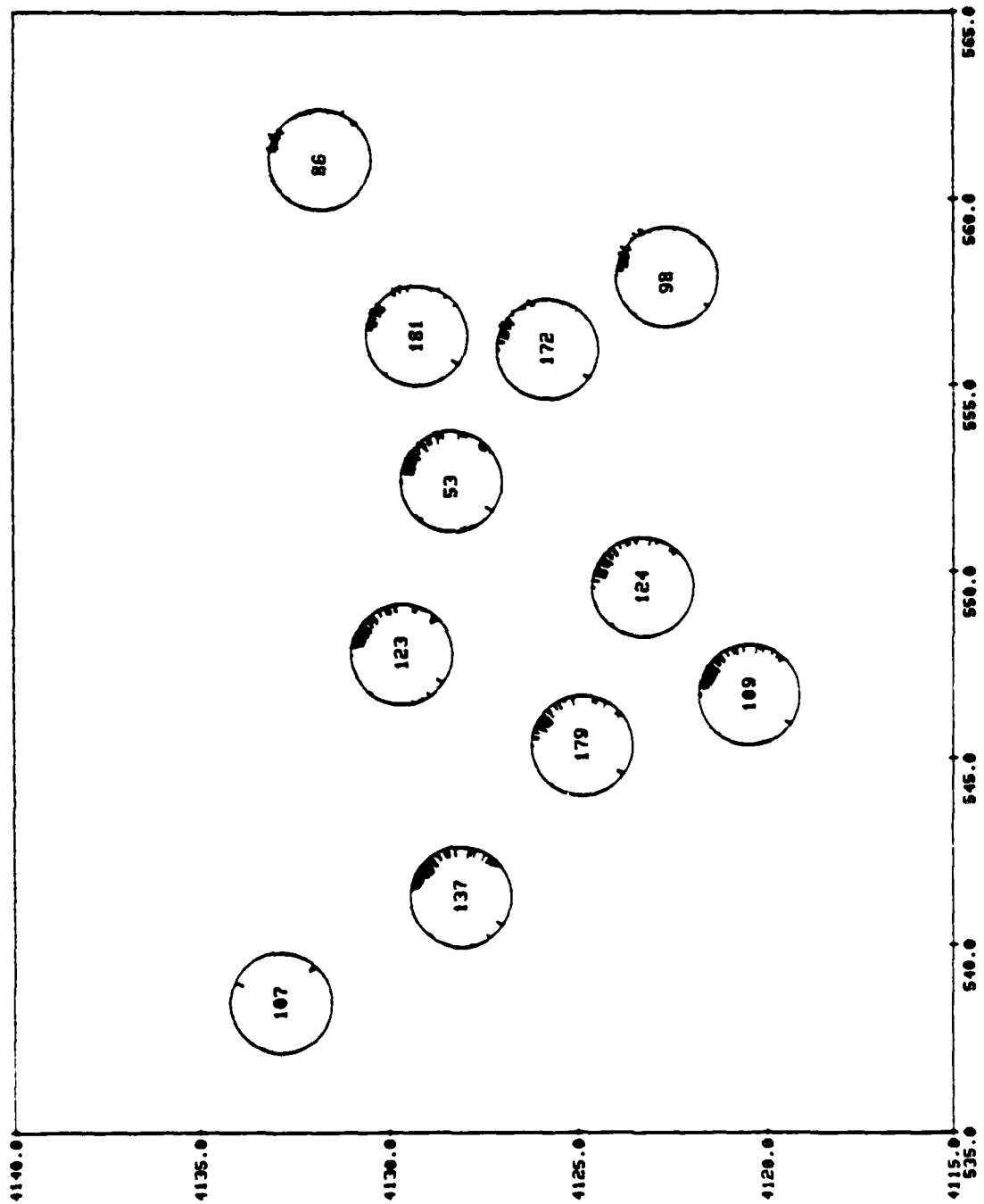


Figure 4.14a. Pahute Mesa.

HAT-20-PH-YF/T65 >>DHAT PREDICTED DATA VECTOR 07-20-81

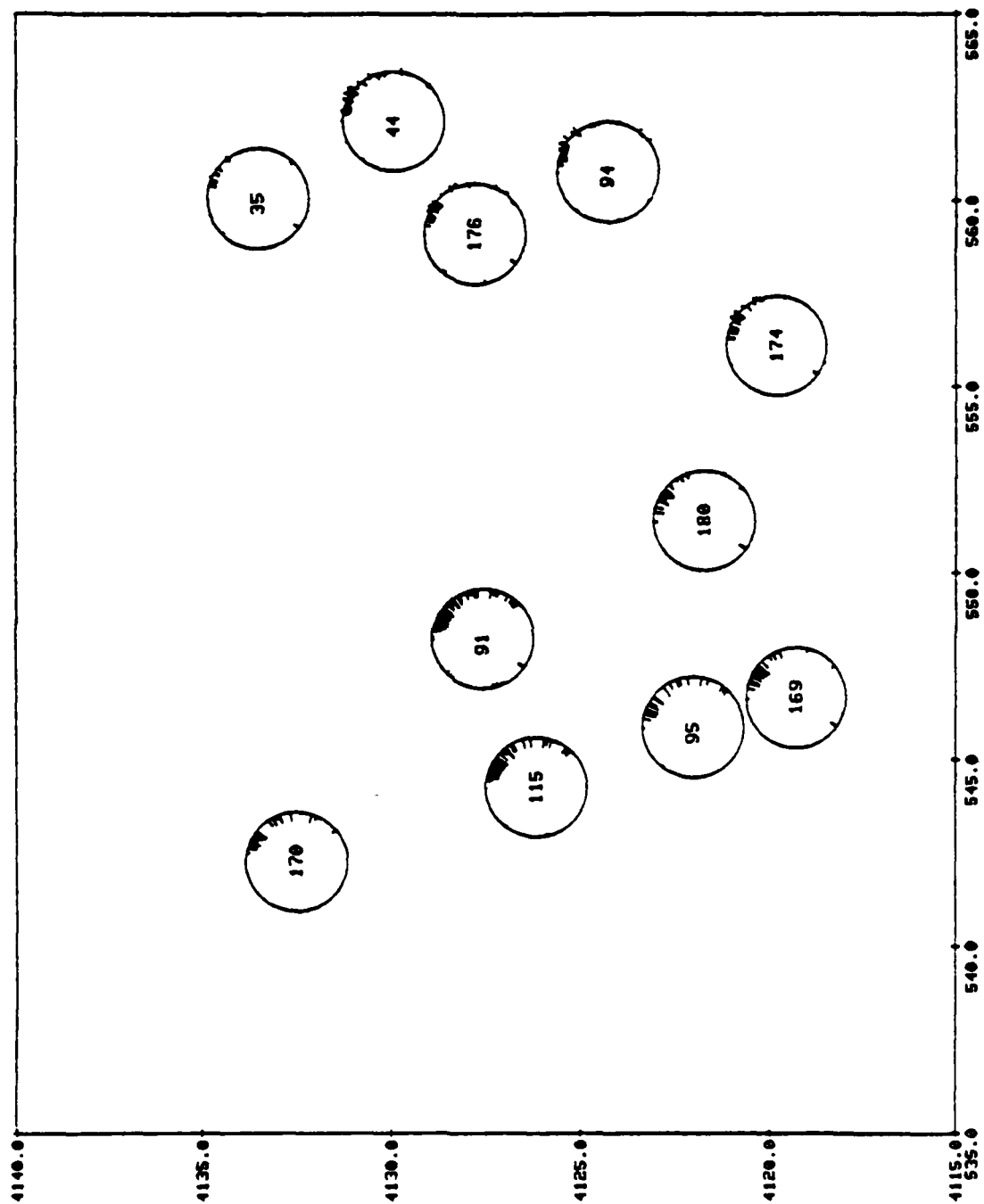


Figure 4.14b. Pahute Mesa.

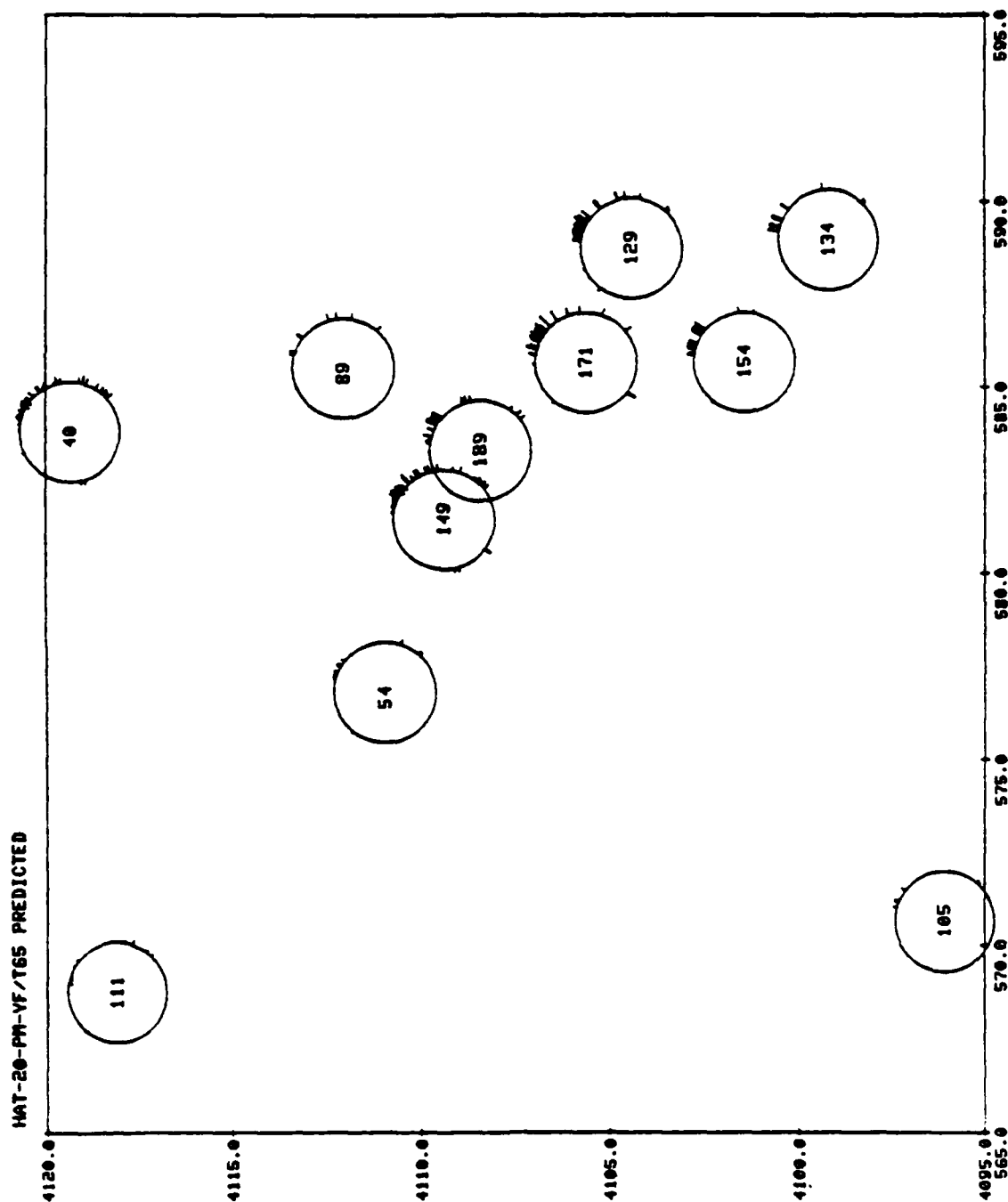


Figure 4.14c. Yucca Flat.

HAT-20-PR-YF/T65 >>HAT PREDICTED DATA VECTOR 07-20-81

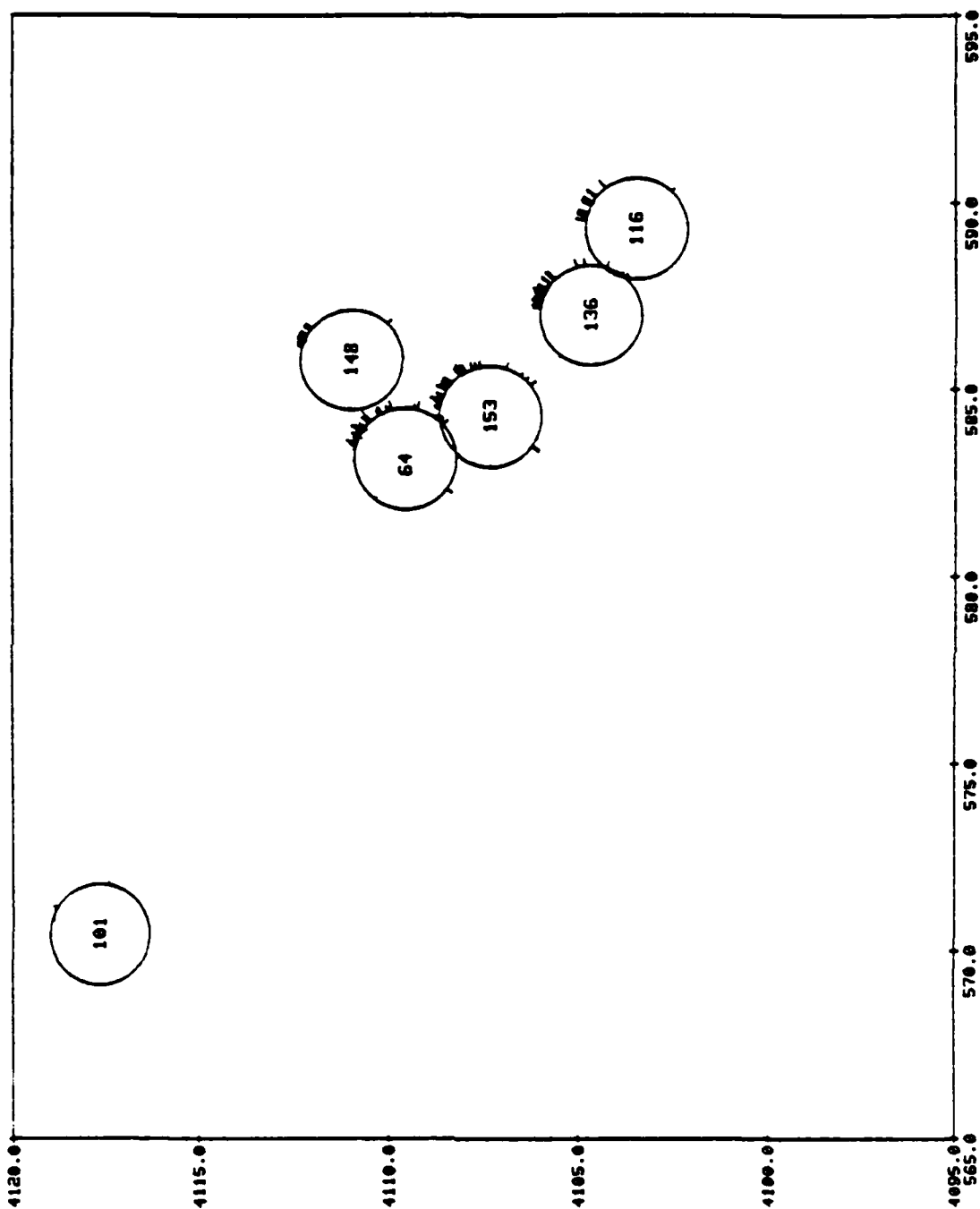


Figure 4.14d. Yucca Flat.

HAT-20-PH-YF/T65 >>DHAT PREDICTED DATA VECTOR 07-20-81

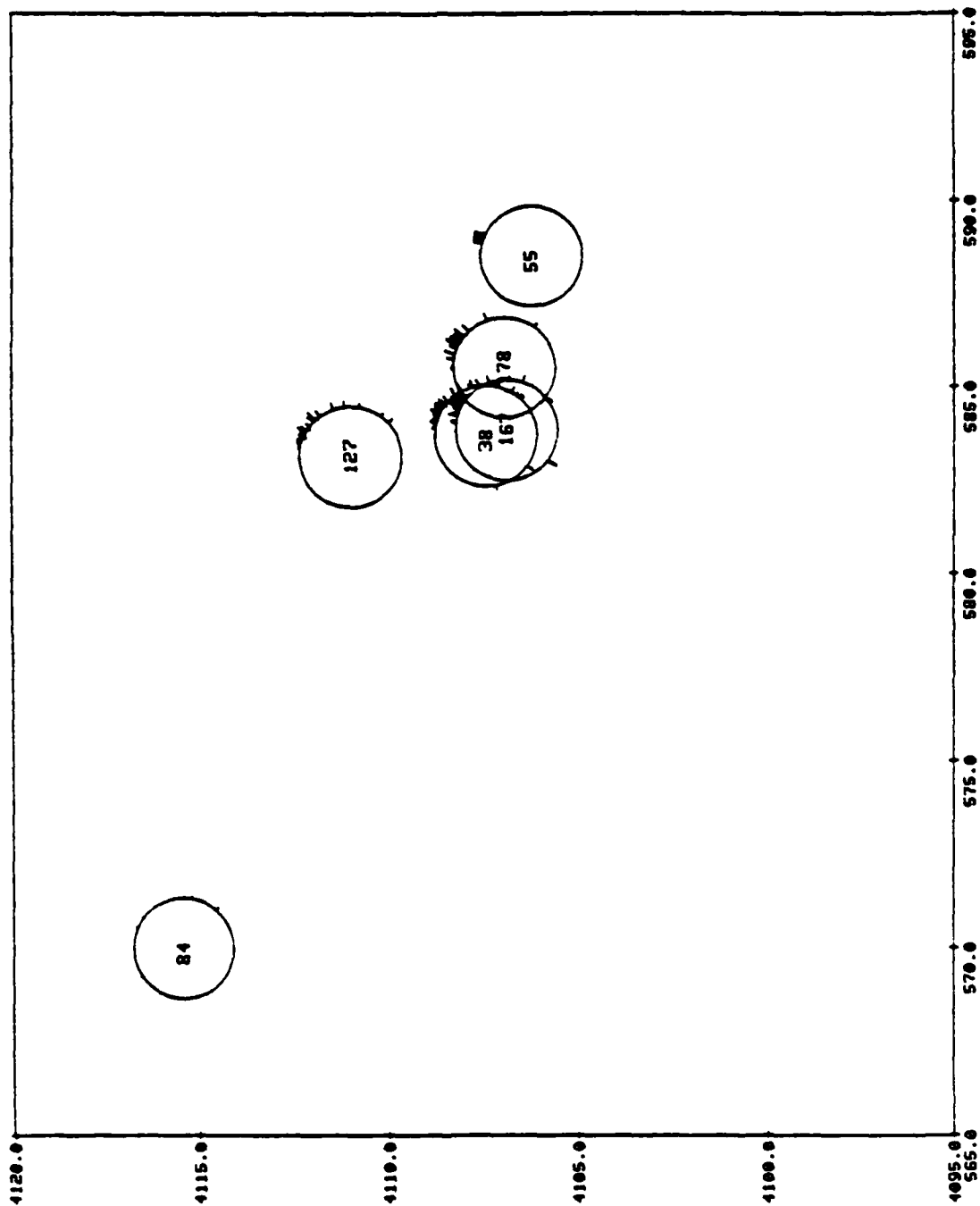


Figure 4.14e. Yucca Flat.

HAT-20-PM-YF/T65 >>DHAT PREDICTED DATA VECTOR 07-20-81

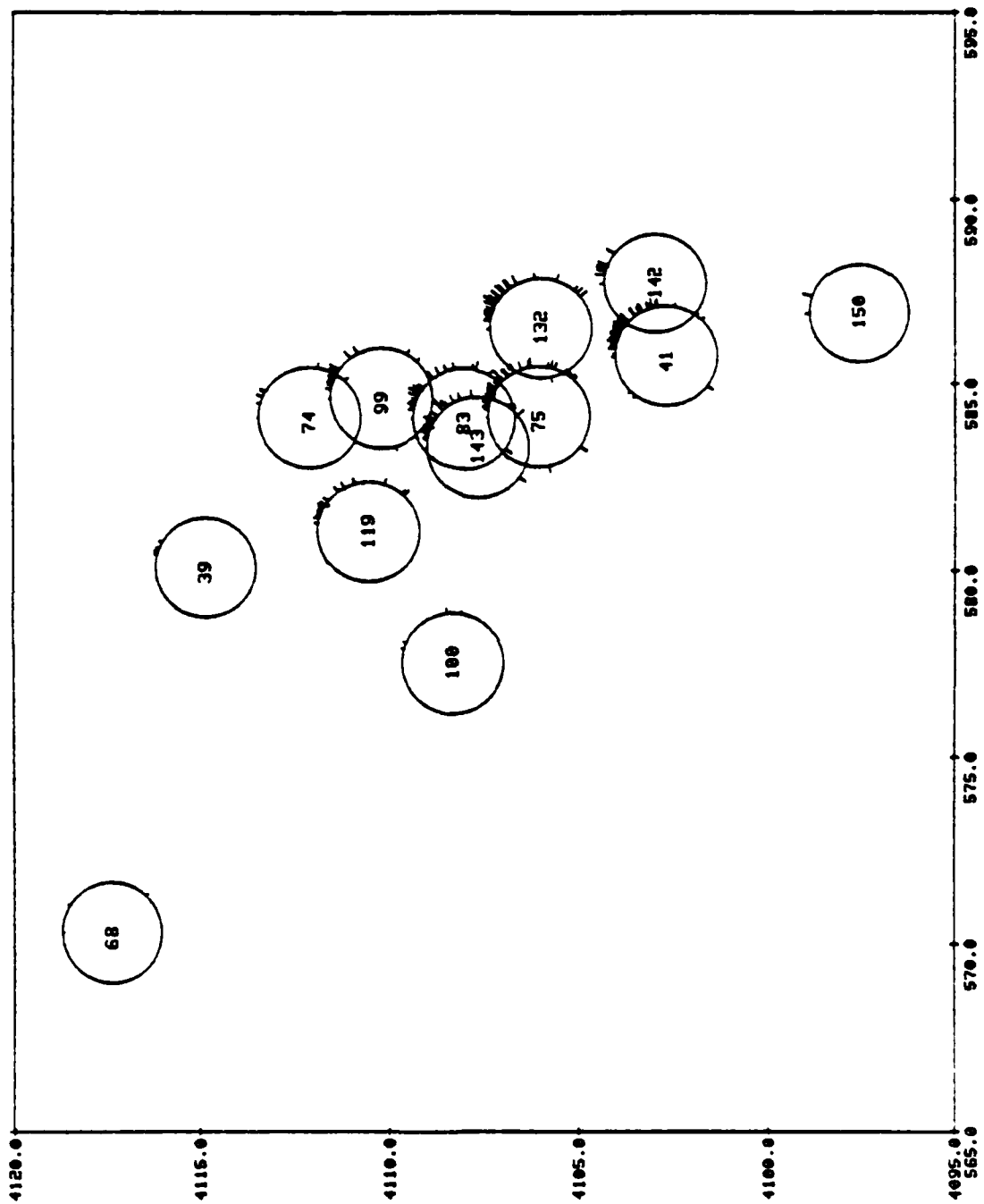


Figure 4.14f. Yucca Flat.

4.14f) is preserved, as can also be seen from the mean vertical delays contoured in Figure 4.9c. Furthermore, the residuals for Rainier Mesa events are generally small, which is consistent with their geographical location, intermediate between the Pahute Mesa and Yucca Valley event groups, and near the null vertical delay contour of Figure 4.9c. (see also Figure 5.1).

2. The azimuthal variations of predicted delays (Figure 4.14) is much smoother than the corresponding variations in the observed delays. As we have mentioned earlier, increasing the NDF does not improve the r.m.s. data fit significantly, and in fact, the more complicated models (for higher NDF's) are also incapable of predicting the observed erratic azimuthal variations, which must be attributed to the high noise level in the data. The total r.m.s. of our final data set is ~ 0.28 sec (Figure 4.7) and is thus of comparable magnitude to the total signal strength in the model, as seen from Figure 4.9c.
3. Another general feature is that the magnitudes of predicted residuals tend to be smaller - by about a factor of two - than the observed values. One reason for this stems from the damping imposed on the inversion procedure which does tend to limit the amplitude of lateral variations in the model, and hence to bias predicted residuals toward smaller values. But the high noise level in the data also tends to create a visual impression that the observations are underpredicted since larger (noisy) residuals in the plots of observed data (Figure 3.6) are much more obvious to the eye than those with more average values, so that visual averaging can actually be quite misleading.

On the other hand, the predicted residuals depicted on Figure 4.14 are free of erratic fluctuations and permit easier detection of more subtle patterns (such as the systematic variation of predicted residuals across Pahute Mesa on Figures 4.14a and 4.14b). These patterns are naturally correlated with model features, and we shall discuss them in the framework of model interpretation in the next section.

V. INTERPRETATION OF INVERSION RESULTS

The velocity model described in the previous sections shows several interesting structural features whose interpretation is important for understanding the travel-time and amplitude anomalies associated with NTS events. Before attempting such an interpretation, however, we shall discuss the various types of modeling errors, focusing particularly on sources of modeling bias.

Errors in the Travel Times

The data culling and grouping procedures discussed in Section III are very effective in eliminating spurious travel-time residuals and reducing the dispersion from random or quasi-random sources of noise such as reading and timing errors. Based on the fit of Model T65-20 to the overall data set, we estimate the standard error in a single travel-time observation to be 0.24 sec. This noise in the data maps into errors in the inversion model through Equation (60); values for particular model blocks are given in Table 5.1. For this particular point on the trade-off curve between error and resolution ($NDF = 20$), the model standard deviations due to random noise are small, typically less than 0.01 km/sec and never greater than 0.02 km/sec, which is much less than the total variation of velocity across the study area (0.2 km/sec in Layer 1). We conclude that the contamination of the model by random errors in the data does not introduce any major spurious features into Model T65-20.

More serious, and more difficult to assess, are the potential problems associated with data bias, which is not accounted for by the variance calculations. For example, the raw teleseismic residuals include the effects of near-receiver structure and other heterogeneities encountered

TABLE 5.1
MODEL STANDARD DEVIATIONS FOR T65-20

Δu = Slowness Perturbation

Δv = Velocity Perturbation = $-v_0^2 \Delta u$

$\sigma_{\Delta u}$ = Slowness Standard Deviation

$\sigma_{\Delta v}$ = Velocity Standard Deviation = $v_0^2 \sigma_{\Delta u}$

σ_0 = Standard Deviation Scale = 0.24 sec

Layer	Cell	Δu (s/km)	$(\sigma_{\Delta u}/\sigma_0)$	Δv (km/s)	$\sigma_{\Delta v}$ (km/s)	v_0 (km/s)
1	(6, 6)*	-0.004006	0.001828	0.14	0.016	6.0
2	(6, 6)	-0.002549	0.001325	0.11	0.013	6.5
3	(6, 6)	-0.001142	0.000581	0.07	0.008	7.8
4	(6, 6)	-0.000876	0.000485	0.05	0.007	7.8
5	(6, 6)	-0.000703	0.000477	0.04	0.007	7.8
6	(6, 6)	-0.000536	0.000464	0.03	0.007	7.8
1	(6, 13)	0.000866	0.002028	-0.03	0.018	6.0
2	(6, 13)	0.000524	0.001016	-0.02	0.010	6.5
3	(6, 13)	0.000347	0.000523	-0.02	0.008	7.8
4	(6, 13)	0.000208	0.000532	-0.01	0.008	7.8
5	(6, 13)	0.000193	0.000449	-0.01	0.007	7.8
6	(6, 13)	0.000280	0.000444	-0.02	0.006	7.8

* See Figure 4.3 for cell indexing scheme.

along the ray paths exterior to the model grid. The data reduction and inversion procedures have been specifically designed to filter out near-receiver structure, but these procedures cannot totally eliminate the effects of heterogeneities along the ray paths immediately beneath the model grid. Another potential problem is the possibility that first motions from low-yield events have been systematically missed, biasing the travel times to larger values. Again we constructed our data processing algorithm to reduce as much as feasible this sort of bias, but we leave open the possibility that it has not been completely eliminated.

Under-Parameterization

The number of parameters in Model T65-20 is large (1188), but the model grid still only crudely approximates the continuously varying distribution of velocity in the study region. Under-parameterization can introduce spurious features into the model and lead to incorrect estimates of resolution and variance (Chou and Booker, 1979). For example, small-scale heterogeneity in the immediate vicinity of the events can be aliased into large-scale features of the model. We have attempted to reduce these effects by optimizing the choice of cell sizes to conform to the data coverage and by using an inversion algorithm that minimizes the horizontal velocity gradients. Nevertheless, the effects of under-parameterization may still be significant, especially near the edges of the model grid where the cell sizes are large.

Nonlinearity

An important approximation in our analysis is the assumption that the travel-time residuals can be linearly related to three-dimensional velocity perturbations defined

with respect to a one-dimensional (horizontally stratified) structure. If the initial velocity model used to compute the ray paths is a poor approximation to NTS structures, then the lengths of the ray paths through specific model cells may be in error. Fortunately, for teleseismic data of the sort used here, the linear approximation appears to be very good (see, for example, the experiments with three-dimensional ray tracing done by Gubbins, 1981), and we expect any errors due to non-linear effects to be small.

Finite Resolving Power

Even if the data could be observed without error and all calculations done exactly, our ability to resolve features beneath NTS would still be limited by the nonuniqueness of the solution to the inverse problem posed in Equation (52). Errors in the data and the other problems discussed above further degrade the resolving power. In the parlance of engineers, our model estimates are the output of a noisy filter, or "black box," whose input is the actual earth structure we seek to describe. Assuming the black box to be a linear device and the noise in the system to be random, we can compute the expected value of its transfer matrix, \mathcal{R} , given by Equation (60). Rows of this transfer matrix are called "resolving kernels," or more appropriately for the case of a discretized model, "resolving vectors." Examples of these vectors for Model T65-20 are given in Appendix E. An analysis of these resolving vectors yields the following conclusions:

1. Near the center of the event groups at Pahute Mesa and Yucca Valley the minimum horizontal scale length of resolvable features at this variance level ($NDF = 20$) is approximately 15 km in the crust (Layers 1 and 2) but

increases rapidly with depth in the mantle. This reflects the poor sampling of the mantle deep beneath the events by the diverging ray paths. In fact, the resolving kernels in the lower reaches of the model (Layers 4 through 6) are not even localized on their target cells, which implies that model values at these depths are interpolated from the peripheral cells sampled by the ray paths.

2. In the crust, the horizontal resolution lengths increase dramatically as one moves from the center to the periphery of the grid and the localization of the kernels decreases, again reflecting the sampling by the ray paths.
3. In all layers the vertical resolution of structural features is poor; minimum vertical resolution lengths are on the order of 30 km, generally achieved in Layers 1 through 3. This lack of vertical resolution is, of course, a consequence of having only data corresponding to nearly vertical ray paths; structural features are, therefore, "smeared out" along these paths.

5.1 GENERAL STRUCTURAL FEATURES OF T65-20

Because the model parameters of T65-20 are only smeared-out estimates of the actual values and are contaminated by noise and other error processes, we shall adopt a conservative approach to the problem of structural interpretation, focusing discussion on those features well constrained by the data set and pointing out possible trade-offs between parameters.

The more robust features of the model appear as features on the map of integrated vertical travel-time residual ("vertical delay time") introduced in the previous section. This map is reproduced for $NDF = 20$ on Figure 5.1, and the full three-dimensional model is summarized on Figure 5.2.

Three features dominate the vertical delay time map:

1. A gradient in the delay times trending to the northwest, essentially along the axis of the model grid. This gradient is a manifestation of southeast-trending velocity gradients present in all layers of the model.
2. A negative travel-time anomaly associated with events on Pahute Mesa. This anomaly corresponds to positive velocity perturbations in all layers. In Layer 1, this perturbation is very nearly centered on the Silent Canyon Caldera, schematically illustrated in Figure 5.3. The anomaly shifts systematically northward with increasing depth, as can be seen in Figures 4.13 and 5.2.
3. A more subtle distortion of the delay-time contours near the northwestern end of Yucca Valley, which introduces a small (0.02 sec) dip in the delay-time surface trending approximately $N40^{\circ}W$. The velocity anomalies associated with this feature are confined to the two crustal layers.

In fact, a notable aspect of the model is the featureless character of the mantle beneath the southeastern part of the model grid. Overall, the lateral velocity structure of the model in Layers 3 to 6 is reasonably well represented by a high-velocity anomaly associated with the Pahute Mesa events superimposed on a uniform southeast-trending gradient.

5.2 THE SOUTHEAST-NORTHWEST VELOCITY GRADIENT

A pervasive feature of the model is the general increase in velocities from southeast to northwest. The direction of this gradient is more or less independent of depth, although its magnitude may decrease slowly with depth.

6-LAYER DEMAND VERTICAL DELAY TIME NKF = 20 T65

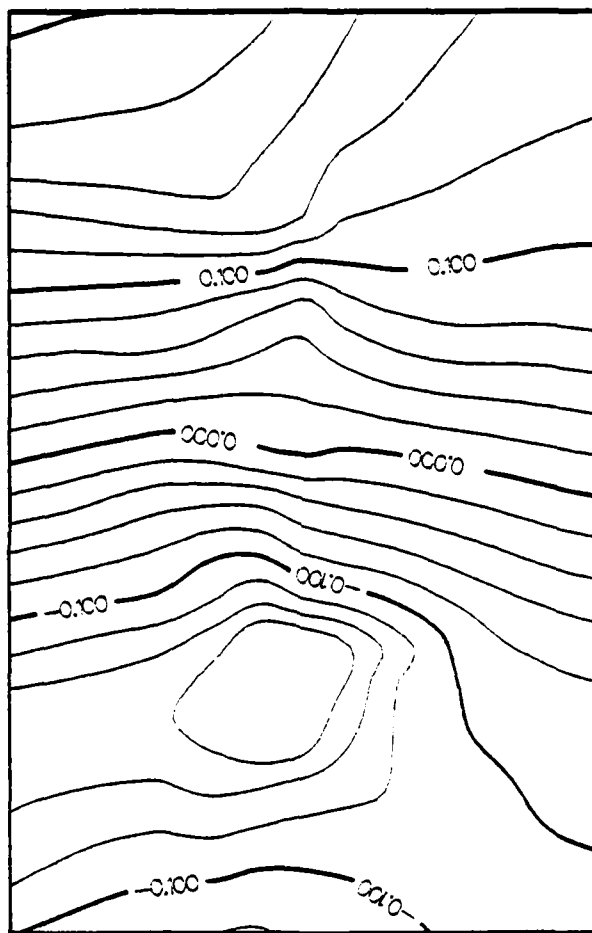
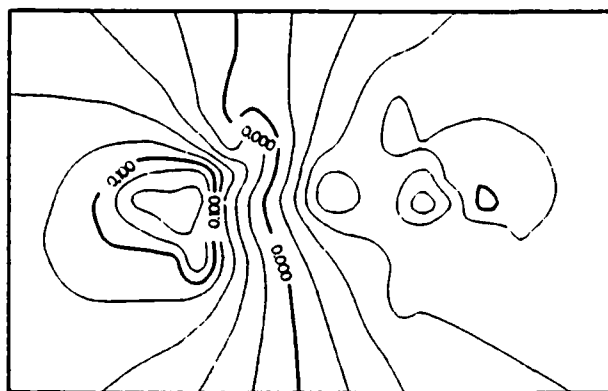
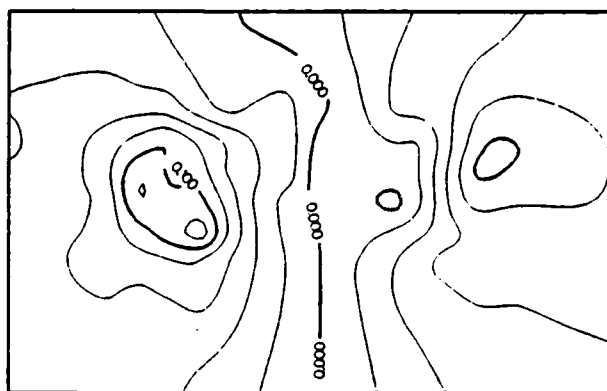


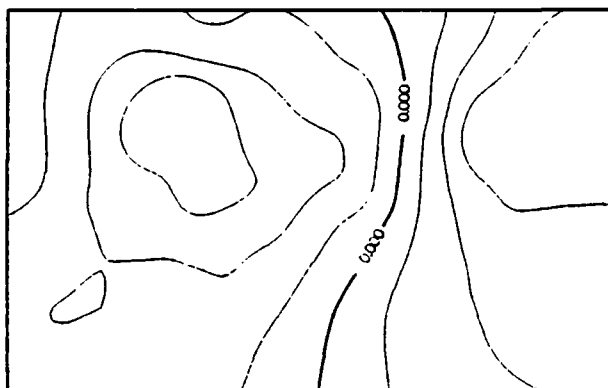
Figure 5.1. Vertical delay time calculated from Model T65-20.



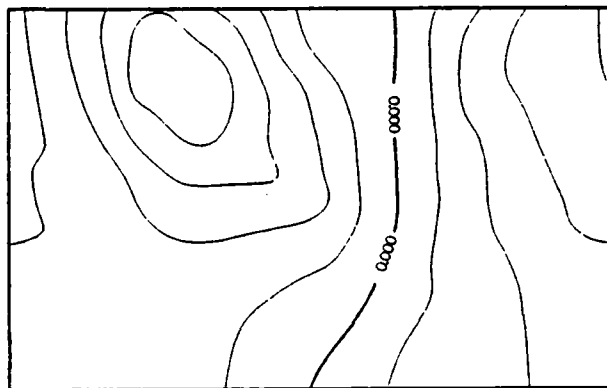
Layer 1 (0 - 12 km)



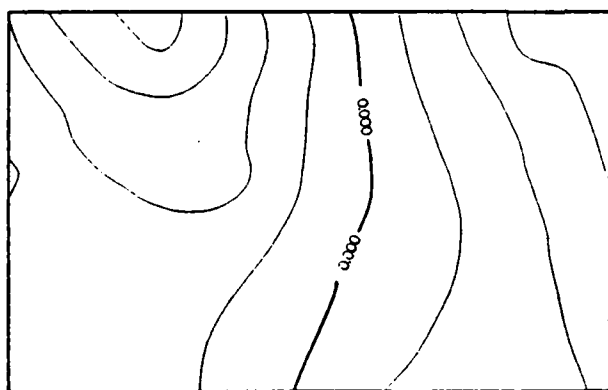
Layer 2 (12 - 28 km)



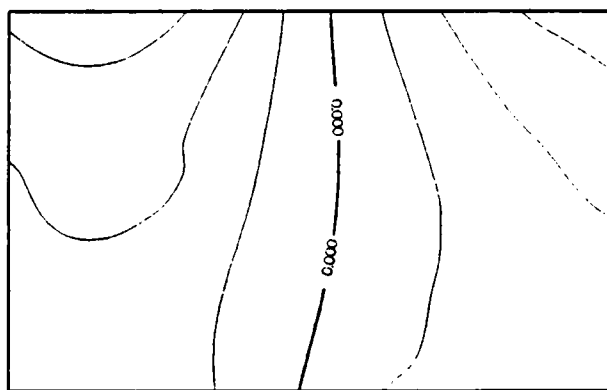
Layer 3 (28 - 48 km)



Layer 4 (48 - 74 km)



Layer 5 (74 - 108 km)



Layer 6 (108 - 152 km)

Figure 5.2 Velocity perturbations in the six layers of Model T65-20 (NDF = 20). Contour interval is 0.02 km/sec.

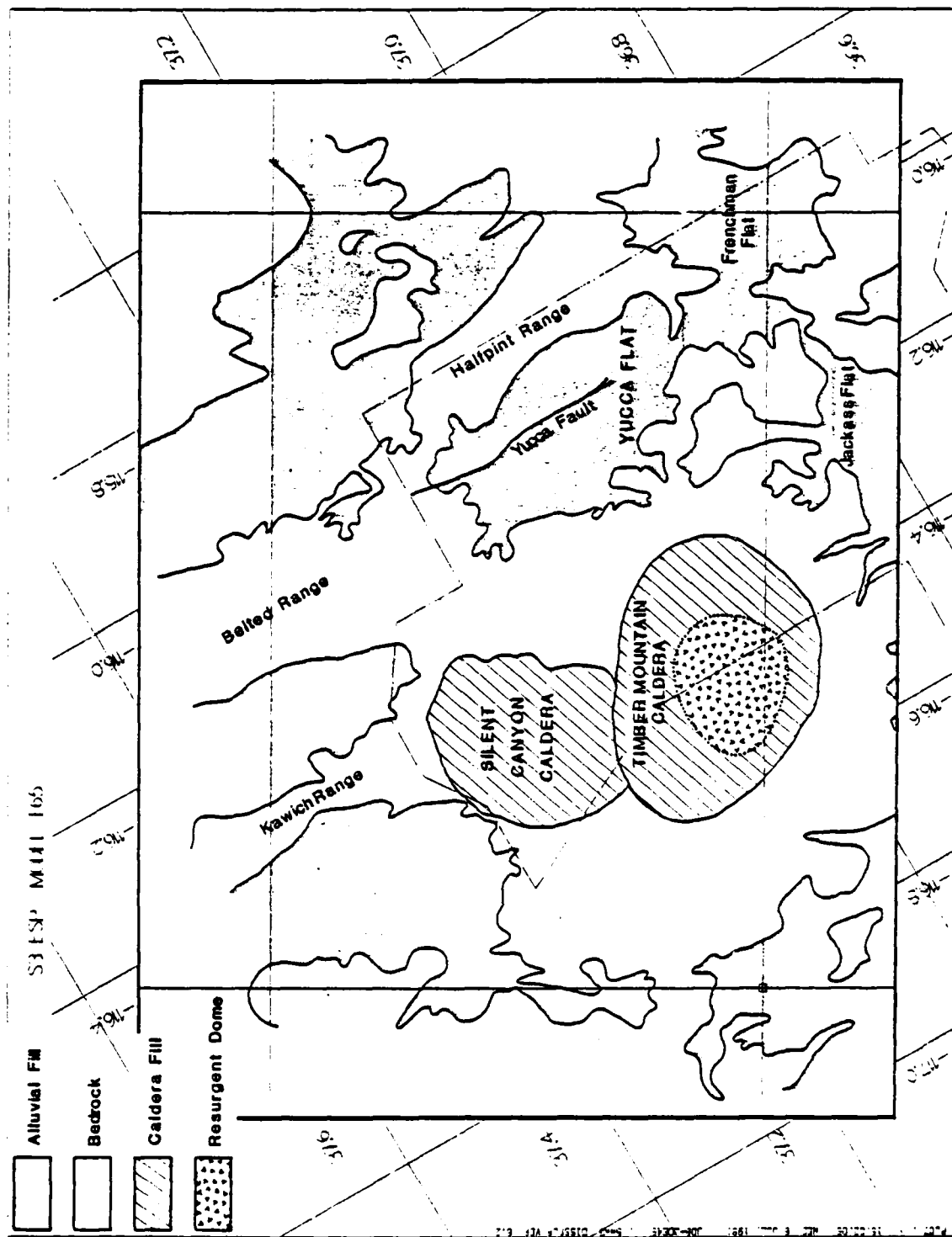


Figure 5.3. Simplified geological features in the NTS region distinguishing between alluvial and bedrock surface geology. Also shown are the outlines of the Silent Canyon and Timber Mountain calderas, as well as the location of the Yucca fault.

The property of the data set which requires this gradient has been mentioned in previous sections: travel times from events in Yucca Flat are generally greater than those from events on Pahute Mesa. The total difference in the mean travel time between these two areas is about 0.3 sec (Figure 3.9), although the range of residuals at northeasterly azimuths reaches 0.6 sec (Figure 3.6). Figure 5.1 shows that the calculated vertical travel times predicted by T65-20 is 0.20 to 0.25 sec greater at Yucca relative to Pahute.

Since the resolving-power calculations discussed above indicate that the data set affords us rather poor vertical resolution, the question arises as to whether or not the lateral velocity variations corresponding to this gradient could, in fact, be much more localized in depth. For instance, confining these gradients above the Mohorovicic discontinuity would require the average crustal velocity beneath Yucca to be about five percent less than beneath Pahute to give a 0.2 sec relative delay. While such a variation in mean velocity cannot be ruled out, it is not easily reconciled with the observations that show the upper crustal velocities within the Silent Canyon Caldera to be significantly less than those characteristic of Yucca Valley (Healey, 1968; Spence, 1974).

A more palatable explanation would ascribe the gradient to an increase in crustal thickness to the southeast. Assuming that the velocity increases across the Moho from 6.5 km/sec to 7.8 km/sec requires a difference in crustal thickness on the order of 10 km, which is large but not implausible (see, for example, Hirn, et al., 1980). However, this explanation is inconsistent with the gravity observations of Healey (1968) (Figure 5.4), which show an increase in the Bouguer field to the southeast, not the decrease implied by this hypothesis.

It appears to be difficult, therefore, to localize the southeast-northwest gradient at or above the Moho, and the

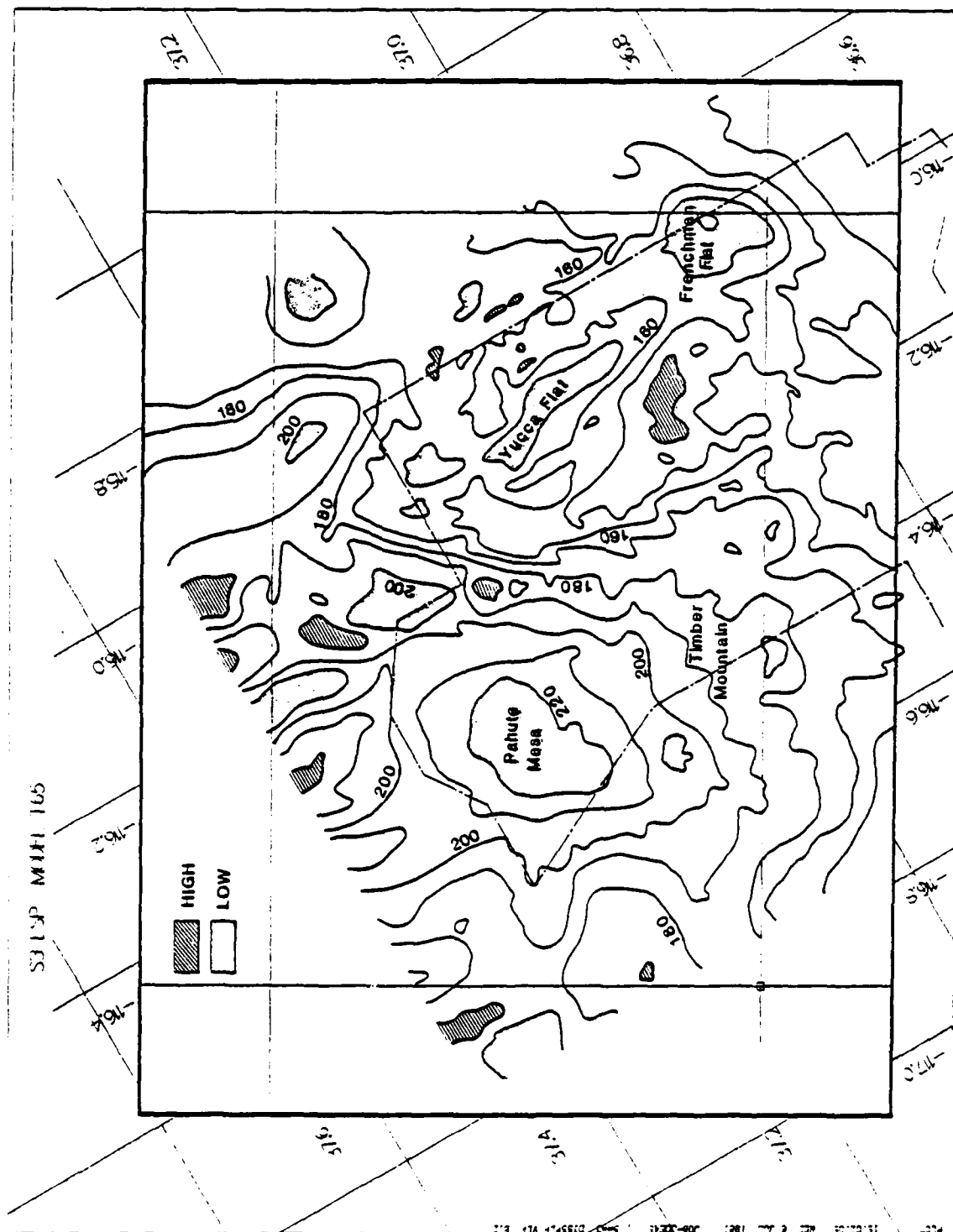


Figure 5.4. Bouguer gravity anomaly map for NTS region (after Healey, 1968).

significant mantle contribution to the gradient implied by the model is probably real.

5.3 THE PAHUTE ANOMALY

The most conspicuous localized anomaly in Model T65-20 appears in the form of a high velocity region beneath Pahute Mesa. It is prominent in the vertical delay map (Figure 5.1), but, more interestingly, it can be followed at depth throughout the model grid. Cross sections on Figure 4.13, as well as the sequence of horizontal sections depicted on Figure 5.2 show that the center of this anomaly shifts to the north-northeast as one proceeds deeper into the mantle. In addition, the horizontal extent of the anomaly is much more localized near the surface, and tends to be smeared laterally in the mantle layers.

We should point out at the outset that the data from Pahute events have not been corrected for the delay due to the Silent Canyon Caldera volcanics. As a result, Model T65-20 actually provides a lower bound to the vertically integrated amplitude of the high velocity anomaly. Based on Healey's (1968) estimate of 5 km for the thickness of low density ($\sim 2.22 \text{ g/cm}^3$) and low velocity (3.6 to 3.9 km/sec) caldera fill, Spence (1974) applied a 0.3 to 0.5 sec correction term to the travel times from Pahute Mesa events. In our data set, this would amount to doubling the average travel time difference between the Pahute and Yucca event groups. Thus, if anything, the integrated amplitude of the Pahute anomaly is underestimated in our model.

Spence's (1974) conclusion that there has to be a velocity anomaly in the mantle beneath Pahute Mesa is based almost exclusively on the large ($\sim 1 \text{ sec}$) advance for steep rays leaving shots within the caldera (particularly GREELEY),

relative to DUMONT (see Figures 3.7 and 3.8). In contrast, we are dealing here with much smaller (~ 0.25 sec to 0.4 sec) relative travel time anomalies between the Pahute Mesa and Yucca Flat events, mostly because the aforementioned correction was not performed. Yet, our model also includes a mantle anomaly at all depths. A significant aspect of this anomaly is that it is controlled partly by the rays leaving Yucca events to the northwest which are less delayed than at other azimuths and, which carry independent information, since they average the three-dimensional structure very differently. This is translated into a decoupling of the averaging kernels across Layer 3 beneath Pahute (Appendix E). In other words, the data set does not allow efficient trade-off between perturbations in the crust and perturbations in the upper mantle beneath Pahute Mesa. We conclude, therefore, that there is indeed a mantle expression of the Pahute travel time anomaly, in agreement with Spence's conclusion, although his and our arguments are more-or-less independent.

Because of better geographical coverage afforded by our data set, we are able to place better constraints on the lateral extent of this anomaly. Spence (1974) considered only eight events). In the top layer, the anomaly is shifted to N60W (along the long axis of the grid) relative to the surface outline of the Silent Canyon Caldera (Figure 5.3). Because the epicenters are clustered around the caldera itself, the northwest and west outlines of the high velocity contours are not well constrained in this layer. What is well controlled, however, is the steep gradient toward Rainier Mesa and Yucca Flat. The contour at 0.1 km/sec bisects the caldera in a N30E direction, and the null contour (0. km/sec) closely approximates the southeast outline of the caldera. In addition, the high velocity ridge extending east from the anomaly is well controlled by numerous rays as can be seen from the hit pattern for that layer (Figure 4.4a). The steep gradient to S60E arises

because of the systematic evolution of residuals at this azimuth across this region of the test site (Figure 3.6). These residuals are generally negative for the easternmost events, and become less negative as one proceeds to the east-southeast, to become positive for Events 98 and 94 and for the Rainier Mesa events (Events 68, 86, 101, 111). Note that residuals for eastern azimuths remain predominantly negative for all Pahute events, giving rise to the high velocity ridge mentioned above.

The same general features persist in Layer 2, but now the northwest and west outlines of the high velocity body are better defined because of a better distribution of rays (Figure 4.4b). Recall, however, that the vertical resolving lengths are at best 30 km in that region, so that a strong correlation between contours in Layers 1 and 2 is not surprising.

The mean vertical delay calculated for the two crustal layers only ranges from -0.05 sec to -0.1 sec near the center of the high velocity region. This could be explained by a 2 km to 4 km crustal thinning beneath the caldera. Again, these estimates are lower bounds since the contribution from the caldera fill was not explicitly included.

The uppermost mantle layer, (Layer 3) is the first one in which we find a northerly shift of the center of the anomaly. This tendency persists in Layer 4, and for the lower layers the anomaly actually migrates outside the inner grid and affects mostly edge cells. This trend is clearly visible on the vertical model section across Pahute Mesa (Figure 4.13b). Two properties of the observations control this behavior. The first one is the systematic variation of the magnitudes of the residuals from the northwest to the southeast across Pahute Mesa into Rainier Mesa which is dramatically illustrated by the observed average residuals shown on Figure 3.9. While most residuals near the central and western portions of the Pahute event group are strongly negative on the average, the eastern

Pahute events show a much more complex pattern of mixed positive and negative residuals, which give way to a tendency for positive residuals for Rainier Mesa explosions. As a result, the data place an eastern boundary of the anomaly near longitude 116.2°W . The other feature is the abrupt change in sign of Pahute residuals for rays with a northern azimuth: rays leaving slightly east of north are clearly fast, but rays leaving slightly west of north are slower by 0.2 to 0.5 seconds (Figures 3.6a and 3.6b). This behavior is reflected in the predicted residuals as well (Figures 4.14a and 4.14b). Since this is true of all Pahute events, the model feature which gives rise to this phenomenon must reside fairly far from the source region, at a distance at least several times the diameter of the Pahute event group (~ 20 km). Thus, only a mantle anomaly can explain this pattern; it is constrained to lie west of 116.2°W , but at an azimuth east of north for the bulk of Pahute events.

Note that the preceding argument does not constrain the latitude of the anomalous body. Unfortunately, the paucity of observations for southern azimuths prevents us from identifying a clear azimuthal pattern of residuals from that direction. More disturbingly, the anomalous body seems to follow the dense bundle of rays leaving Pahute Mesa toward the north-northeast to Canadian and European stations. This is particularly obvious on the vertical section on Figure 4.13b. Some control is afforded by rays from the Yucca event group to the northwest, which cross the high velocity body in Layer 4 and do indeed exhibit some negative residuals in that direction (e.g., Events 149, 64, 136, etc.). However, we lack control on the southern limit of the anomaly, because of a lack of southern residuals from Pahute events and a lack of western residuals from Yucca events. This is painfully clear on the hit pattern for Layer 4, where cells between 37.2°N and 37.3°N and between 116.3°W and 116.5°W are not sampled at all. The

model structure for that region is thus exclusively controlled by the smoothness constraint in the inversion, and the corresponding resolving kernels are very unlocalized, and do not even peak in the target cell (Appendix E). Further south, cells are somewhat better sampled and there is a weak tendency for the contours to be deflected to the west; it is therefore unlikely that the high velocity anomaly should extend as far to the south as it does to the north.

In the final analysis, the north-northeast bias of the high velocity region as one goes deeper into the mantle is probably real. However, the southern outline of this body is highly uncertain and we cannot exclude the possibility that it is also present directly beneath Pahute Mesa.

Finally, we should note that the problems discussed for Layer 4 only become more severe in Layers 5 and 6, in which the anomaly migrates out of the inner grid. The hit pattern for these layers show that we have essentially no control on the structure directly beneath the events, and the resolving kernels are completely unlocalized. As a result, no reliable conclusion can be reached as to the depth extent of the high velocity body based on our data set alone.

5.4 YUCCA VALLEY

The three-dimensional structure beneath the Yucca event group is characterized by two main properties (Figures 5.2 and 5.3):

1. Minor, localized velocity variations in the two crustal layers, with a relative velocity high on the west side of the Yucca fault, and a corresponding low on the east side, with a total velocity contrast of the order of 0.05 to 0.1 km/sec.

2. A remarkably featureless mantle structure, aside from the southeast-northwest gradient discussed earlier.

In addition, the top layer exhibits a weak low-velocity anomaly near Rainier Mesa which is rather poorly controlled by the data and which we shall ignore in the absence of other evidence.

The fact that structural features are practically confined to the crust in that portion of the study area is further illustrated by the cross sections on Figures 4.13a and 4.13c. The main difficulty encountered with the Yucca event group stems from the nearly linear distribution of shot points, which severely limits our ability to resolve the depth of anomalies for directions perpendicular to the valley. This narrow pattern of epicenters leads to a lack of independence among the data since most cells tend to be crossed by nearly parallel rays.

It is gratifying to find on the average faster velocities on the west side of the Yucca Fault than on the east side, since this is consistent with the known throw of the fault, which brings basement rocks closer to the surface on the west side. This property is probably resolvable in the sense that the resolving kernel centered on the positive anomaly at (37.12°N, 116.8°W) (Appendix E) shows that the horizontal resolution is of the order of three model block dimensions, or locally 12 to 15 km. There is strong coupling between the two crustal layers, so that the depth resolution is poor in the crust, but there is clear decoupling between Layers 2 and 3, an indication that this anomaly does not extend into the mantle.

As in the case of the Pahute anomaly, the most obvious trend in the data which is consistent with this model feature is the systematic variation of averaged travel time residuals across the Yucca fault, shown in Figure 3.9. Individual residuals, on the other hand, show even more scatter than in the

case of Pahute, and trends are exceedingly difficult to identify by simple inspection.

The actual existence of a structural contrast between the two sides of the Yucca fault is probably the only conclusion which can be justified, however. The positive anomaly involves only four blocks at the most in the top layer, a representation too coarse to permit a reliable outline of the structure. In addition, as can be seen from the corresponding hit pattern, the data give us very little control on the true lateral extent of these features, since the surrounding blocks are either poorly sampled or not sampled at all.

5.5 RECAPITULATION

From the preceding descriptions, there emerges a three-dimensional picture of the crust and upper mantle beneath the study area which may be characterized in terms of the three primary features:

1. A general apparent velocity gradient with slower velocities to the southeast.
2. A high velocity body extending from the Silent Canyon Caldera near the surface to depths exceeding 100 km, with a tendency to migrate northward with increasing depth in the mantle.
3. A localized structural gradient across the Yucca region, which is confined to the crust.

The main weaknesses of the model arise from the rather poor distribution of rays: (1) this places severe limitations on our ability to resolve the vertical extent of velocity anomalies, and (2) this also prevents us to define the horizontal outline of these features, in Layer 1 because only the central cells are sampled properly, and in the deepest layers because only the outer cells contain a useful number of rays.

The apparent horizontal gradient affects all layers. Although it may be due in part to a shallow structural trend (e.g., crustal thickening to the southeast) this hypothesis conflicts with the Bouguer gravity data. Previously published crustal studies for the western United States (e.g., Pakiser, 1963; Pakiser and Hill, 1963; Prodehl, 1970) are of little help because they are concerned with much larger scales and cannot adequately address this feature, since it must necessarily be fairly local to the NTS region if it reflects a shallow structural trend. In view of the conflict with gravity data, we favor the hypothesis that a sizable fraction of the trend in vertical delay times actually originates in the mantle.

Overall, our model is consistent with Spence's (1974) conclusion, based on a more limited data set, that a high-velocity body underlies the Silent Canyon Caldera, although the total velocity contrast appears to be somewhat less than the 0.3 to 0.5 km/sec advocated by him. We have noted, however, that this contrast would be increased by correcting for caldera fill, and there is clearly a trade-off between the contrast of this feature and its depth extent. Our results indicate a north-northwest-ward trend in these high velocities with increasing depth which is essentially perpendicular to the more diffuse northwest-southeast velocity gradient. These basic features of the model may, in fact, be generically related. The high velocities associated with the Silent Canyon Caldera do not extend to the south-southwest in the model, but, as we have noted, our resolution at these azimuths is limited.

5.6 MAGNITUDE ANOMALIES

This study has been based exclusively on travel time information. We now turn to a comparison of the results with the independent data set which consists of the magnitude

anomalies summarized on Figures 5.5a through 5.5c. These anomalies constitute a crude measure of relative variations of teleseismic amplitudes after normalization to a common source yield. Comparison of magnitude anomalies with observed mean travel-time anomalies (e.g., Figure 3.9 or calculated vertical delay times e.g., Figure 5.1) shows that a relationship exists between the two data sets, but that this correlation is quite different in Pahute Mesa and in Yucca Flat. While magnitude residuals increase to the south and east within Pahute Mesa, and thus correlate negatively with travel-time anomalies, the opposite occurs in Yucca Flat, where magnitude residuals decrease as one traverses the site from west to east, and thus correlate positively with travel time anomalies.

This observation prompts us to make several comments.

1. If magnitude residuals are controlled by lateral variation of attenuation in the upper mantle beneath NTS then one should expect positive magnitude anomalies near the center of Pahute Mesa, decreasing toward the periphery, since, as noted by Spence (1974) higher velocity material is usually less attenuating. Observations indicate precisely the opposite correlation. Furthermore, such an interpretation could not easily explain the large differences of magnitude residuals between neighboring events within the Yucca group, particularly in view of the lack of upper mantle velocity variations in that region. One must therefore invoke a mechanism which is capable of overcoming and reversing the pattern anticipated across Pahute Mesa on the basis of the suspected high Q upper mantle body beneath the volcanic massif.

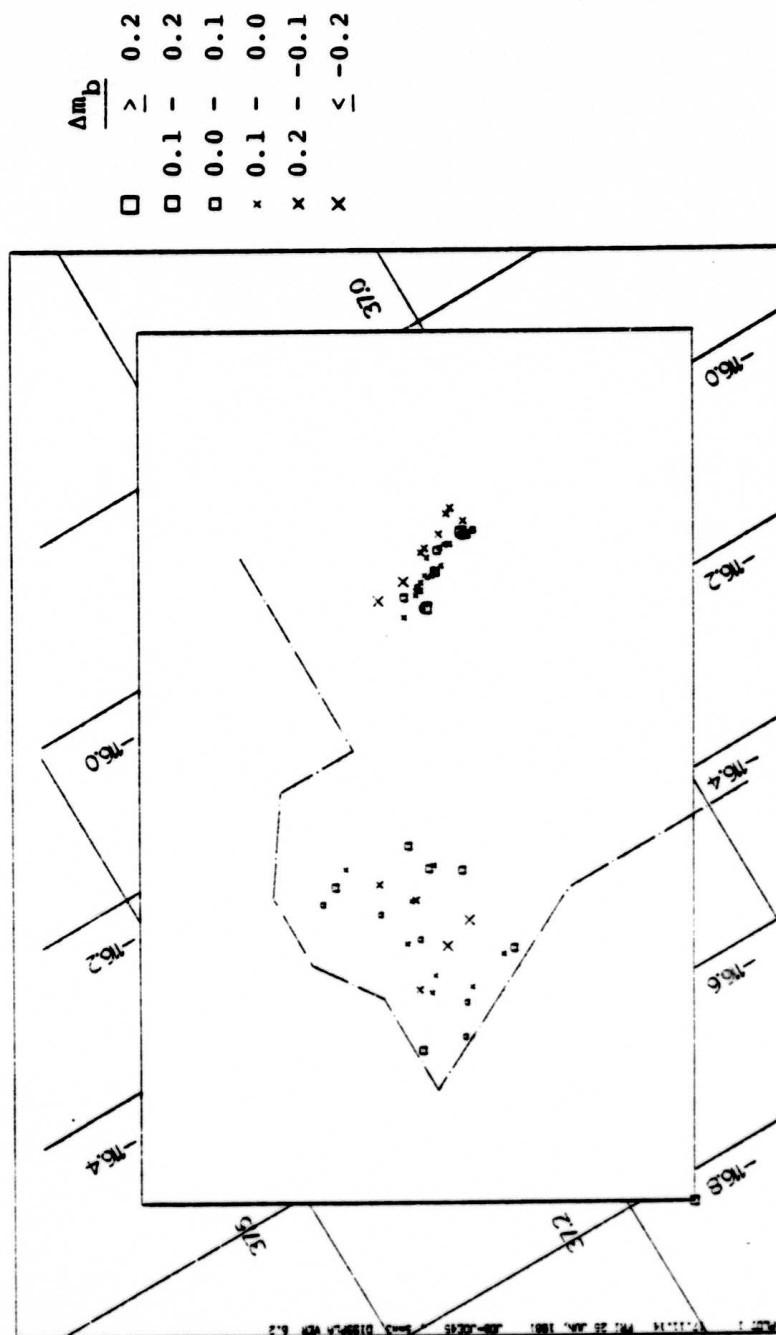


Figure 5.5a. Magnitude anomalies for NTS events from Alewine, et al. (1977).

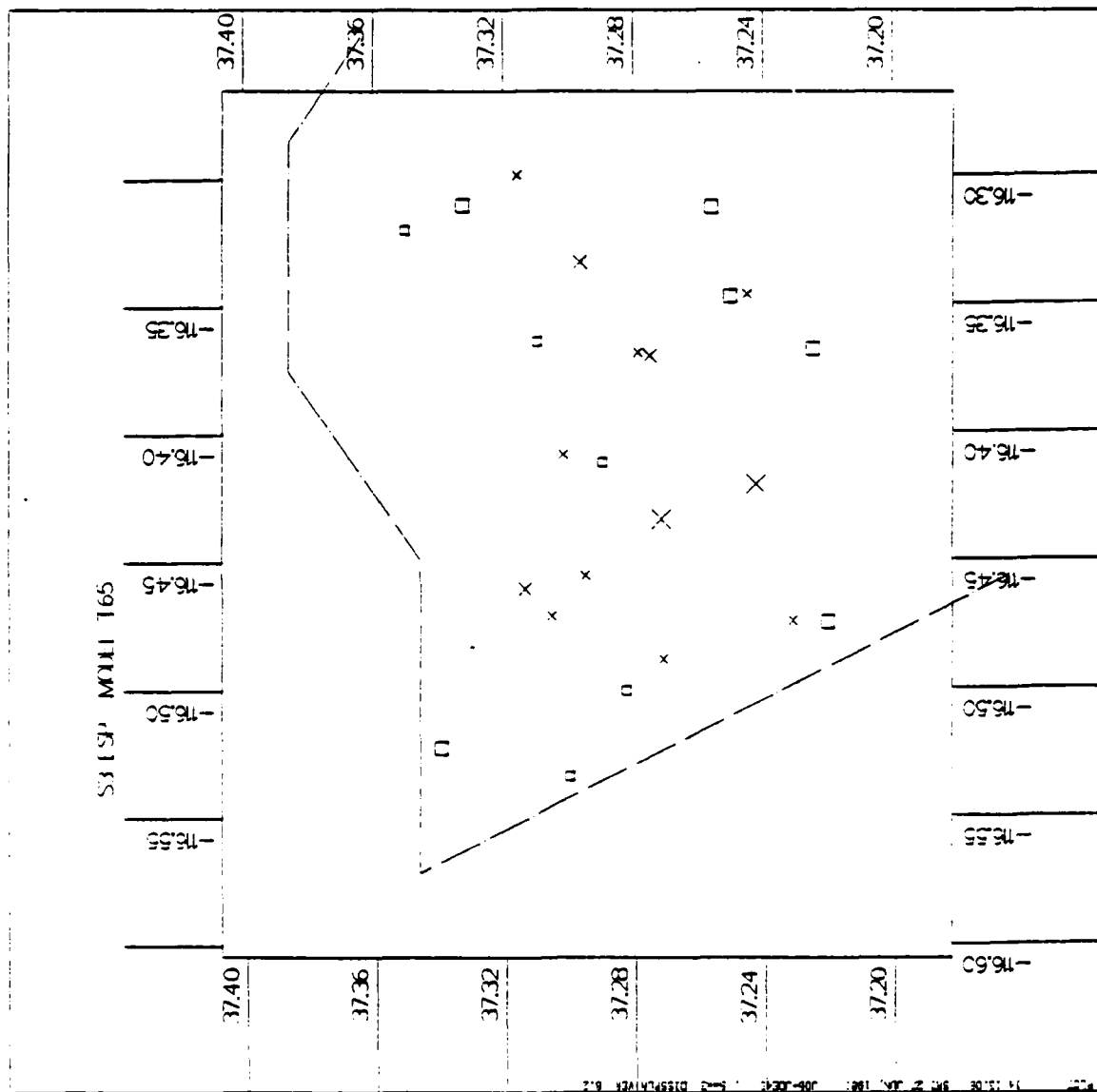


Figure 5.5b. Magnitude anomalies for Pahute Mesa, enlarged from Figure 5.5a.

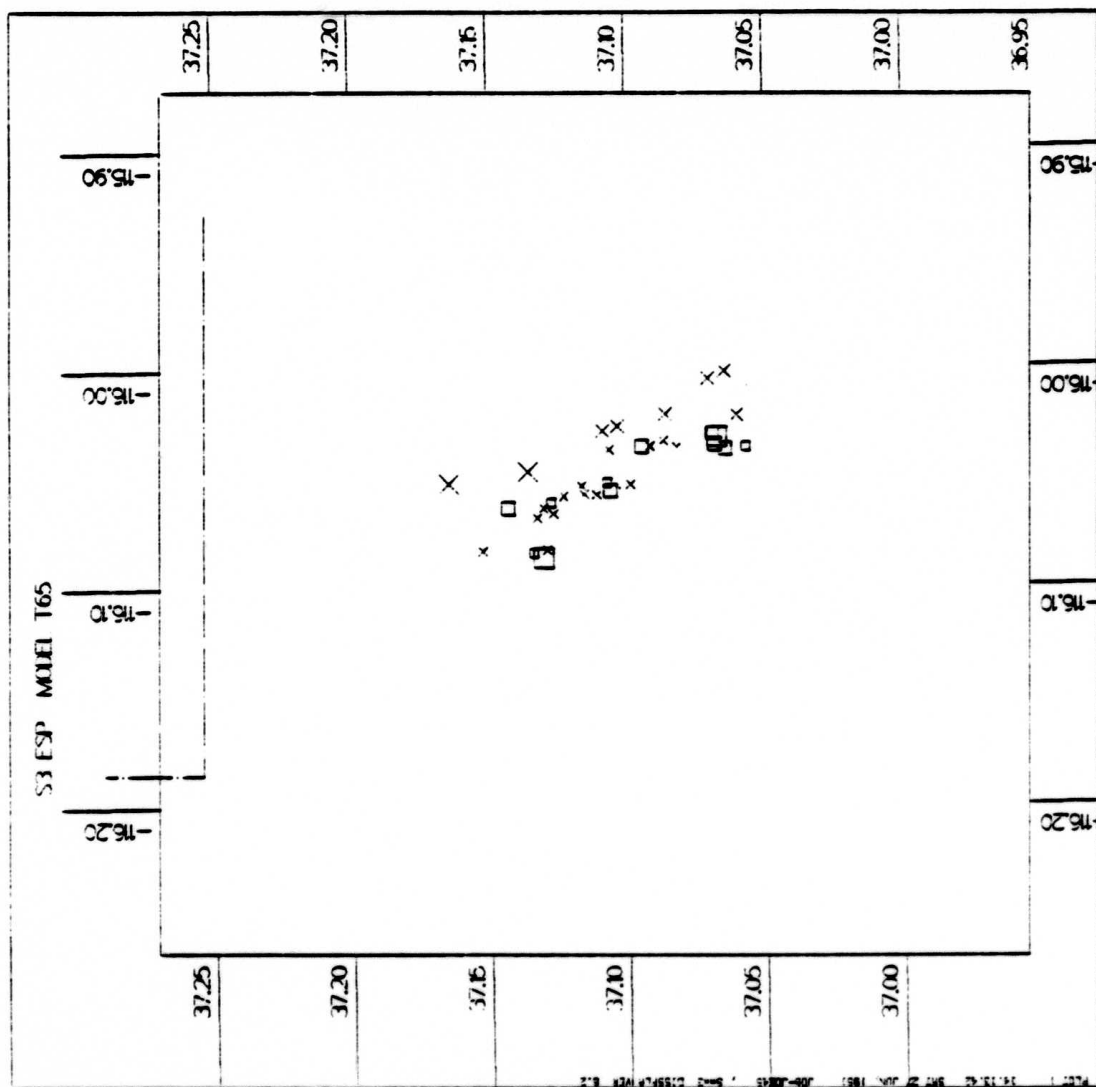


Figure 5.5c. Magnitude anomalies for Yucca Flat events, enlarged from Figure 5.5a.

2. One such potential mechanism relies on the focusing-defocusing properties of the mantle velocity anomaly beneath Pahute Mesa. This would be verified experimentally by a systematic study of amplitudes from Pahute events at individual stations: rays which remain predominantly within the anomaly can be expected to exhibit lower amplitudes (and thus the corresponding stations yield negative magnitude residuals) than rays which skirt the anomaly. This effect can be quantified theoretically by three-dimensional ray tracing through our Model T65-20 for selected source locations in and around Pahute Mesa. This possibility then raises two questions: (1) is this effect of sufficient magnitude to overcome Q-effects? and (2) how does one account for the Yucca pattern with such a mechanism? The virtually featureless upper mantle structure beneath Yucca in our model points to the need for yet another mechanism if all NTS magnitude residuals are to be accounted for by a common explanation.
3. Focusing and defocusing effects due to shallow structure could be a valid explanation. For purposes of argument, let us assume that the lateral velocity variations in the lower crust are predominantly due to moho topography. Model T65-20 then predicts a doming of the moho beneath Pahute Mesa, with rapid crustal thickening in all directions away from the caldera. On the other hand, the model would

also predict localized thinning of the crustal column on the west side of Yucca Valley, or crustal thickening on the east side. (Moho topography is of course not necessarily smooth, and these variations could be due to abrupt vertical offsets not resolved by our model.) In that case, the defocusing properties of a moho upwarp could operate in Pahute Mesa and yield amplitude anomalies in qualitative agreement with the observed magnitude residuals. Whether quantitative agreement can be achieved through such a mechanism requires further study. In Yucca Valley, however, we do not have a parallel situation since moho upwarp would then be associated with positive magnitude residuals, in contrast to the Pahute Mesa situation. Although this difference is not sufficient to dismiss moho topography as the explanation of amplitude anomalies, it does point to the fact that a focusing-defocusing interpretation involves some unresolved complexities.

4. Lateral variations within the crustal column, where velocity increases are associated with a concomitant decrease in Q constitute yet another possibility. Such might be the case if the lower part of the crust beneath Pahute Mesa is invaded by highly attenuating, yet high velocity volcanic material. If a local moho upwarp is invoked instead, then we could have very attenuating submoho material in greater volume beneath the caldera. Such mechanisms do not have an obvious parallel in

the case of Yucca, however. In addition, because rays spend very little time in that part of the model (~ 3 to 4 sec) a significant amplitude anomaly (say, a factor of two) requires very low values of Q ($Q \sim 20$ or less)!

5. Another candidate explanation is related to the superficial layer. We note that there exists a clear correlation between magnitude residuals and the properties of near-surface geology. In both Pahute and Yucca test areas, negative magnitude residuals tend to be associated with a thick, low velocity, low density surface layer: thicker sediments on the east side of Yucca Valley, and caldera fill in the center of Pahute Mesa. The effects of such a near-source environment on teleseismic amplitudes are not very well understood, and may result from a combination of several phenomena, among which
 - A. the coupling efficiency as a function of material properties near the working point,
 - B. reverberations within a laterally varying, low velocity surface layer,
 - C. linear and nonlinear interactions of the near-source wave field with the free surface, which may affect timing and amplitude of reflected phases.
 - D. Linear and nonlinear (i.e., high strain) attenuation mechanism in the vicinity of the sources.

In summary, a comparison of magnitude residuals with the travel time modeling results of this study indicates that,

if a parallel explanation (e.g., focusing-defocusing by velocity anomalies) is sought which explains both Pahute and Yucca amplitude anomalies, then it must invoke a mechanism which involves predominantly shallow (crustal or moho) structures. Furthermore, the effects of such a mechanism must be sufficiently strong to overcome Q effects in the upper mantle beneath Pahute Mesa. Of course nothing in the present work requires that parallel explanations apply simultaneously to Pahute Mesa and Yucca Flat. In fact, the geology of these two regions of the test site points to fundamentally different tectonic regimes and any parallel drawn between them should be viewed with a fair degree of skepticism.

VI. CONCLUSIONS AND RECOMMENDATIONS

The main conclusion of this study is the confirmation of Spence's (1974) suggestion that a high-velocity body underlies the volcanic massif at Pahute Mesa, and that this body extends into the mantle to depths exceeding 100 km. There is a suggestion that the center of the anomaly does not extend vertically beneath the Silent Canyon Caldera, but rather migrates to the north with increasing depth, and that it is surrounded by a more diffuse anomaly which gives rise to an apparent northwest-southeast velocity gradient in the NTS region. Otherwise, lateral variations beneath Yucca Flat appear to be confined to the crust, and not to be associated with local anomalies in the mantle. Further refinements of this study can be achieved as follows:

1. One aspect of our model which clearly requires further investigation is the clear conflict between the Bouguer and velocity anomalies. The localized Bouguer anomalies reflect shallow structures (e.g., Healey, 1968; Spence, 1974) which are not resolved by the velocity model; however, it is not known whether near surface contributions are sufficient to account for the conflict between gravity and velocity trends across the study area. Simultaneous inversion of gravity and travel time (e.g., Rodi, et al., 1980) requires assembling a gravity data set extending beyond the study area, and removal of contributions from both local, superficial density anomalies within the model grid (e.g., caldera fill) and from density anomalies outside the grid. This can be done by generalizing the denuisancing

technique, a method superior to the classical low-pass filtering treatment of gravity data because it does not introduce biases in the gravity data set.

2. Our analysis of catalogued travel time data has convinced us that it is contaminated by noise which is not easily removed, and which is comparable in magnitude to the actual "signal" generated by local three-dimensional structure. Many of the contributing sources of noise are absent from the reciprocal experiment which consists of recording teleseisms locally in the study area. Adjunction of a set of teleseismic travel times recorded around NTS would also offer the following potential advantages: (1) it would permit more uniform geographical sampling of the area by locating stations away from the narrow lineation of sources used in this study, (2) it would permit much better azimuthal coverage for southern and western directions by recording events from the western and southern Pacific seismic zones, and from Central and South America, (3) if new observations should be collected, the station locations could be chosen optimally for the purpose of testing specific features of the model.

As a first step, we recommend that a data set of existing teleseismic travel times recorded at NTS stations be compared with the predicted values from our model, and, if necessary, inverted jointly with the data already collected for this study. In addition, we recommend that

PKP data also be included because their steep incidence angle would permit improved sampling of the structure directly beneath the study area. More specifically, particular care should be given to the selection of data for a better definition of the south-southwest outline of the Pahute anomaly in the mantle layers.

3. Better constraints on the shallow structure (the crust) would result in much improved vertical resolution by limiting the trade-off possibilities between shallow and deep anomalies. We have successfully coupled the inversion of teleseismic travel times and of travel times from local events in a study of the Hanford area in eastern Washington (Rodi, et al., 1980) and shown that this procedure permits much more reliable structural interpretation. Although crustal seismicity around NTS is not particularly intense, an effort should be started to identify and collect local seismic data for the purpose of better constraining crustal structure laterally and vertically.

Although our attempts at modeling the Pahute Mesa anomaly on a much finer scale in the early stages of this study have not been particularly successful, this was mainly due to the noisy character of the data, and the lack of local control in the crustal layers. With an upgraded data set according to the preceding recommendations, a local inversion for Pahute Mesa or Yucca Flat should be attempted again with considerably enhanced chances of success.

VII. REFERENCES

- Aki, K., A. Christoffersson and E. S. Husebye (1976), "Three-Dimensional Seismic Structure of the Lithosphere Under Montana Lasa," BSSA, 66, pp. 501-524.
- Aki, K., A. Christoffersson and E. S. Husebye (1977), "Determination of the Three-Dimensional Seismic Structure of the Lithosphere," JGR, 82, pp. 277-296.
- Alewine, R. W., G. B. Young, D. L. Springer and R. W. Klepinger (1977), "Teleseismic P-Wave Magnitude-Yield Relations for Well-Coupled Nevada Test Site Explosions," Unpublished Report.
- Archambeau, C. B., E. A. Flinn and D. G. Lambert (1969), "Fine Structure of the Upper Mantle," JGR, 74, pp. 5825-5865.
- Bache, T. C., S. M. Day and J. M. Savino (1979), "Automated Magnitude Measures, Earthquake Source Monitoring, VFM Discriminant Testing and Summary of Current Research," Systems, Science and Software Quarterly Technical Report submitted to the Advanced Research Projects Agency, SSS-R-79-3933, February.
- Backus, G. and F. Gilbert (1970), "Uniqueness in the Inversion of Inaccurate Gross Earth Data," Phil. Trans. Roy. Soc. (London), Ser. A., 266, pp. 123.
- Burdick, L. J. and D. V. Helmlberger (1978), "The Upper Mantle P Velocity Structure of the Western United States," JGR, 83, pp. 1699-1712.
- Chou, C. W. and J. R. Booker (1979), "A Backus-Gilbert Approach to Inversion of Travel-Time Data for Three-Dimensional Velocity Structure," Geophys. J. R. astr. Soc., 59, pp. 325-344.
- Claerbout, J. F. (1976), Fundamentals of Geophysical Data Processing, McGraw-Hill, Inc.
- Frasier, C. W. and J. Filson (1972), "A Direct Measurement of the Earth's Short Period Attenuation Along a Teleseismic Ray Path," JGR, 77, pp. 3782-3787.
- Gubbins, D. (1981), "Source Location in Laterally Varying Media," Proceedings of the NATO Advanced Study Institute on Identification of Seismic Sources-Earthquake or Underground Explosion, Oslo, Norway, September 8-18, 1980, in press.

REFERENCES (continued)

- Haddon, R. A. W. and E. S. Husebye (1978), "Joint Interpretation of P-Wave Time and Amplitude Anomalies in Terms of Lithospheric Heterogeneities," Geophys. J. R. astr. Soc., 55, pp. 19-44.
- Healey, D. L. (1968), "Application of Gravity Data to Geologic Problems at Nevada Test Site," in Geol. Soc. Am. Memoir 110, Nevada Test Site, edited by E. B. Eckel, Geol. Soc. Am., Boulder, Colorado, pp. 147-156.
- Helmberger, D. V. and G. R. Engen (1974), "Upper Mantle Shear Structure," JGR, 79, pp. 4017-4028.
- Herrin, E. (1968), "Introduction to 1968 Seismological Tables for P Phases-Times of P," BSSA, 58, pp. 1193-1219.
- Hirn, A., M. Daigmeves, J. Gallart and M. Vadell (1980), "Explosion Seismic Sounding of Throws and Dips in the Continental Moho," Geophys. Res. Let., 7, pp. 263-266.
- Husebye, E., A. Christoffersson, K. Aki and C. Powell (1976), "Preliminary Results on the Three-Dimensional Seismic Structure of the Lithosphere Under the USGS Central California Seismic Array," Geophys. J. Roy. astr. Soc., 46, pp. 319-340.
- Jordan, T. H. (1973), "Estimation of the Radial Variation of Seismic Velocities and Density in the Earth," Ph.D. Thesis, California Institute of Technology.
- Lanczos, C. (1961), Linear Differential Operators, Van Nostrand, New York.
- Lundquist, G. M., G. R. Mellman and R. S. Hart (1980), "Review of the Estimation of m_b and Yield of Underground Explosions," Sierra Geophysics, Inc. Topical Report submitted to the Advanced Research Projects Agency, SGI-R-80-031, November.
- Pakiser, L. C. (1963), "Structure of the Crust and Upper Mantle in the Western United States," JGR, 68, pp. 5747-5756.

REFERENCES (continued)

- Pakiser, L. C. and D. P. Hill (1963), "Crustal Structure in Nevada and Southern Idaho from Nuclear Explosions," JGR, 68, pp. 5757-5766.
- Pavlis, G. L. and J. R. Booker (1980), "The Mixed Discrete-Continuous Inverse Problem: Application to the Simultaneous Determination of Earthquake Hypocenters and Velocity Structure," JGR, 85, pp. 4801-4810.
- Prodehl, C. (1970), "Seismic Refraction Study of the Crustal Structure in the Western United States," Geol. Soc. Am. Bull., 81, pp. 2629-2646.
- Ramspott, L. D. and N. W. Howard (1975), "Average Properties of Nuclear Test Areas and Media at the USERDA Nevada Test Site," Lawrence Livermore Laboratory Report prepared for the U. S. Energy Research and Development Administration, UCRL-51948, September.
- Rodi, W. L., T. H. Jordan, J. F. Masso and J. M. Savino (1980), "Determination of Three-Dimensional Structure of Eastern Washington from the Joint Inversion of Gravity and Earthquake Travel Time Data," Systems, Science and Software Final Report submitted to Weston Geophysical Corporation, SSS-R-80-4516, June.
- Rodi, W. L., J. F. Masso, J. M. Savino, T. H. Jordan and J. B. Minster (1981), "Relocation of Earthquakes in Eastern Washington Based on a Three-Dimensional Velocity Model," Systems, Science and Software Final Report submitted to Weston Geophysical Corporation, SSS-R-81-4957, April.
- Ryall, A. S. (1978), "Crustal Structural Trends in the Vicinity of the Nevada Test Site," Earthquake Notes, 49, pp. 10.
- Savino, J. M., W. L. Rodi, R. C. Goff, T. H. Jordan, J. H. Alexander and D. G. Lambert (1977), "Inversion of Combined Geophysical Data for Determination of Structure Beneath the Imperial Valley Geothermal Region," Systems, Science and Software Final Technical Report submitted to the Department of Energy, SSS-R-79-3412, September.
- Spence, W. (1974), "P-Wave Residual Differences and Inferences on an Upper Mantle Source for the Silent Canyon Volcanic Centre, Southern Great Basin, Nevada," Geophys. J. R. astr. Soc., 38, pp. 505-523.
- Spencer, C. and D. Gubbins (1980), "Travel-Time Inversion for Simultaneous Earthquake Location and Velocity Structure Determination in Laterally Varying Media," Geophys. J. R. astr. Soc., 63, pp. 95-116.

REFERENCES (concluded)

- Springer, D. L. and R. L. Kinnaman (1971), "Seismic Source Summary for U. S. Underground Nuclear Explosions, 1961-1970," BSSA, 61, pp. 1073-1098.
- Springer, D. L. and R. L. Kinnaman (1975), "Seismic-Source Summary for U. S. Underground Nuclear Explosions, 1971-1973," BSSA, 65, pp. 343-350.
- Trembly, L. D. and J. W. Berg (1968), "Seismic Source Characteristics from Explosion-Generated P Waves," BSSA, 58, pp. 1833-1848.
- Walck, M. C. and J. B. Minster (1981), "Relative Array Analysis of Upper Mantle Lateral Velocity Variations in Southern California," submitted to the JGR.
- Wiggins, R. A. (1972), "The General Linear Inverse Problem: Implication of Surface Waves and Free Oscillations for Earth Structure," Rev. Geophys., 10, pp. 251-285.
- Wiggins, R. A., K. L. Larner and R. D. Wisecup (1976), "Residual Statics Analysis as a General Linear Inverse Problem," Geophysics, 41, pp. 922-938.

APPENDIX A

STATION AND EVENT DATA BASES

TABLE A.1
STATION DATA BASE

The set of 369 seismograph stations recording 4484 P-wave arrivals at telseismic distances from 82 NTS explosions, ordered by station group and station code. Distance and azimuth are computed with respect to the approximate centroid of the NTS explosions (37.18°N , 116.27°W). The last column gives the number of P-wave arrivals reported from the 82 explosions.

**Best
Available
Copy**

STATION		LATITUDE DEGS MINS	LONGITUDE DEGS MINS	DISTANCE DEGREES	AZIMUTH DEGREES	A-O-I DEGREES	FLFVA. METERS	# EVENTS
CMC	NORTHWEST TERRITORY	67 50.00	-115 5.00	30.71	8.88	28.56	31	4
RES	NORTHWEST TERRITORY	74 41.03	-94 54.00	38.94	8.86	26.86	15	15
YMC	NORTHWEST TERRITORY	62 28.12	-114 28.07	25.34	1.95	30.04	198	26
BLC	NORTHWEST TERRITORY	64 19.00	-96 1.00	29.76	17.69	28.69	16	14
FCC	MANITOBA	58 45.12	-94 5.03	25.97	26.72	29.61	39	17
FBC	NORTHWEST TERRITORY	63 44.00	-68 28.00	38.96	31.62	26.86	45	24
FPB	CANADA	63 44.80	-68 32.80	38.93	31.58	26.87	18	15
GMC	QUEBEC	55 17.50	-77 45.20	31.67	42.71	29.37	8	7
SCH	LABRADOR	54 49.00	-66 47.00	37.72	45.99	27.15	540	20
AGM	MAINE	47 4.90	-69 1.40	35.92	58.80	27.58	238	2
CBM	MAINE	46 55.95	-68 7.25	36.54	59.02	27.43	250	7
SFA	QUEBEC	47 7.40	-70 49.60	34.69	58.76	27.84	232	12
SIC	QUEBEC	50 10.50	-66 44.50	37.42	53.61	27.72	283	17
SUD	ONTARIO	46 28.00	-80 58.00	27.70	59.24	28.90	267	5
AAM	MICHIGAN	42 17.98	-83 39.37	25.50	66.25	29.92	254	16
APT	CONNECTICUT	41 18.96	-72 3.83	34.20	69.12	27.93	3	6
BCT	CONNECTICUT	41 29.60	-73 23.03	33.20	69.03	28.12	69	4
BNH	NEW HAMPSHIRE	44 35.43	-71 15.38	34.47	63.24	27.88	472	15
BPT	CONNECTICUT	41 13.33	-73 14.53	33.33	69.50	28.10	83	6
ECT	CONNECTICUT	41 50.08	-73 24.68	33.14	68.42	28.13	342	1
EMH	MAINE	44 44.35	-67 29.37	37.14	62.62	27.29	20	9
FLR	MASSACHUSETTS	41 43.00	-71 7.29	34.85	68.25	27.80	52	2
HAL	NOVA SCOTIA	44 38.00	-63 36.00	39.90	62.25	26.64	56	18
HOM	CONNECTICUT	41 29.15	-72 31.39	33.84	68.90	28.00	24	5
HMH	NEW HAMPSHIRE	43 42.32	-72 17.13	33.79	64.90	28.01	180	7
INY	NEW YORK	42 26.63	-76 29.02	30.81	67.65	28.54	238	7
LND	ONTARIO	43 2.40	-81 11.00	27.33	66.63	29.00	246	1
MIM	MAINE	45 14.62	-69 2.42	36.00	61.97	27.56	140	10
MNT	QUEBEC	45 30.15	-73 37.38	32.76	61.70	28.19	112	37
OTT	ONTARIO	45 23.63	-75 42.95	31.29	61.90	28.44	83	15
PTN	NEW YORK	44 34.35	-74 58.97	31.81	63.47	28.34	278	7
RPO	NEW YORK	43 7.90	-77 32.32	30.00	66.37	28.67	141	1
ROC	NEW YORK	43 7.50	-77 35.54	29.96	66.38	28.67	155	7
TMT	CONNECTICUT	41 48.68	-72 47.93	33.59	68.37	28.75	290	5
UCT	CONNECTICUT	41 49.90	-72 15.03	34.00	68.24	27.97	149	6
WES	MASSACHUSETTS	42 23.08	-71 19.33	34.62	67.12	27.85	60	17
BGO	OHIO	41 22.68	-83 39.55	25.50	70.39	29.92	212	10
BLA	VIRGINIA	37 12.68	-80 25.27	28.45	78.92	28.80	634	20
CBN	VIRGINIA	38 12.30	-77 22.40	30.65	76.04	28.57	70	1
CLE	OHIO	41 29.46	-81 31.87	27.10	70.02	29.07	326	38
GEO	DISTRICT OF COLOMBIA	38 54.00	-77 4.00	30.76	74.62	28.55	43	9
MRG	WEST VIRGINIA	39 27.98	-79 57.27	28.44	73.79	28.80	282	27
NLM	MARYLAND	39 1.94	-76 58.83	30.81	74.35	28.54	114	1
PAL	NEW YORK	41 1.42	-73 54.52	32.86	70.01	28.17	103	5
PHI	PENNSYLVANIA	39 57.53	-75 10.50	32.05	72.19	28.30	5	1
PNJ	NEW JERSEY	40 54.43	-74 9.29	32.69	70.23	28.20	71	6
SCP	PENNSYLVANIA	40 47.70	-77 51.90	29.91	71.07	28.68	252	7
WAS	DISTRICT OF COLOMBIA	38 53.55	-77 1.98	30.79	74.63	28.54	1	1
WSC	MARYLAND	39 3.03	-77 7.42	30.70	74.35	28.56	100	16
ATL	GEORGIA	33 26.00	-84 20.25	26.26	88.59	28.44	27	4
BEC	BERMUDA	32 22.77	-64 40.87	42.22	80.64	26.10	41	6
CEH	NORTH CAROLINA	35 53.45	-79 5.57	29.78	81.10	28.69	102	7
CHC	NORTH CAROLINA	35 55.00	-79 3.00	29.81	81.04	28.69	144	10
CSC	SOUTH CAROLINA	34 1.00	-81 2.00	28.73	85.68	28.76	94	7
ORT	TENNESSEE	35 55.41	-84 18.71	25.64	80.08	28.82	102	10
HOJ	JAMAICA	18 1.12	-76 45.00	19.54	177.47	26.72	200	1

STH	JAMAICA	18	4.68	-76	48.84	79.45	177.57	26.74	427	1
AHU	EL SALVADOR	13	55.30	-29	50.75	33.03	127.50	28.14	0	1
ARZ	COSTA RICA	10	33.68	-84	57.60	38.77	125.10	26.91	763	1
AR6	COSTA RICA	10	26.38	-84	54.63	38.81	125.24	26.89	1000	1
AR8	COSTA RICA	10	11.55	-85	31.23	38.60	126.22	26.94	511	1
BHP	CANAL ZONE	8	57.65	-79	33.48	43.47	170.87	25.60	76	4
COM	MEXICO	16	15.20	-92	7.68	29.84	127.85	28.68	1528	5
LPS	EL SALVADOR	14	17.53	-89	9.72	33.19	126.21	28.12	1000	27
PBJ	MEXICO	16	26.20	-95	24.40	27.70	172.67	28.91	213	10
VHM	MEXICO	17	10.60	-96	44.72	26.33	133.93	29.40	1829	12
VMO	MEXICO	17	14.17	-96	43.93	26.29	133.83	29.42	1685	1
BAH	HAWAII	21	20.38	-158	8.63	39.40	258.26	26.75	0	1
HON	HAWAII	21	19.30	-158	8.50	39.36	258.18	26.76	24	10
HVO	HAWAII	19	25.40	-155	17.60	38.33	253.40	27.00	1240	8
KIP	HAWAII	21	25.40	-158	8.90	39.31	258.32	26.77	70	21
KKH	HAWAII	19	39.85	-156	8.53	38.74	254.34	26.91	0	1
KPH	HAWAII	21	34.57	-158	16.53	39.43	258.73	26.74	0	1
MOK	HAWAII	21	27.39	-157	44.19	39.07	258.14	26.83	0	2
AO-	ALASKA	51	52.50	-176	40.75	44.22	309.38	25.61	61	1
ADA	ALASKA	51	51.80	-176	39.30	44.21	309.36	25.61	0	1
ADK	ALASKA	51	53.02	-176	34.82	44.16	309.38	25.63	0	31
NIK	ALASKA	52	58.46	-168	51.18	39.40	310.82	26.75	207	7
PMA	ALASKA	55	58.72	-160	29.83	34.98	316.85	27.77	314	2
ANV	ALASKA	64	33.93	-165	22.30	39.78	329.32	26.67	330	1
BIG	ALASKA	59	23.40	-155	13.00	33.40	324.24	28.79	562	14
KDC	ALASKA	57	44.87	-152	29.50	31.42	322.56	28.42	0	20
MTD	ALASKA	59	25.67	-146	20.33	29.48	328.64	28.71	37	1
SV-	ALASKA	61	6.49	-155	37.10	34.31	326.89	27.91	762	19
TTA	ALASKA	62	55.80	-156	1.32	35.31	329.59	27.71	914	6
BLR	ALASKA	63	30.10	-145	50.70	31.85	325.19	28.34	792	11
COL	ALASKA	64	54.00	-147	47.60	33.42	326.11	28.08	370	59
FYU	ALASKA	66	33.63	-145	13.60	33.79	339.62	28.21	177	8
GIL	ALASKA	64	58.50	-147	29.70	33.37	336.37	28.09	350	36
GPA	ALASKA	65	25.72	-161	17.92	38.47	331.64	26.97	860	16
JMA	ALASKA	66	4.11	-153	40.72	36.08	325.11	27.54	1390	5
MCS	ALASKA	64	43.70	-147	13.60	33.12	336.16	28.13	200	1
PJO	ALASKA	65	2.10	-147	30.50	33.42	326.44	28.08	740	19
PMR	ALASKA	61	35.53	-149	7.85	31.86	330.56	28.33	0	38
PNL	ALASKA	59	40.12	-139	23.82	26.97	323.92	29.12	579	1
SCM	ALASKA	61	50.00	-147	19.70	31.31	321.90	28.44	1070	19
TNN	ALASKA	65	15.40	-151	54.70	35.01	324.69	27.77	504	14
TOA	ALASKA	62	6.29	-146	10.34	31.06	322.96	28.49	909	5
BTZ	ALASKA	69	37.40	-145	53.70	36.22	342.96	27.51	1100	6
BRW	ALASKA	71	18.20	-156	48.90	40.05	341.01	26.61	0	27
INX	NORTHWEST TERRITORY	68	17.08	-123	38.00	72.60	348.19	28.71	46	10
MBC	NORTHWEST TERRITORY	76	14.08	-119	21.10	39.18	358.83	26.91	15	56
NP-	CANADA	76	15.13	-119	22.30	39.19	358.63	26.80	54	23
ALE	NORTHWEST TERRITORY	82	29.00	-62	24.00	48.81	8.12	24.44	65	42
DAG	GREENLAND	76	46.20	-18	46.20	55.84	16.02	22.74	16	23
ILG	GREENLAND	77	56.80	-79	11.00	51.26	15.23	23.64	2401	6
NOR	GREENLAND	81	36.00	-16	41.00	54.86	10.21	22.97	76	30
GDN	GREENLAND	69	15.00	-53	32.00	46.16	26.05	25.12	23	39
STJ	NEWFOUNDLAND	47	34.05	-52	44.00	46.86	56.19	24.94	62	10
ANG	ANTIGUA	17	9.30	-61	49.82	51.65	97.36	27.74	23	2
DCM	DOMINICA	15	17.75	-61	23.47	53.08	98.98	23.41	15	1
MWI	MONTSEPRAT	16	42.76	-62	13.31	51.59	98.09	23.76	46	5
SCG	GUADLOUPE	16	1.77	-61	40.93	52.40	98.43	23.56	646	2
SJG	PUERTO RICO	19	6.70	-66	9.00	47.70	99.35	24.73	457	41
SKI	ST. KITTS	17	20.00	-62	44.34	50.87	97.87	23.94	376	6
CAR	VENEZUELA	10	70.40	-66	55.66	51.67	177.87	27.75	1075	47
CUM	VENEZUELA	10	27.90	-64	10.17	53.76	125.79	23.24	0	7
GRE	GREENADA	10	2.82	-61	44.76	54.67	172.46	23.02	15	6
SIR	VENEZUELA	10	30.50	-66	30.50	51.54	127.56	27.67	1000	4
TPN	TRINIDAD	10	78.93	-61	24.17	55.79	173.55	27.75	24	27
BCR	COLOMBIA	7	1.17	-73	10.58	49.31	116.58	24.72	77	7
BCG	COLOMBIA	4	37.38	-74	3.90	50.36	119.67	24.76	260	14

FUQ	COLOMBIA	5	26.20	-73	44.73	49.90	118.57	24.15	256	4
GAL	COLOMBIA	10	47.12	-75	15.73	45.24	114.79	25.76	21	0
SGV	VENEZUELA	8	53.17	-70	38.00	49.69	112.54	24.17	1590	4
TOV	VENEZUELA	9	47.22	-69	47.55	49.93	110.95	24.17	650	0
UAV	VENEZUELA	8	36.60	-71	8.68	49.70	113.25	24.22	1600	9
CHN	COLOMBIA	4	58.00	-75	37.00	49.04	120.75	24.39	1360	4
PSO	COLOMBIA	1	11.52	-77	19.52	50.69	125.69	23.98	7010	7
QUI	ECUADOR	0	12.08	-78	30.03	51.00	128.00	23.90	2837	10
MOY	MIDWAY ISLANDS	28	12.40	-177	20.00	51.39	276.73	23.81	0	1
SMY	ALASKA	52	43.30	174	7.20	49.70	311.61	24.22	46	1
NBS	SPITSBERGEN	78	55.05	11	55.43	60.34	10.09	21.66	46	40
AKU	ICELAND	65	41.20	-18	6.40	59.95	28.26	21.75	24	17
KTG	GREENLAND	70	25.00	-21	59.00	56.80	23.67	22.48	6	60
REY	ICELAND	64	8.33	-21	54.37	59.06	30.66	21.95	44	6
SIO	ICELAND	63	47.15	-18	3.50	60.76	30.25	21.97	26	2
ADH	AZORES	38	39.30	-27	14.10	67.37	58.02	20.13	83	1
MOR	AZORES	38	31.80	-28	37.80	66.48	58.73	20.32	58	1
MUA	PERU	-12	2.30	-75	19.37	62.26	133.58	21.24	7313	11
LM2	PERU	-12	5.10	-77	3.50	61.30	135.18	21.45	0	1
NNA	PERU	-11	59.25	-76	50.53	61.35	134.92	21.44	575	0
RKT	FRENCH POLYNESIA	-23	7.18	-134	58.40	62.51	199.44	21.19	100	7
AFR	FRENCH POLYNESIA	-17	32.30	-149	46.67	62.92	216.27	21.10	50	18
PAE	FRENCH POLYNESIA	-17	39.72	-149	34.80	62.94	216.02	21.09	40	17
PMO	FRENCH POLYNESIA	-15	.22	-147	53.83	59.84	215.88	21.77	2	18
PPN	TAHITI	-17	31.85	-149	25.93	62.76	215.95	21.13	0	25
PPT	TAHITI	-17	34.13	-149	34.53	62.86	216.06	21.11	300	32
RUV	FRENCH POLYNESIA	-15	11.33	-147	23.03	59.77	215.28	21.79	3	16
TMT	TAHITI	-17	34.14	-149	34.45	62.85	216.06	21.11	337	3
TPT	TAHITI	-14	59.13	-147	37.18	59.70	215.62	21.81	0	27
TVO	FRENCH POLYNESIA	-17	46.95	-149	15.10	62.89	215.64	21.10	660	10
VAH	FRENCH POLYNESIA	-15	14.33	-147	37.87	59.92	215.49	21.76	3	19
KEV	FINLAND	69	45.35	27	.75	70.05	12.79	19.49	80	22
KIR	SWEDEN	67	50.40	20	25.00	70.35	16.04	19.40	390	61
KJF	FINLAND	64	11.95	27	42.88	75.03	15.45	18.19	160	0
KJN	FINLAND	64	5.12	27	42.72	75.13	15.51	18.17	250	52
KRK	NORWAY	69	43.45	30	3.75	70.59	11.82	19.33	0	16
NUR	FINLAND	60	30.54	24	39.09	77.52	18.63	17.59	102	39
QUL	FINLAND	65	5.12	25	53.78	73.87	15.69	19.47	50	40
SOD	FINLAND	67	22.27	26	37.74	72.04	14.21	18.92	181	42
TRO	NORWAY	69	37.95	18	55.66	68.58	15.37	19.45	15	35
UME	SWEDEN	63	48.90	20	14.20	73.61	18.56	18.43	16	50
APP	SWEDEN	60	32.43	13	55.77	74.44	22.00	18.33	354	5
BER	NORWAY	60	23.22	5	19.55	71.67	26.47	19.02	50	17
COP	DENMARK	55	41.00	12	26.00	77.70	26.97	17.55	13	10
DEL	SWEDEN	56	28.20	13	52.00	77.60	25.75	17.57	150	0
GOT	SWEDEN	57	41.90	11	58.70	75.99	25.76	17.97	66	10
HFS	SWEDEN	60	8.02	13	41.73	74.68	23.44	18.28	223	17
KON	NORWAY	59	39.95	9	37.90	73.70	25.37	18.51	200	61
LHN	NORWAY	61	2.95	10	52.80	73.00	23.92	18.66	505	00
SKA	SWEDEN	63	34.80	12	16.90	71.61	21.64	19.04	580	17
SLL	SWEDEN	60	28.62	13	19.37	74.30	23.36	18.37	400	6
UOD	SWEDEN	60	5.40	13	36.40	74.69	23.50	18.27	240	15
UPP	SWEDEN	59	51.50	17	37.60	76.11	22.00	17.94	14	61
DBN	NETHERLANDS	52	6.17	5	10.60	77.49	32.62	17.60	3	7
OUR	ENGLAND	54	46.00	-1	35.00	72.72	33.47	18.75	103	14
EAB	SCOTLAND	56	11.28	-4	20.40	70.60	33.36	19.33	250	7
EAU	SCOTLAND	55	50.67	-3	27.28	71.20	33.31	19.16	350	1
EBH	SCOTLAND	56	14.88	-3	30.48	70.97	33.07	19.24	375	7
EGL	SCOTLAND	55	51.70	-2	44.30	71.51	33.03	19.07	245	1
EKA	SCOTLAND	55	19.98	-3	9.55	71.66	33.62	19.02	263	24
ESK	SCOTLAND	55	19.00	-3	12.30	71.65	33.65	19.03	242	17
FLN	FRANCE	48	45.75	0	29.92	77.27	27.66	17.67	270	53
GPR	FRANCE	48	23.30	0	51.50	77.29	28.12	17.65	202	50
KFW	ENGLAND	51	28.10	0	18.78	75.47	25.52	18.10	1	0
LPF	FRANCE	48	1.89	-1	2.45	77.44	26.47	17.61	150	16
SGR	FRANCE	47	42.56	0	55.38	77.71	26.66	17.74	0	7

SSC	FRANCE	48	35.65	0	6.45	77.50	77.60	17.59	570	54
VAL	IRELAND	51	56.37	-10	15.65	70.35	75.19	19.40	14	0
WIT	NETHERLANDS	52	48.80	6	40.18	77.61	71.44	17.57	1	25
PIO	PORTUGAL	41	8.32	-8	36.13	77.80	47.42	17.52	86	14
CCH	BOLIVIA	-17	22.93	-66	8.57	71.92	129.57	18.95	2500	4
ANT	CHILE	-23	42.30	-70	28.92	74.37	136.92	18.35	80	17
ARE	PERU	-16	27.72	-71	29.45	68.00	133.21	19.08	2452	44
CAC	CHILE	-22	28.79	-69	1.57	74.17	135.10	18.40	2000	1
LPB	BOLIVIA	-16	31.96	-68	5.90	70.08	130.52	19.48	2292	37
PNS	BOLIVIA	-16	16.03	-68	28.40	69.64	130.64	17.59	1986	37
SLN	CHILE	-23	9.23	-69	36.67	74.38	135.97	18.35	1350	1
TRJ	BOLIVIA	-21	30.78	-64	46.57	75.89	131.30	17.99	2100	5
RAR	COOK ISLANDS	-21	12.75	-159	46.40	71.09	222.77	19.19	29	7
AUI	SAMOA ISLANDS	-13	54.56	-171	46.64	72.81	236.91	18.72	706	8
NUE	COOK ISLANDS	-19	4.58	-169	55.68	75.40	231.93	18.11	56	4
HSS	JAPAN	42	57.88	141	13.95	73.64	311.67	18.52	215	7
KMU	HOKKAIDO	42	14.32	142	58.03	73.01	310.29	18.67	195	14
ANK	TURKEY	39	55.00	32	49.00	98.19	23.53	14.48	0	1
BPA	CZECHOSLOVAKIA	48	10.10	17	6.30	85.42	29.22	15.46	270	31
BUC	GDP	50	52.43	13	56.75	92.02	29.25	16.44	296	7
BRG	ROMANIA	44	24.82	26	5.80	91.93	25.97	14.63	82	1
CIN	TURKEY	37	36.00	28	5.20	98.62	27.92	14.47	0	2
CLL	EAST GERMANY	51	18.54	13	.26	81.31	29.44	16.63	230	47
DEV	ROMANIA	45	53.00	22	54.20	99.52	27.18	14.74	250	1
DMK	TURKEY	41	49.30	27	45.43	94.78	26.14	14.57	315	1
EZN	TURKEY	39	49.55	26	19.52	96.01	28.06	14.53	50	7
HLE	EAST GERMANY	51	29.88	11	57.41	80.75	29.84	16.76	92	6
IAS	ROMANIA	47	11.60	27	33.70	89.98	23.74	14.70	160	1
ISK	TURKEY	41	3.93	29	3.55	95.91	25.62	14.53	172	4
IST	TURKEY	41	2.73	28	59.75	95.90	25.68	14.53	50	1
KAS	TURKEY	41	22.30	33	46.00	97.16	22.27	14.50	700	1
KDZ	BULGARIA	41	38.47	25	21.00	94.07	27.81	14.58	329	5
KLS	SWEDEN	56	9.00	15	35.50	78.44	25.18	17.36	11	7
KRA	POLAND	50	3.37	19	56.78	94.93	26.61	15.59	223	14
NIE	POLAND	49	25.42	20	19.32	95.59	26.75	15.42	555	25
PLG	GREECE	40	22.42	23	26.73	94.43	29.70	14.57	580	1
PRA	CZECHOSLOVAKIA	50	4.22	14	25.98	92.85	29.50	16.21	225	1
PPU	CZECHOSLOVAKIA	49	59.30	14	32.50	92.96	29.49	16.18	300	46
PSZ	HUNGARY	47	55.17	19	53.67	96.69	27.82	15.21	940	1
PVL	BULGARIA	43	8.80	25	10.30	92.70	27.18	14.62	197	4
SPC	CZECHOSLOVAKIA	49	11.33	20	14.70	85.76	26.92	15.38	1772	7
VPO	CZECHOSLOVAKIA	47	48.80	18	18.80	86.18	26.76	15.30	150	10
SAY	YUGOSLAVIA	41	19.26	22	34.20	93.28	29.77	14.61	168	4
VIE	AUSTRIA	48	14.90	16	21.70	95.07	29.58	15.55	196	9
VKA	AUSTRIA	48	15.90	16	19.10	85.04	29.59	15.56	400	24
ZST	CZECHOSLOVAKIA	48	11.77	17	6.15	85.40	29.21	15.46	250	7
ARM	FRANCE	45	.58	1	18.70	80.69	39.58	16.76	320	9
ATH	GREECE	37	58.33	23	43.00	96.59	30.77	14.52	5	2
AVF	FRANCE	46	47.43	3	21.16	80.45	37.28	16.84	225	1
BAF	FRANCE	47	50.08	6	59.72	81.40	34.74	16.60	1070	2
BAS	SWITZERLAND	47	32.40	7	34.97	81.89	34.64	16.48	309	2
BES	FRANCE	47	14.98	5	59.25	81.37	35.64	16.61	311	9
BMG	FRG	47	43.28	12	52.73	84.07	31.77	15.85	475	4
BNS	WEST GERMANY	50	57.83	7	10.63	79.18	32.50	17.16	200	47
BSF	FRANCE	47	50.00	6	47.63	81.31	34.84	16.63	1200	27
BUH	WEST GERMANY	48	40.53	8	13.71	81.32	33.55	16.62	750	17
CDL	FRANCE	48	23.65	7	16.24	81.11	34.22	16.67	1100	25
CDR	FRANCE	47	40.50	5	46.02	83.88	36.20	15.91	366	7
CFF	FRANCE	45	45.77	3	6.15	81.06	36.14	16.69	400	7
DOU	BELGIUM	50	5.76	4	35.65	78.67	34.32	17.39	224	31
FEL	WEST GERMANY	47	52.20	6	1.00	81.84	34.00	16.49	1495	7
FUR	WEST GERMANY	48	9.97	11	16.58	83.04	32.37	16.16	545	34
GAP	FRG	47	28.60	11	7.87	83.48	32.88	16.73	708	7
GEN	ITALY	44	25.09	8	55.80	84.85	36.01	15.61	53	1
GIP	BELGIUM	50	35.53	5	58.45	78.97	33.37	17.33	1	1
GRC	FRANCE	47	17.74	3	4.42	79.96	37.06	16.96	191	10

GRF	WEST GERMANY	49	41.52	11	17.70	91.84	71.38	16.49	575	10
HAU	FRANCE	48	.32	6	21.00	90.98	74.94	16.70	570	14
HEE	NETHERLANDS	50	53.10	5	59.90	76.72	73.11	17.26	115	11
HEI	WEST GERMANY	40	23.92	8	43.58	81.01	32.81	16.70	560	5
HOF	FRG	50	18.82	11	52.65	81.63	30.64	16.55	566	2
ISO	FRANCE	44	11.00	7	3.00	84.13	37.18	15.83	870	27
JAN	GREECE	39	39.40	20	51.05	93.98	31.78	14.58	540	1
KHC	CZECHOSLOVAKIA	49	7.85	13	34.70	83.25	70.52	16.10	700	54
KRL	WEST GERMANY	49	.65	8	24.73	81.16	33.27	16.66	114	17
LBF	FRANCE	46	59.07	3	58.63	80.61	76.83	16.80	715	26
LFF	FRANCE	44	56.25	0	44.18	80.45	39.92	16.84	190	17
LJU	YUGOSLAVIA	46	2.60	14	32.00	86.09	31.90	15.31	396	1
LNR	FRANCE	43	20.00	6	30.55	94.50	38.05	15.72	270	11
LNS	FRANCE	45	17.33	6	54.88	83.25	36.51	16.10	1480	19
LOR	FRANCE	47	16.00	3	51.08	80.35	36.70	16.87	530	63
LPO	FRANCE	44	41.00	1	11.23	80.85	39.88	16.74	320	17
LRG	FRANCE	43	27.25	6	21.63	84.33	38.05	15.77	100	12
LSF	FRANCE	46	15.00	1	31.77	79.93	78.57	16.97	470	14
LUX	LUXEMBOURG	49	26.00	6	8.00	79.72	33.94	17.02	0	1
MFF	FRANCE	46	36.13	0	8.75	78.85	79.12	17.25	270	19
MNY	FRANCE	44	57.63	5	41.47	82.90	37.37	16.20	0	7
MOA	AUSTRIA	47	50.97	14	15.96	84.54	30.95	15.71	572	12
MOX	WEST GERMANY	50	38.77	11	36.97	81.27	30.56	16.64	454	32
MZF	FRANCE	46	12.93	2	35.03	80.48	38.07	16.84	490	1
OMR	YUGOSLAVIA	41	6.68	20	47.93	92.74	71.02	14.62	739	2
RAV	WEST GERMANY	47	47.00	9	36.83	82.61	33.44	16.28	460	1
RJF	FRANCE	45	18.27	1	30.98	80.59	39.26	16.81	410	9
RMP	ITALY	41	48.67	12	42.14	88.62	35.55	14.85	380	4
RSL	FRANCE	45	41.30	6	37.53	82.81	36.39	16.22	1583	12
SKO	YUGOSLAVIA	41	58.32	21	26.37	92.27	30.15	14.62	346	9
SMF	FRANCE	46	38.72	3	50.47	80.79	37.14	16.75	459	1
SPF	FRANCE	43	33.83	6	41.77	84.42	37.79	15.74	340	17
SSB	FRANCE	45	16.75	4	32.51	82.11	37.75	16.42	700	2
SSF	FRANCE	47	3.68	3	30.41	80.37	37.01	16.87	360	61
STB	FRG	50	35.72	6	50.40	79.30	32.91	17.13	270	2
STR	FRANCE	48	35.08	7	45.95	81.19	73.84	16.65	125	18
STU	WEST GERMANY	48	46.25	9	11.60	81.68	73.00	16.53	375	14
TCF	FRANCE	46	17.28	2	12.83	80.25	38.21	16.89	640	25
TNS	WEST GERMANY	50	13.42	8	26.93	80.27	72.39	16.89	815	2
TPI	ITALY	45	42.53	13	45.85	86.07	72.54	15.73	106	7
VLS	GREECE	38	10.60	20	35.78	95.10	72.76	14.56	375	1
VOU	FRANCE	46	23.93	5	39.05	81.83	76.40	15.49	0	7
WET	FRG	49	8.72	12	52.80	82.95	30.87	16.18	613	2
WLS	FRANCE	48	24.77	7	21.22	81.14	74.16	16.67	775	11
WBM	BELGIUM	49	50.00	5	22.83	79.21	74.14	17.15	242	4
WTS	NETHERLANDS	51	59.73	6	48.60	76.27	71.95	17.40	43	1
ZAG	YUGOSLAVIA	45	49.00	15	59.00	86.89	31.27	15.17	155	1
ALI	SPAIN	38	21.32	0	29.23	84.37	45.35	15.77	75	11
ALM	SPAIN	36	51.15	-2	27.59	84.22	47.57	15.80	65	4
BOB	FRANCE	43	3.90	0	8.90	81.42	41.59	16.60	561	5
COI	PORTUGAL	40	12.40	-8	25.10	78.50	48.07	17.34	140	4
EBR	SPAIN	40	49.23	0	29.60	83.17	43.04	16.12	50	16
LIS	PORTUGAL	38	42.99	-9	8.95	79.00	49.61	17.71	77	17
MAL	SPAIN	36	43.65	-4	24.67	83.14	48.68	16.13	60	4
MTE	PORTUGAL	40	24.20	-7	32.20	78.89	47.48	17.24	815	7
SET	ALGERIA	36	12.00	5	24.00	89.16	43.51	14.78	1070	7
SFS	SPAIN	36	27.70	-6	12.33	82.23	49.84	16.36	24	1
TOL	SPAIN	39	52.88	-4	2.92	81.26	46.11	16.64	480	5
AVE	MOROCCO	32	17.88	-7	24.83	83.52	52.91	15.71	270	17
BAB	ALGERIA	30	7.28	-2	11.17	88.97	50.20	14.80	0	5
IFR	MOROCCO	33	30.99	-5	7.63	84.87	51.48	15.62	1670	21
KES	MOROCCO	31	59.70	-4	27.70	96.27	52.24	15.26	1124	7
RBA	MOROCCO	34	.57	-6	50.43	83.44	52.05	16.74	70	7
RBZ	MOROCCO	33	55.75	-6	50.40	83.49	52.11	16.70	110	7
TAM	ALGERIA	22	47.50	5	31.40	99.01	50.59	14.45	1205	17
TEN	CANARY ISLANDS	28	27.86	-16	14.73	90.67	61.40	16.80	1	1

KDS	SENEGAL	12	74.12	-12	12.67	93.40	71.59	14.60	110	1
KIC	IVORY COAST	6	21.63	-4	44.47	103.01	71.61	14.77	175	6
LIC	IVORY COAST	6	13.47	-5	1.67	102.68	71.91	14.77	100	4
MBO	SENEGAL	14	23.45	-16	57.28	86.66	73.04	14.85	3	7
BAE	BRAZIL	-15	50.47	-47	49.20	83.16	115.63	16.12	1270	7
BAO	BRAZIL	-15	38.09	-47	59.49	80.90	115.58	16.20	1011	6
BDF	BRAZIL	-15	39.83	-47	54.20	82.98	115.55	16.17	1260	1
CEN	ARGENTINA	-31	34.55	-68	45.25	91.55	140.48	16.57	900	13
LVV	CHILE	-33	57.33	-71	24.65	82.18	143.72	16.40	3	1
MOZ	ARGENTINA	-32	53.00	-68	51.00	82.55	141.33	16.70	826	11
MEN	ARGENTINA	-32	54.30	-66	51.85	82.56	141.35	16.29	267	2
PEL	CHILE	-33	8.62	-70	41.12	81.66	142.75	16.49	690	6
SAN	CHILE	-33	27.18	-70	39.70	82.12	142.91	16.41	533	3
HJZ	NEW ZEALAND	-43	59.23	170	27.97	104.50	225.56	14.34	1000	1
MNG	NEW ZEALAND	-40	37.12	175	28.92	99.49	225.80	14.44	396	3
KOU	NEW CALEDONIA	-20	33.72	164	16.86	94.19	247.47	14.58	17	7
LMP	NEW HEBRIDES	-16	25.53	167	48.02	89.01	246.60	14.80	60	4
LVN	NEW HEBRIDES	-15	51.12	166	9.60	86.38	246.82	14.89	6	4
LUG	NEW HEBRIDES	-15	31.07	167	7.90	88.94	246.71	14.81	150	5
NDF	FIJI	-17	45.41	177	27.00	82.89	241.55	16.20	70	6
NOU	NEW CALEDONIA	-22	18.60	166	27.03	93.68	244.85	14.59	105	6
QUA	LOYALTY ISLANDS	-20	46.48	167	14.63	92.15	245.58	14.63	29	4
PVC	NEW HEBRIDES	-17	44.40	168	18.72	89.46	247.28	14.74	80	5
VUN	FIJI ISLANDS	-18	2.56	178	27.82	82.37	240.68	16.34	160	2
HNR	SOLOMON ISLANDS	-9	25.93	159	56.83	90.72	258.80	14.66	72	7
ESA	D'ENTRECASTEAUX IS	-9	44.30	150	48.84	98.12	263.97	14.46	46	1
KOA	SOLOMON ISLANDS	-6	13.45	155	37.14	92.22	263.93	14.63	65	2
KRT	NEW BRITAIN	-4	21.17	152	3.10	93.94	267.55	14.58	20	1
PMG	PAPUA	-9	24.55	147	9.23	100.84	266.40	14.41	70	1
RAB	NEW BRITAIN	-4	11.48	152	10.19	93.75	267.61	14.59	184	3
RAL	NEW BRITAIN	-4	13.22	152	12.12	93.74	267.57	14.59	91	2
TAV	NEW BRITAIN	-4	13.87	152	13.22	93.73	267.55	14.59	31	2
VUL	NEW BRITAIN	-4	16.97	152	8.74	93.82	267.55	14.59	332	2
WAN	NEW BRITAIN	-4	11.66	152	10.54	93.75	267.60	14.59	25	1
GUA	MARIANA ISLANDS	13	32.10	144	54.70	88.81	286.00	14.83	230	3
ABU	HONSHU	34	51.53	135	34.37	82.09	307.91	16.42	200	6
BAG	PHILIPPINES	16	24.65	120	34.78	104.49	303.91	14.34	1507	2
DDR	HONSHU	35	59.90	139	11.60	79.08	306.92	17.19	800	30
KYS	HONSHU	35	11.86	140	8.89	78.95	305.79	17.22	230	17
MAT	HONSHU	36	32.50	138	12.53	79.36	307.86	17.12	440	37
OIS	HONSHU	34	6.32	135	19.64	82.73	307.47	16.25	678	9
OYM	JAPAN	35	25.20	139	14.56	79.40	306.44	17.11	600	3
SHK	HONSHU	34	31.93	132	40.65	84.11	309.23	15.84	255	25
SRT	HONSHU	34	10.57	135	44.76	82.42	307.30	16.33	470	2
SRY	HONSHU	35	36.50	139	16.45	79.26	306.57	17.14	254	14
TSK	HONSHU	36	12.65	140	6.58	78.36	306.63	17.37	280	26
WU	HONSHU	34	11.27	135	10.38	82.77	307.61	16.23	10	11
SEO	SOUTH KOREA	37	34.00	126	58.00	85.44	314.62	15.45	86	13
KBL	AFGHANISTAN	34	32.45	69	2.59	108.48	355.38	14.26	1920	3

TABLE A.2
EVENT DATA BASE

The set of 82 NTS explosions for which travel-time residuals were determined at the 369 teleseismic stations listed in Table A.1. The first column lists an event identification number. The last column gives the number of P-wave arrivals reported for each event.

EVENT	DATE	TIME HR MIN SEC	LATITUDE DEG MIN SEC	LONGITUDE DEG MIN SEC	DEPTH (KM)	ELEVATION (M)	# STATIONS
*0001	64/01/16	16:00: .15	37 8 32.2	-116 2 56.8	.49	1289.	9
*0009	65/03/26	15:34: 8.16	37 8 51.4	-116 2 34.4	.54	1297.	14
*0017	65/12/16	19:15: .04	37 4 21.2	-116 1 44.8	.50	1250.	21
*0035	66/05/06	15:00: .08	37 20 52.8	-116 19 19.0	.67	2091.	34
*0037	66/05/13	13:30: .04	37 5 12.7	-116 2 .4	.55	1267.	23
*0038	66/05/19	13:56:29.14	37 6 40.1	-116 3 28.5	.67	1278.	68
*0039	66/05/27	20:00: .04	37 10 42.2	-116 5 51.9	.74	1406.	12
*0040	66/06/02	15:30: .09	37 13 37.4	-116 3 19.9	.46	1551.	64
*0041	66/06/03	14:00: .04	37 4 6.4	-116 2 7.1	.56	1248.	65
*0044	66/06/30	22:15: .07	37 18 56.9	-116 17 56.3	.82	2069.	99
*0053	66/12/20	15:30: .08	37 18 7.4	-116 24 29.9	1.21	1972.	173
*0054	67/01/19	16:45: .14	37 8 37.2	-116 8 6.7	.76	1452.	27
*0055	67/01/20	17:40: 3.41	37 5 59.5	-116 0 13.8	.56	1332.	14
*0058	67/02/23	18:50: .10	37 7 36.7	-116 3 59.0	.73	1297.	74
*0064	67/05/20	15:00: .10	37 7 49.4	-116 3 50.2	.75	1297.	101
*0065	67/05/23	14:00: .04	37 16 30.3	-116 22 11.9	.98	2260.	92
*0066	67/05/26	15:00: 1.50	37 14 52.6	-116 28 48.6	.63	1905.	76
*0068	67/06/26	16:00: .10	37 12 7.6	-116 12 28.2	.37	2225.	7
*0074	67/09/07	13:45: .10	37 9 11.4	-116 3 10.0	.52	1297.	12
*0075	67/09/27	17:00: .04	37 5 55.6	-116 3 11.6	.67	1267.	43
*0076	67/10/18	14:30: .10	37 6 56.1	-116 3 27.4	.71	1281.	68
*0083	68/02/21	15:30: .10	37 6 59.6	-116 3 13.3	.64	1279.	70
*0084	68/02/29	17:08:30.04	37 11 8.6	-116 12 41.2	.41	2287.	16
*0086	68/03/22	15:00: .04	37 19 57.4	-116 18 38.4	.67	2062.	61
*0089	68/04/18	14:05: .10	37 9 9.1	-116 2 13.2	.49	1706.	19
*0091	68/04/26	15:00: .10	37 17 43.5	-116 27 20.5	1.16	1941.	147
*0094	68/06/15	13:59:59.97	37 15 53.7	-116 16 52.7	.66	2147.	92
*0095	68/06/28	12:22: .10	37 14 43.8	-116 28 58.3	.61	1903.	43
*0098	68/08/29	22:45: .04	37 15 1.2	-116 20 48.8	.73	2083.	96
*0099	68/09/06	14:00: .13	37 8 9.8	-116 2 49.8	.58	1286.	49
*0100	68/09/17	14:00: .04	37 7 11.5	-116 7 38.9	.47	1796.	9
*0101	68/09/24	17:05: .09	37 12 17.2	-116 12 23.0	.23	2191.	12
*0105	68/11/20	18:00: .03	37 0 35.4	-116 12 23.1	.71	1958.	16
*0107	68/12/08	16:00: .14	37 20 36.3	-116 33 57.1	.11	1695.	11
*0109	68/12/19	16:30: .04	37 13 53.3	-116 28 24.9	1.40	1914.	173
*0111	69/01/15	19:30: .04	37 12 32.9	-116 13 31.4	.52	2290.	75
*0112	69/01/30	15:00: .04	37 3 11.9	-116 1 45.7	.45	1230.	6
*0115	69/05/07	13:45: .04	37 16 58.4	-116 30 2.7	.60	1855.	57
*0116	69/05/27	14:15: .04	37 4 30.4	-116 59 47.1	.51	1297.	71
*0119	69/07/16	14:55: .04	37 8 22.3	-116 5 14.9	.55	1327.	57
*0123	69/09/16	14:30: .04	37 18 50.9	-116 27 38.4	1.16	1925.	140
*0124	69/10/08	14:30: .14	37 15 24.2	-116 26 26.7	.62	1991.	61
*0127	69/10/29	22:01:51.43	37 8 35.9	-116 3 49.8	.62	1310.	56
*0128	69/11/21	14:52: .04	37 1 52.2	-116 0 7.4	.79	1722.	16
*0129	69/12/17	15:00: .04	37 5 1.7	-116 0 5.7	.55	1701.	46
*0132	70/02/04	17:00: .04	37 5 53.1	-116 1 35.4	.55	1796.	59
*0134	70/02/25	14:28:38.04	37 2 12.0	-116 59 58.5	.41	1232.	30
*0136	70/03/23	23:05: .04	37 5 10.4	-116 1 16.0	.56	1278.	51
*0137	70/03/26	19:00: .20	37 18 1.7	-116 32 2.8	1.21	1799.	144
*0142	70/05/21	14:15: .04	37 4 14.9	-116 0 46.9	.48	1264.	15
*0143	70/05/26	15:00: .05	37 6 48.1	-116 3 44.4	.53	1277.	70
*0148	70/12/16	16:00: .17	37 8 34.4	-116 2 2.4	.29	1297.	32
*0149	70/12/17	16:05: .16	37 7 44.0	-116 4 58.8	.56	1711.	70
*0150	71/06/23	15:30: .04	37 1 19.1	-116 1 21.6	.46	1217.	1
*0151	71/06/24	14:00: .16	37 8 48.1	-116 4 .6	.52	1714.	11
*0153	71/07/08	14:00: .08	37 6 36.4	-116 3 5.1	.53	1777.	7

*0154	71/08/18	14:00:	.03	37	3	25.9	-116	2	17.8	.53	1233.	70
*0157	72/09/21	15:30:	.19	37	4	55.4	-116	2	11.6	.56	1252.	73
*0159	73/03/08	16:10:	.19	37	6	12.9	-116	1	26.2	.57	1708.	71
*0161	73/04/26	17:15:	.16	37	7	23.0	-116	3	37.6	.56	1265.	40
*0162	73/06/06	13:00:	.08	37	14	42.7	-116	20	45.7	1.06	2095.	77
*0164	74/07/10	16:00:	.10	37	4	3.1	-116	1	54.6	.64	1250.	40
*0165	74/08/30	15:00:	.20	37	9	8.9	-116	4	59.9	.66	1325.	30
*0167	75/02/28	15:15:	.20	37	6	22.3	-116	3	22.6	.71	1280.	65
*0169	75/05/14	14:00:	.40	37	13	14.8	-116	26	27.0	.77	1907.	81
*0170	75/06/03	14:20:	.20	37	20	24.2	-116	31	22.4	.73	1694.	39
*0171	75/06/03	14:40:	.10	37	5	41.4	-116	2	10.0	.64	1274.	59
*0172	75/06/26	12:30:	.20	37	16	44.1	-116	22	6.9	1.71	2060.	79
*0173	75/10/28	14:30:	.20	37	17	24.2	-116	24	41.6	1.27	1984.	26
*0174	75/11/20	15:00:	.10	37	13	29.8	-116	22	3.2	.82	2053.	70
*0176	76/01/03	19:15:	.20	37	17	47.6	-116	19	59.5	1.45	2109.	117
*0177	76/02/04	14:20:	.10	37	4	9.3	-116	1	48.6	.64	1245.	40
*0178	76/02/04	14:40:	.20	37	6	23.7	-116	2	14.7	.66	1285.	48
*0179	76/02/12	14:45:	.20	37	16	17.1	-116	29	16.4	1.22	1864.	121
*0180	76/02/14	11:30:	.20	37	14	33.5	-116	25	12.8	1.17	1974.	66
*0181	76/03/09	14:00:	.10	37	18	35.9	-116	21	51.2	.87	2053.	60
*0182	76/03/14	12:30:	.20	37	18	21.6	-116	28	17.3	1.27	1931.	108
*0183	76/03/17	14:15:	.10	37	15	21.2	-116	18	42.9	.86	2103.	76
*0184	76/03/17	14:45:	.10	37	6	26.2	-116	3	8.9	.78	1271.	71
*0188	76/12/28	18:00:	.10	37	6	1.8	-116	2	11.3	.64	1282.	36
*0189	77/04/05	15:00:	.20	37	7	12.8	-116	3	44.2	.69	1286.	53
*0192	78/03/23	16:30:	.20	37	6	6.4	-116	3	4.1	.64	1266.	55

APPENDIX B

NEAR SURFACE VELOCITY MODELS FOR PAHUTE
MESA AND RAINIER MESA

TABLE B.1

Near-surface velocity models used in the travel-time elevation correction for events in Pahute Mesa and Rainier Mesa (models from Bache, et al., 1979). The corresponding regions of the test site are shown on Figure 3.4, Page 42.

>>>> MODEL # 1 SOURCE EVENT = HAST (PAHUTF MESA)

LAYER	DEPTH(KM)	THICKNESS(KM)	VEL(KM/S)	DENSITY(CGS)
1	.32	.32	2.38	1.66
2	.67	.35	3.50	2.20
3	1.10	.43	3.50	2.10
4	1.58	.48	4.00	2.60
5	1.72	.14	3.50	2.30
6	1.77	.35	3.50	2.30
7	2.09	.32	4.50	2.60
8	5.99	7.90	4.70	2.60
9	11.99	6.00	5.40	2.70
10	24.99	17.00	6.00	2.80

>>>> MODEL # 2 SOURCE EVENT = MUENSTER (PAHUTF M.)

LAYER	DEPTH(KM)	THICKNESS(KM)	VEL(KM/S)	DENSITY(CGS)
1	.34	.34	2.92	2.00
2	.82	.48	4.43	2.12
3	.76	.24	3.00	1.95
4	.91	.15	3.00	2.00
5	1.50	.59	3.00	2.23
6	2.10	.60	4.30	2.60
7	6.00	7.90	4.70	2.60
8	12.00	6.00	5.40	2.70
9	20.00	6.00	6.00	2.80
10	25.00	5.00	6.00	2.80

>>>> MODEL # 3 SOURCE EVENT = CAMBREPT (PAHUTE M.)

LAYER	DEPTH(KM)	THICKNESS(KM)	VEL(KM/S)	DENSITY(CGS)
1	.34	.34	2.92	2.00
2	.82	.48	4.43	2.12
3	1.50	1.00	3.00	2.10
4	2.10	.60	4.30	2.60
5	6.00	7.90	4.70	2.60
6	12.00	6.00	5.40	2.70
7	25.00	17.00	6.00	2.80

>>>> MODEL # 4 SOURCE EVENT = CHESHIRE (PAHUTE M.)

LAYER	DEPTH(KM)	THICKNESS(KM)	VEL(KM/S)	DENSITY(CGS)
1	.34	.34	2.92	2.00
2	.82	.48	4.43	2.12
3	.76	.24	3.00	1.95
4	.91	.15	3.00	2.00
5	1.50	.59	3.00	2.23
6	2.10	.60	4.30	2.60
7	6.00	7.90	4.70	2.60
8	12.00	6.00	5.40	2.70
9	20.00	6.00	6.00	2.80
10	25.00	5.00	6.00	2.80

>>>> MODEL # 5 SOURCE EVENT = KASSEPI (PAHUTF MESA)

LAYER	DEPTH(KM)	THICKNESS(KM)	VEL(KM/S)	DENSITY(CGS)
1	.11	.11	3.05	2.10
2	.73	.62	2.75	1.85
3	.82	.09	2.50	1.70
4	.50	.00	2.50	1.70
5	.91	.41	2.80	1.90
6	1.50	.59	3.11	2.20
7	2.10	.60	4.30	2.60
8	6.00	7.90	4.70	2.60
9	12.00	6.00	5.40	2.70
10	25.00	17.00	6.00	2.80

>>>> MODEL # 6 SOURCE EVENT = KNICKERBOCKER (P.M.)

LAYER	DEPTH(KM)	THICKNESS(KM)	VEL(KM/S)	DENSITY(CGS)
1	.26	.26	1.80	1.70
2	.32	.06	2.60	1.90
3	.33	.01	3.60	2.10
4	.80	.47	4.26	2.38
5	1.20	.40	4.00	2.32
6	1.60	.40	4.00	2.50
7	2.10	.50	4.30	2.60
8	6.00	3.90	4.70	2.60
9	12.00	6.00	5.40	2.70
10	20.00	8.00	6.00	2.80
11	25.00	5.00	6.00	2.80

>>>> MODEL # 7 SOURCE EVENT = FONTINA(PAHUTE MESA)

LAYER	DEPTH(KM)	THICKNESS(KM)	VEL(KM/S)	DENSITY(CGS)
1	.34	.34	2.92	2.00
2	.42	.08	4.40	2.12
3	.76	.34	2.60	1.90
4	.91	.15	2.88	2.02
5	1.50	.59	3.31	2.20
6	2.10	.60	4.30	2.60
7	6.00	3.90	4.70	2.60
8	12.00	6.10	5.40	2.70
9	25.00	13.00	6.00	2.80

>>>> MODEL # 8 SOURCE EVENT = STILTON(PAHUTE MESA)

LAYER	DEPTH(KM)	THICKNESS(KM)	VEL(KM/S)	DENSITY(CGS)
1	.74	.34	2.92	2.00
2	.82	.08	4.40	2.12
3	.50	.08	2.90	1.90
4	.76	.26	2.60	1.90
5	.91	.15	2.88	2.02
6	1.50	.59	3.31	2.20
7	2.10	.60	4.30	2.60
8	6.00	3.90	4.70	2.60
9	12.00	6.10	5.40	2.70
10	25.00	13.00	6.00	2.80

>>>> MODEL # 10 SOURCE EVENT = RAINIER MESA

LAYER	DEPTH(KM)	THICKNESS(KM)	VEL(KM/S)	DENSITY(CGS)
1	.09	.09	3.17	2.34
2	.31	.22	3.10	1.70
3	.32	.01	3.10	1.74
4	.34	.02	2.40	1.60
5	.44	.10	2.50	1.36
6	.85	.41	2.66	1.39
7	.95	.10	5.00	2.70
8	25.00	24.05	6.00	2.78

APPENDIX C

TRAVEL TIME STATISTICS FOR PAHUTE
MESA AND YUCCA FLAT EVENTS

The following two tables give the statistics of the travel-time data after dynamic screening by the procedure described in Section 3.3.1. The statistics are determined separately for data from Pahute Mesa explosions (Table C.1) and for data from Yucca Flat explosions (Table C.2). In each table the stations are ordered by group index given by the five digit number listed in the last column. The first two digits define the epicentral distance range (01 for 0°-25°, 02 for 25°-45°, 03 for 45°-56°, 04 for 56°-68°, 05 for 68°-78°, 06 for 78°-110°), while the last three digits are an index (i) which identifies the azimuthal sector (azimuth between $(i-1) \times 10^\circ$ and $i \times 10^\circ$). Stations rejected from the final travel-time residual data set based on the culling procedure described in Section 3.3.3 are tagged with an "x."

TABLE C.1

STATION STATISTICS AFTER DYNAMIC SCREENING OF RESIDUAL
DATA FROM 28 PAHUTE MESA EXPLOSIONS

STATION COUNT	STATION CODE	# EVENTS	MEAN RESIDUAL	STATION STD DEV	DISTANCE DEGREES	AZIMUTH DEGREES	A-O-I DEGREES	GROUP IDCXX
1	CMC	4	.157	.210	30.71	.88	28.56	02001
2	RES	5	-.644	.249	38.94	8.86	26.86	02001
3	YKC	16	.126	.180	25.74	1.95	30.04	02001
4	BLC	12	-.908	.138	29.76	17.69	28.69	02002
5	FCC	11	.331	.287	25.97	26.72	29.61	02003
6	FBC	10	.752	.223	38.96	31.62	26.86	02004
7	FRB	10	.474	.116	38.93	31.58	26.87	02004
8	GWC	2	.057	.252	31.67	42.71	28.77	02005
9	SCH	9	-.503	.300	37.72	45.99	27.15	02005
10	AGM X	2	.665	.158	35.92	58.80	27.58	02006
11	CBM	3	.084	.029	36.54	59.02	27.43	02006
12	SFA	8	.086	.087	34.69	58.76	27.84	02006
13	SIC	10	.233	.210	37.42	53.61	27.22	02006
14	SUD	5	.588	.223	27.70	59.24	28.90	02006
15	AAM X	7	.353	.412	25.50	68.25	29.92	02007
16	APT	5	1.036	.127	34.20	69.12	27.93	02007
17	BCT	4	.668	.046	33.20	69.03	28.12	02007
18	BNH	12	.682	.246	34.47	63.24	27.88	02007
19	BPT	6	.513	.106	33.73	69.50	28.10	02007
20	EMM	6	.983	.133	37.14	62.62	27.29	02007
21	FLR X	2	1.893	.564	34.85	68.25	27.80	02007
22	HAL X	9	1.086	.414	39.90	62.25	26.64	02007
23	HDM	5	.916	.096	33.84	68.90	28.00	02007
24	MNH X	3	1.530	.172	33.79	64.90	28.01	02007
25	INY X	2	.340	.369	30.81	67.65	28.54	02007
26	MIM	6	.709	.145	36.00	61.93	27.56	02007
27	MNT	23	.167	.255	37.76	61.77	28.19	02007
28	OTT	14	.195	.245	31.29	61.90	28.44	02007
29	PTN X	2	.299	.170	31.81	63.47	28.34	02007
30	ROC	4	.791	.310	29.96	66.38	28.67	02007
31	TMT	5	.742	.033	33.59	68.37	28.25	02007
32	UCT	5	1.001	.087	34.00	68.24	27.97	02007
33	WES	15	1.053	.274	34.62	67.12	27.85	02007
34	BGO X	3	1.159	.457	25.50	70.39	29.92	02008
35	SLA	10	1.689	.176	28.45	78.92	28.80	02008
36	CLE	20	.384	.408	27.10	70.02	29.07	02008
37	GEO	6	.840	.131	30.76	74.62	28.55	02008
38	MRG	11	1.489	.396	28.44	73.79	28.80	02008
39	PAL	3	.143	.249	32.86	70.01	28.17	02008
40	PNJ	5	1.093	.287	32.69	70.23	28.20	02008
41	SCP	3	.859	.160	29.91	71.07	28.68	02008
42	WSC	6	.885	.078	30.70	74.35	29.56	02008
43	BEC X	4	.543	.451	42.22	80.64	26.10	02009
44	CEM	3	.854	.162	29.78	81.10	28.69	02009
45	CHC	5	1.115	.168	29.81	81.04	28.69	02009
46	CSC X	2	1.082	.460	28.73	85.68	28.76	02009
47	ORT	15	1.656	.255	25.64	83.08	29.82	02009
48	BHP X	3	-.178	.505	43.47	120.87	25.80	02013
49	LPS	12	2.238	.203	33.19	176.21	28.12	02013
50	PBJ X	2	2.498	.666	27.70	132.67	28.91	02014
51	VHM	4	3.170	.236	26.73	173.97	29.40	02014
52	HON	7	2.801	.157	39.76	258.19	26.76	02026
53	HVO	4	1.695	.111	38.73	253.40	27.00	02026
54	KIP	10	2.296	.264	39.71	258.32	26.77	02026
55	MOK X	2	1.802	.027	39.07	258.14	26.83	02026
56	ADM	11	1.173	.165	44.16	309.38	25.63	02021

57	NIK	2	1.649	.040	39.40	310.87	26.75	02012
58	PHA	2	2.664	.131	34.98	316.85	27.77	02012
59	BIG	7	1.740	.167	33.40	324.24	28.09	02013
60	KOC	11	2.751	.150	31.42	322.56	28.42	02013
61	SVW	10	1.638	.135	34.31	326.89	27.91	02013
62	TTA	5	1.575	.090	35.31	329.59	27.71	02013
63	BLR X	6	1.962	.322	31.85	335.19	28.34	02014
64	COL	21	1.312	.157	32.42	336.11	28.06	02014
65	FYU	5	1.969	.107	33.79	339.62	28.01	02014
66	GIL	15	1.762	.147	33.37	336.37	28.09	02014
67	GMA	7	1.596	.061	38.47	331.64	26.97	02014
68	IHA	4	1.625	.077	36.08	335.11	27.54	02014
69	PJD	9	1.806	.152	33.42	336.44	28.06	02014
70	PMR	16	2.010	.109	31.86	330.56	28.33	02014
71	SCM	8	2.505	.195	31.31	331.90	28.44	02014
72	TNN	8	1.823	.196	35.01	334.69	27.77	02014
73	TOA X	3	3.038	.042	31.06	332.96	29.49	02014
74	BI2	3	1.925	.027	36.22	342.96	27.51	02015
75	BRW	11	.949	.361	40.05	341.01	26.61	02015
76	INK	9	.684	.245	32.60	348.19	28.21	02015
77	MBC	22	1.136	.244	39.18	358.83	26.81	02016
78	NP-	7	.829	.177	39.19	358.83	26.80	02016
79	ALC	15	-.885	.132	48.81	8.12	24.44	03001
80	DAG	11	-1.445	.148	55.84	16.02	22.74	03002
81	ILG	3	-1.063	.161	51.26	15.23	23.84	03002
82	NOR	7	-.808	.191	54.86	10.21	22.97	03002
83	GDH	20	.551	.294	46.16	26.05	25.12	03003
84	STJ	5	.403	.141	46.86	56.19	24.94	03006
85	ANG X	2	-.312	.304	51.65	97.36	23.74	03010
86	MWI	4	.661	.286	51.59	98.09	23.76	03010
87	SCG X	2	.260	.457	52.40	98.43	23.56	03010
88	SJG	15	1.234	.243	47.70	99.35	24.73	03010
89	SKI X	4	-.284	.535	50.83	97.80	23.94	03010
90	CAR	20	1.474	.205	51.63	107.69	23.75	03011
91	CUM X	5	2.045	.456	53.76	105.79	23.24	03011
92	GRE X	3	-.033	.360	54.67	102.46	23.02	03011
93	SIR X	2	1.563	.160	51.94	107.56	23.67	03011
94	TRN	18	-1.356	.153	55.78	103.55	22.75	03011
95	BCR X	4	1.074	.423	49.31	116.58	24.32	03012
96	BOG	8	3.060	.280	50.36	119.60	24.06	03012
97	FUG	2	1.208	.237	49.99	118.53	24.15	03012
98	SDV X	3	1.683	.402	49.89	112.54	24.17	03012
99	UAV	5	2.670	.178	49.70	113.25	24.22	03012
100	PSO	3	2.699	.067	50.69	125.69	23.98	03013
101	QUI	5	3.617	.399	51.00	128.00	23.90	03013
102	KBS	19	.618	.189	60.34	10.08	21.66	04002
103	AKU X	6	.803	.482	59.95	28.26	21.75	04003
104	MTG	23	-.108	.223	56.86	23.67	22.46	04003
105	REY X	4	1.536	.475	59.06	30.66	21.95	04004
106	SID X	2	.705	.567	60.76	30.25	21.57	04004
107	HUA	5	2.813	.204	62.26	133.58	21.24	04014
108	NNA	3	1.028	.303	61.35	134.92	21.44	04014
109	RKT	6	1.605	.149	67.51	199.44	21.19	04020
110	AFR	8	2.020	.114	62.92	216.27	21.10	04022
111	PAE	7	2.055	.120	62.94	216.02	21.09	04022
112	PHO	8	2.128	.127	59.84	215.88	21.77	04022
113	PPN	11	1.952	.110	62.76	215.95	21.13	04022
114	PPT	15	2.122	.131	62.86	216.06	21.11	04022
115	RUV	9	2.251	.124	59.77	215.28	21.79	04022
116	TPT	14	2.000	.161	59.70	215.62	21.81	04022
117	TVO	8	2.221	.196	62.89	215.64	21.10	04022
118	VAH	9	2.146	.135	59.92	215.49	21.76	04022
119	KEV	5	-1.514	.183	70.05	12.79	19.49	05002
120	KIR	21	-1.040	.193	70.35	16.04	19.40	05002
121	KJN	15	-.651	.252	75.13	15.51	18.17	05002
122	KRK	8	-.814	.320	70.59	11.82	19.33	05002

123	NUR	12	-.608	.235	77.52	18.67	17.59	05002
124	OUL X	9	-1.546	.422	77.87	15.60	18.47	05002
125	SOD	13	-1.042	.165	72.04	14.21	18.92	05002
126	TRO	14	-.366	.218	68.58	15.37	19.85	05002
127	UME	23	-1.101	.193	73.61	18.56	18.53	05002
128	APP X	2	-.649	.080	74.44	23.08	18.33	05003
129	BER	10	-.354	.334	71.67	26.47	19.02	05003
130	COP	8	.020	.140	77.70	26.90	17.55	05003
131	GOT X	4	-.392	.093	75.99	25.76	17.97	05003
132	HFS X	3	-.745	.168	74.68	23.44	18.28	05003
133	KON	19	-.065	.269	73.70	25.37	18.51	05003
134	LHN	10	-.433	.176	73.08	23.92	18.66	05003
135	SKA	5	-.702	.133	71.61	21.64	19.04	05003
136	SLL X	2	-.427	.060	74.30	23.36	18.37	05003
137	UDD	5	-.702	.187	74.69	23.50	18.27	05003
138	UPP	20	-.873	.166	76.11	22.00	17.94	05003
139	DBN X	2	1.339	.393	77.49	32.62	17.60	05004
140	DUR X	7	-.028	.468	72.72	33.47	18.75	05004
141	EKA	12	-.567	.185	71.66	33.62	19.02	05004
142	ESK	7	-.676	.291	71.65	33.65	19.03	05004
143	FLN	22	.371	.236	77.22	37.66	17.67	05004
144	GRR X	20	.516	.201	77.29	38.12	17.65	05004
145	KEW	3	.260	.183	75.47	35.57	18.10	05004
146	LPF	9	.405	.188	77.44	38.47	17.61	05004
147	SGR	5	.249	.197	77.71	38.66	17.54	05004
148	SSC	21	.306	.152	77.52	37.62	17.59	05004
149	VAL	7	-.710	.285	70.35	39.19	19.40	05004
150	WIT	16	1.273	.344	77.61	31.44	17.57	05004
151	PTO	11	-.662	.393	77.80	47.42	17.52	05005
152	CCH	2	.376	.205	71.92	129.57	18.95	05013
153	ANT	10	1.779	.291	74.37	136.92	18.35	05014
154	ARE	16	2.538	.150	68.00	133.21	19.98	05014
155	LPB	14	1.419	.192	70.08	130.52	19.48	05014
156	PNS	13	1.424	.155	69.64	130.64	19.59	05014
157	TRJ X	2	1.577	.173	75.89	131.30	17.79	05014
158	RAR	3	1.907	.408	71.09	222.77	19.19	05023
159	AFI	2	.742	.041	72.81	236.91	18.72	05024
160	NUE	2	1.492	.273	75.40	231.93	18.11	05024
161	KMU	4	.306	.096	73.01	310.28	18.67	05032
162	BRA	8	-.179	.379	85.42	29.22	15.46	06003
163	CIN X	2	-2.649	.661	98.62	27.92	14.47	06003
164	CLL	22	-.031	.324	81.31	29.44	16.63	06003
165	EZN X	3	-1.411	.232	96.01	28.06	14.53	06003
166	ISK	4	-.462	.254	95.91	25.62	14.53	06003
167	KDZ	4	.066	.322	94.07	27.81	14.58	06003
168	KLS X	3	-.926	.021	78.44	25.18	17.36	06003
169	KRA	5	.308	.237	84.93	26.61	15.59	06003
170	NIE	10	.653	.283	85.59	26.75	15.42	06003
171	PRU	17	.082	.185	82.96	29.49	16.16	06003
172	PVL X	3	-1.034	.395	92.70	27.18	14.62	06003
173	SRO X	3	1.482	.076	86.18	28.76	15.30	06003
174	VAY	4	-.345	.159	93.28	29.77	14.61	06003
175	VIE	5	.022	.270	85.07	29.58	15.55	06003
176	VKA	13	.194	.190	85.04	29.59	15.56	06003
177	ARM X	2	-.544	.087	80.69	39.58	16.78	06004
178	ATH X	2	-1.045	.012	96.59	30.77	14.52	06004
179	BAF X	2	.010	.353	81.40	34.74	16.60	06004
180	BAS X	2	.777	.078	81.89	34.64	16.48	06004
181	BES X	4	-.091	.268	81.37	35.64	16.61	06004
182	BHG X	2	.029	.076	84.07	31.77	15.85	06004
183	BNS	18	.486	.166	79.18	32.50	17.16	06004
184	BSF	9	.370	.199	81.31	34.84	16.63	06004
185	BUH	10	.504	.166	81.33	33.55	16.62	06004
186	COF	11	.358	.130	81.11	34.22	16.67	06004
187	CDR	7	.556	.175	83.88	38.22	15.91	06004
188	DOU X	5	1.368	.312	78.67	34.32	17.29	06004

189	FEL	X	2	.121	.263	81.84	34.27	16.49	06004
190	FUR	X	16	.562	.379	87.24	72.33	16.16	06004
191	GAP	X	2	.697	.232	83.48	72.68	16.03	06004
192	GIP	X	2	.499	.209	76.93	33.32	17.23	06004
193	GRC		10	.076	.203	79.96	37.06	16.06	06004
194	GRF		7	.828	.148	81.84	31.38	16.49	06004
195	HAU		11	.299	.175	87.98	34.94	16.70	06004
196	HEE		7	.655	.202	78.72	33.11	17.28	06004
197	HEI		3	.531	.180	81.01	32.81	16.70	06004
198	ISO		9	.413	.266	84.13	37.14	15.83	06004
199	KHC		20	.325	.216	83.25	30.52	16.10	06004
200	KRL		9	.961	.241	81.16	33.27	16.66	06004
201	LBF		10	.129	.180	80.61	36.83	16.80	06004
202	LFF		6	.458	.158	87.45	39.92	16.84	06004
203	LMR		7	.303	.164	84.50	38.05	15.72	06004
204	LNS		7	1.061	.191	83.25	36.51	16.10	06004
205	LOR		22	.335	.211	87.35	36.70	16.87	06004
206	LPO		6	.329	.150	87.85	39.88	16.74	06004
207	LRG		8	.529	.166	84.33	38.05	15.77	06004
208	LSF		6	.073	.122	79.93	38.57	16.97	06004
209	MFF		9	.385	.209	78.85	39.12	17.25	06004
210	MNY	X	2	.268	.480	82.90	37.37	16.20	06004
211	MOA		6	.012	.131	84.54	30.95	15.71	06004
212	MOX		18	.063	.284	81.27	30.56	16.64	06004
213	RJF		6	.195	.127	80.59	39.26	16.81	06004
214	RMP	X	3	-.316	.379	88.62	35.55	14.85	06004
215	RSL	X	5	.511	.341	82.81	36.39	16.22	06004
216	SKO	X	5	-.777	.139	92.27	30.15	14.62	06004
217	SPF		10	.266	.162	84.42	37.79	15.74	06004
218	SSB	X	2	.107	.106	82.11	37.75	16.42	06004
219	SSF		20	.069	.167	87.33	37.01	16.87	06004
220	STR	X	8	.730	.411	81.19	33.84	16.65	06004
221	STU		8	.210	.097	81.68	33.00	16.53	06004
222	TCF		9	.051	.130	80.25	38.21	16.89	06004
223	TNS	X	2	.691	.125	80.27	32.39	16.89	06004
224	TRI	X	6	-.224	.593	86.03	32.54	15.33	06004
225	VQU	X	2	.088	.014	81.83	36.40	16.49	06004
226	WLS	X	4	.363	.125	81.14	34.16	16.67	06004
227	WRM	X	3	1.685	.345	79.21	34.14	17.15	06004
228	ALI		5	.220	.179	84.33	45.35	15.77	06005
229	ALM		3	-.433	.360	84.22	47.53	15.80	06005
230	COI		4	-.122	.148	78.50	48.07	17.34	06005
231	EBP		7	.276	.344	83.17	43.04	16.12	06005
232	LIS		5	.145	.129	79.00	49.61	17.21	06005
233	MTC		3	-.245	.258	78.89	47.48	17.24	06005
234	SET	X	2	-.564	.611	89.16	43.51	14.78	06005
235	TOL		5	.283	.131	81.26	46.11	16.64	06005
236	AVE		8	.113	.512	83.53	52.91	16.01	06006
237	BAB		3	-.103	.461	88.97	52.29	14.80	06006
238	IFR		10	.671	.313	84.83	51.48	15.62	06006
239	RBA		2	.065	.350	83.44	52.05	16.04	06006
240	RBZ		3	-.381	.277	83.49	52.11	16.02	06006
241	TAM		5	.767	.409	97.01	52.58	14.45	06006
242	KIC		4	-.709	.124	103.01	71.61	14.37	06008
243	LIC		4	-.797	.205	102.88	71.91	14.37	06008
244	BAE		3	1.188	.265	83.16	115.63	16.12	06012
245	BAO		4	1.021	.172	82.90	115.58	16.20	06012
246	CEN		9	1.366	.110	81.55	140.48	16.57	06015
247	MOZ		5	1.057	.134	82.55	141.33	16.30	06015
248	PEL		3	.857	.198	81.86	142.75	16.49	06015
249	SAN		3	.788	.166	82.12	142.91	16.41	06015
250	KOU		5	1.770	.441	94.19	247.47	14.58	06025
251	LMP		3	1.265	.113	89.01	248.60	14.80	06025
252	LNR		2	1.170	.440	88.38	248.82	14.89	06025
253	LUG		4	.257	.434	88.94	249.71	14.81	06025
254	NDF		5	2.406	.505	82.89	241.55	16.20	06025

255	NOU	6	1.672	.318	93.68	244.85	14.59	06025
256	OUA	4	1.211	.429	92.15	245.58	14.63	06025
257	PVC	4	.230	.060	89.46	247.28	14.74	06025
258	HNR	3	.869	.117	90.72	258.80	14.66	06026
259	KOA X	2	1.018	.520	92.22	263.93	14.63	06027
260	PAB	2	-.659	.134	93.75	267.61	14.59	06027
261	RAL	2	-1.149	.028	93.74	267.57	14.59	06027
262	TAV	2	-1.062	.078	93.73	267.55	14.59	06027
263	VUL	2	-.532	.033	93.82	267.55	14.59	06027
264	GUA	3	-.678	.220	88.81	286.00	14.83	06029
265	ABU	4	1.039	.311	82.09	307.91	16.42	06031
266	BAG X	2	-1.262	.215	104.49	303.91	14.34	06031
267	DOP X	14	.668	.360	79.08	306.92	17.19	06031
268	KYS X	8	1.091	.400	78.95	305.79	17.22	06031
269	MAT	15	.473	.156	79.36	307.86	17.12	06031
270	OIS X	7	.812	.342	82.73	307.47	16.25	06031
271	OYM	3	.222	.108	79.40	306.44	17.11	06031
272	SHK	11	.860	.192	84.11	309.23	15.84	06031
273	SRT X	2	.753	.055	82.42	307.30	16.33	06031
274	SRV	9	.580	.295	79.26	306.57	17.14	06031
275	TSK	12	.087	.310	78.36	306.63	17.37	06031
276	WNU	7	.839	.262	82.77	307.61	16.23	06031
277	SEO	4	.566	.409	85.44	314.62	15.45	06032
278	KBL	2	.086	.007	108.48	355.38	14.26	06036

TABLE C.2

STATION STATISTICS AFTER DYNAMIC SCREENING OF RESIDUAL
DATA FROM 54 YUCCA FLAT EXPLOSIONS

STATION COUNT	STATION CODE	# EVENTS	MEAN RESIDUAL	STATION STD DEV	DISTANCE DEGREES	AZIMUTH DEGREES	A-O-Y DEGREES	GROUP INDEX
1	RES	10	-.372	.294	38.94	8.86	26.86	02001
2	YKC	8	.188	.223	25.34	1.95	30.04	02001
3	BLC	2	-.527	.146	29.76	17.69	28.69	02002
4	FBC	12	.843	.213	38.96	31.62	26.86	02004
5	FRB X	2	.595	.030	38.93	31.58	26.87	02004
6	GWC	4	.365	.044	31.67	42.71	28.37	02005
7	SCH	7	-.250	.218	37.72	45.90	27.15	02005
8	CBM	4	.485	.183	36.54	59.02	27.43	02006
9	SFA	?	.332	.023	34.69	58.76	27.84	02006
10	SIC	6	.527	.119	37.42	53.61	27.72	02006
11	AAH	5	.964	.347	25.50	68.25	29.92	02007
12	BNH X	3	1.051	.529	34.47	63.24	27.88	02007
13	EMH	3	1.120	.250	37.14	62.62	27.29	02007
14	HAL	8	1.310	.129	39.90	62.25	26.64	02007
15	MIH	?	1.153	.272	36.00	61.93	27.56	02007
16	MNT	14	.482	.262	37.76	61.70	28.19	02007
17	BGO	4	1.356	.199	25.50	70.30	29.92	02008
18	BLA	9	1.665	.463	28.45	78.92	28.80	02008
19	CLE	18	.793	.435	27.10	70.02	29.07	02008
20	GEO	3	.874	.096	30.76	74.62	28.55	02008
21	MRG	11	2.275	.421	28.44	73.79	28.80	02008
22	PAL X	2	.390	.419	32.86	70.01	28.17	02008
23	SCP	6	.608	.317	29.91	71.07	28.68	02008
24	WSC	7	1.148	.342	30.70	74.35	28.56	02008
25	ATL	3	1.284	.126	26.26	88.59	29.44	02009
26	BEC	2	1.229	.332	42.22	80.64	26.10	02009
27	CHC	2	2.172	.035	29.81	81.04	28.69	02009
28	CSC	3	.815	.494	28.73	85.68	28.76	02009
29	ORT	11	2.094	.332	25.64	83.08	29.82	02009
30	COM X	2	2.661	.742	29.84	127.85	28.68	02013
31	LPS	13	2.308	.309	33.19	126.21	28.12	02013
32	PBJ	5	3.261	.183	27.70	122.67	28.91	02014
33	VHM	5	2.966	.377	26.33	123.97	29.40	02014
34	HON	?	2.908	.159	39.36	258.18	28.76	02026
35	HVO	4	2.089	.341	38.33	253.40	27.00	02026
36	KIP	7	2.779	.145	39.31	258.32	28.77	02026
37	ADK	18	1.113	.257	44.16	309.38	25.63	02031
38	RIG	6	1.550	.281	33.40	324.24	28.79	02033
39	KDC	7	2.605	.160	31.42	322.56	28.42	02033
40	SVW	7	1.628	.181	34.31	326.89	27.91	02033
41	BLP X	3	3.527	.428	31.85	335.19	28.74	02034
42	COL	24	1.203	.159	33.42	336.11	28.08	02034
43	FYU	3	1.894	.123	33.79	339.67	28.01	02034
44	GIL	19	1.648	.110	33.37	336.37	28.09	02034
45	GMA	8	1.548	.241	38.47	331.64	26.97	02034
46	PJO	7	1.575	.169	33.42	336.44	28.08	02034
47	PHO X	21	2.123	.203	31.86	330.56	28.33	02034
48	SCM X	9	2.513	.394	31.71	331.90	28.44	02034
49	TNN X	5	1.870	.265	35.01	334.60	27.77	02034
50	RIZ	3	1.714	.087	36.22	342.96	27.51	02035
51	RRW X	11	.740	.485	40.05	341.01	26.61	02035
52	INX	3	.279	.256	32.60	348.19	28.71	02035
53	MBC	34	.997	.238	39.18	358.87	26.81	02036
54	NP-	15	.970	.177	30.19	358.87	26.80	02036
55	ALE	19	-.763	.120	48.51	4.10	24.44	02001
56	DAG	11	-1.017	.730	55.84	16.02	27.74	02002

57	ILG	X	3	-.659	.527	51.26	15.23	27.24	03001
58	NOR		20	-.613	.315	54.86	10.21	22.97	03002
59	GDM		16	.742	.167	46.16	26.05	25.12	03003
60	STJ		4	.785	.236	46.86	56.19	24.94	03006
61	SJG		24	1.542	.289	47.70	99.35	24.73	03010
62	CAR		16	1.832	.160	51.63	107.89	27.75	03011
63	SIR		2	1.700	.172	51.94	107.56	23.67	03011
64	TRN		7	-1.247	.143	55.78	103.55	22.75	03011
65	BCP		2	1.253	.106	49.31	116.58	24.32	03012
66	BOG		6	3.580	.143	50.36	119.60	24.06	03012
67	UAV	X	2	2.333	.676	49.70	113.25	24.72	03012
68	PSC		2	2.566	.398	50.69	125.69	23.98	03013
69	QUI	X	2	3.943	.646	51.00	128.00	23.90	03013
70	KBS		21	.937	.326	60.34	10.08	21.66	04002
71	AKU	X	4	.995	.338	59.95	28.26	21.75	04003
72	KTG		35	.225	.190	56.88	23.67	22.48	04003
73	HUA		4	2.979	.145	62.26	133.58	21.24	04014
74	NNA		3	.777	.145	61.35	134.92	21.44	04014
75	AFR		9	2.296	.108	62.92	216.27	21.10	04022
76	PAE		9	2.452	.095	62.94	216.02	21.09	04022
77	PMO		8	2.413	.118	59.84	215.88	21.77	04022
78	PPN		11	2.280	.135	62.76	215.95	21.13	04022
79	PPT		17	2.417	.212	62.86	216.06	21.11	04022
80	RUV		7	2.487	.136	59.77	215.28	21.79	04022
81	THT	X	3	2.669	.451	62.85	216.06	21.11	04022
82	TPT		12	2.349	.131	59.70	215.62	21.81	04022
83	TVO		10	2.493	.231	67.89	215.64	21.10	04022
84	VAH		10	2.475	.146	59.92	215.40	21.76	04022
85	KEV		17	-1.117	.329	70.05	12.79	19.49	05002
86	KIP		35	-.657	.167	70.35	16.04	19.40	05002
87	KJF	X	7	-.305	.287	75.03	15.45	18.19	05002
88	KJN		36	-.435	.261	75.13	15.51	18.17	05002
89	KRK	X	7	-.602	.284	70.59	11.82	19.33	05002
90	NUR		26	-.267	.162	77.52	18.63	17.59	05002
91	OUL	X	28	-1.119	.408	73.87	15.69	18.47	05002
92	SOD		29	-.783	.166	72.04	14.21	18.92	05002
93	TRO		16	-.102	.309	68.58	15.37	19.85	05002
94	UME		37	-.837	.156	73.61	18.56	18.53	05002
95	APP	X	3	-.316	.158	74.44	23.08	18.73	05003
96	BEP		5	-.031	.249	71.67	26.47	19.02	05003
97	GOT		6	-.055	.125	75.99	25.76	17.97	05003
98	HFS		8	-.052	.217	74.68	23.44	18.28	05003
99	KON	X	33	-.368	.202	71.70	25.37	18.51	05003
100	LHN	X	11	-.090	.384	77.08	23.92	18.46	05003
101	SKA		8	-.385	.323	71.61	21.64	19.04	05003
102	SLL	X	4	-.036	.290	74.30	23.36	18.77	05003
103	UOD		5	-.175	.220	74.69	23.50	18.27	05003
104	UPP		36	-.669	.163	76.11	22.00	17.94	05003
105	CUR	X	2	2.224	.432	72.72	33.47	18.75	05004
106	EKA		15	-.125	.197	71.66	33.62	19.02	05004
107	ESK		8	-.514	.286	71.65	33.65	19.03	05004
108	FLH		23	.715	.177	77.22	37.68	17.67	05004
109	GRR		25	.822	.190	77.29	38.12	17.65	05004
110	KEW		6	.596	.324	75.47	35.52	18.10	05004
111	LPF		7	.817	.067	77.44	38.47	17.61	05004
112	SSC		25	.701	.206	77.52	37.62	17.59	05004
113	VAL	X	2	1.058	.442	77.35	39.19	19.40	05004
114	WIT	X	10	2.046	.415	77.61	31.44	17.57	05004
115	PTO		7	-.247	.266	77.80	47.42	17.52	05005
116	ANT		6	1.847	.278	74.37	176.92	19.75	05014
117	ARE		25	2.773	.155	68.70	173.21	19.98	05014
118	LPR		15	1.644	.260	77.08	170.52	19.48	05014
119	PNS		12	1.636	.171	65.64	170.64	19.59	05014
120	TRJ	X	2	.966	.008	75.49	171.37	17.09	05014
121	AFI		2	1.577	.140	72.81	276.91	19.72	05014
122	HSS		2	.283	.100	77.64	311.07	19.00	05014

123	KMU	9	.330	.269	77.01	210.22	14.67	06003
124	BRA	11	.367	.409	85.42	29.22	17.46	06003
125	BRG X	2	.437	.067	82.02	79.25	16.44	06003
126	CLL	19	.365	.220	81.31	29.44	16.63	06003
127	HLE	5	.448	.409	80.75	29.84	16.76	06003
128	KLS	4	-.413	.108	78.44	25.18	17.36	06003
129	KRA	8	.432	.252	84.93	26.61	15.59	06003
130	NIE	15	1.215	.364	85.59	26.75	15.42	06003
131	PRU	25	.546	.347	82.96	29.49	16.18	06003
132	SRO X	2	-.671	.087	86.18	28.76	15.70	06003
133	VIF	4	.271	.143	85.07	29.58	15.55	06003
134	VKA	10	.613	.293	85.04	29.59	15.56	06003
135	ZST	3	1.221	.352	85.40	29.21	15.46	06003
136	ARM	7	.926	.158	80.69	29.58	16.78	06004
137	BHG X	2	.754	.204	84.07	31.77	15.85	06004
138	BNS	25	.926	.284	79.18	32.50	17.16	06004
139	BSF	14	.736	.165	81.71	34.84	16.63	06004
140	BUH	7	.742	.181	81.33	33.55	16.62	06004
141	COF	13	.698	.212	81.11	34.22	16.67	06004
142	DOU X	10	.506	.394	78.67	34.32	17.29	06004
143	FUR	14	1.171	.075	83.04	32.33	16.16	06004
144	GAP X	3	1.057	.250	83.48	32.84	16.03	06004
145	GRC X	4	.453	.231	79.96	37.06	16.96	06004
146	GRF	5	1.268	.164	81.84	31.38	16.49	06004
147	HAU	12	.634	.162	80.98	34.94	16.70	06004
148	HEE X	3	.794	.058	78.72	33.11	17.28	06004
149	HEI X	2	.883	.120	81.01	32.81	16.70	06004
150	ISO	11	.755	.251	84.13	37.18	15.83	06004
151	KHC	26	.595	.210	83.25	30.52	16.10	06004
152	LBF	16	.607	.188	80.61	36.83	16.80	06004
153	LEF	11	.864	.220	80.45	39.92	16.84	06004
154	LNR X	4	.884	.293	84.50	38.05	15.72	06004
155	LNS X	7	1.002	.358	83.25	36.51	16.10	06004
156	LOR	39	.798	.247	80.35	36.70	16.87	06004
157	LPO	11	.789	.141	80.85	39.88	16.74	06004
158	LRG X	4	1.030	.121	84.33	38.05	15.77	06004
159	LSF	7	.562	.204	79.93	38.57	16.97	06004
160	MFF	9	.803	.196	78.85	39.12	17.25	06004
161	MNY X	2	.717	.174	82.90	37.37	16.20	06004
162	MOA	6	.205	.151	84.54	30.95	15.71	06004
163	MOX X	14	.514	.376	81.27	30.56	16.64	06004
164	RJF X	3	.502	.112	80.59	39.26	16.81	06004
165	RSL	5	.821	.220	82.81	36.39	16.22	06004
166	SPF	7	.779	.133	84.42	37.79	15.74	06004
167	SSF	35	.477	.210	80.33	37.01	16.87	06004
168	STP X	7	1.594	.371	81.19	33.64	16.65	06004
169	STU	6	.603	.168	81.68	33.00	16.53	06004
170	TCF	16	.531	.175	80.25	38.21	16.89	06004
171	WET X	2	.223	.175	82.95	30.67	16.18	06004
172	WLS	7	.918	.260	81.14	34.16	16.67	06004
173	ALZ	2	2.054	.263	84.33	45.35	15.77	06005
174	RDR	2	1.647	.349	81.43	41.59	16.60	06005
175	EBR	6	.870	.394	83.17	43.04	16.12	06005
176	LIS X	3	1.113	.541	79.00	49.61	17.21	06005
177	MAL	2	1.967	.274	83.14	48.64	16.13	06005
178	TOL	3	.786	.200	81.76	46.11	16.64	06005
179	AVE	9	.721	.377	83.53	52.91	16.71	06006
180	BAB X	2	.352	.426	88.97	52.22	14.80	06006
181	IFR	11	1.040	.157	64.83	51.44	15.62	06006
182	TAM	8	.870	.360	99.01	52.55	14.45	06006
183	BAE X	4	1.423	.470	87.16	115.67	16.12	06012
184	CEV	3	1.815	.180	51.55	140.48	16.97	06015
185	POZ	4	1.307	.160	82.55	141.37	16.70	06015
186	MEN X	2	1.435	.456	82.56	141.35	16.79	06015
187	HNP X	2	2.054	.594	50.72	258.87	14.66	06076
188	DOO	14	.538	.791	79.06	306.90	17.19	06071

189	KYS	X	3	.822	.529	75.95	305.79	17.72	06031
190	MAT		21	.230	.025	79.36	307.66	17.12	06031
191	OIS	X	2	.570	.118	62.73	307.47	16.25	06031
192	SHK		10	.666	.299	84.11	309.27	15.84	06031
193	SRY		5	.512	.315	70.26	306.57	17.14	06031
194	TSK		10	.100	.142	78.36	306.63	17.37	06031
195	WNU		4	.849	.724	82.77	307.61	16.23	06031
196	SEO		5	.740	.759	85.44	314.62	15.45	06032

APPENDIX D

VELOCITY PERTURBATIONS IN MODEL T65-20 IN CELLS

Figures D.1a through D.1f show the velocity perturbations in each grid cell of Model T65-20. The number in a cell is Δv in units of 0.01 km/sec. Both outer grid and inner grid can be overlayed with corresponding figures in the text.

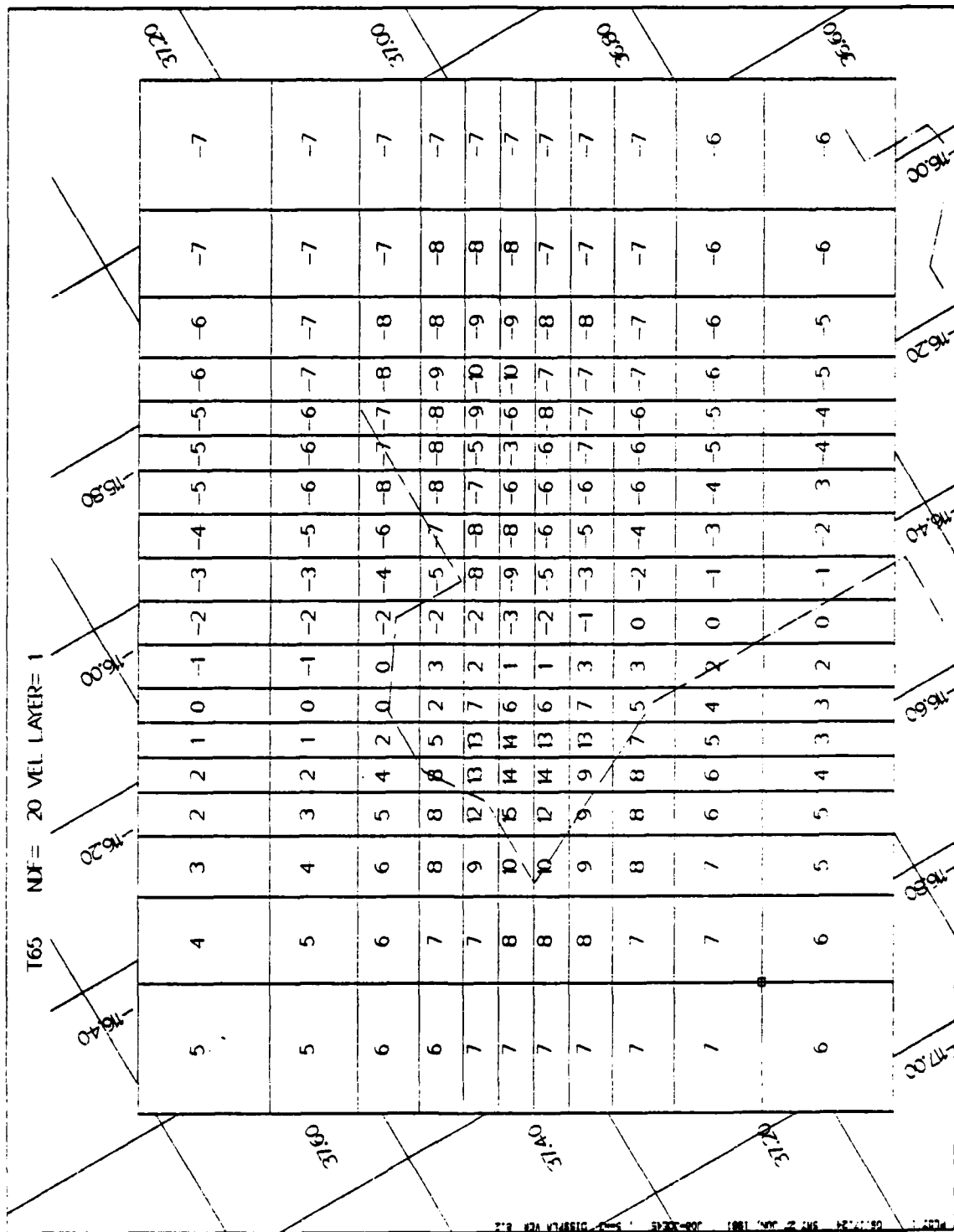


Figure D.1a. Model T65-20, Layer 1 (0 - 12 km).

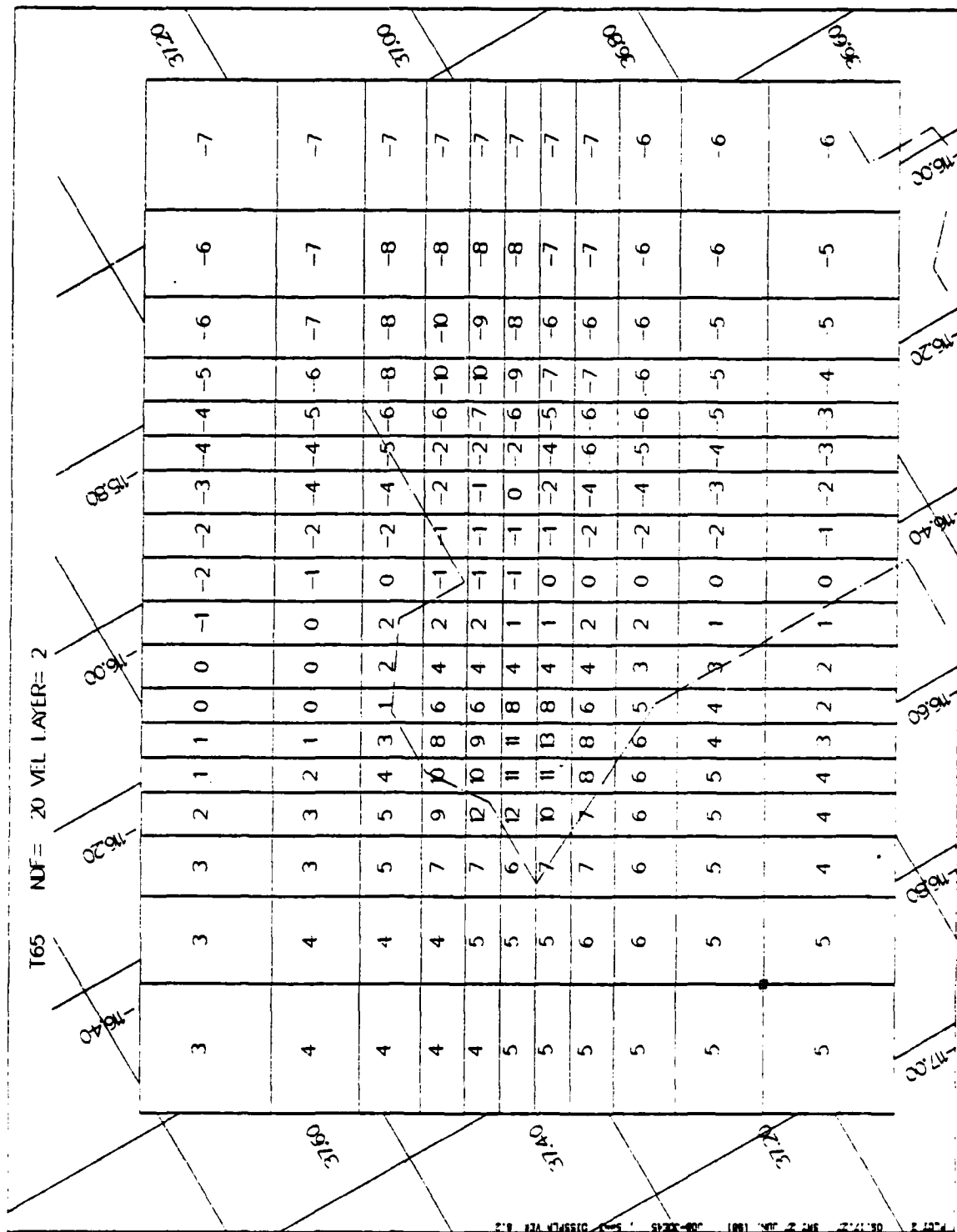


Figure D.lb. Model T65-20, Layer 2 (12 - 28 km).

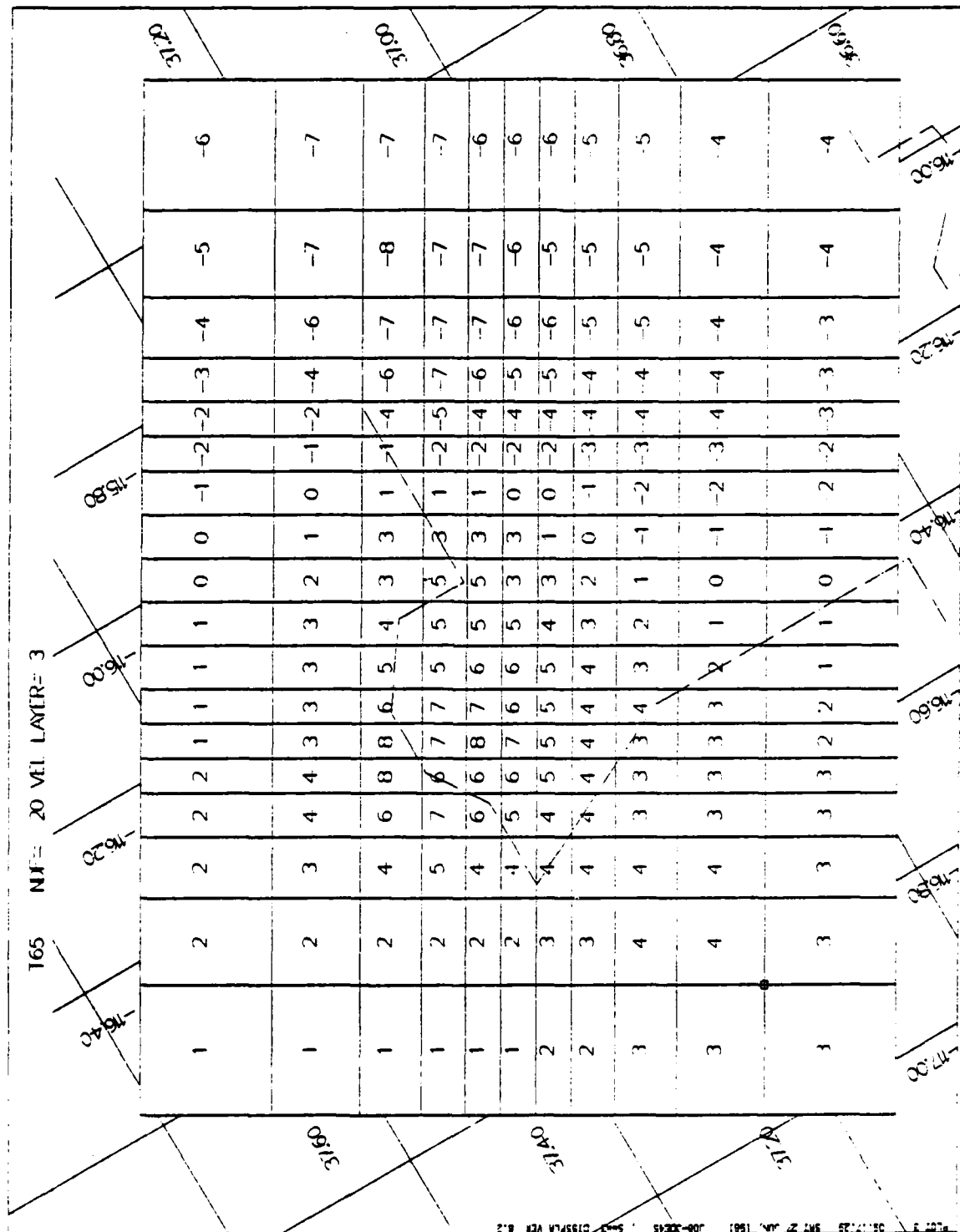


Figure D.1c. Model T65-20, Layer 3 (28 - 48 km) .

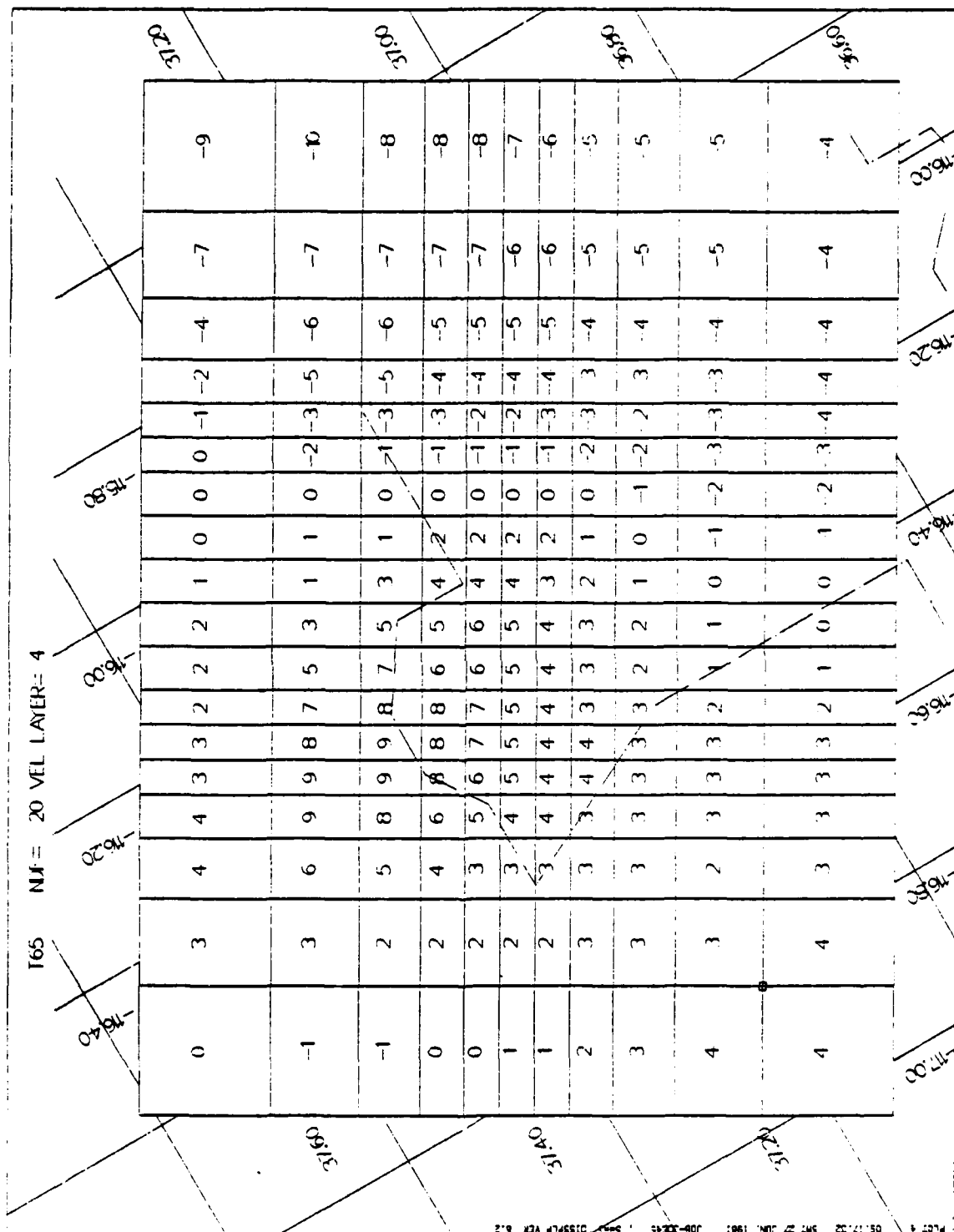


Figure D.1d. Model T65-20, Layer 4 (48 - 74 km).

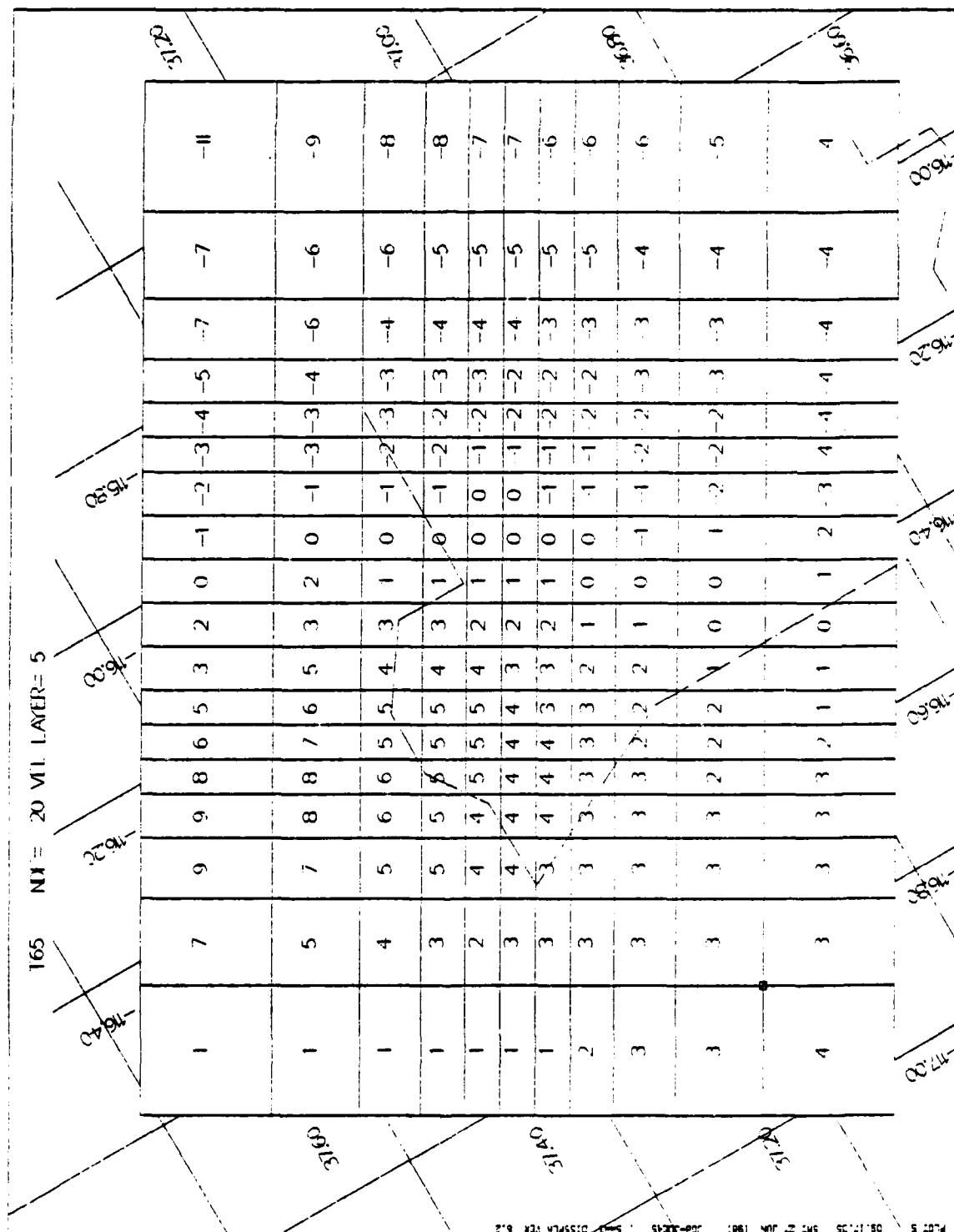


Figure D.le. Model T65-20, Layer 5 (74 - 108 km).

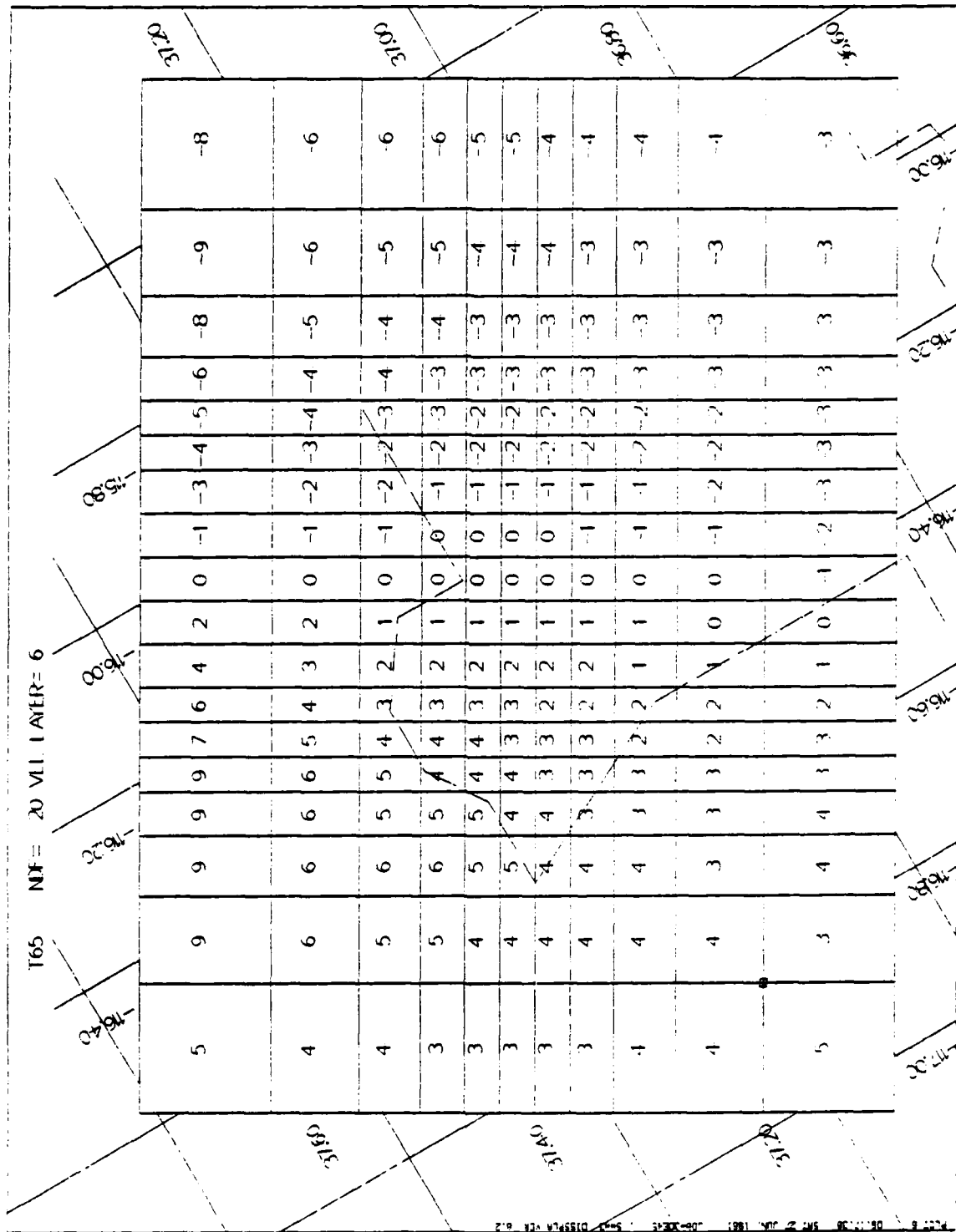


Figure D.1f. Model T65-20, Layer 6 (108 - 152 km).

APPENDIX E

SELECTED RESOLVING VECTORS FOR MODEL T65-20

This appendix gives the resolving vectors calculated for twelve target cells (Cells (6,6) Tables E.1a through E.1f for six layers and Cells (6,13) Tables E.2a through E.2f for six layers; see Figure 4.10). Each resolving vector has the same length as a model vector, and components for each cell are listed for the six consecutive layers in each case. Labels are as follows:

NDF: number of degrees of freedom
(20 for Model T65-20)

IK2, LAYER: layer index

other labels are for internal
purposes only.

The units have been scaled appropriately, such that values of resolving kernel components can be compared directly within and between layers.

Note that each kernel sums to zero in each layer, a consequence of denuisancing.

Target cells have been framed for each kernel.

LAYER 1, CELL (6,6)

[illegible][illegible][illegible]

NDF	IX2	LAYER	IRUV	ICPL	IRK															
20	4	4	2	0	1															
RK WRT SLO IN MODEL UNITS (1 UNIT = -6.0840-003) :																				
-4	8		5	-16	-16	-5	-14	2	6	-20	33	17	-1	15	-15	-77	59			
99	-37	-4	-18	-20	-53	-4	-31	-4	-11	-21	16	48	-13	67	-6	8	-2			
55	0	-5	-11	-16	-39	51	-31	-5	-9	1	10	17	-17	2	0	-4	-8			
9	-3	-29	-4	-1	-28	-6	-2	-4	0	11	17	22	7	2	0	-4	-26			
29	44	-13	-13	-11	-8	0	-1	-1	-10	11	-27	-6	-3	-1	-1	-3	-6			
7	5	0	0	0	-1	-3	0	0	-3	16	4	-15	0	0	0	0	-5			
2	6	3	0	0	0	-3	0	0	25	36	33	8	12	8	6	5	-16			
0	0	2	-1	-1	-10	-6	-16	-17	-11	-11	4	0	0	0	0	0	-31			
0	-14	35	11	7	-10	-5	-13	-5	-12	-5	0	0	1	1	-2	2	-20			
15	-2	-1	3	7	51	-22	-9	-9	1	1	1	0	2	0	0	-1	-2			
5	4	-17	-11	-35	30	-25	0	-1	0	0	0	-16	0	0	0	0	0			

NOF	IX2	LAYER	IRUV	ICPL	IRK												
20	5	5	2	0	1												
RM WRT SLO IN MODEL UNITS (1 UNIT = -6.0840-003) :																	
62	-98	-15	-69	54	100	-8	-59	-23	-46	27	13	-33	84	38	63	-5	13
51	-12	-42	-7	-12	-50	13	3	3	-7	-2	0	8	-18	10	5	7	-14

TABLE E.1b

LAYER 2, CELL (6,6)

[illegible][illegible][illegible][illegible]

NOF	IX2	LAYER	IRUV	ICPL	IRK												
20	5	5	2	0	1												
RM =RT SLO IN MODEL UNITS (1 UNIT = -6.0840-003) :																	
32	-35	-32	-47	-13	60	5	-125	-28	-47	29	54	1	68	-9	20	-13	-29
16	-4	-18	-18	-47	85	105	30	1	-17	-2	0	4	-6	A	8	4	-15

TABLE E.1b (continued)

NOF	IX2	LAYER	IRUV	ICPL	IRK
20	6	6	2	0	1
10	-9	0	5	2	3
20	7	13	1	1	0
30	0	0	0	2	0
40	0	0	0	1	0
50	0	0	0	2	0
60	0	0	0	1	0
70	0	0	0	2	0
80	0	0	0	1	0
90	0	0	0	2	0
100	0	0	0	1	0
110	0	0	0	2	0
120	0	0	0	1	0
130	0	0	0	2	0
140	0	0	0	1	0
150	0	0	0	2	0
160	0	0	0	1	0
170	0	0	0	2	0
180	0	0	0	1	0
190	0	0	0	2	0
200	0	0	0	1	0
210	0	0	0	2	0
220	0	0	0	1	0
230	0	0	0	2	0
240	0	0	0	1	0
250	0	0	0	2	0
260	0	0	0	1	0
270	0	0	0	2	0
280	0	0	0	1	0
290	0	0	0	2	0
300	0	0	0	1	0
310	0	0	0	2	0
320	0	0	0	1	0
330	0	0	0	2	0
340	0	0	0	1	0
350	0	0	0	2	0
360	0	0	0	1	0
370	0	0	0	2	0
380	0	0	0	1	0
390	0	0	0	2	0
400	0	0	0	1	0
410	0	0	0	2	0
420	0	0	0	1	0
430	0	0	0	2	0
440	0	0	0	1	0
450	0	0	0	2	0
460	0	0	0	1	0
470	0	0	0	2	0
480	0	0	0	1	0
490	0	0	0	2	0
500	0	0	0	1	0
510	0	0	0	2	0
520	0	0	0	1	0
530	0	0	0	2	0
540	0	0	0	1	0
550	0	0	0	2	0
560	0	0	0	1	0
570	0	0	0	2	0
580	0	0	0	1	0
590	0	0	0	2	0
600	0	0	0	1	0
610	0	0	0	2	0
620	0	0	0	1	0
630	0	0	0	2	0
640	0	0	0	1	0
650	0	0	0	2	0
660	0	0	0	1	0
670	0	0	0	2	0
680	0	0	0	1	0
690	0	0	0	2	0
700	0	0	0	1	0
710	0	0	0	2	0
720	0	0	0	1	0
730	0	0	0	2	0
740	0	0	0	1	0
750	0	0	0	2	0
760	0	0	0	1	0
770	0	0	0	2	0
780	0	0	0	1	0
790	0	0	0	2	0
800	0	0	0	1	0
810	0	0	0	2	0
820	0	0	0	1	0
830	0	0	0	2	0
840	0	0	0	1	0
850	0	0	0	2	0
860	0	0	0	1	0
870	0	0	0	2	0

LAYER 3, CELL (6,6)

[illegible]

```

      NDF    IXZ   LAYER IRUV ICPL   IRK
      20     2     2       2    Q     1
RM BRT SLO IN MODEL UNITS (1 UNIT = -4.2250-003) :

```

[illegible][illegible]

NOF	IX2	LAYER	IRUY	ICPL	IRK												
20	5	5	2	0	1												
RK =RT SLQ IN MODEL UNITS (1 UNIT = -6.0840-003) :																	
2	8	-19	-38	-32	1	-32	-48	-27	-7								
-20	19	-12	-8	-18	191	-3	53	0	-16	-1	5	18	25	-17	14	-1	-25
											0	4	-5	-2	-3	-3	-1

LAYER 4, CELL (6,6)

[illegible][illegible][illegible]

NDF	IX2	LAYER	IRUV	ICPL	IRK
20	4	4	2	0	1

RK=RT SLO IN MODEL UNITS (1 UNIT = -6.0840-063) :

-14	21	24	-18	-15	-16	11	4	21	7	-12	-24	17	13	13	-14	-15	14
-8	-14	0	-6	-10	10	-25	12	-20	-10	-22	-12	10	-9	-23	-14	-15	14
-12	-6	-7	6	-19	47	16	4	-6	-4	-13	-12	-1	-2	-2	-16	-15	14
-4	-4	-1	6	28	22	10	4	-1	1	4	-1	0	0	-1	-12	-15	14
-26	-17	0	20	28	28	19	17	9	2	2	-1	0	0	-1	-1	-15	14
-30	-5	-4	0	7	11	8	13	0	-1	5	-1	0	0	-1	-1	-15	14
-12	-11	0	0	0	0	0	0	0	0	0	-1	0	0	-1	-1	-15	14
0	-2	1	3	2	1	3	16	15	6	0	3	-1	1	0	-1	-1	14
0	1	1	3	2	1	3	0	0	1	0	0	-1	1	0	-1	-1	14
1	-6	-10	3	-7	18	-2	-1	0	0	0	0	-1	1	0	-1	-1	14
-4	1	0	3	5	5	-4	0	0	0	0	0	-1	1	0	-1	-1	14

NOF	IX2	LAYER	IRUV	ICPL	IRK												
20	5	5	2	0	1												
RK WRT SLO IN MODEL UNITS (1 UNIT = -6.0840-003) :																	
4	11	-23	-27	-1	14	-1	-31	-19	-21	-14	19	11	16	-12	-6	-3	-23
-14	26	3	2	13	61	9	77	7	9	3	0	3	8	4	12	2	3

TABLE E.1d (continued)

[illegible]

TABLE E.1e

LAYER 5, CELL (6,6)

[illegible][illegible][illegible][illegible]

NOF	IX2	LAYER	IRUV	ICPL	IRK												
20	5	5	2	0	1												
RK WRT SLO IN MODEL UNITS (1 UNIT = -6.0840-003) :																	
30	6	-19	-24	18	20	3	-11	-12	-10	-17							
17	9	-4	2	9	25	1	22	-2	-7	6	2	15	18	-20	-11	-23	-13
											0	3	-10	-4	-14	-5	13

TABLE E.1e (continued)

[illegible]

TABLE E.1f
LAYER 6, CELL (6,6)

NOF 20	IX2 1	LAYER 1	IRUV 2	ICPL 0	IRK 1
RK	WRT	SLO	IN	MODEL	UNITS (1 UNIT = -3.6000-003) :
0	0	0	0	0	0
0	0	0	0	0	0
0	0	0	0	0	0
0	0	0	0	0	0
0	0	0	0	0	0
0	0	0	0	0	0
0	0	0	0	0	0
0	0	0	0	0	0
0	0	0	0	0	0
0	0	0	0	0	0
0	0	0	0	0	0
0	0	0	0	0	0
0	0	0	0	0	0
0	0	0	0	0	0
0	0	0	0	0	0
0	0	0	0	0	0
0	0	0	0	0	0
0	0	0	0	0	0
0	0	0	0	0	0
0	0	0	0	0	0
0	0	0	0	0	0

NOF 20	IX2 2	LAYER 2	IRUV 2	ICPL 0	IRK 1
RK	WRT	SLO	IN	MODEL	UNITS (1 UNIT = -4.2250-003) :
0	0	0	0	0	0
0	0	0	0	0	0
0	0	0	0	0	0
0	0	0	0	0	0
0	0	0	0	0	0
0	0	0	0	0	0
0	0	0	0	0	0
0	0	0	0	0	0
0	0	0	0	0	0
0	0	0	0	0	0
0	0	0	0	0	0
0	0	0	0	0	0
0	0	0	0	0	0
0	0	0	0	0	0
0	0	0	0	0	0
0	0	0	0	0	0
0	0	0	0	0	0
0	0	0	0	0	0
0	0	0	0	0	0
0	0	0	0	0	0
0	0	0	0	0	0

NOF 20	IX2 3	LAYER 3	IRUV 2	ICPL 0	IRK 1
RK	WRT	SLO	IN	MODEL	UNITS (1 UNIT = -6.0840-003) :
0	0	0	0	0	0
0	0	0	0	0	0
0	0	0	0	0	0
0	0	0	0	0	0
0	0	0	0	0	0
0	0	0	0	0	0
0	0	0	0	0	0
0	0	0	0	0	0
0	0	0	0	0	0
0	0	0	0	0	0
0	0	0	0	0	0
0	0	0	0	0	0
0	0	0	0	0	0
0	0	0	0	0	0
0	0	0	0	0	0
0	0	0	0	0	0
0	0	0	0	0	0
0	0	0	0	0	0
0	0	0	0	0	0
0	0	0	0	0	0
0	0	0	0	0	0

NOF 20	IX2 4	LAYER 4	IRUV 2	ICPL 0	IRK 1
RK	WRT	SLO	IN	MODEL	UNITS (1 UNIT = -6.0840-003) :
-12	16	31	29	0	-7
-14	14	-	-17	0	-22
-15	10	-	11	0	33
-16	10	-	11	0	20
-17	10	-	11	0	5
-18	10	-	11	0	-11
-19	10	-	11	0	120
-20	10	-	11	0	15
-21	10	-	11	0	17
-22	10	-	11	0	15
-23	10	-	11	0	-16
-24	10	-	11	0	-65
-25	10	-	11	0	59
-26	10	-	11	0	27
-27	10	-	11	0	13
-28	10	-	11	0	16

NOF 20	IX2 5	LAYER 5	IRUV 2	ICPL 0	IRK 1
RK	WRT	SLO	IN	MODEL	UNITS (1 UNIT = -6.0840-003) :
22	-2	-12	20	39	-10
23	9	-10	-9	16	-17
24	9	-10	-9	16	-13
25	9	-10	-9	16	27
26	9	-10	-9	16	9
27	9	-10	-9	16	-2
28	9	-10	-9	16	-13
29	9	-10	-9	16	2
30	9	-10	-9	16	15
31	9	-10	-9	16	0
32	9	-10	-9	16	3
33	9	-10	-9	16	-9
34	9	-10	-9	16	-17
35	9	-10	-9	16	-18
36	9	-10	-9	16	-25
37	9	-10	-9	16	13

TABLE E.1f (continued)

[illegible]

LAYER 1, CELL (6,13)

[illegible][illegible][illegible][illegible]

NDF	IX2	LAYER	IRUV	ICPL	IRK												
20	5	5	2	0	1												
RK WRT SLO IN MODEL UNITS (1 UNIT = -6.0840-003) :																	
27	77	19	-11	28	79	-10	36	-34	-93	117	-34	-125	184	-131	-21	-82	82
-49	53	20	-4	-6	-1A	-7	-5	-2	-23	-4	-1	33	-22	-11	-11	-31	-2

TABLE E.2a (continued)

[illegible]

LAYER 2, CELL (6,13)

[illegible][illegible][illegible]

NOF	IX2	LAYER	IRUV	ICPL	IRK												
20	4	4	2	0	1												
RK WRT SLO IN MODEL UNITS (1 UNIT = -6.084C-003) :																	
-23	39	26	-4	-21	-5	23		3	-11	-35	-19	-21	-18	-19	-12	-68	38
-28	-6	13	2	11	6	0	18	-16	-14	-24	-29	-48	-45	-12	-5	-3	-5
-23	-3	-7	14	20	7	2	12	-12	-14	-22	-1	23	15	-5	4	20	-7
-8	-3	-9	-1	-5	-4	5	-2	-2	4	-1	-9	0	0	1	11	20	-8
-15	-19	-8	-9	-5	-4	-9	-20	4	2	-1	-9	-9	0	0	0	20	-1
-23	-5	-9	-9	0	-3	-5	0	6	0	3	-5	-3	-2	4	20	-2	-5
-14	-17	0	0	0	0	0	0	0	1	-3	-5	-3	-2	4	20	-2	-5
0	-4	1	1	-1	0	-3	2	-4	0	-1	-2	-1	-3	-1	26	1	-1
-2	-3	3	3	2	-1	-2	1	3	0	0	8	-1	-2	0	0	-6	0
-14	0	-4	7	-15	12	-2	2	0	0	0	12	-20	-5	0	0	0	0

NDF	IX2	LAYER	IRUV	ICPL	IRK												
20	5	5	2	0	1												
RK WRT SLO IN MODEL UNITS (1 UNIT = -6.0840-003) :																	
-16	27	11	3	37	41	10	-8	-44	-75	45	8	-62	58	-89	26	-18	-30
-22	29	11	17	17	21	-5	6	-5	-19	2	0	20	-13	-9	4	-9	19

TABLE E.2b (continued)

[illegible]

LAYER 3, CELL (6,13)

```

NOF  IX2  LAYER  IRUV  ICP  IRK
23    1      1      2      5      1
RK WRT SLO IN MODEL UNITS (1 UNIT = -3.6000-003) :

```

[illegible][illegible][illegible]

NDF	IX2	LAYER	IRUV	ICPL	IRK												
20	5	5	2	0	1												
RK WRT SLO IN MODEL UNITS (1 UNIT = -6.084E-003) :																	
-15	9	-3	-15	25	38	19	-25	-17	-29	-26	-11	-1	6	-40	16	-2	-24
-14	20	-3	3	-2	19	3	0	-3	-1	26	0	16	1	2	3	-5	11

TABLE E.2c (continued)

-5	-15	0	1	1	2	1	1	1	1	1	1	1	1	1	1	1
-11	-7	0	1	1	1	1	1	1	1	1	1	1	1	1	1	1
-22	-17	0	1	1	1	1	1	1	1	1	1	1	1	1	1	1
-11	0	0	0	0	0	0	0	0	0	0	0	0	0	0	0	0
-19	0	0	0	0	0	0	0	0	0	0	0	0	0	0	0	0
-2	0	0	0	0	0	0	0	0	0	0	0	0	0	0	0	0
-12	0	0	0	0	0	0	0	0	0	0	0	0	0	0	0	0
-13	-1	1	1	1	1	1	1	1	1	1	1	1	1	1	1	1
												</				

TABLE E.2d (continued)

IRK	ICPL	IRUV	LAYER	IX2	NDF
1	0	2	6	6	20
1	1	1	1	1	1
2	1	1	1	1	1
3	1	1	1	1	1
4	1	1	1	1	1
5	1	1	1	1	1
6	1	1	1	1	1
7	1	1	1	1	1
8	1	1	1	1	1
9	1	1	1	1	1
10	1	1	1	1	1
11	1	1	1	1	1
12	1	1	1	1	1
13	1	1	1	1	1
14	1	1	1	1	1
15	1	1	1	1	1
16	1	1	1	1	1
17	1	1	1	1	1
18	1	1	1	1	1
19	1	1	1	1	1
20	1	1	1	1	1

LAYER 5, CELL (6,13)

```

      NDF      IX2  LAYR  IRUV  ICPL  IRK
       20         1        1        2        0        1
RK WRT SLO IN MODEL UNITS (1 UNIT = -3.6COC-003) :

```

[illegible][illegible][illegible]

NOF	IX2	LAYER	IRUV	ICPL	IRK													
20	5	5	2	0	1													
RM WRT SLO IN MODEL UNITS (1 UNIT = -6.0840-003) :																		
9	-28	-32	-22	18	36	3	9	-10	-1	-10	-17	-3	9	-17	18	4	19	
12	5	-18	-9	-8	0	-7	3	-2	-4	11	0	8	-4	4	0	-16	-18	

TABLE E.2e (continued)

[illegible]

LAYER 6, CELL (6,13)

[illegible][illegible][illegible]

NOF	1X2	LAYER	IRUV	ICPL	IRK													
20	4	4	2	0	1													
RK WRT SLO IN MODEL UNITS (1 UNIT = -6.0840-C03) :																		
-10	7	24	27	1	-7	-22	30	24	-6	-13	-16	21	0	15	-9	-58	53	
21	-10	-21	-23	-6	10	-9	-4	-11	-13	-10	-11	16	-11	-11	-4	-3	13	
14	1	-19	-18	00	00	3	0	1	-1	2	2	-4	-3	1	5	4	1	
9	-8	1	-2	1	-4	1	1	6	1	2	2	1	1	1	0	4	9	
1	-2	-6	00	00	00	-1	0	5	8	2	-3	1	1	0	1	1	10	
4	-2	0	00	00	00	0	2	5	8	2	-3	1	1	0	1	1	1	
0	-1	0	1	1	-2	0	-9	10	-5	-6	-2	-1	-1	-1	0	-10		
0	-4	-1	5	2	1	1	0	-2	0	0	5	2	1	0	0	3	1	
4	3	-6	5	8	0	1	0	0	0	0	5	11	8	0	0	0	0	

```

NOF  IX2  LAYER  IRUV  ICPL  IRK
 20    5      5      2    0      1

RM WRT SLO IN MODEL UNITS (1 UNIT = -6.0840-003) :
37  -33  -45   -8   -30  -15   -3   8   -1  -7   9  22   6   6  -18   16  -7
14   6  -21  -17  -10   4   -3   4   -1  -9   7   0   5   -4  -2   -2  -2

```


TABLE E.2f (continued)

[illegible]